

Mid-Infrared Galaxy Morphology from the *Spitzer Survey of Stellar Structure in Galaxies* (S⁴G): The Imprint of the de Vaucouleurs Revised Hubble-Sandage Classification System at 3.6 μ m

Ronald J. Buta¹, Kartik Sheth^{2,3,4}, Michael Regan⁵, Joannah L. Hinz⁶, Armando Gil de Paz⁷, Karin Menéndez-Delmestre⁸, Juan-Carlos Munoz-Mateos⁷, Mark Seibert⁸, Eija Laurikainen⁹, Heikki Salo⁹, Dimitri A. Gadotti¹⁰, E. Athanassoula¹¹, Albert Bosma¹¹, Johan H. Knapen^{12,13}, Luis C. Ho⁸, Barry F. Madore⁸, Debra M. Elmegreen¹⁴, Karen L. Masters¹⁵, Sebastien Comerón¹⁶, Manuel Aravena²

Received _____; accepted _____

¹Department of Physics and Astronomy, University of Alabama, Box 870324, Tuscaloosa, AL 35487

²National Radio Astronomy Observatory / NAASC, 520 Edgemont Road, Charlottesville, VA 22903

³Spitzer Science Center, 1200 East California Boulevard, Pasadena, CA 91125

⁴California Institute of Technology, 1200 East California Boulevard, Pasadena, CA 91125

⁵Space Telescope Science Institute, 3700 San Martin Drive, Baltimore, MD 21218

⁶Steward Observatory, University of Arizona, 933 N. Cherry Ave., Tucson, AZ 85721

⁷Departamento de Astrofísica y CC. de la Atmósfera, Universidad Complutense de Madrid, Avda. de la Complutense, s/n, E-28040 Madrid, Spain

⁸The Observatories of the Carnegie Institution for Science, California Institute of Technology, MC 249-17, Pasadena, CA 91125

⁹Division of Astronomy, Department of Physical Sciences, University of Oulu, Oulu, FIN-90014, Finland

¹⁰European Southern Observatory, Casilla 19001, Santiago 19, Chile

¹¹Laboratoire d'Astrophysique de Marseille, Université de Provence/CNRS UMR 6110, 38 rue Frédéric Joliot Curie, 13388 Marseille Cédex 4, France

¹²Instituto de Astrofísica de Canarias, E-38200 La Laguna, Tenerife, Spain

¹³Departamento de Astrofísica, Universidad de La Laguna, E-38205 La Laguna, Tenerife, Spain

¹⁴Department of Physics & Astronomy, Vassar College, Poughkeepsie, NY 12604

¹⁵Institute for Cosmology and Gravitation, University of Portsmouth, Dennis Sciama Building, Burnaby Road, Portsmouth, PO1 3FX, UK

¹⁶Korea Astronomy and Space Science Institute 838, Daedeokdae-ro, Yuseong-gu, Daejeon Republic of Korea 305-38

ABSTRACT

Spitzer Space Telescope Infrared Array Camera (IRAC) imaging provides an opportunity to study all known morphological types of galaxies in the mid-IR at a depth significantly better than ground-based near-infrared and optical images. The goal of this study is to examine the imprint of the de Vaucouleurs classification volume in the $3.6\mu\text{m}$ band, which is the best *Spitzer* waveband for galactic stellar mass morphology owing to its depth and its reddening-free sensitivity mainly to older stars. For this purpose, we have prepared classification images for 207 galaxies from the *Spitzer* archive, most of which are formally part of the *Spitzer Survey of Stellar Structure in Galaxies* (S⁴G), a *Spitzer* post-cryogenic (“warm”) mission Exploration Science Legacy Program survey of 2,331 galaxies closer than 40 Mpc. For the purposes of morphology, the galaxies are interpreted as if the images are *blue light*, the historical waveband for classical galaxy classification studies. We find that $3.6\mu\text{m}$ classifications are well-correlated with blue-light classifications, to the point where the essential features of many galaxies look very similar in the two very different wavelength regimes. Drastic differences are found only for the most dusty galaxies. Consistent with a previous study by Eskridge et al. (2002), the main difference between blue light and mid-IR types is an ≈ 1 stage interval difference for S0/a to Sbc or Sc galaxies, which tend to appear “earlier” in type at $3.6\mu\text{m}$ due to the slightly increased prominence of the bulge, the reduced effects of extinction, and the reduced (but not completely eliminated) effect of the extreme population I stellar component. We present an atlas of all of the 207 galaxies analyzed here, and bring attention to special features or galaxy types, such as nuclear rings, pseudobulges, flocculent spiral galaxies, I0 galaxies, double-stage and double-variety galaxies, and outer rings, that are particularly distinctive in the mid-IR.

Subject headings: galaxies: spiral; galaxies: morphology; galaxies: structure

1. Introduction

The *Spitzer Survey of Stellar Structure in Galaxies* (S⁴G, Sheth et al. 2010) is a systematic imaging survey with the Infrared Array Camera (IRAC, Fazio et al. 2004a) of 2,331 galaxies in 3.6 and 4.5 μ m bands. The goal of the project is to derive basic photometric parameters for quantitative analysis of these galaxies for a variety of studies. Independent of these studies, however, the S⁴G database is an obvious goldmine for new investigations of galaxy morphology in the mid-infrared, if only because the images are deeper than anything achievable from reasonable ground-based near-IR observations and also because the images are homogeneous with respect to the point-spread function (PSF).

In this paper, we examine the imprint of the de Vaucouleurs revised Hubble-Sandage classification system on galaxy morphology at 3.6 μ m, using a subset of *Spitzer* archival images of galaxies that meet the selection criteria of the S⁴G (or are prominent companions to those galaxies). These images have been processed through the S⁴G Pipeline as described in Sheth et al. (2010), and have significantly improved quality compared to the post-Basic Calibrated Data (PBCD) mosaics provided in the SSC archive for photometric analysis. The goal of our analysis is not merely general Hubble classifications, but detailed types as described in the *de Vaucouleurs Atlas of Galaxies* (Buta, Corwin & Odewahn 2007, hereafter the dVA). We want to know how closely optical galaxy morphology maps into the mid-IR. Section 2 gives some background to IR morphological studies, while section 3 describes how we prepared the S⁴G Pipeline processed *Spitzer* images for detailed morphological study. Section 4 summarizes our analysis of the *Spitzer* archival 3.6 μ m images. Our conclusions are summarized in section 5.

2. Near- and Mid-IR Galaxy Morphology

Galaxy morphology in the near- and mid-IR, as in other wavebands, is important to examine because of the information morphology carries on processes of galactic evolution. Morphology is strongly correlated with galactic star formation history, environmental density and interaction/merger history, and the effectiveness with which internal perturbations (such as bars) interact with other internal components (such as the halo and the basic state of the disk). Early evolution was probably dominated by merger events, and this has found support in recent studies of the merger rate (e.g., Mihos & Hernquist 1996). Slower internal secular evolution has been increasingly invoked to explain the disk-like properties of “pseudobulges” (e.g., Kormendy & Kennicutt 2004, Athanassoula 2005) and to account for the development of other features, such as rings and spiral arms, in response to perturbations such as bars and ovals. Together, these processes appear to combine to produce the wide range of galaxy types that we see nearby.

Galaxy classification is still an important part of modern extragalactic studies. Catalogues of galaxy Hubble types or Hubble-related types are often the starting point of observational investigations, and nearly 80 years of research have not negated or made obsolete the classification systems (e.g., Hubble 1926, 1936; Sandage 1961; Sandage & Bedke 1994; de Vaucouleurs 1959) that form the basis of catalogued types. The frequency and statistical properties of structures in galaxies need to be known in order to determine how these structures fit into the general scheme of galaxy evolution. As noted by Fukugita et al. (2007), who used Sloan Digital Sky Survey (SDSS) color images to classify 2253 bright galaxies, visual classification “remains the best approach for classifying each galaxy into a Hubble type with high confidence, at least for bright galaxies.” This survey was followed up by a more detailed morphological analysis by Nair & Abraham (2010), who recorded rings, bars, Hubble types, and other features for more than 14,000 SDSS galaxies, as a means

of facilitating automatic classification. In addition, the Galaxy Zoo project (Lintott et al. 2008) has provided basic morphological information for nearly a million galaxies, from citizen science participation (see also Banerj et al. 2010).

Although as a topic of research galaxy morphological studies began with blue-sensitive photographic plates, in recent years the emphasis has shifted considerably towards longer wavelengths. Early red and near-infrared imaging showed that galaxies which, in blue light, show a patchiness due to dust and complexes of recent star formation, become smoother at the longer wavelengths owing to the reduced effects of extinction and the de-emphasis of the younger component. The longer wavelengths emphasize the older stellar components, including old disk giants and Population II stars. Although photographic red and near-infrared imaging were possible in the 1950s-1980s, and were even the subjects of large sky surveys, no large-scale systematic galaxy morphological studies were ever based on these surveys. Only the blue surveys were used for systematic galaxy classification (e.g., Nilson 1973; Lauberts 1982; Corwin et al. 1985; Buta 1995), because the original Hubble system was based on blue light photographs. Even so, it was already known that features like inner bars (e.g., Hackwell & Schweizer 1983; Scoville et al. 1988; Thronson et al. 1989; Telesco et al. 1991; Block & Wainscoat 1991; Rix & Rieke 1993), triaxial nuclear bulges (e.g., Zaritsky & Lo 1986), and regular bars (e.g., Talbot et al. 1979) could be partly obscured or simply less prominent in blue light images, but become more visible in the red and infrared. Detailed studies of bar fractions in the near-IR have shown a comparable (or sometimes slightly larger) fraction to that given by the early blue light studies. This issue is further discussed in section 4.6.

It was also known that spiral structure which may appear “flocculent” in blue light and at $0.8\mu\text{m}$ (Elmegreen 1981) could appear more global (i.e., continuous and large-scale, or “grand design”) at $2.2\mu\text{m}$ (Thornley 1996). The differences between optical and near-IR

morphologies for some galaxies appeared to be so great that in early studies, it was suggested that there is a “duality” of galactic structure, in the sense that the Population I and II morphologies are decoupled (Block & Wainscoat 1991; Block et al. 1994, 2004).

Several developments brought large-scale digital IR imaging to the forefront of galaxy morphological studies. The first was extending near-IR imaging from individual galaxies or parts of galaxies to statistical-sized samples. This began with near-IR surface photometry of 50 spirals by Elmegreen & Elmegreen (1984, 1987) and of 86 galaxies by de Jong & van der Kruit (1994). The first major near-IR survey designed for large-scale morphological studies was the Ohio State University Bright Spiral Galaxy Survey (OSUBSGS, Eskridge et al. 2002), which included optical $BVRI$ and near-IR JHK images of 205 bright galaxies of types S0/a to Sm in a statistically well-defined sample selected to have total blue magnitude $B_T \leq 12.0$ and isophotal diameter $D_{25} \leq 6'.5$. This survey allowed a direct demonstration of how galaxy morphology actually changes from optical to near-IR wavelengths, not merely for a small, selected sample of galaxies, but for a large sample covering all spiral subtypes.

The OSUBSGS was later complemented by the *Near-Infrared S0 Survey* (NIRS0S, Laurikainen et al. 2005, 2006, 2010; Buta et al. 2006), a K_s -band imaging survey of about 180 early-type galaxies in the type range S0⁻ to Sa, but mostly including S0s, some of which were misclassified as ellipticals in the Third Reference Catalogue of Bright Galaxies (RC3, de Vaucouleurs et al. 1991; see below). Although S0 galaxies are dominated by old stars and are smooth even in blue light images, the K_s band was chosen to complement the OSUBSGS sample of spirals in order to make a fair comparison between bar strengths and bulge properties of S0s and spirals. Also, S0 galaxies are not necessarily dust-free, and near-IR imaging is still necessary to penetrate what dust they have.

The second development was the *Two-Micron All-Sky Survey* (2MASS, Skrutskie et al. 1997), which provided JHK_s images of a much larger galaxy sample, although these lack

the depth of the OSUBSGS and NIRS0S images in general. 2MASS provided considerable information on near-infrared galaxy morphology, which led to the extensive *2MASS Large Galaxy Atlas* (Jarrett et al. 2003). 2MASS images were also used by Menéndez-Delmestre et al. (2007) to study quantitative near-IR bar classification and its comparison to RC3 classifications.

The third development was the launch of the *Spitzer Space Telescope* (Werner et al. 2004) and subsequent IRAC imaging surveys such as the *Spitzer Infrared Nearby Galaxies Survey* (SINGS, Kennicutt et al. 2003). SINGS provided both optical and mid-IR imaging of 75 galaxies of all types at a depth much greater than that of the OSUBSGS, NIRS0S, or 2MASS. SINGS was followed by the *Local Volume Legacy* project (LVL, Kennicutt et al. 2007), which will provide IRAC images (as well as images in other passbands) of 258 mostly late-type galaxies nearer than 11 Mpc.

Among these various sets of data, the NIRS0S is the only IR imaging survey carried out to a significant extent with 4-m class telescopes. The full width at half maximum (FWHM) of the stellar PSF for these images is generally $<1''$ compared to $1''.5$ - $2''$ for OSUBSGS images, $3''$ for 2MASS images, and $1''.75$ for SINGS images.

The S⁴G has been designed to provide a set of very deep mid-IR images at good spatial resolution of an unprecedentedly large sample of nearby galaxies: 2,331 galaxies of all Hubble types within a distance of 40Mpc. The images are being obtained in the IRAC 3.6 and $4.5\mu\text{m}$ bands. Of this sample, 597 galaxies are already in the *Spitzer* archive, and the goal of the S⁴G is to add the 1,734 remaining sample galaxies as part of the *Spitzer* Warm Mission. The advantages of *Spitzer* images lie in their homogeneity and, most of all, in their considerable depth at wavelengths where ground-based observations (e.g., at $2.2\mu\text{m}$) would suffer very high background (sky) emission. Also, the IRAC 3.6 and $4.5\mu\text{m}$ bands are in a regime where extinction is even lower than in the near-IR *JHK* bands, and

where contamination by dust heated by stellar processes is also still low, so that the bands are largely sampling the backbone of stellar mass in galaxies (Pahre et al. 2004). However, there is still a contribution from young stars, the nature of which is discussed in section 4.5.

We use a subsample of 167 S⁴G-pipeline processed *Spitzer* archival 3.6 μ m images to classify 207 bright galaxies (including 24 pairs and 16 additional galaxies in small groups) in the formal framework of the de Vaucouleurs revised Hubble-Sandage classification system, as revised and updated in the dVA. This subset has no distinguishing characteristics other than being archival galaxies selected by S⁴G team members for initial study and analysis. Such a sample will have the selections of a variety of programs that were granted observing time. Figure 2 shows the frequency distributions (solid histograms) of RC3 classifications (stages, families, and varieties), absolute blue magnitudes M_B^o , total extinction-corrected color indices $(B - V)_T^o$, and extinction-corrected mean blue light effective surface brightnesses $(m'_e)_o$, the latter three parameters also from, or based on, RC3 data. These plots show that the sample galaxies cover a broad range of properties. The full range of galaxy types, from E to Im, as well as giants and dwarfs, is represented. For comparison, Figure 2 also shows the frequency distributions (dashed histograms) of the same parameters for the full S⁴G sample. The distributions are similar except that our subset has relatively more E and S0 galaxies and high luminosity galaxies than the full S⁴G sample.

A partial attempt to classify galaxies using the de Vaucouleurs system was also made by Eskridge et al. (2002), who applied the system using OSUBSGS near-IR *H*-band (1.65 μ m) images *as if they were blue light images*. That is, the framework of the de Vaucouleurs system was used without regard to the wavelength used to actually define the system. Eskridge et al. showed that although some galaxies can look very different in the near-IR as compared to the *B*-band, in general the differences are not so large as

to make near-IR types uncorrelated with optical types. As we will show here also, the imprint of the de Vaucouleurs B -band classification volume holds well in the *Spitzer* $3.6\mu\text{m}$ band, and the classifications correlate closely. The same was also found to hold true in the mid/near-UV, at least for later type galaxies (e.g., Windhorst et al. 2002). Taylor-Mager et al. (2007) also found only a mild dependence of concentration-asymmetry-star formation (CAS) parameters on wavelength, suggesting that good morphological correlation between different wavelength regimes is probably valid at all wavelengths dominated by the emission from stellar photospheres.

3. Preparation of the Images

The goals of the S⁴G project are described by Sheth et al. (2010). One goal was the processing of the *Spitzer* images of all archival galaxies with the same S⁴G pipeline as the new Warm Mission data in the S⁴G sample. This processing was done to prepare the images for detailed studies such as photometric decompositions, Fourier analysis, and color index analysis. Like the SINGS images, the scale of the final S⁴G pipeline-processed images is $0''.75$ per pixel, with a FWHM of $\approx 1''.8$.

The requirements for galaxy morphological classification are no less stringent than they would be for photometric analysis. The images must be accurately background-subtracted, and the point-spread function should be reasonably narrow (FWHM $< 2''.5$), allowing about 100 resolution elements across the major axis. The background in *Spitzer* images is low, but variations due to zodiacal light are sometimes present. Bright foreground stars can affect some archival images, but scattered light from such stars should be less of a problem for the 1,734 Warm Mission galaxies because special precautions are being taken to prevent bright stars from falling into scattering zones.

In order to classify the galaxies, each processed image was converted to units of magnitudes per square arcsecond (the same approach as used in the dVA). Because all the pipeline-processed images are in the same final physical units, MJy/sr, this conversion was performed using the same zero point, 17.69, based on the Vega magnitude calibration given in the *IRAC Instrument Handbook*. The images were then displayed in ds9 using IRAF routine DISPLAY with a faint limit of 28.0 mag arcsec⁻² and a bright limit depending on the galaxy, ranging from as bright as 11.0 mag arcsec⁻² to 18.0 mag arcsec⁻² or fainter. The classification images prepared in this manner are illustrated in Figures 1.1 - 1.197.

The reason for using this approach is that images in units of mag arcsec⁻² reveal the morphology over the whole range of surface brightnesses, from the center to the outer disk, much better than do linear intensity images. In early classifications, photographic plates gave a limited range in the linear relation between photographic density and the logarithm of the intensity. IRAC data have a much larger dynamic range, and hence all the details of a galaxy, including subtle ones, can be displayed at once. This is useful for accurate classification, and especially for recognizing the subtle distinctions between elliptical galaxies and very early S0 galaxies. We examined all images using a 24-bit image display, and in each case a stretch was chosen (by varying contrast and brightness) that maximized the morphological information visible. This display setting was then saved in uncompressed jpeg format. Thus, the present survey is based on a variable dynamic range, as opposed to the surveys based on homogeneous photographic material, i.e. the dwarfs are displayed with a shorter dynamic range, and higher contrast, than the bright spirals.

4. 3.6 μ m Morphological Classification

With a final set of images in hand, the galaxies were classified using the three dimensions of the de Vaucouleurs revised Hubble-Sandage system (de Vaucouleurs 1959).

Full types include the *stage* (E, E⁺, S0⁻, S0^o, S0⁺, Sa, Sab, Sb, Sbc, Sc, Scd, Sd, Sdm, Sm, and Im), the *family* (SA, SAB, SB), the *variety* (r, rs, s), the *outer ring or pseudoring* classification (R or R', if present), and indications of a *spindle* shape (sp, meaning edge-on or near edge-on orientation) and the presence of any *peculiarity* (pec, often referring to unusual and likely interaction-driven asymmetries).

The classifications were made by RB and independently verified by JK, and are consistent with the dVA and RC3 classification systems. Any systematic differences between the actual blue light classification and the mid-IR classification can then be mostly attributed to the effects of bandpass. The “scatter” in type classifications by individual observers is quantified by Naim et al. (1995).

4.1. Assigning Stage, Family, and Variety

In de Vaucouleurs’s classification approach, the implication for bars, inner rings, and stages is a continuum of forms (de Vaucouleurs 1959). The stage for spirals is based on the appearance of the spiral arms (degree of openness and resolution) and also on the relative prominence of the bulge or central concentration. These are the criteria originally applied by Hubble (1926, 1936). Sa, Sb, and Sc spirals are mostly as defined by Hubble, with the additional stages Sd, Sm, and Im as appended by de Vaucouleurs. Intermediate stages (Sab, Sbc, Scd, Sdm) are almost as common as the main types. In some cases, the three spiral criteria are inconsistent, or other factors enter in that affect the type (Sandage 1961; Sandage & Bedke 1994). In general, the bulge-to-total luminosity ratio is directly related to Hubble type, but there is considerable scatter at a given type (see Simien & de Vaucouleurs 1986; Laurikainen et al. 2007, Graham & Worley 2008).

The family classifications SA, SAB, and SB are the purely visual estimates of bar

strength. The intermediate bar classification SAB is one of the hallmarks of the de Vaucouleurs system, and is used to recognize galaxies having characteristics intermediate between barred and nonbarred galaxies. Underline notation SAB and SAB (de Vaucouleurs 1963) is used to further underscore the continuity of this characteristic.

Although a bar that looks relatively weak in blue light can appear stronger in the near- or mid-IR, IR imaging does *not* necessarily change the *rankings* of bars. A bar which appears strong in blue light may also appear even stronger in the IR. Studies of the maximum relative bar torque parameter Q_b (e. g., Buta et al. 2005), show that what we usually call “SB” has a wide range of strengths. Q_b is the maximum relative bar torque per unit mass per unit square of the circular speed, and has been found to range from 0 for no bar to at least 0.7 for the strongest bars. Buta et al. (2005; see also the dVA) defined the Q_b family as follows: SA types have $Q_b < 0.05$; SAB types have $0.05 \leq Q_b < 0.10$; SAB types have $0.10 \leq Q_b < 0.20$; SAB types have $0.20 \leq Q_b < 0.25$, while SB types have $Q_b \geq 0.25$. The Q_b family is an approximate quantitative representation of the visual bar strength classes.

Variety is also treated as a continuous classification parameter, ranging from closed inner rings (r) to open spirals (s). The intermediate variety (rs) is also well-defined. As for family, underline notation rs and rs is used to underscore further continuity.

The classification of S0 galaxies depends on recognizing the presence of a disk and a bulge at minimum, and usually a lens as well, and no spiral arms. A lens is a galaxy component having a shallow brightness distribution interior to a sharp edge. Even if a lens isn’t obvious, a galaxy could still be an S0. (Lenses are also not exclusive to S0s.) Other structures, such as bars and rings, can enter in the classification of S0s. The stage sequence $S0^-$, $S0^0$, $S0^+$ is a sequence of increasing detail. Exceptionally early nonbarred S0s can look very much like ellipticals, and in fact some galaxies classified as ellipticals in RC3 are

classified as S0 galaxies in the *Revised Shapley-Ames Catalogue* (RSA, Sandage & Tammann 1981). The transition type S0/a is the formal beginning of the spiral stage sequence.

In mag arcsec⁻² units, luminous elliptical galaxies usually have very smooth light distributions with no trace of a lens or any other structures. In principle, we should be able to classify ellipticals more consistently with digital images than with photographic plates, but the distinction from early S0s can still be very subtle in some cases as we have noted. de Souza et al. (2004) found that about a third of elliptical galaxies can be misclassified as S0s, and that it is equally easy to misclassify an elliptical as an S0 as the other way around. Type E⁺ was originally intended by de Vaucouleurs (1959) to describe “late” ellipticals, or “the first stage of the transition to the S0 class.”

Outer ring and pseudoring classifications are made in the same manner as in blue light: the more closed outer rings are classified as (R) preceding the main type symbols, while large pseudorings made of outer spiral arms whose variable pitch angle causes them to close together are classified as (R′). In general, these classifications are not very sensitive to the difference between blue and near-IR bands, although one or the other may facilitate detecting the structures better.

A *spindle* is a highly inclined disk galaxy. For blue-light images, usually an “sp” after the classification would almost automatically imply considerable uncertainty in the interpretation, because stage, family, and variety are not easily distinguished when the inclination is high. Even in the near-IR, classifying spindles is still difficult, but nevertheless can be better than in blue light because planar absorption lanes are far less significant. One important development in the classification of edge-on galaxies has been the ability to recognize edge-on bars through boxy/peanut and “X”-shapes. Boxy/peanut bulges in edge-on galaxies were proven to be bars seen edge-on from kinematic considerations (cf. Kuijken & Merrifield 1995; see also Bureau & Freeman 1999). These shapes can be more

clearly evident in *Spitzer* images than in blue-light images. An example here is NGC 2683 (Figure 1.47).

A few classification details are used here that were not originally part of the de Vaucouleurs system, but were used or discussed in the dVA. For example, the notation “E (shells/ripples)” or “S0 (shells/ripples)” is used to denote an elliptical or S0 galaxy that shows faint arc-like or curved enhancements (Malin & Carter 1980, 1983). The term “shells” implies a particular three-dimensional geometry that Schweizer & Seitzer (1988) argued imposes a prejudice on the interpretation of the structures. They proposed instead the alternate term “ripples,” which implies less of a restrictive geometry. The *Spitzer* images are deep enough to reveal even the inner shells in ellipticals well, if they are there, and at least 4 shell galaxies were identified in the relatively small subsample of the S⁴G studied here. We use the notation E(d) for disk ellipticals and E(b) for boxy ellipticals, after Kormendy & Bender (1996). Although quantifiable in terms of Fourier analysis, our classification is by eye and thus selects the most obvious cases. These distinctions, which relate to velocity anisotropy, can be seen mainly in ellipticals harboring edge-on disks.

Following Kormendy (1979), we also recognize both inner lenses (l) and outer lenses (L). We also recognize the “outer Lindblad resonance (OLR)” subcategories of outer rings and pseudorings, R_1 , R'_1 , R'_2 , and $R_1R'_2$, following Buta & Crocker (1991) and Buta (1995). An R'_1 outer pseudoring is defined by a 180° winding of two spiral arms relative to the bar ends, while an R'_2 outer pseudoring is defined by a 270° winding. R_1 outer rings are more detached versions of R'_1 outer pseudorings, while the double outer ring/pseudoring morphology $R_1R'_2$ is a distinctive combination of features including an R_1 component surrounded by an R'_2 pseudoring.

The prominence of nuclear rings and bars in $3.6\mu\text{m}$ images further necessitates additional classification symbols beyond those just described. The nuclear rings in our

sample are so distinctive that we have used notation suggested by Buta & Combes (1996) to recognize them. For example, NGC 3351 is classified as (R')SB(r,nr)a, where “nr” is the symbol for nuclear ring (“nl” if a lens instead). Comerón et al. (2010) have compiled an atlas of known nuclear rings and made a statistical study of their sizes and other characteristics. In addition, nuclear bars are seen in several of the sample galaxies, and are distinctive enough features that we have also recognized them with the type classification “nb.” Thus, the classification of NGC 5850 is (R')SB(r,nr,nb)ab. We caution, however, that we cannot provide these classifications for all S⁴G galaxies where nuclear rings and bars may be present because the resolution (in parsecs) is critical for detecting them, and as a result we can never make a claim that the classification is complete.

4.2. Comparison of Classifications

Our 3.6 μ m classifications are listed in Table 1, together with the classifications for the same galaxies given in the RC3, the RSA, the dVA, and also in Eskridge et al. (2002), which has 22 galaxies in common with our sample. Following de Vaucouleurs (1963), we use “:” or “?” to indicate different levels of uncertainty, with “?” implying greater uncertainty. In order to compare the 3.6 μ m stages, families, and varieties with those listed in the RC3, the RSA, and the dVA, we use convenient numerical indices. For the stage, the 15 types from E to Im are assigned numerical T values as follows: -5 (E), -4 (E⁺), -3 (S0⁻), -2 (S0^o), -1 (S0⁺), 0 (S0/a), 1 (Sa), 2 (Sab), 3 (Sb), 4 (Sbc), 5 (Sc), 6 (Scd), 7 (Sd), 8 (Sdm), 9 (Sm), and 10 (Im) (de Vaucouleurs & de Vaucouleurs 1964). For family and variety, we use the numerical indices adopted by de Vaucouleurs & Buta (1980): $F=-1$ for SA, 0 for SAB, and $+1$ for SB families, and $V=-1$ for (r), 0 for (rs), and $+1$ for (s) varieties. Underline notations in all cases are assigned half steps. The comparisons are plotted as histograms of the numerical index difference, $\Delta(T, F, V) = T, F, V(S^4G) - T, F, V(other)$

in Figures 3 - 5. All of the top frames in these figures are $\Delta(T)$ comparisons. If $\Delta(T) < 0$, the S⁴G classification is earlier than the other source’s classification, while if $\Delta(T) > 0$, the S⁴G classification is later. The $\Delta(F)$ comparisons are in the two lower left frames. If $\Delta(F) < 0$, the S⁴G bar classification is more nonbarred than the other source’s classification, while if $\Delta(F) > 0$, the S⁴G bar classification is more barred. The $\Delta(V)$ comparisons are in the two lower right frames. If $\Delta(V) < 0$, the S⁴G variety classification is more ringed than the other source’s classification, while if $\Delta(V) > 0$, the S⁴G variety classification is more spiral-shaped.

The RC3 stage comparisons in Figure 3 (top left frame and lower three frames) show first that the bin with the largest number of galaxies has $\Delta(T) = 0$, meaning the 3.6 μ m stage and the RC3 stage are the same. The largest difference is found for RC3 stages S0/a-Sc, where many galaxies are classified 1 stage interval *earlier* than in RC3. This is very similar to what was found by Eskridge et al. (2002) using ground-based 1.65 μ m *H*-band images for classifications, where galaxies with RC3 types Sab to Sc were classified about 1 stage interval earlier at 1.65 μ m than in RC3. The same systematic effect was found for types Sa to Scd when these authors compared their 1.65 μ m types with their own *B*-band types estimated from OSUBSGS images.

In the family and variety comparisons (upper right panels of Figure 3), the most populated bins again have $\Delta=0$. In fact, in these the concentration in the $\Delta=0$ bin is much larger than that in the stage comparisons in the upper panels. The plots show considerable consistency between RC3 families and varieties and our Table 1 judgments. Surprisingly, in this comparison we do not see a tendency for $\Delta(F)$ to be greater than zero (the “stronger bar” effect), which is what we would see if many 3.6 μ m bar classifications advanced to higher bar strengths compared to RC3 classifications. That is, a big shift of SA to SAB and SAB to SB is not seen. In contrast, Eskridge et al. (2000) report a factor of 2 more SBs

than in RC3. The problem with this kind of comparison is that blue light SB-type bars, as seen in the IR, do not have a new classification bin to be placed in if they look stronger in the IR, while blue light SAB-type bars do have a new bin - type SB. This appears to increase the number of strong bars when in fact there is little change in bar rankings. In Table 1 there are 16 galaxies in common with Eskridge et al., and of those, 12/16 are classified as SB by Eskridge et al., 8/16 are SB in Table 1, and 7/16 are SB in RC3. The difference between Eskridge et al. on one hand, and the Table 1 classifications on the other, is likely not due to small number statistics in the Eskridge et al. sample, but to a difference in what is called an SB. Our result is more consistent with Menéndez-Delmestre et al. (2007) and Sheth et al. (2008), who found the same bar frequency from the B -band to the K -band, based on a semi-automated method of bar detection.

The comparisons shown in Figure 4 for RSA galaxies are different because the RSA represents a different classification system. There are very few RSA galaxies classified as later than Sc, and the classification of S0s is somewhat different. Nevertheless, we assigned the same numerical indices to types S0/a to Im as for RC3, and we assigned values of -3 , -2 , and -1 for types S0₁, S0₂, and S0₃, the same as for types S0⁻, S0^o, and S0⁺, respectively. Ellipticals are assigned $T=-5$, just as in RC3. Classifications like “E7/S0⁻” were assigned $T=-4$. The comparison shows that for the full range of RSA types, there is little systematic difference between RSA and 3.6 μ m stages. However, for RSA stages Sab-Sbc, the “earlier effect” is definitely seen, while for RSA stages Sc-Im, the 3.6 μ m types are actually later. Only for types E-Sa is little or no systematic difference seen. The family comparison shows that bar classifications are definitely stronger on average in the 3.6 μ m types as compared to the RSA, and inner rings are classified more often in the 3.6 μ m sample than in the RSA. Most of these differences are due to differences between the RSA and de Vaucouleurs classification systems, and not to wavelength effects. The use of the SAB symbolism allows RC3 types to be more discriminatory on bar classifications than

RSA types; a “stronger bar” effect is seen even in a comparison of RC3 and RSA blue light classifications, due mainly to RC3 SAB galaxies classified mostly as S in the RSA. In the case of variety, any inner ring that is made of tightly-wrapped spiral arms is classified as (s) variety in the RSA, and usually as (r) in RC3 or (r) or (rs) in Table 1.

The dVA comparisons in Figure 5 are similar to the RC3 comparisons, but show slightly more prominent “earlier type” and “stronger bar” effects. The comparisons of dVA and $3.6\mu\text{m}$ types show less scatter not because of greater precision, but because the same observer classified both data sets. Thus, Figure 5 is more of an internal, rather than an external, comparison.

4.3. Noteworthy Examples

The results from the previous section are illustrated in Figures 6- 10. These compare S⁴G $3.6\mu\text{m}$ images in mag arcsec⁻² units with *B*-band images in the same units. Most of the *B*-band images are from the dVA.

The four galaxies shown in Figure 6 cover a wide range of types. The images of the Sdm/Sm galaxy NGC 428 are barely different. This is true also for the Sc galaxy NGC 628, although its inner arms are smoother in the $3.6\mu\text{m}$ image than in the *B*-band image. The image of NGC 1097 definitely looks a little earlier at $3.6\mu\text{m}$, but still the differences are relatively small. NGC 584 is an early-type galaxy shown in the figure that highlights the greater depth of the $3.6\mu\text{m}$ image compared to a typical optical image. Although classified as type E in RC3, NGC 584 is definitely an early S0 galaxy.

The four ringed galaxies in Figure 7 all show the “earlier effect”: S0/a galaxy NGC 1291 becomes type S0⁺; SBab galaxies NGC 1433 and NGC 1512 become type SBa; and SBb galaxy NGC 3351 becomes type SBa. Even with these type changes, the overall

morphology of all four galaxies looks nearly the same in the two filters.

Figure 8 and the top panels of Figure 9 show three classic “flocculent” spirals, NGC 2841, 5055, and 7793 (Elmegreen 1981). In blue light all three have rather piece-wise continuous spiral structures, but not the global patterns characteristic of grand design spirals. In NGC 2841 and 5055, dust is a major factor in the appearance of the spiral structure.

NGC 2841 changes from type Sb in the B -band to type Sa at $3.6\mu\text{m}$, mostly because of the penetration of this dust. Even so, the overall appearance of the more coherent B -band spiral features in NGC 2841 is about the same at $3.6\mu\text{m}$. The $3.6\mu\text{m}$ image also reveals a weak bar in NGC 2841, $\approx 30''$ in radius and with a position angle of $\approx 160^\circ$ (compared to the galaxy major axis position angle of 147° listed in RC3). This is not the same bar-like feature described by Varela et al. (1996), who identified a nuclear bar-like structure about $10''$ in radius. The inner ring in NGC 2841 recognized in Table 1 is a large feature, 3:1 in angular diameter, but the structure of the whole galaxy is very much a series of ring-like features.

In NGC 5055, the flocculent spiral pattern looks more global at $3.6\mu\text{m}$. However, the appearance of the main arms still favors an Sbc classification, the same as the RC3 B -band type. The main difference is that the feature classified as an inner pseudoring in RC3 [the type is SA(rs)bc] is a smooth inner spiral at $3.6\mu\text{m}$. The ring/lens (rl) feature recognized in the Table 1 classification lies *inside* the RC3 pseudoring (as seen also in the $2.2\mu\text{m}$ image shown in Thornley 1996). In the inner parts of NGC 5055, and throughout the disk of NGC 2841, star-forming regions are not prominent, but throughout the outer disk of NGC 5055, the $3.6\mu\text{m}$ image reveals many large star-forming complexes.

The images of NGC 7793 in Figure 9 show a slightly more coherent spiral pattern in the $3.6\mu\text{m}$ as compared to B , but which is still largely flocculent. The most noticeable

difference is in the size of the bulge, which seems more prominent at $3.6\mu\text{m}$. However, in this case the IRAC image is not as deep as the B -band image. Because of the more prominent bulge and more coherent pattern at $3.6\mu\text{m}$, the classification given in Table 1 is Sc compared to the B -band type of Sd.

The second row of Figure 9 shows NGC 4527. This highly inclined, dusty spindle shows a well-defined nuclear ring and a weak bar and partial inner ring. Similar to NGC 5055, NGC 4527 does not look like an earlier type at $3.6\mu\text{m}$. The third row shows NGC 4579, an example where the B -band bar (type SAB in the dVA) becomes type SB at $3.6\mu\text{m}$. The $3.6\mu\text{m}$ image also reveals a faint outer ring, not recognized in the RC3, RSA, or the dVA, tightly surrounding the inner spiral. The ring has dimensions of $4'4 \times 3'2$, and may have been missed in the earlier blue light classifications owing to the uncertain effects of extinction, not because of faintness. The fourth row shows NGC 4736, a galaxy with a very wide range of surface brightness from the center to the outer disk. The change in type from B to $3.6\mu\text{m}$ is only Sab to Sa. The most striking aspect of the $3.6\mu\text{m}$ morphology of NGC 4736 is how the broad, intermediate oval zone (the basis for the Table 1 classification SAB) becomes a large ring/lens feature. The prominent B -band inner pseudoring is still a pseudoring at $3.6\mu\text{m}$, but following Knapen (2005) and Comerón et al. (2010), this feature is interpreted as a nuclear pseudoring (nr') in Table 1. The nuclear lens (nl) and nuclear bar (nb) in the Table 1 classification are inside the nr' .

Figure 10 shows images of four very late-type galaxies. The top row shows NGC 1705, typed as SA0^- : pec in the RC3 and Amorphous in the RSA. Meurer et al. (1989) interpreted the galaxy as a nucleated blue compact dwarf (BCD), where the nucleus in this case is a super star cluster having absolute blue magnitude -15 (Melnick et al. 1985). The peculiar morphology with strange filaments is evident in the B -band image, and accounts partly for the dVA type of I0/BCD, but at $3.6\mu\text{m}$, NGC 1705 looks more like a dwarf

elliptical with a slightly miscentered nucleus. This accounts for the classification “dE3, N” in Table 1, meaning nucleated dwarf elliptical (Binggelli et al. 1985). Table 1 also includes a few galaxies classified as “dE (Im)”; NGC 3738, shown in the second row of Figure 10, is an example. This refers to an object where the structure in blue light consists of an irregular, bright inner star-forming zone, surrounded by smoother elliptical isophotes. At $3.6\mu\text{m}$, the inner star-forming zone may be subdued, and the smooth elliptical background takes prominence.

The third and fourth rows of Figure 10 show NGC 3906 and NGC 4618, two examples of very late type barred spirals where the bar is miscentered within very regular outer isophotes. These offcentered barred galaxies have been extensively discussed by de Vaucouleurs & Freeman (1972; see also Freeman 1975). The asymmetry of these galaxies is characteristic of these very late types and it is possible to still recognize them in the edge-on view. For example, we interpret IC 2233 (Figure 1.168) as an edge-on SBdm galaxy, because it has a bright elongated, somewhat offset inner zone that is likely to be an off-center bar as in NGC 3906. By the same token, NGC 55 (Figure 1.3) is interpreted to be a nearly edge-on view of NGC 4618. In this case, the bar is seen on the northwest side of the major axis, while the considerable amount of light to the northeast would be the single main spiral arm. In many other of the very late-types in Table 1, we suspect that inner boxy zones, or bright miscentered zones of limited extent, are edge-on views of bars.

4.4. Special Cases

We note the following special cases in our small subsample of 207 mostly S⁴G galaxies.

I0 Galaxies - Two of the galaxies in our sample are classified as types I0 in RC3. The top panels of Figure 11 show NGC 5195, the familiar companion of M51. Hidden behind the

dust in the B -band image is a very regular early-type galaxy with a relatively weak bar oriented north-south and a broad and diffuse inner ring. The lower panels in Figure 11 show NGC 2968. We do not have a B -band digital image of NGC 2968, and the figure shows the photograph of the galaxy from the Carnegie Atlas of Galaxies (Sandage & Bedke 1994), as downloaded from the NASA/IPAC Extragalactic Database (NED) website. Although the Carnegie Atlas photograph is not very deep, it is sufficient to show a complex, dusty early-type system typical of I0 galaxies. The $3.6\mu\text{m}$ image of NGC 2968 reveals a beautifully symmetric late barred S0. These are the only galaxies in the sample of 207 where the $3.6\mu\text{m}$ morphology looks drastically different from the B -band. For these galaxies, the I0 class is not needed at $3.6\mu\text{m}$.

Pseudobulges - The top two panels of Figure 12 show two galaxies having prominent pseudobulges (Kormendy & Kennicutt 2004) or disk bulges (Athanasoula 2005). Both NGC 470 and 4536 have bulge isophotes that align with the major axis, indicating significant bulge flattening. This argues that they are very disk-like, which is one of the criteria for recognizing such bulges.

Another criterion for pseudobulges is the presence of a nuclear bar. These are identified using the notation “nb” in the classification, and include NGC 1291, 1433, 4725, 5728, and 5850. Each of these galaxies has a clear primary bar, and four have an inner ring.

A third criterion for a pseudobulge is the presence of a boxy or boxy/peanut inner structure. In our sample, these are evident in NGC 2683 (Figure 1.47), 4527 (Figure 1.115), and 5353 (Figure 1.141), among others. In the case of the spindle galaxy NGC 2683, the inner boxy/X zone is so distinctive that in Table 1 we use the notation “SB_X” to recognize it is as a barred galaxy without actually seeing the extent of the bar.

Double-Stage Galaxies - Some galaxies in the S⁴G sample are large-scale S0 or S0/a galaxies with smaller-scale inner spirals. Four are shown in Figure 12 (lower two rows). The inner

spirals in these galaxies are only a small fraction of the size of the system. In effect, these are “double-stage” galaxies, because the large-scale structure is that of an early-type galaxy and the inner structure is that of a later-type galaxy. The final type we have adopted is usually a compromise unless one characteristic dominates (see notes to Table 1). The double-stage character in NGC 5713, where an inner asymmetric star-forming component lies within a smooth, asymmetric outer ring, could be linked to an interaction (Vergani et al. 2007). Double-stage spirals were described by Vorontsov-Velyaminov (1987) as cases where an inner spiral pattern gives a different type from an outer spiral pattern.

Double-Variety Galaxies - We have already described NGC 5055 as having an inner pseudoring and an inner ring/lens in the $3.6\mu\text{m}$ image, which makes the galaxy an unusual case of a double variety system. This characteristic was not readily evident in blue light. Both features, especially the inner pseudoring, are visible in the $3.6\mu\text{m}$ radial luminosity profile of NGC 5055 shown by de Blok et al. (2008). While the two variety patterns are completely separated in this case, they can also overlap. For example, NGC 986 (Figure 1.21) has a very strong s-shaped spiral superposed on a diffuse inner ring. The two varieties in this case do not seem related, i.e., there is an inner ring but the main arms are not related to the ring.

Inner Disks - Among the spindles in our sample, NGC 24 (Figure 1.1) is unique in showing a very bright, well-centered inner component that aligns almost exactly with the major axis, suggesting that the component is an inner disk and not an inner bar. The galaxy is not exactly edge-on, and a ring is recognizable in the spiral morphology. The inner disk component greatly underfills this ring, another characteristic that suggests the feature is not a bar. This shows the advantage of the mid-IR for morphological studies of edge-on disks (see also Fazio et al. 2004b).

Outer Rings - One of the stated goals of the S⁴G project was to take advantage of the

considerable depth of Warm Mission images to detect previously unrecognized outer rings, especially rings so faint that optical images failed to reveal them. In blue light, such rings tend to have surface brightnesses $\mu_B \geq 25.0 \text{ mag arcsec}^{-2}$, and some could be lost due to extinction or exceptional intrinsic faintness. Although we expect that some faint outer rings will be found when the entire survey is completed, none were identified in the subsample of S⁴G that we have examined here. The main new outer ring we detected is in NGC 4579 (Figure 9), but, as we have already noted, it was missed in the RC3, RSA, and dVA only because of the uncertain effects of internal extinction, not because of exceptional faintness.

The main reason few outer rings were detected in our sample here is probably because the sample has a large fraction of late-type galaxies, where outer rings are infrequently seen (Buta & Combes 1996). The images of NGC 1291 in Figure 7 show that even an exceptionally bright outer ring in blue light can have considerably reduced contrast at $3.6\mu\text{m}$. The outer ring in NGC 1291 is where most of the recent star formation is taking place, and is prominent in blue light as a result, but at $3.6\mu\text{m}$, the feature barely stands out as a broadly oval enhancement in a rounder diffuse background.

4.5. The Nature of Resolved $3.6\mu\text{m}$ Objects

The strong similarity between *B*-band and 3.6 micron images in many of the galaxies we show here is one of the most important findings from this study. It is perhaps surprising that at $3.6\mu\text{m}$, the “degree of resolution” effect can still play a role in the classification of spirals, when the common assumption is that IR light traces mass and de-emphasizes the massive OB star complexes that line the arms in blue light. Nevertheless, young stars can impact morphology in the near- and mid-IR. Rix & Rieke (1993) and Rhoads (1998) showed using the CO index that young red supergiant stars no more than 10^7 yr old may contribute substantial local flux at $2\mu\text{m}$ even if the global $2\mu\text{m}$ flux is dominated by old stars.

Detailed comparison of resolved objects in B -band and $3.6\mu\text{m}$ images shows that, in many cases, the same complexes are being seen. An especially good illustration of this is provided by NGC 1559, whose type [SB(s)cd] is essentially the same in the two filters (Figure 13). Although the considerably reduced sky background in $3.6\mu\text{m}$ images allows a flurry of faint foreground stars to appear, the resolved objects we see in NGC 1559 follow the spiral arms closely and are not randomly scattered. A color index map (not shown) reveals that most of the resolved sources are redder in the [3.6]–[4.5] color index than the galaxy background light.

Figure 14 shows a color-magnitude plot of 159 of these objects as compared to a similar-sized sample of surrounding field objects (foreground stars and background galaxies). A redshift-independent distance modulus of 30.95 (NED) has been used for the absolute magnitude scale. Photometry was performed with IRAF routine PHOT using a measuring aperture of 2 pix and background estimates taken from 3-5 pix for each object. A bright foreground star off the galaxy was used to determine an aperture correction of 0.88 mag, which has been subtracted from the 2 pix radius $3.6\mu\text{m}$ magnitude [3.6]. These graphs can be compared to Figures 7 and 8 of Mould et al. (2008), who analyzed IRAC data for the resolved stellar population in M31 and a comparison SWIRE control field. Mould et al. detected luminous red supergiants in M31, some showing evidence of mass loss. As also shown by Mould et al., field objects will overlap the distribution of galaxy objects in such plots. The asymptotic giant branch reaches to only $M[3.6]\approx-10$ (see also Jackson et al. 2007), while the brightest evolved supergiants in M31 reach [3.6]=9.5, or $M[3.6]\approx-15$. Figure 14 shows that most of the resolved objects in NGC 1559 are more luminous than this, which is consistent with their slightly fuzzy appearance; these are complexes rather than merely individual stars, although some of the faintest objects could be individual stars. The individual AGB population is largely out of reach at the distance of NGC 1559, and we conclude that the resolved objects in the arms are likely groups of massive young

stars. However, it is not clear that we can think of the resolved objects entirely in terms of groups of young red stars.

Mentuch et al. (2009) modeled the spectral energy distributions of high redshift galaxies and concluded that a previously discovered excess of infrared flux in the $2\text{-}5\mu\text{m}$ region can be best interpreted in terms of modified blackbody emission from dust at 850K together with the well-known polycyclic aromatic hydrocarbon (PAH) emission at $3.3\mu\text{m}$. The excess emission is believed to come from the puffed up inner edges of circumstellar disks in massive star-forming regions. Given what we have described above, this mechanism could account for some of the light of the resolved sources we see in S⁴G images. Further studies should be able to clarify this issue.

Note that use of $4.5\mu\text{m}$ images will not necessarily avoid the effects of the resolved objects on morphological interpretations. Comparison between the 3.6 and $4.5\mu\text{m}$ images of virtually all the galaxies in our sample shows little difference in apparent morphology. The resolved objects are just as conspicuous at $4.5\mu\text{m}$ as they are at $3.6\mu\text{m}$. Given this, the question arises: which IR domain, near or mid, might be better for revealing the true “stellar backbone,” or what is called the “star-dominated Population II disk” by Block et al. (2004). Figure 15 shows the IRAC $3.6\mu\text{m}$ image of M51 (right frame) as compared to a $2.2\mu\text{m}$ K_s -band image obtained in May 2009 by RB using the FLAMINGOS IR imaging camera attached to the Kitt Peak 2.1m telescope. The on-source exposure time of the latter image was 30min. The comparison shows that the spiral arms of M51 are smoother and less affected by star-forming regions in the K_s band than in the $3.6\mu\text{m}$ *Spitzer* band, perhaps arguing in favor of the K_s band for stellar mass studies. However, this comparison also displays the considerably greater depth of the $3.6\mu\text{m}$ image compared with a typical, K_s -band image. Although the $3.6\mu\text{m}$ image is affected by star formation, the light is still dominated by the “stellar backbone” of old stars and the best approach to getting at this

background would be to find ways to correct $3.6\mu\text{m}$ images for the younger “contaminants.” This will be extensively discussed in a future S⁴G paper (S. Meidt et al., in preparation).

4.6. Bar Fraction

We conclude our analysis by examining the bar fraction in our subsample of S⁴G galaxies. The bar fraction has cosmological significance (Sheth et al. 2008), and has been the topic of many recent optical and near-IR studies (e.g., Knapen et al. 2000; Eskridge et al. 2000; Laurikainen et al. 2004; Menéndez-Delmestre et al. 2007; Marinova & Jogee 2007; Barazza et al. 2008; Sheth et al. 2008; Aguerri et al. 2009; Marinova et al. 2009; Mèndez-Abreu et al. 2010; Masters et al. 2010). In general, these studies are in fairly good agreement on this parameter, in spite of different methodologies. Some find a slightly higher bar fraction in the near-IR than in the optical (e. g., Knapen et al 2000, Eskridge et al 2000), while others do not (e. g., Menéndez-Delmestre et al. 2007; Sheth et al. 2008). Eskridge et al. (2000) found that the fraction of *strongly* barred galaxies (i.e., classified as SB) rises by almost a factor of 2 from the optical to the near-IR. The rise is mainly due to reclassification of SAB-type bars to SBs because bars are often more prominent at near-IR than at blue wavelengths, but the overall SAB+SB bar fraction is similar in the two wavelength domains as shown by Whyte et al. (2002), Menéndez-Delmestre et al. (2007), and Sheth et al. (2008), among others. Menéndez-Delmestre et al. (2007) and Sheth et al. (2008) also found that almost as many galaxies in the near-IR get classified from barred to nonbarred as are classified from nonbarred to barred. However, these constituted only a small percentage of the sample. In fact, 127/139 galaxies did not change bar type when these authors compared G to IR images, 7 went from SA to SAB, 4 from SAB to SA, and 1 from SB to SA. Thus, over 90% looked the same. The ones that did not were faint, small, or close to the inclination cut-off, and as a consequence were hard to classify.

Table 2 compiles counts of the galaxies in Table 1 classified as types SA, SAB, SAB, SAB, and SB, for the full sample of 207 galaxies (Col. 2, including all types), and for several subsamples. Column 3 lists the counts for galaxies restricted to the Table 1 type range S0/a-Sm. Columns 4 and 5 are the same as columns 2 and 3, but after rejection of any galaxy classified as a spindle (sp) in Table 1. This is reasonable since morphology-based bar classification is difficult in highly inclined galaxies. We consider any galaxy classified as SAB, SAB, or SB to be a barred galaxy, and define the bar fraction as the number of those galaxies relative to the number in the given subset in Table 2. Over all types and even after removal of spindles, the bar fraction is about 50%. However, when restricted to spirals, the fraction is 64-66%, similar to previous studies (e.g., Laurikainen et al. 2004). In the OSUBSGS sample, Eskridge et al. (2000) found a bar fraction of 73% based on *H*-band images. The SB bar fraction in our (non-spindle) spiral sample, $36\% \pm 4\%$, is higher than the same fraction, $29.4\% \pm 0.5\%$ estimated by Masters et al. (2010) from the optical Galaxy Zoo project, which could partly be the “stronger bar effect.” The bar fraction in our subsample is consistent with that estimated from RC3 classifications (see Table 1 of Eskridge et al. 2000).

5. Conclusions

We have used a subsample of S⁴G pipeline-processed archival *Spitzer Space Telescope* images to examine the imprint of the de Vaucouleurs revised Hubble-Sandage classification system in the IRAC 3.6 μ m band. Although our sample includes less than 10% of what will be the final S⁴G sample, it is sufficient for us to achieve some interesting results. We find that 3.6 μ m classifications are well-correlated with blue light classifications in RC3. The most significant difference occurs for S0/a to Sc galaxies, where 3.6 μ m types average about 1 stage interval earlier than *B*-band types. This is consistent with the previous findings of

Eskridge et al. (2002), which were based on OSUBSGS H -band $1.65\mu\text{m}$ images. The great advantage of the IRAC $3.6\mu\text{m}$ images is their considerably better depth than any previous ground-based IR images, allowing a more complete picture of global IR galaxy morphology, rather just the inner regions which were all that were revealed in earlier studies.

The use of the same classification methods for $3.6\mu\text{m}$ images as for blue light images is a strength of our analysis. Had we used different methods we likely would have found spurious differences. This is actually illustrated by our comparison of our $3.6\mu\text{m}$ classifications, evaluated as in the RC3/dVA, and the classifications for the same galaxies given in the RSA. This comparison revealed large systematic differences that are only partly attributable to the wavelength difference between blue light photographic plates and S⁴G images. Instead, most of the differences are due to methodological differences between RSA and RC3/dVA classifications. Another issue is that morphological classification is based on important properties, not minor details. In classifying a galaxy, we look at whether a particular feature exists, is predominant, secondary or non-existent, and to the extent that we see these features, the structure of the old and the young populations do not differ that wildly.

Deep $3.6\mu\text{m}$ galaxy morphology provides an effective, dust-penetrated alternative to historical blue light morphology, and in principle could one day fully replace blue light as the standard passband for galaxy classification. However, the band is not completely free of the effects of young star forming regions, and thus may not show the “stellar backbone” of galactic disks as effectively as in other bands, such as the K -band (e.g., Block et al. 2004). For the future, our goal is to classify the entire S⁴G sample in the same manner as described here, to facilitate statistical studies of various morphological features, and to provide a morphological backdrop to the quantitative analyses that will come out of the survey.

We thank the referee for many helpful comments that improved the presentation of

this paper. We also thank D. L. Block for additional comments and for pointing us to a useful reference, as well as the other members of the S⁴G Team for helping to make the project possible. RB acknowledges the support of NSF Grant AST 05-07140. EA and AB thank the Centre National d'Etudes Spatiales for financial support. K.L.M. acknowledges funding from the Peter and Patricia Gruber Foundation as the 2008 IAU Fellow, from the University of Portsmouth and from SEPnet (www.sepnet.ac.uk). HS and EL acknowledge the Academy of Finland for support. JHK acknowledges support by the Instituto de Astrofísica de Canarias (312407). KMD is supported by an NSF Astronomy and Astrophysics Postdoctoral Fellowship under award AST-0802399. A.G.dP and J.C.M.M are partially financed by the Spanish Programa Nacional de Astronomía y Astrofísica under grants AyA2006-02358 and AyA2009-10368, and by the Spanish MEC under the Consolider-Ingenio 2010 Program grant CSD2006-00070: first Science with the GTC. A.G.dP is also financed by the Spanish Ramón y Cajal program. J.C.M.M. acknowledges the receipt of a Formación del Profesorado Universitario fellowship. SC is supported by a KASI Postdoctoral Fellowship. This work is based [in part] on archival data obtained with the Spitzer Space Telescope, which is operated by the Jet Propulsion Laboratory, California Institute of Technology under a contract with NASA. Support for this work was provided by an award issued by JPL/Caltech. Funding for the OSUBSGS was provided by grants from the NSF (grants AST 92-17716 and AST 96-17006), with additional funding from the Ohio State University. Funding for the creation and distribution of the SDSS Archive has been provided by the Alfred P. Sloan Foundation, the Participating Institutions, NASA, NSF, the U.S. Department of Energy, the Japanese Monbukagakusho, and Max Planck Society. NED is operated by the Jet Propulsion Laboratory, California Institute of Technology, under contract with NASA.

REFERENCES

- Athanassoula, E. 2005, MNRAS, 358, 1477
- Aguerri, J. A. L., Méndez-Abreu, J., & Corsini, E. M. 2009, A&A, 495, 491
- Banerj, M. et al. 2010, astro-ph 0908.2033
- Barazza, F. D., Jogee, S., & Marinova, I. 2008, ApJ, 675, 1194
- Bingelli, B., Sandage, A., & Tammann, G. A. 1985, AJ, 90, 1681
- Block, D. L., Bertin, G., Stockton, A., Grosbol, P., Moorwood, A. F. M., Peletier, R. F. 1994, A&A, 288, 365
- Block, D., Freeman, K. C., Puerari, I., Combes, F., Buta, R., Jarrett, T., & Worthey, G. 2004, in Penetrating Bars Through Masks of Cosmic Dust, eds. D. L. Block, I. Puerari, K. C. Freeman, R. Groess, & E. Block, Springer, Kluwer, p. 15
- Block, D. L. & Wainscoat, R. J. 1991, Nature, 353, 48
- Bureau, M. & Freeman, K. C. 1999, AJ, 118, 126
- Buta, R. 1995, ApJS, 96, 39
- Buta, R. & Combes, F. 1996, Fund. Cosmic Phys. 17, 95
- Buta, R. & Crocker, D. A. 1991, AJ, 102, 1715
- Buta, R. J., Corwin, H. G., & Odewahn, S. C. 2007, The de Vaucouleurs Atlas of Galaxies, Cambridge: Cambridge U. Press (dVA)
- Buta, R., Vasylyev, S., Salo, H., & Laurikainen, E. 2005, AJ, 130, 506
- Buta, R., Laurikainen, E., Salo, H., Block, D. L., & Knapen, J. H. 2006, AJ, 132, 1859
- Comerón, S., Knapen, J. H., Beckman, J. E., Laurikainen, E., Salo, H., Martínez-Valpuesta,

I., & Buta, R. J. 2010, MNRAS, 402, 2462

Corwin, H., de Vaucouleurs, A., & de Vaucouleurs, G. 1985, Southern Galaxy Catalogue, Univ. Texas Monographs, No. 4.

Davidge, T. J. 2003, AJ, 125, 30

de Blok, W. J. G., Walter, F., Brinks, E., Trachternach, C., Oh, S.-H., & Kennicutt, R. C. 2008, AJ, 136, 2648

de Jong, R. S. & van der Kruit, P. C. 1994, A&AS, 106, 451

de Souza, R. E., Gadotti, D. A., & dos Anjos, S. 2004, ApJS, 153, 411

de Vaucouleurs, G. 1959, Handbuch der Physik, 53, 275

de Vaucouleurs, G. 1963, ApJS, 8, 31

de Vaucouleurs, G. & Buta, R. 1980, ApJS, 44, 451

de Vaucouleurs, G. & de Vaucouleurs 1964, Reference Catalog of Bright Galaxies, University of Texas Monographs in Astronomy, No. 1 (RC1)

de Vaucouleurs, G. & Freeman, K. C. 1972, Vista in Astr. 14, 163

de Vaucouleurs, G., de Vaucouleurs, A., Corwin, H. G., Buta, R. J., Paturel, G., & Fouque, P. 1991, Third Reference Catalog of Bright Galaxies (New York: Springer) (RC3)

Elmegreen, D. 1981, ApJS, 47, 229

Elmegreen, D. M. & Elmegreen, B. G. 1984, ApJS, 54, 127

Elmegreen, D. M. & Elmegreen, B. G. 1987, ApJ, 314, 3

Eskridge, P. et al. 2000, AJ, 119, 536

Eskridge, P. et al. 2002, ApJS, 143, 73

Fazio, G. G. et al. 2004, *ApJS*, 154, 10

Fazio, G. G., Pahre, M. A., Willner, S. P., & Ashby, M. L. N. 2004b, in *Penetrating Bars Through Masks of Cosmic Dust*, eds. D. L. Block, I. Puerari, K. C. Freeman, R. Groess, & E. Block, Springer, Kluwer, p. 389

Freeman, K.C.1975, in *Galaxies and the Universe*, A. Sandage, M. Sandage, & J. Kristian, eds., Chicago, University of Chicago Press, p. 409

Fukugita, M. et al. 2007, *AJ*, 134, 570

Graham, A. W. & Worley, C. C. 2008, *MNRAS*, 388, 1708

Hackwell, J. & Schweizer, F. 1983, *ApJ*, 265, 643

Holmberg, E. 1950, *Medd. Lunds. Astron. Obs., Ser. II*, No. 128

Hubble, E. 1926, *ApJ*, 64, 321

Hubble, E. 1936, *The Realm of the Nebulae*, Yale, Yale University Press

Jackson, D. C., Skillman, E. D., Gehrz, R. D., Polomski, E., & Woodward, C. E. 2007, *ApJ*, 656, 818

Jarrett, T. H. et al. 2003, *AJ*, 125, 525

Kennicutt, R. C. et al. 2003, *PASP*, 115, 928

Kennicutt, R. C. et al. 2007, *BAAS*, 211, 9502

Knapen, J. H. 2005, *A&A*, 429, 141

Knapen, J., Shlosman, I., & Peletier, R. 2007, *ApJ*, 529, 93

Kormendy, J. 1979, *ApJ*, 227, 714

Kormendy, J. & Bender, R. 1996, *ApJ*, 464, L119

- Kormendy, J. & Kennicutt, R. 2004, *ARAA*, 42, 603 (KK04)
- Lauberts, A. 1982, *The ESO-Uppsala Survey of the ESO (B) Atlas*, ESO
- Laurikainen, E., Salo, H., & Buta, R. 2004, *ApJ*, 607, 103
- Laurikainen, E., Salo, H., & Buta, R. 2005, *MNRAS*, 362, 1319
- Laurikainen, E., Salo, H., Buta, R., Knapen, J., Speltincx, T., & Block, D. L. 2006, *MNRAS*, 132, 2634
- Laurikainen, E., Salo, H., Buta, R., Knapen, J. H., & Comerón, S. 2010, *MNRAS*, in press (astro-ph 1002.4370)
- Lintott, C. et al. 2008, *MNRAS*, 389, 1179
- Malin, D. & Carter, D. 1980, *Nature*, 285, 643
- Malin, D. & Carter, D. 1983, *ApJ*, 274, 534
- Marinova, I. & Jogee, S. 2007, *ApJ*, 659, 1176
- Marinova, I. et al. 2009, *ApJ*, 698, 1639
- Masters, K. et al. 2010, astro-ph 1003.0449
- Méndez-Abreu, J. Sánchez-Janssen, & Aguerri, J. A. L. 2010, *ApJ*, 711, L61
- Mentuch, E. et al. 2009, *ApJ*, 706, 1020
- Menéndez-Delmestre, K., Sheth, K., Schinnerer, E., Jarrett, T., & Scoville, N. Z. 2007, *ApJ*, 657, 790
- Meurer, G., Freeman, K. C., & Dopita, M. A. 1989, *Ap&SS*, 156, 141
- Melnick, J., Moles, M., & Terlevich, R. 1985, *AJ*, 149, L24

- Mihos, J. C. & Hernquist, L. 1996, ApJ, 464, 641
- Naim, A. et al. 1995, MNRAS, 274, 1107
- Nair, P. B. & Abraham, R. G. 2010, ApJS, 186, 427
- Pahre, M., Ashby, M. L. N., Fazio, G. G., & Willner, S. P. 2004, ApJS, 154, 235
- Rhoads, J. E. 1998, AJ, 115, 472
- Rix, H.-W. & Rieke, M. J. 1993, ApJ, 418, 123
- Sandage, A. 1961, The Hubble Atlas of Galaxies, Carnegie Inst. of Wash. Publ. No. 618
- Sandage, A. and Bedke, J. 1994, *The Carnegie Atlas of Galaxies*, Carnegie Institute of Washington Publ. No. 638
- Schweizer, F. & Seitzer, P. 1988, ApJ, 328, 88
- Scoville, N. Z., Matthews, K., Carico, D. P., & Sanders, D. B. 1988, ApJ, 327, L61
- Sheth, K. et al. 2008, ApJ, 675, 1141
- Sheth, K. et al. 2010, PASP, submitted
- Simien, F. & de Vaucouleurs, G. 1986, ApJ, 302, 564
- Skrutskie, M. et al. 1997, ASSL, 210, 25
- Talbot, R. J., Jensen, E. B., & Dufour, R. J. 1979, ApJ, 229, 91
- Taylor, V. A., Jansen, R. A., Windhorst, R. A., Odewahn, S. C., & Hibbard, J. E. 2005, ApJ, 630, 784
- Taylor-Mager, V. A., Conselice, C. J., Windhorst, R. A., & Jansen, R. A. ApJ, 659, 162
- Telesco, C. M., Joy, M., Dietz, K., Decher, R., & Campins, H. 1991, ApJ, 369, 135

- Thornley, M. 1996, ApJ, 469, L45
- Thronson, H. A., Hereld, M., Majewski, S., Greenhouse, M., Johnson, P., Spillar, E., Woodward, C. E., Harper, D. A., & Rauscher, B. J. 1989, ApJ, 343, 158
- Varela, A. M., Munoz-Tunon, C., & Simmoneau, E. 1996, A&A, 306, 381
- Vergani, D., Pizzella, A., Corsini, E. M., van Driel, W., Buson, L. M., Dettmar, R.-J., & Bertola, F. 2007, A&A, 463, 883
- Vorontsov-Velyaminov, B. A. 1987, Extragalactic Astronomy, New York, Harwood Academic Publishers
- Werner, M. W. et al. 2004, ApJS, 154, 1
- Whitmore, B. C., Lucas, R. A., McElroy, D. B., Steiman-Cameron, T. Y., Sackett, P. D., & Olling, R. P. 1990, AJ, 100, 1489
- Whyte, L. F., Abraham, R. G., Merrifield, M. R., Eskridge, P. B., Frogel, J. A., Pogge, R. W. 2002, MNRAS, 336, 1281
- Windhorst, R. et al. 2002, ApJS, 143, 113
- Zaritsky, D. & Lo, K. Y. 1986, ApJ, 303, 66

Table 1. $3.6\mu\text{m}$ Morphological Classifications^a

Galaxy	Fig 1.	S ⁴ G mid-IR type	RC3 blue type	RSA blue type	dVA blue type	OSU near-IR type
1	2	3	4	5	6	7
NGC 24	1	S(rs)d: sp	SA(s)c	Sc(s)
NGC 45	2	SA(s)dm	SA(s)dm	Scd(s)	SA(s)d
NGC 55	3	SB(s)m sp	SB(s)m: sp	Sc
NGC 59	4	dE5,N	SA(rs)0 ⁻ :
NGC 247	5	SAB(s)d	SAB(s)d	Sc(s)	<u>S</u> AB(s)d
NGC 274	6	(R)SA(l)0 ⁻	SAB(r)0 ⁻ pec	S0 ₁ (0)
NGC 275	6	S pec	SB(rs)cd pec	S pec
NGC 300	7	SA(s)dm	SA(s)d	Sc	SA(s)d
NGC 337	8	SAB(s)cd: pec	SB(s)d	Sc(s) pec
NGC 428	9	SAB(s)dm	SAB(s)m	Sc(s)	SAB(s)m	SBm
NGC 470	10	<u>S</u> AB(rs)ab	SA(rs)b	Sbc(s)
NGC 474	11	(R)SAB0/a (shells) pec	SA(s)0 ^o	RS0/a
NGC 584	12	<u>S</u> AB0 ⁻	E4	S0 ₁ (3,5)	SA0 ⁻
NGC 628	13	SA(s)c	SA(s)c	Sc(s)	SA(s)c
NGC 660 ^b	14	PRG	SB(s)a pec
NGC 672	15	(R')SB(s)d	SB(s)cd	SBc(s)
NGC 691	16	(R)SA(r)ab	SA(rs)bc
NGC 784	17	SBm: sp	SBdm: sp

Table 1—Continued

Galaxy	Fig 1.	S ⁴ G mid-IR type	RC3 blue type	RSA blue type	dVA blue type	OSU near-IR type
1	2	3	4	5	6	7
NGC 814	18	SAB0 ⁻ :	
NGC 855	19	SA0 ⁻	E
NGC 941	20	(R':)S <u>A</u> B(r:)c	SAB(rs)c	Scd
NGC 986	21	(R')SB(rs,nb)ab	SB(rs)ab	SBb(rs)
NGC 1068	22	(R)SA(s,nr)a	(R)SA(rs)b	Sb(rs)	(R)SA(rs)b
NGC 1097	23	(R')SB(rs,nr)ab pec	SB(s)b	SBbc(rs)	(R' ₁)SB(rs)b
NGC 1097A	24	dE5	E pec
NGC 1291	25	(R)SAB(l,nb)0 ⁺	(R)SB(s)0/a	SBa	(R)SAB(l)0/a
NGC 1311	26	SBdm: sp	SB(s)m? sp
NGC 1313	27	SB(s) <u>d</u> m pec	SB(s)d	SBc(s)	SB(s) <u>d</u> m
NGC 1365	28	SB(<u>r</u> s,nr)bc	SB(s)b	SBb(s)	SB(s)bc
NGC 1433	29	(R' ₁)SB(r,nr,nb)a	(R')SB(r)ab	SBb(s)	(R' ₁)SB(r)ab
NGC 1448	30	SA(rs)c sp	SAcd: sp	Sc
NGC 1481	31	SA(l)0 ⁻ : pec	SA0 ⁻ :
NGC 1482	32	Sa: sp	SA0 ⁺ pec sp
NGC 1487	33	Pec	Pec	S pec(merger)
NGC 1510	34	SA0 ⁺ :	SA0 ^o pec	SA(s)0/a pec
NGC 1512	35	(RL)SB(r,nr)a	SB(r)a	SBb(rs) pec	(R')SB(r)ab pec

Table 1—Continued

Galaxy	Fig 1.	S ⁴ G mid-IR type	RC3 blue type	RSA blue type	dVA blue type	OSU near-IR type
1	2	3	4	5	6	7
NGC 1559	36	SB(s)cd	SB(s)cd	SBc(s)	SB(s)cd	SBcd
NGC 1566	37	(R ₁ ')SAB(s)b	SAB(s)bc	Sc(s)	(R ₁ ')SAB(s)bc
NGC 1672	38	(R')SAB(rs,nr)b	SB(s)b	Sb(rs)
NGC 1705	39	dE3,N	SA0 ⁻ pec	Amorphous	I0 pec/BCD
NGC 1744	40	SB(s)d	SB(s)d	SBcd(s)
NGC 1808	41	(R ₁)SAB(s,nr)a	(R)SAB(s)a	Sbc pec	(R ₁)SAB(s)b pec	SBa
NGC 2500	42	SAB(s)d	SB(rs)d	Sc(s)
NGC 2552	43	(R')SAB(s)m	SA(s)m?	Sc
NGC 2633	44	SAB(rs)b	SB(s)b	SBb(s)
NGC 2634	45	SA(nl)0 ⁻ (shells)	E1:
NGC 2634A	46	SB(s)m: sp	SB(s)bc? sp
NGC 2683	47	(RL)SB _x (rs)0/a sp	SA(rs)b	Sb
NGC 2742	48	SA(s)c	SA(s)c:	Sc(rs)
NGC 2798	49	SAB(s)a pec	SB(s)a pec	SBa(s)
NGC 2799	49	SB(s)dm? pec sp	SB(s)m?
NGC 2805	50	(R)SAB(rs)c pec	SAB(rs)d
NGC 2814	51	S pec sp	Sb:
NGC 2820	52	Sc sp	SB(s)c pec sp

Table 1—Continued

Galaxy	Fig 1.	S ⁴ G mid-IR type	RC3 blue type	RSA blue type	dVA blue type	OSU near-IR type
1	2	3	4	5	6	7
NGC 2841	53	S <u>A</u> B(r)a	SA(r)b:	Sb	SA(r)b
NGC 2854	54	SAB(r)a	SB(s)b
NGC 2856	55	SAB(r)a:	S?
NGC 2893	56	(RL)SAB(l)0 ⁺	(R)SB0/a
NGC 2903	57	(R')SB(rs,nr)b	SAB(rs)bc	Sc(s)
NGC 2964	58	S <u>A</u> B(r <u>s</u>)b	SAB(r)bc:	Sc(s)	S <u>A</u> B(r <u>s</u>)b	SABb pec
NGC 2968	59	SB(r <u>s</u>)0 ⁺	I0	Amorphous
NGC 2974	60	SA(r)0/a	E4	E4
NGC 2976	61	SAB(s):d	SAc pec	Sd	SA d pec
NGC 3018	62	SB(s)d:	SB(s)b pec
NGC 3023	62	SB(s)dm	SAB(s)c pec
NGC 3049	63	SB(s)ab:	SB(rs)ab
NGC 3073	64	S0 ⁻	SAB0 ⁻
NGC 3115	65	S0 ⁻ /E7 sp	S0 ⁻ sp	S0 ₁ (7)	S0 ⁻ sp
NGC 3147	66	S <u>A</u> B(r <u>s</u>)b	SA(rs)bc	Sb(s)
NGC 3184	67	SA(r <u>s</u>)bc	SAB(rs)cd	Sc(r)	S <u>A</u> B(r <u>s</u>)c
NGC 3198	68	SAB(r <u>s</u>)bc	SB(rs)c	Sc(rs)
NGC 3299	69	S <u>A</u> Bd:	SAB(s)dm

Table 1—Continued

Galaxy	Fig 1.	S ⁴ G mid-IR type	RC3 blue type	RSA blue type	dVA blue type	OSU near-IR type
1	2	3	4	5	6	7
NGC 3344	70	SAB(r)bc	(R)SAB(r)bc	SBbc(rs)
NGC 3351	71	(R')SB(r,nr)a	SB(r)b	SBb(r)	SB(r)b
NGC 3377 ^j	72	E(d)5	E5	E6	E5-6
NGC 3377A	73	Im	SAB(s)m
NGC 3437	74	SA(rs)c	SAB(rs)c:	Sc(s)
NGC 3489	75	(R)SB(r:) ⁰	SAB(rs) ⁰⁺	Sc
NGC 3495	76	(R')SB(rs)c:	Sd:	Sc(s)
NGC 3504	77	(R' ₁)SAB(<u>rs</u> ,nl)a	(R)SAB(s)ab	Sb/SBb(s)	(R' ₁)SAB(<u>rs</u>)ab	(R)SB(r)a
NGC 3512	78	SA(s)bc	SAB(rs)c	Sc(rs)
NGC 3608	79	E2	E2	E1	E2
NGC 3627	80	SB(s)b pec	SAB(s)b	Sb(s)	SAB(s)b
NGC 3738	81	dE (Im)	Im	Sd
NGC 3769 ^c	82	(R')SB(s)cd	SB(r)b:	SBc(s)
NGC 3794 ^d	83	SAB(s)dm	SAB(s)d
NGC 3870	84	SB(rs) ⁰ ?	S0?
NGC 3906	85	SB(l)dm	SB(s)d	SB(rs)dm
NGC 3938	86	SA(s)c	SA(s)c	Sc(s)	SA(s)c	Sb
NGC 3953	87	SB(r) <u>bc</u>	SB(r)bc	SBbc(r)	SB(r)bc

Table 1—Continued

Galaxy	Fig 1.	S ⁴ G mid-IR type	RC3 blue type	RSA blue type	dVA blue type	OSU near-IR type
1	2	3	4	5	6	7
NGC 4020	88	SAB(s)d	SBd? sp
NGC 4068	89	Im	IAm
NGC 4117	90	S0 ⁻ sp	S0 ^o :
NGC 4118	91	dE3-4:	S0 ⁺
NGC 4157	92	SAB(s)c:	SAB(s)b? sp	Sbc	Sc sp
NGC 4163	93	dE (Im)	IAm
NGC 4178	94	(R ₂)SB(s)d	SB(rs)dm	SBc(s)	SB(s)d	SBc? edge-on
NGC 4203	95	S <u>A</u> B0 ⁻	SAB0 ⁻ :	S0 ₂ (1)
NGC 4244	96	Sd sp	SA(s)cd: sp	Scd
NGC 4245	97	(RL)SB(r,nr)0 ⁺	SB(r)0/a:	SBa(s)	SB(r)0/a
NGC 4254	98	SA(s)c pec	SA(s)c	Sc(s)	SA(s)c	SABc
NGC 4266	99	S0 ^o sp	SB(s)a? sp
NGC 4268	100	SA:(<u>rs</u>)0 ⁺ sp	SB0/a: sp
NGC 4270	101	S0 ⁺ sp?	S0	S0 ₁ (6)
NGC 4273	102	S <u>A</u> B(s)c pec	SB(s)c	SBc(s)
NGC 4277	103	SAB(rs)0 ⁺	SAB(rs)0/a:
NGC 4281	104	E(d)5	S0 ⁺ : sp	S0 ₃ (6)
NGC 4294	105	SB(s)d	SB(s)cd	SBc(s)

Table 1—Continued

Galaxy	Fig 1.	S ⁴ G mid-IR type	RC3 blue type	RSA blue type	dVA blue type	OSU near-IR type
1	2	3	4	5	6	7
NGC 4299	106	SA(s)dm	SAB(s)dm:	Sd(s)
NGC 4314	107	(R' ₁)SB(rl,nr)a	SB(rs)a	SBa(rs) pec	(R' ₁)SB(r'l)a	(R)SBa
NGC 4321	108	SAB(r _s ,nr)bc	SAB(s)bc	Sc(s)	SAB(s)bc
NGC 4323	109	dE3,N
NGC 4328	110	dSA(l)0 ⁻	SA0 ⁻ :
NGC 4369 ^e	111	(R)SB(rs)0/a: pec	(R)SA(rs)a	Sc(s)
NGC 4383 ^k	112	E(twist?)/SAB0 ⁻ :	Sa? pec	S0:
NGC 4396	113	Scd: pec sp	SAd: sp
NGC 4437 ^f	114	Sc sp	SA(s)cd: sp	Sc
NGC 4527	115	(R' ₂)SAB(rs,nr)bc	SAB(s)bc	Sb(s)	SAB(s)bc	SABab
NGC 4536	116	SAB(rs)bc	SAB(rs)bc	Sc(s)	SAB(rs)bc
NGC 4550	117	S0 ⁻ sp	SB0 ^o : sp	E7/S0 ₁ (7)
NGC 4559	118	SB(s)cd	SAB(rs)cd	Sc(s)
NGC 4567	119	SA(rs)bc	SA(rs)bc	Sc(s)	SA(r _s)bc
NGC 4568	119	SA(r _s)bc	SA(rs)bc	Sc(s)	SA(s)c	Sbc
NGC 4579	120	(R)SB(r _s)a	SAB(rs)b	Sab(s)	SAB(r _s)ab	SBa
NGC 4605	121	IB(s)m sp	SB(s)c pec	Sc(s)
NGC 4618	122	(R')SB(r _s)m	SB(rs)m	SBbc(rs) pec	(R')SB(rs)m	SBm

Table 1—Continued

Galaxy	Fig 1.	S ⁴ G mid-IR type	RC3 blue type	RSA blue type	dVA blue type	OSU near-IR type
1	2	3	4	5	6	7
NGC 4625	123	(R')SAB(rs)m	SAB(rs)m pec	SAB(rs)m pec
NGC 4647	124	SAB(rs)cd	SAB(rs)c	Sc(rs)	S <u>A</u> B(<u>rs</u>)c	SBbc
NGC 4649	125	SA0 ⁻	E2	S0 ₁ (2)	E ⁺ 2/SA0 ⁻
NGC 4707	126	Im	Sm:
NGC 4725	127	SAB(r,nb)a	SAB(r)ab pec	Sb/SBb(r)	(R')SAB(r)ab pec
NGC 4736	128	(R)S <u>A</u> B(rl,nr',nl,nb)a	(R)SA(r)ab	Sab(s)	(R)S <u>A</u> B(<u>rs</u>)ab
NGC 4750	129	(R')SA(<u>rs</u>)a	(R)SA(rs)ab	Sb(r) pec
NGC 4789A	130	Im	IB(s)m
NGC 5018	131	SAB0 ⁻ (shells) pec	E3:	E4
NGC 5022	132	Sab sp	SBb pec sp
NGC 5055	133	SA(rs,rl)bc	SA(rs)bc	Sbc(s)
NGC 5068	134	SB(<u>rs</u>)d	SAB(rs)cd	SBc(s)
NGC 5173	135	E ⁺ 1	E0:
NGC 5194	136	S <u>A</u> B(rs,nr)bc	SA(s)bc pec	Sbc(s)	SA(s)bc
NGC 5195	136	SAB(r)0/a	I0 pec	SB0 ₁ pec	I0/SB(r)0 ⁺ pec
NGC 5216	137	E0(shells?) pec	E0 pec
NGC 5218	137	SB(rs)a pec	SB(s)b? pec
NGC 5248	138	SAB(s,nr) <u>bc</u>	SAB(rs)bc	Sbc(s)	(R')SAB(rs)bc	Sb

Table 1—Continued

Galaxy	Fig 1.	S ⁴ G mid-IR type	RC3 blue type	RSA blue type	dVA blue type	OSU near-IR type
1	2	3	4	5	6	7
NGC 5338	139	SB(<u>rs</u>)0 ^o	SB0:
NGC 5350	140	SB(<u>rs</u>)ab	SB(r)b	SBbc(rs)
NGC 5353	141	S0 ⁺ sp	S0 sp	S0 ₁ (7)/E7
NGC 5354	141	SA0 ⁻	S0 sp
NGC 5355	142	SAB(s)0 ^o	S0?
NGC 5358	143	S0 ^o sp	S0/a
NGC 5377	144	(R ₁)SAB(s)0/a	(R)SB(s)a	SBa	(R' ₁)SAB(rs)a
NGC 5426	145	S <u>AB</u> (rs)c	SA(s)c pec	Sbc(rs)	SA(s)c
NGC 5427	145	SA(r)bc	SA(s)c pec	Sbc(s)	SA(rs)b <u>c</u>	Sc
NGC 5448	146	(R ₁)SAB(<u>rs</u>)a	(R)SAB(r)a	Sa(s)	(R' ₁)S <u>AB</u> (<u>rs</u>)ab	SABa
NGC 5520	147	SA(l)bc	Sb
NGC 5713 ^g	148	(R')SB(rs)ab: pec	SAB(rs)bc pec	Sbc(s) pec	SBdm
NGC 5728	149	(R ₁)SB(<u>rs</u> ,nr,nb)0/a	SAB(r)a:	SBb(s)	(R ₁)S <u>AB</u> (r)a
NGC 5846	150	E ⁺ 0/SA0 ⁻	E0	S0 ₁ (0)
NGC 5850	151	(R')SB(r,nr,nb)ab	SB(r)b	SBb(sr)	SB(r)b	SB(r)0/a
NGC 5981	152	S0 ⁺ sp	Sc? sp
NGC 5982	153	E2	E3	E3
NGC 5985	154	SAB(s)ab	SAB(r)b	SBb(r)	SAB(r)b

Table 1—Continued

Galaxy	Fig 1.	S ⁴ G mid-IR type	RC3 blue type	RSA blue type	dVA blue type	OSU near-IR type
1	2	3	4	5	6	7
NGC 7064	155	Sd sp	SB(s)c? sp	Scd
NGC 7479	156	(R')SB(s)b	SB(s)c	SBbc(s)	SB(s)c	(R)SBbc
NGC 7552	157	(R' ₁)SB(r _g ,nr)a	(R')SB(s)ab	SBbc(s)	(R' ₁)SB(s)ab	(R)SBa
NGC 7731	158	(R ₁ R' ₂)SAB(r)a	(R)SBa pec
NGC 7732	158	SBd: sp	Scd pec sp
NGC 7793	159	SA(s)c	SA(s)d	Sd(s)	SA(s)d
IC 749	160	SB(rs)cd	SAB(rs)cd	SBc(rs)
IC 750 ^h	161	SA(s)a	Sab: sp	S(b)
IC 797	162	SAB(s)dm:	SBcd?
IC 1066	163	SAbc:	S?
IC 1067	164	SB(r)b	SB(s)b
IC 1574	165	IBm sp?	IB(s)m
IC 1727	166	SB(s)m	SB(s)m
IC 1959	167	SBd sp	SB(s)m: sp
IC 2233	168	SBdm sp	SB(s)d: sp	Sd sp
IC 2574	169	IB(s)m	SAB(s)m	SAB(s)m
IC 3392 ⁱ	170	SA(rs)ab	SAb:
IC 4182	171	SA(s)m	SA(s)m	SA(s)m	dI

Table 1—Continued

Galaxy	Fig 1.	S ⁴ G mid-IR type	RC3 blue type	RSA blue type	dVA blue type	OSU near-IR type
1	2	3	4	5	6	7
IC 4951	172	SB(s)dm: sp	SB(s)dm: sp
IC 5052	173	Sd sp	SBd: sp	Sd	Sd sp
IC 5332	174	SAB(s)cd	SA(s)d	Sc(s)
PGC 6667	175	SB(s)dm	SB(s)d
UGC 1176	176	Im	Im
UGC 4305	177	Im	Im	IAB(s)m
UGC 4426	178	Im	Im:
UGC 5139	179	Im	IAB(s)m
UGC 5459	180	SBdm sp	SB(s)c? sp
UGC 6817	181	Im	Im
UGC 6956	182	SB(s)dm:	SB(s)m
UGC 7504	183	S0 ⁻
ESO 115- 21	184	SB(s)m sp	SBdm: sp
ESO 119- 16	185	(R')SAB(s)dm:	IB(s)m
ESO 149- 3	186	IBm: sp	IB(s)m: sp
ESO 154- 23	187	SB(s)d sp	SB(s)m
ESO 245- 5	188	IAB(s)m	IB(s)m
ESO 245- 7	189	Im	IAm

Table 1—Continued

Galaxy	Fig 1.	S ⁴ G	RC3	RSA	dVA	OSU
		mid-IR	blue	blue	blue	near-IR
		type	type	type	type	type
1	2	3	4	5	6	7
ESO 362- 9	190	S <u>A</u> B(s)dm	SAB(s)m
ESO 418- 8	191	(R')SB(s)dm:	SAB(rs)dm
ESO 471- 6	192	SBd: sp	SB(s)m: sp
ESO 483- 13	193	dE4,N/SA0 ⁻	SA0 ⁻ :
ESO 486- 21	194	dE (Im)	S?
ESO 503- 22	195	SB(s)m:	IB(s)m: pec
ESO 544- 30	196	SAB(s)m	SB(s)dm pec
MCG8-21-76	82	IBm:
CGCG265-55	197	dE (Im)

^aCol. 1: galaxy name; col. 2: Figure 1 plate number; col. 3: mid-IR classification using the precepts and notation of the dVA; col. 4: decoded RC3 blue light classification; index; col 5: RSA blue light classification; col. 6: dVA classification (mostly blue, some visual); col. 7: Eskridge et al. (2002) OSUBGS *H*-band classification

^bPRG=polar ring galaxy (see Whitmore et al. 1990)

^cdouble-stage: SB(s)cd/S0⁻

^dNGC 3804 in RC3

^edouble-stage: SB(s)m/S0/a

^fNGC 4517 in RC3 and RSA

^gdouble-stage: SB(rs)m/S0/a

^hdouble-stage: SA(rs)ab/S0/a

ⁱdouble-stage: SA(s)b/S0^o

^jdisky inner regions only; boxy at larger radii

^kapparent bar could also be inner disk

Table 2. Bar Fraction Analysis^a

	All Types	$0 \leq T \leq 9$	All Types	$0 \leq T \leq 9$
			no spindles	no spindles
1	2	3	4	5
SA	17 ± 3	17 ± 3	19 ± 3	20 ± 4
<u>SAB</u>	8 ± 2	11 ± 3	10 ± 2	13 ± 3
SAB	18 ± 3	22 ± 4	21 ± 3	26 ± 4
<u>SAB</u>	2 ± 1	3 ± 1	2 ± 1	4 ± 2
SB	31 ± 3	40 ± 4	28 ± 3	36 ± 4
no family	24 ± 3	7 ± 2	19 ± 3	1 ± 1
bar fraction ^b	51 ± 3	64 ± 4	52 ± 4	66 ± 4
Number	207	138	173	114

^aCol. 1: category or parameter; cols. 2-5: percentage of that category out of the number listed on line 8.

^bThe sum of SAB, SAB, and SB classifications.

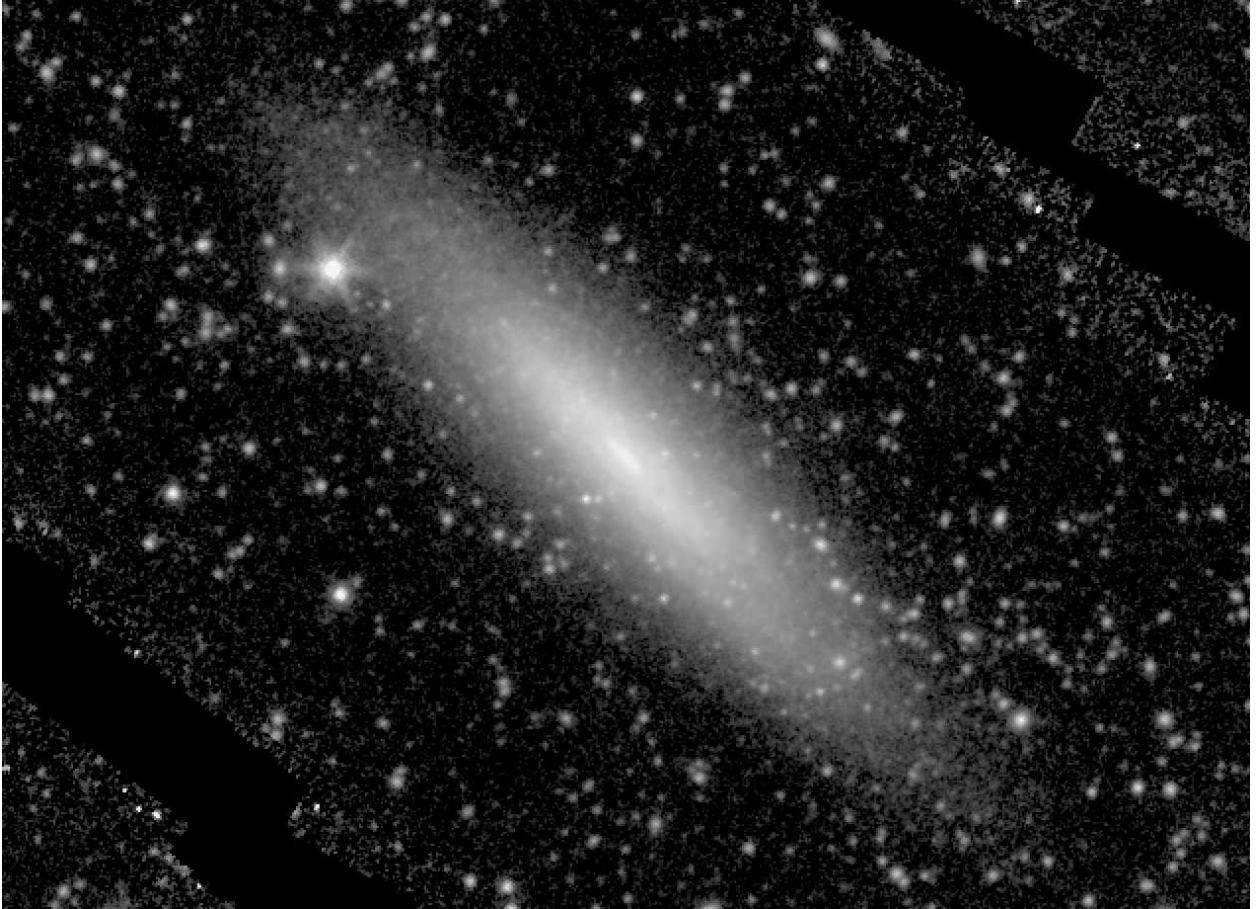


Fig. 1.1.— **NGC 24** - S⁴G mid-IR classification: S(rs)d: sp ; Filter: IRAC 3.6 μ m; North: up, East: left; Field dimensions: 7.9 \times 5.8 arcmin; Surface brightness range displayed: 16.5–28.0 mag arcsec⁻²



Fig. 1.2.— **NGC 45** - S⁴G mid-IR classification: SA(s)dm ; Filter: IRAC 3.6 μ m; North: up, East: left; Field dimensions: 11.3 \times 8.2 arcmin; Surface brightness range displayed: 18.7–28.0 mag arcsec⁻²

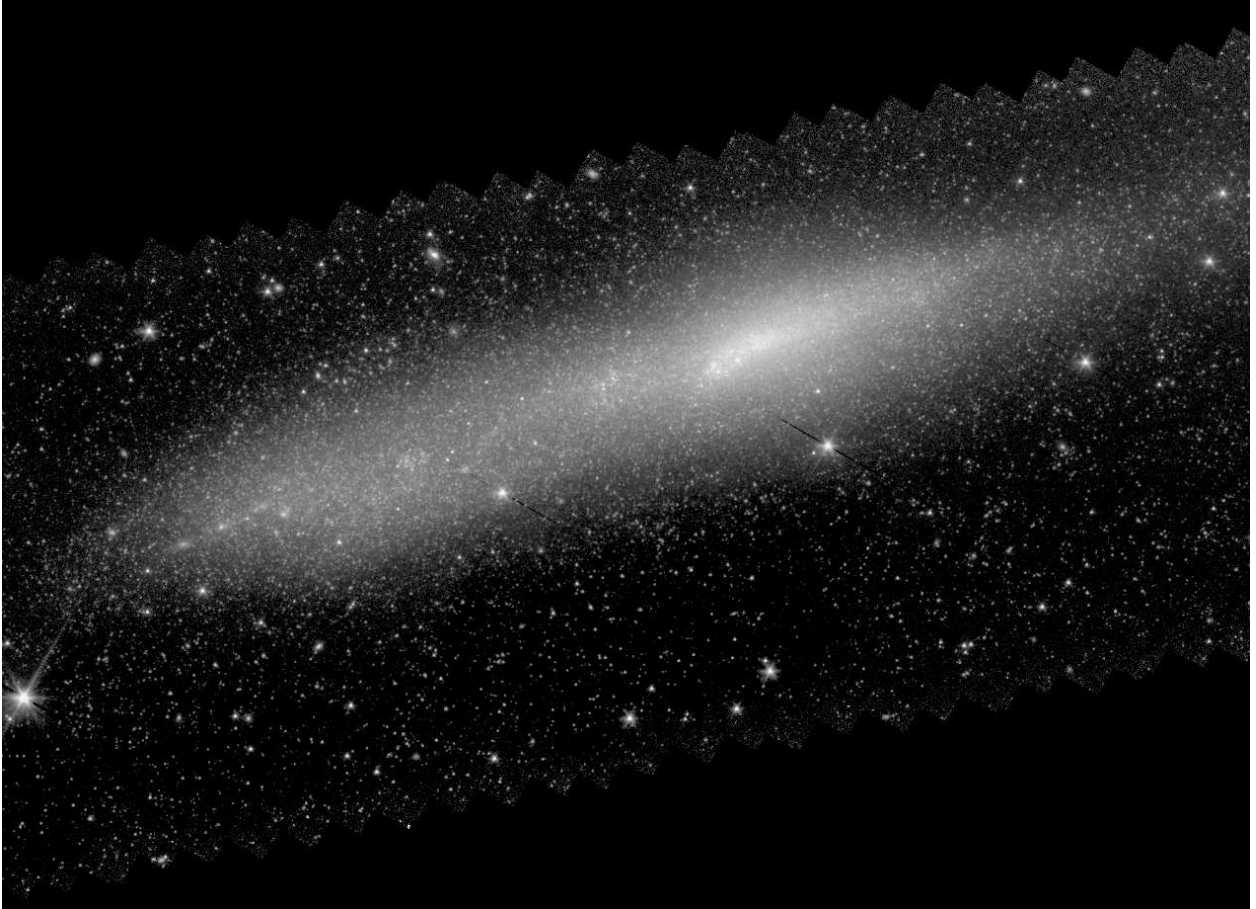


Fig. 1.3.— **NGC 55** - S^4G mid-IR classification: SB(s)m sp ; Filter: IRAC $3.6\mu\text{m}$; North: up, East: left; Field dimensions: 31.5×23.0 arcmin; Surface brightness range displayed: $16.0\text{--}28.0$ mag arcsec $^{-2}$

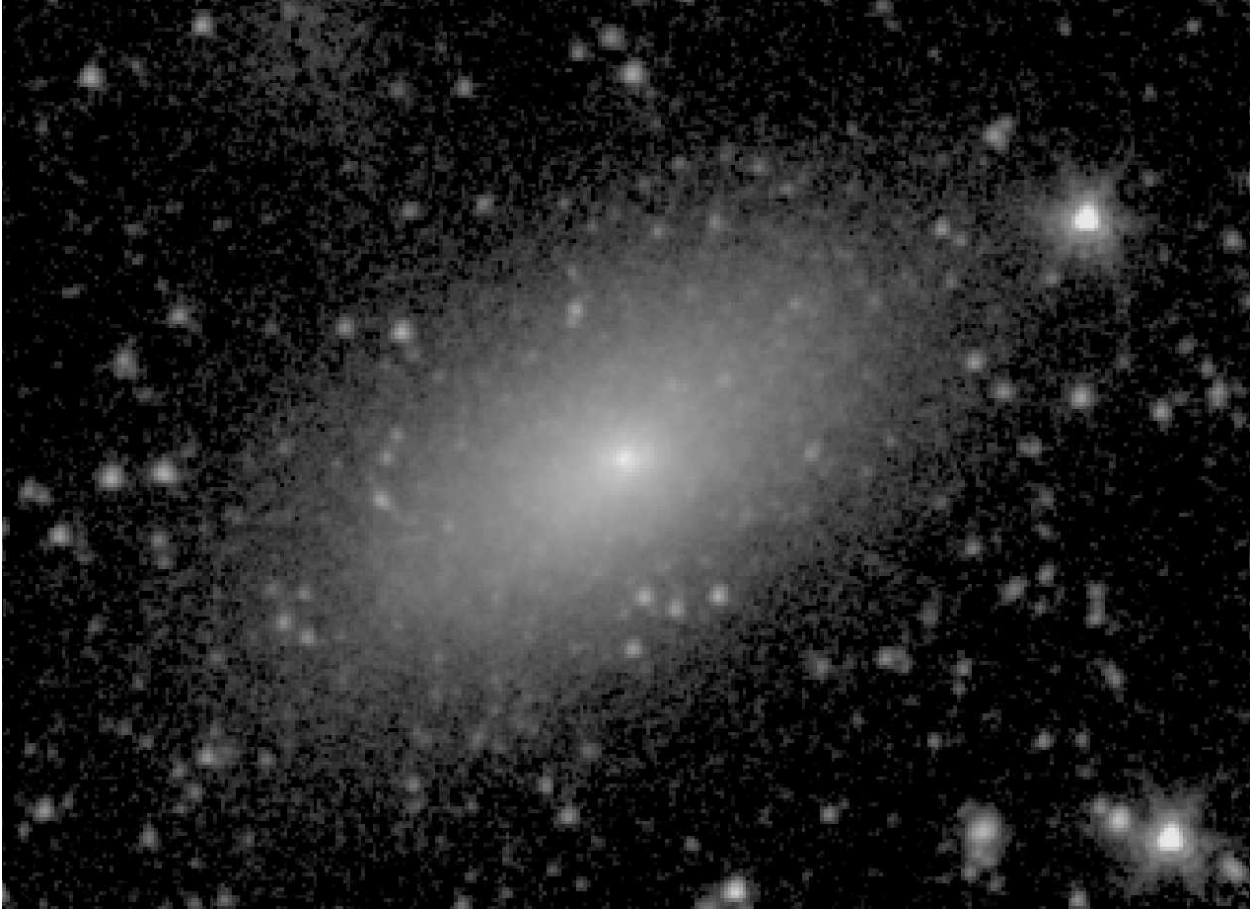


Fig. 1.4.— **NGC 59** - S⁴G mid-IR classification: dE5,N ; Filter: IRAC 3.6 μ m; North: up, East: left; Field dimensions: 4.2 \times 3.1 arcmin; Surface brightness range displayed: 16.0–28.0 mag arcsec⁻²

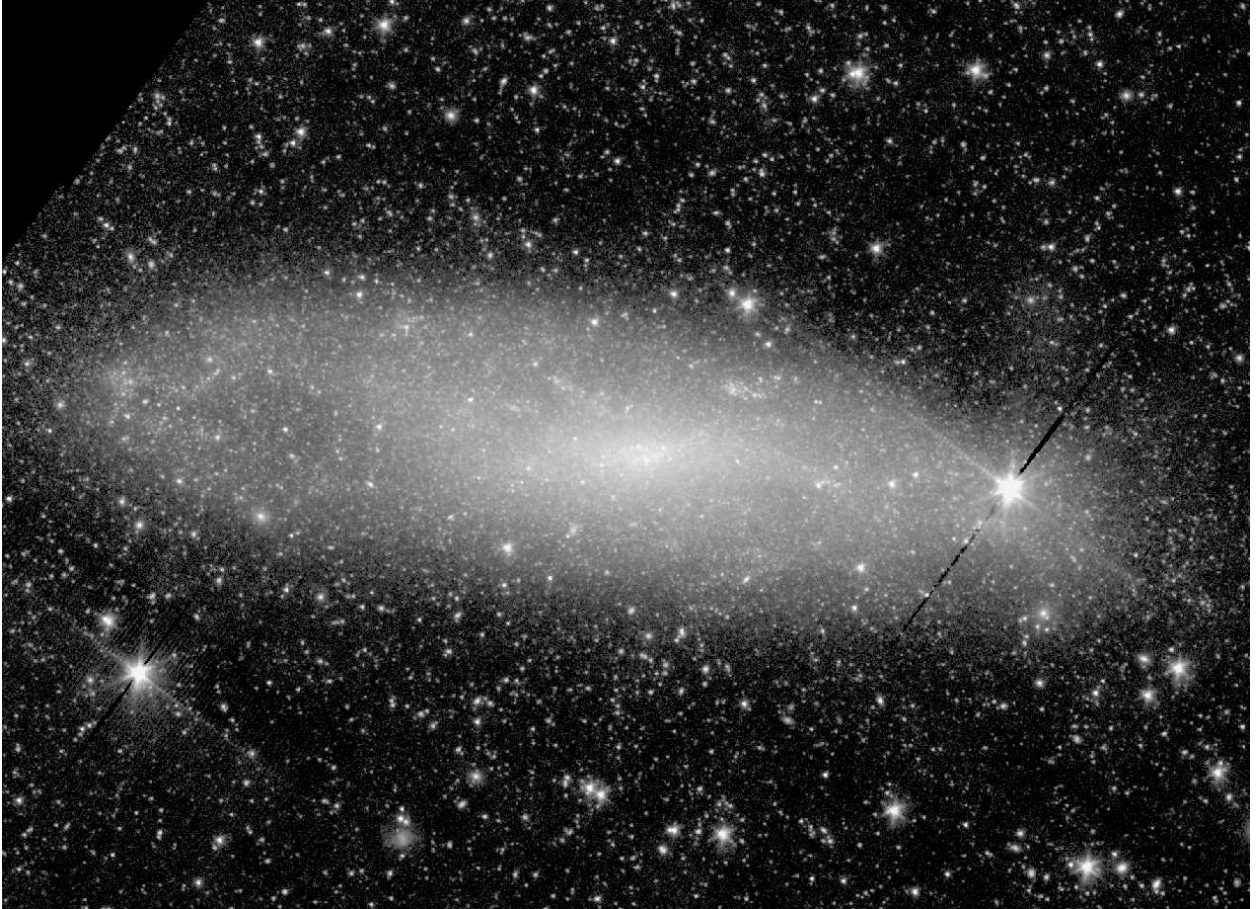


Fig. 1.5.— **NGC 247** - S⁴G mid-IR classification: SAB(s)d ; Filter: IRAC 3.6 μ m; North: left, East: down; Field dimensions: 22.6 \times 16.4 arcmin; Surface brightness range displayed: 17.5–28.0 mag arcsec⁻²



Fig. 1.6.— **NGC 274** (upper right) and **NGC 275** (lower left) - S⁴G mid-IR classifications: (R)SA(1)0⁻, S pec, respectively; Filter: IRAC 3.6 μ m; North: up, East: left; Field dimensions: 5.3 \times 3.8 arcmin; Surface brightness range displayed: 13.5–28.0 mag arcsec⁻²

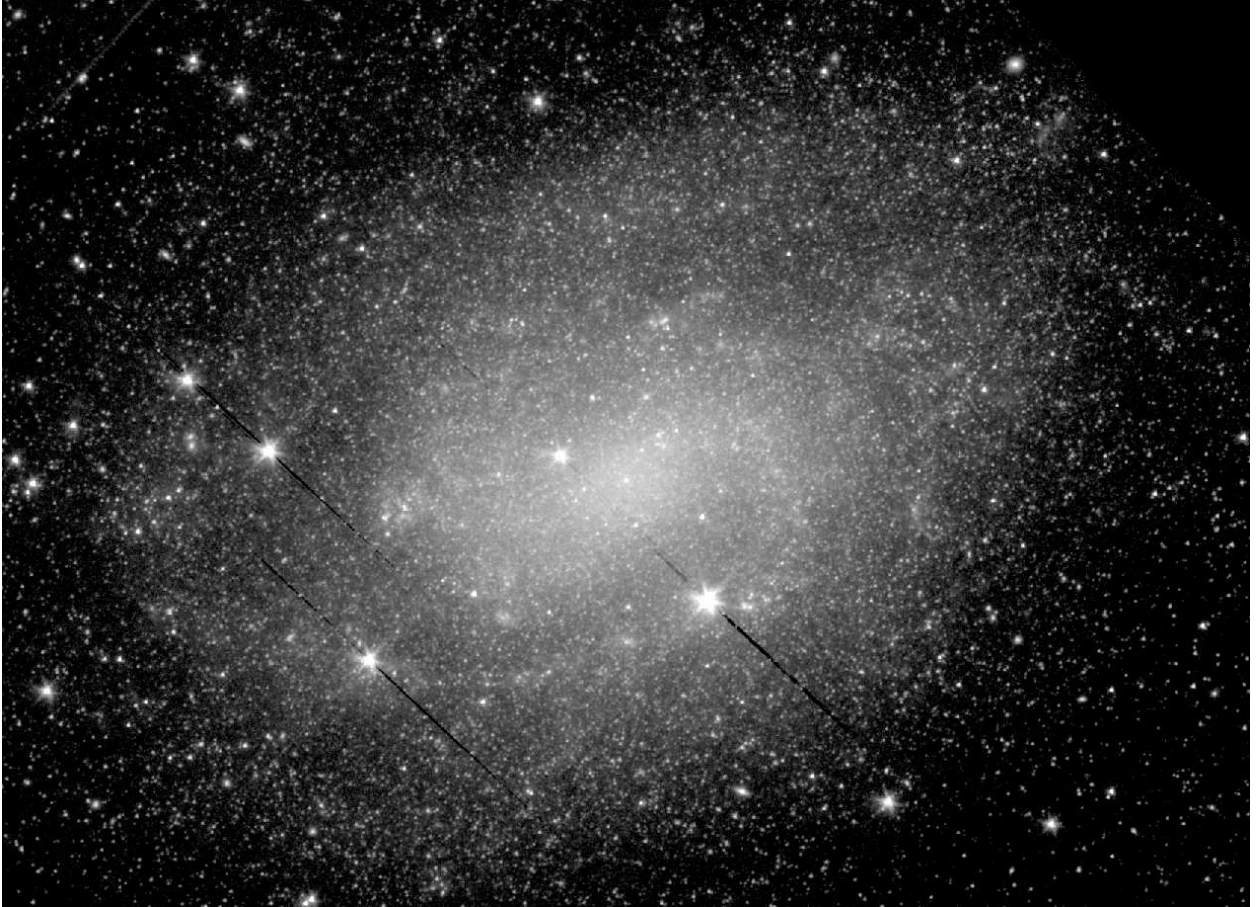


Fig. 1.7.— **NGC 300** - S⁴G mid-IR classification: SA(s)dm ; Filter: IRAC 3.6 μ m; North: up, East: left; Field dimensions: 21.0 \times 15.3 arcmin; Surface brightness range displayed: 16.5–28.0 mag arcsec⁻²

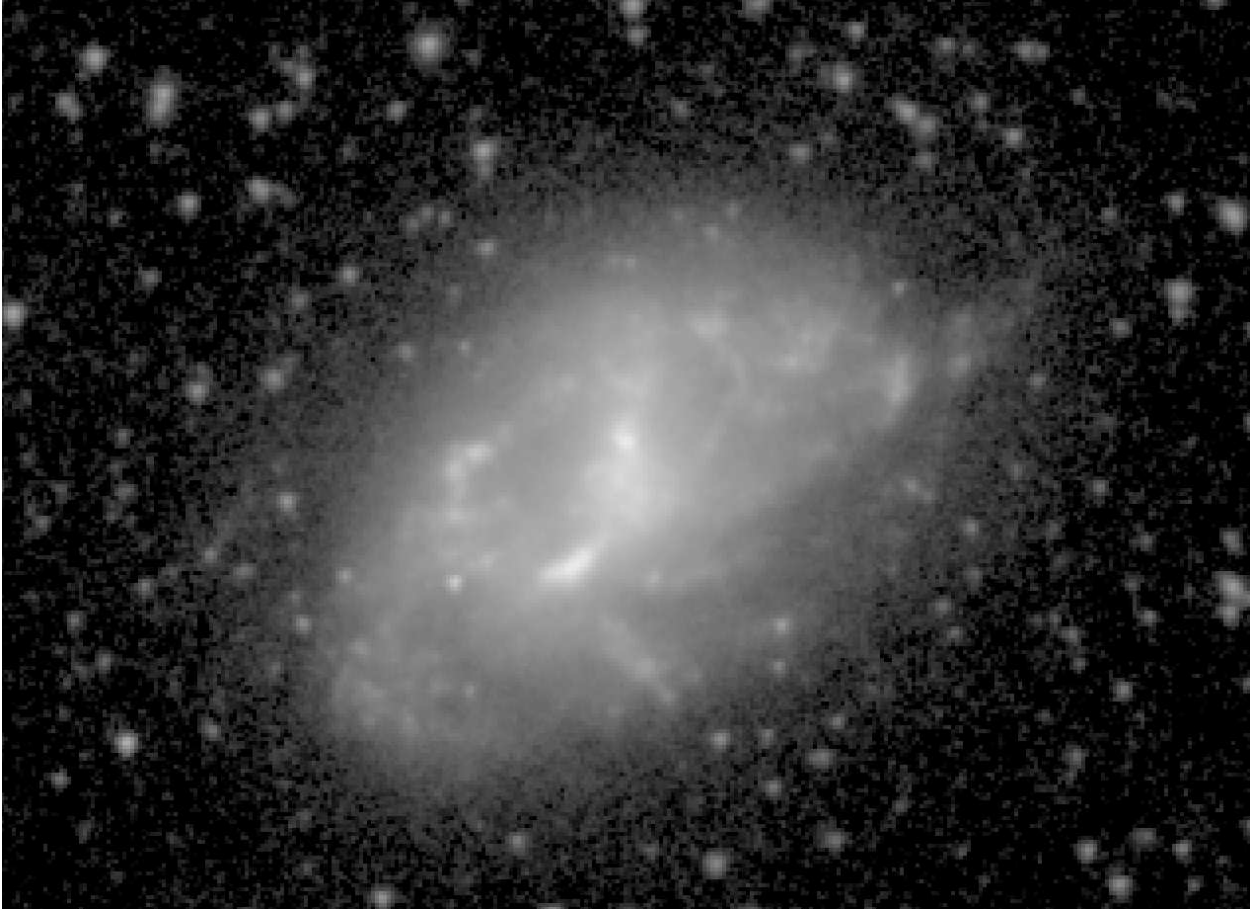


Fig. 1.8.— **NGC 337** - S⁴G mid-IR classification: SAB(s)cd: pec ; Filter: IRAC 3.6 μ m; North: up, East: left; Field dimensions: 4.0 \times 2.9 arcmin; Surface brightness range displayed: 15.5–28.0 mag arcsec⁻²

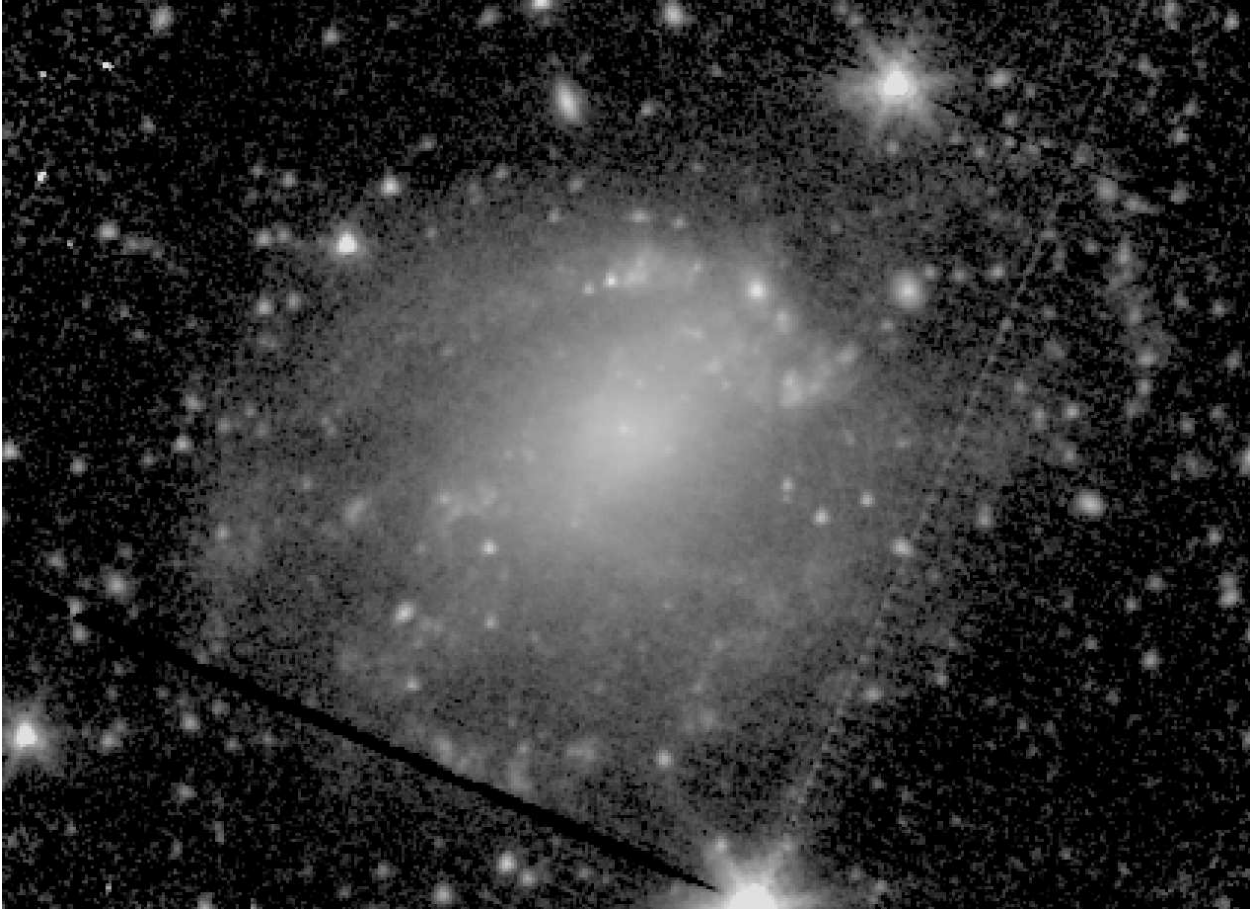


Fig. 1.9.— **NGC 428** - S⁴G mid-IR classification: SAB(s)dm ; Filter: IRAC 3.6μm; North: up, East: left; Field dimensions: 5.3× 3.8 arcmin; Surface brightness range displayed: 16.5–28.0 mag arcsec⁻²

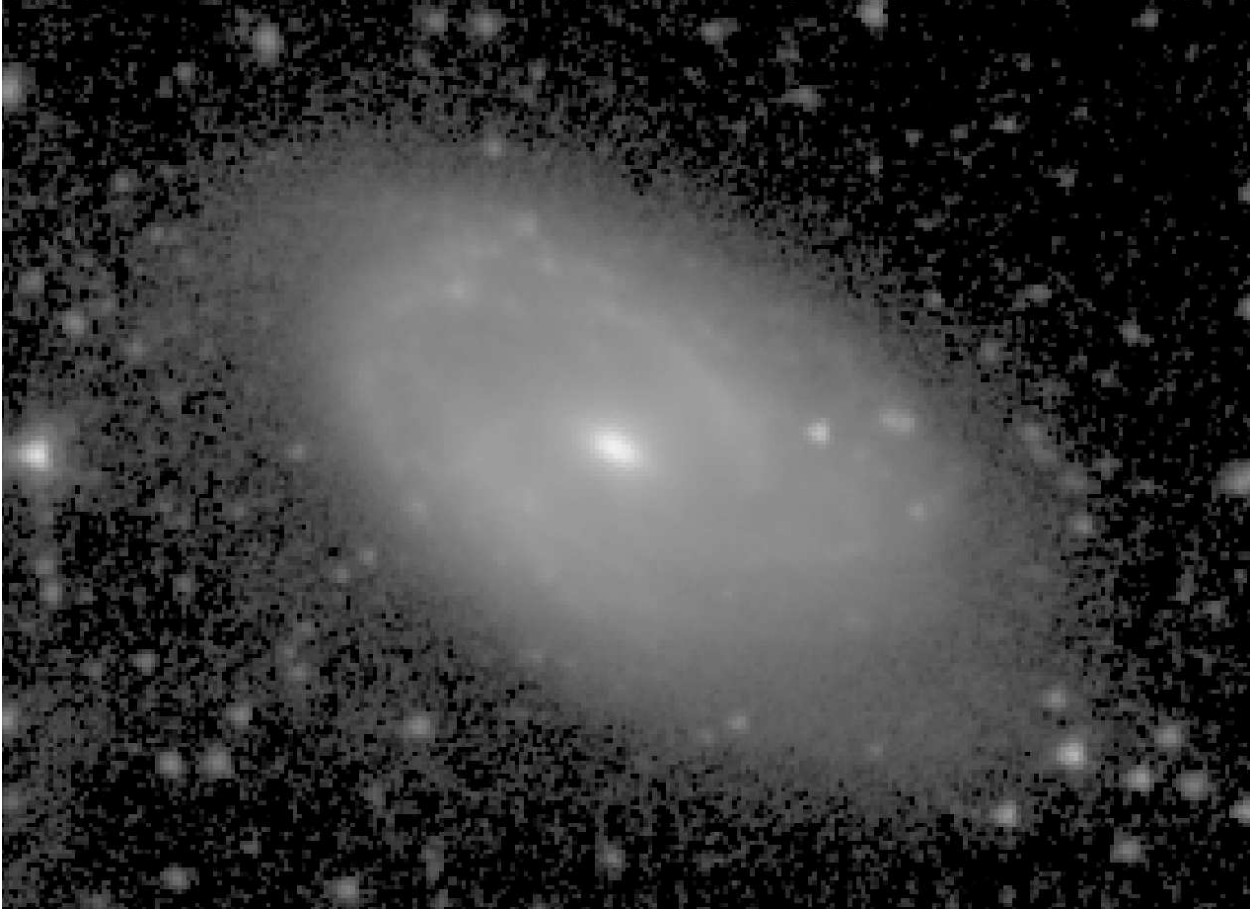


Fig. 1.10.— **NGC 470** - S^4G mid-IR classification: $S_{AB}(r_{95})_{ab}$; Filter: IRAC $3.6\mu\text{m}$; North: left, East: down; Field dimensions: 3.5×2.6 arcmin; Surface brightness range displayed: $13.0\text{--}28.0$ mag arcsec $^{-2}$



Fig. 1.11.— **NGC 474** - S⁴G mid-IR classification: (R)SAB0/a (shells/ripples) pec ; Filter: IRAC 3.6 μ m; North: up, East: left; Field dimensions: 7.0 \times 5.1 arcmin; Surface brightness range displayed: 13.5–28.0 mag arcsec⁻²



Fig. 1.12.— **NGC 584** - S⁴G mid-IR classification: S**A**B0⁻ ; Filter: IRAC 3.6 μ m; North: up, East: left; Field dimensions: 6.3 \times 4.6 arcmin; Surface brightness range displayed: 12.0–28.0 mag arcsec⁻²



Fig. 1.13.— **NGC 628** - S⁴G mid-IR classification: SA(s)c ; Filter: IRAC 3.6 μ m; North: up, East: left; Field dimensions: 14.4 \times 10.5 arcmin; Surface brightness range displayed: 15.0–28.0 mag arcsec⁻²

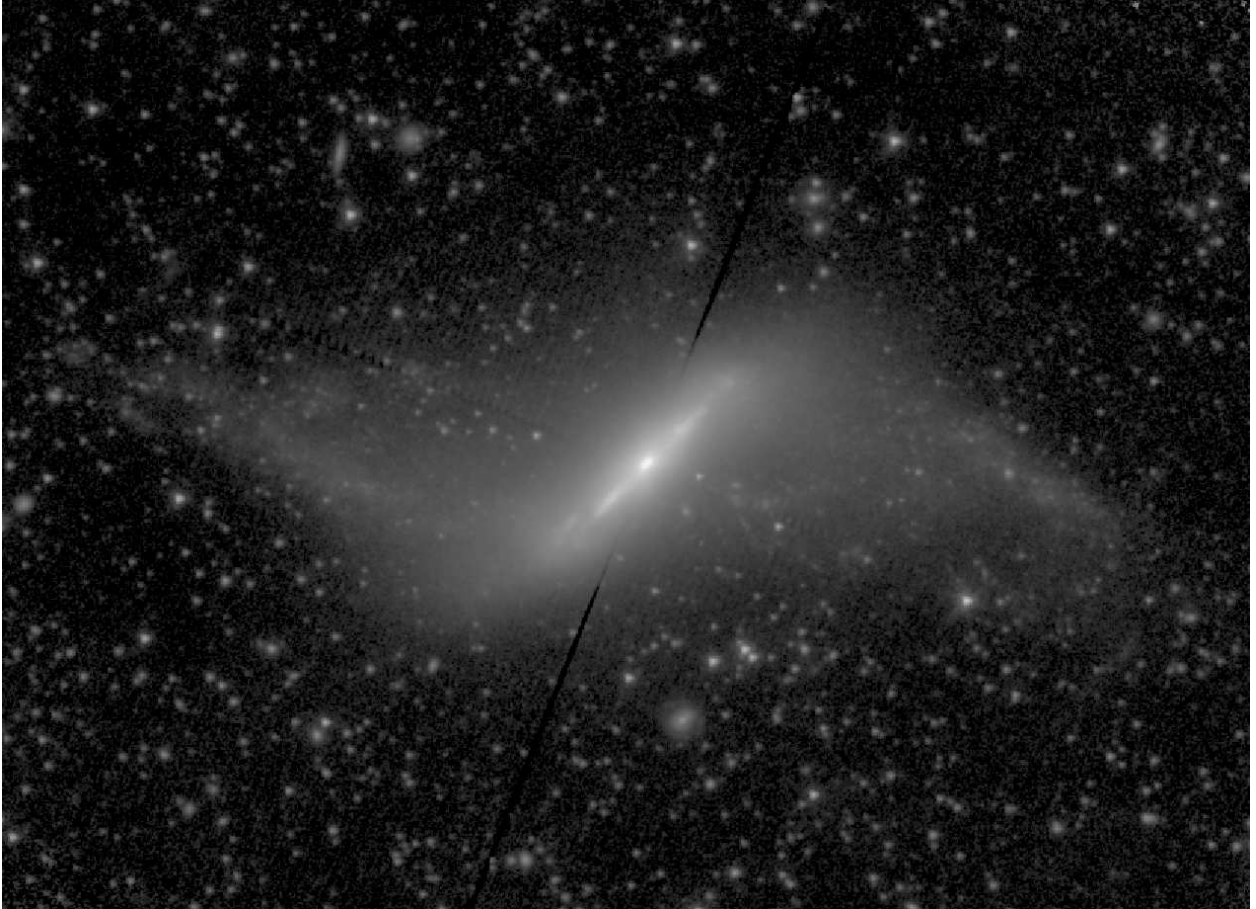


Fig. 1.14.— **NGC 660** - S⁴G mid-IR classification: PRG ; Filter: IRAC 3.6 μ m; North: left, East: down; Field dimensions: 10.5 \times 7.7 arcmin; Surface brightness range displayed: 11.5–28.0 mag arcsec⁻²

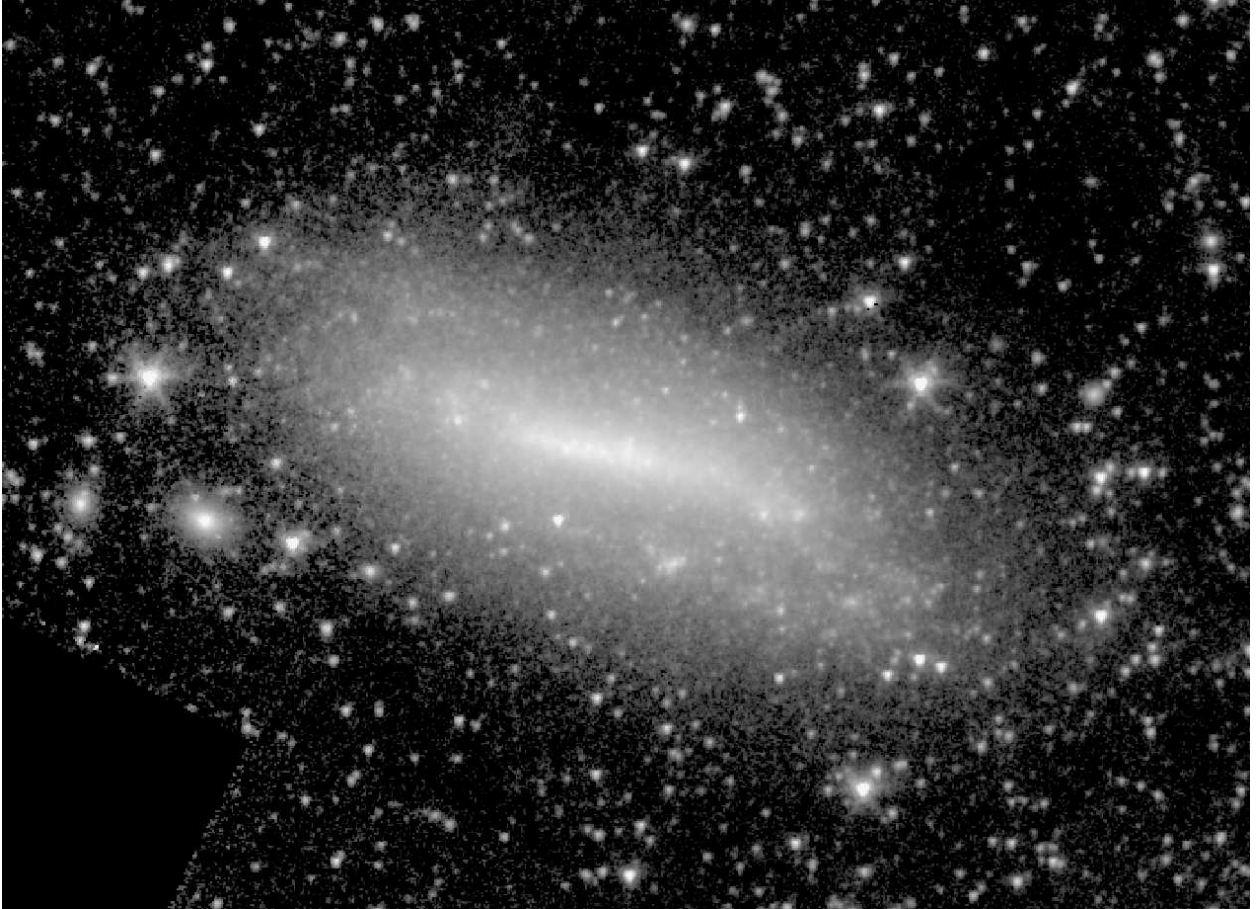


Fig. 1.15.— **NGC 672** - S⁴G mid-IR classification: (R')SB(s)d ; Filter: IRAC 3.6 μ m; North: up, East: left; Field dimensions: 8.8 \times 6.4 arcmin; Surface brightness range displayed: 17.0–28.0 mag arcsec⁻²



Fig. 1.16.— **NGC 691** - S⁴G mid-IR classification: (R)SA(r)ab ; Filter: IRAC 3.6 μ m; North: up, East: left; Field dimensions: 5.3 \times 3.8 arcmin; Surface brightness range displayed: 14.5–28.0 mag arcsec⁻²

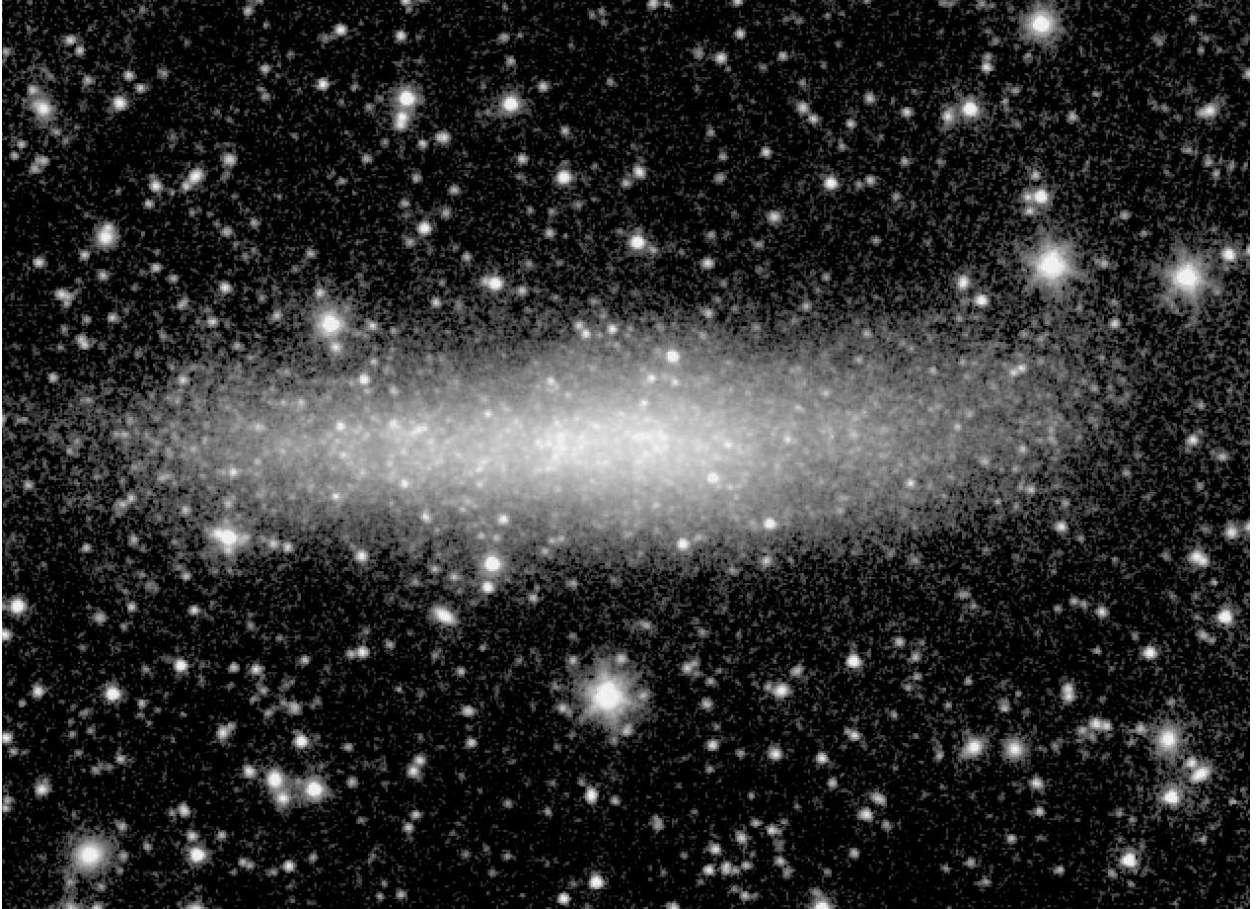


Fig. 1.17.— **NGC 784** - S⁴G mid-IR classification: SBm: sp ; Filter: IRAC 3.6 μ m; North: left, East: down; Field dimensions: 7.9 \times 5.8 arcmin; Surface brightness range displayed: 18.5–28.0 mag arcsec⁻²

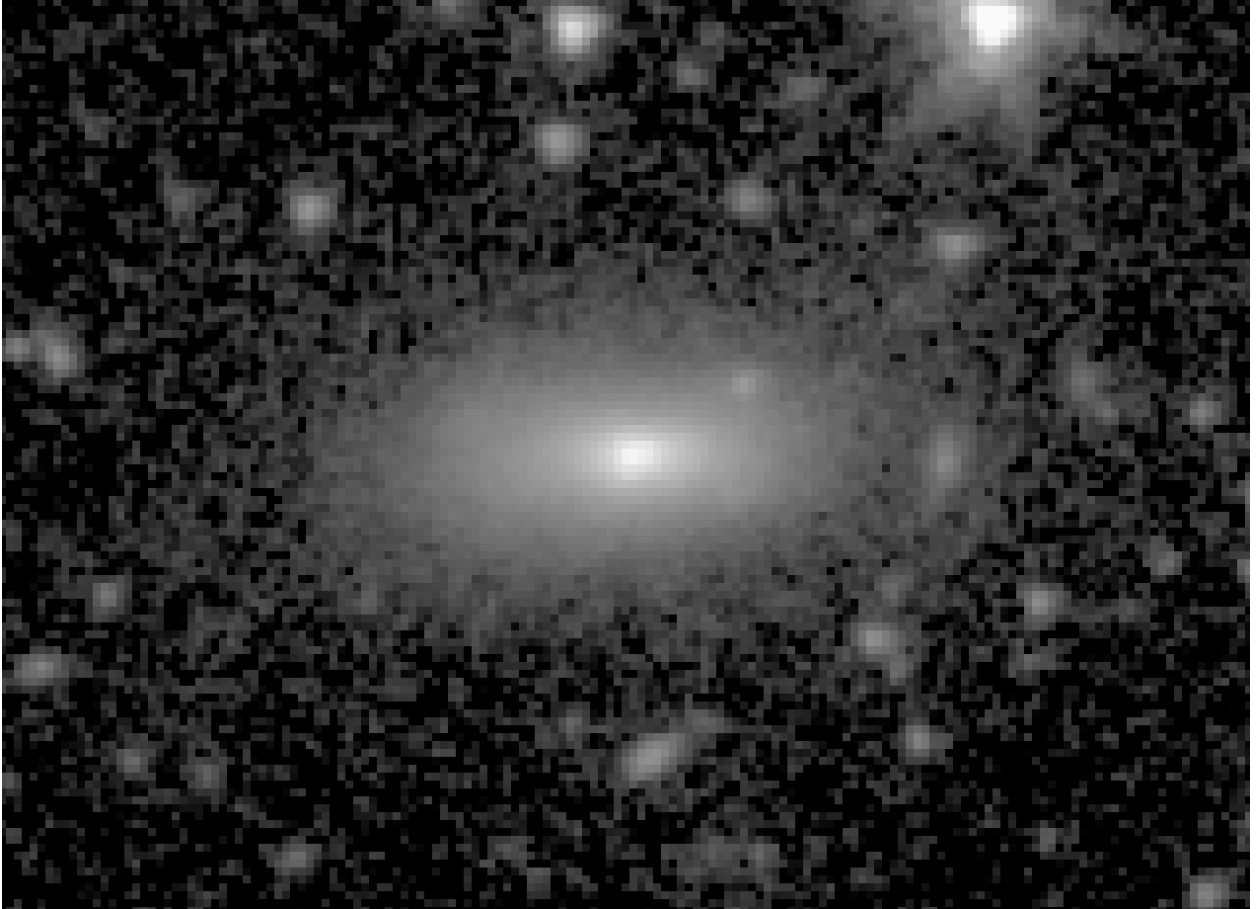


Fig. 1.18.— **NGC 814** - S⁴G mid-IR classification: SAB0⁻; Filter: IRAC 3.6 μ m; North: left, East: down; Field dimensions: 2.0 \times 1.4 arcmin; Surface brightness range displayed: 14.5–28.0 mag arcsec⁻²



Fig. 1.19.— **NGC 855** - S⁴G mid-IR classification: SA0⁻ ; Filter: IRAC 3.6 μ m; North: up, East: left; Field dimensions: 3.8 \times 2.7 arcmin; Surface brightness range displayed: 15.0–28.0 mag arcsec⁻²



Fig. 1.20.— **NGC 941** - S⁴G mid-IR classification: (R′:)SAB(r:)c ; Filter: IRAC 3.6μm; North: left, East: down; Field dimensions: 4.0× 2.9 arcmin; Surface brightness range displayed: 16.5–28.0 mag arcsec⁻²

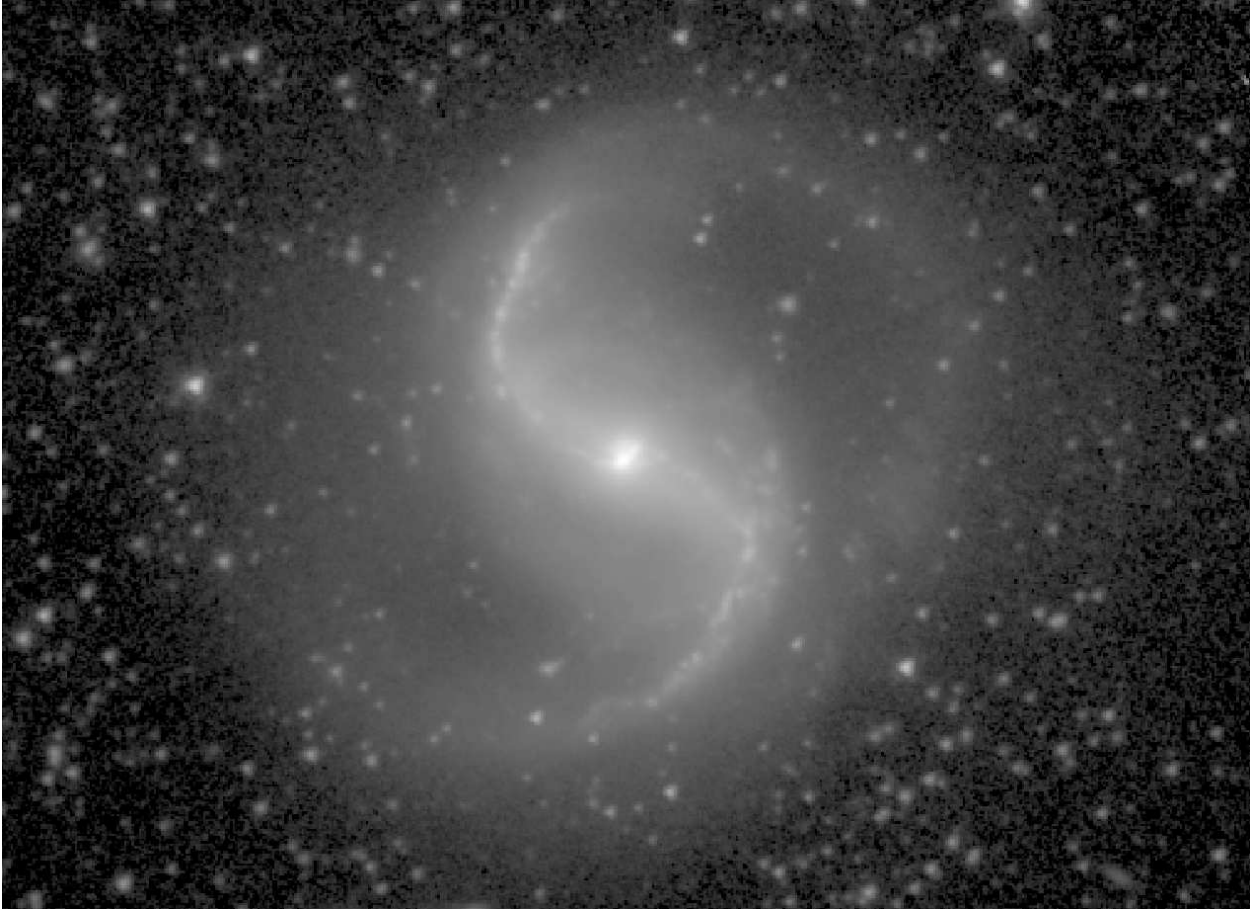


Fig. 1.21.— **NGC 986** - S⁴G mid-IR classification: (R')SB(rs,nb)ab ; Filter: IRAC 3.6 μ m; North: up, East: left; Field dimensions: 6.3 \times 4.6 arcmin; Surface brightness range displayed: 13.0–28.0 mag arcsec⁻²

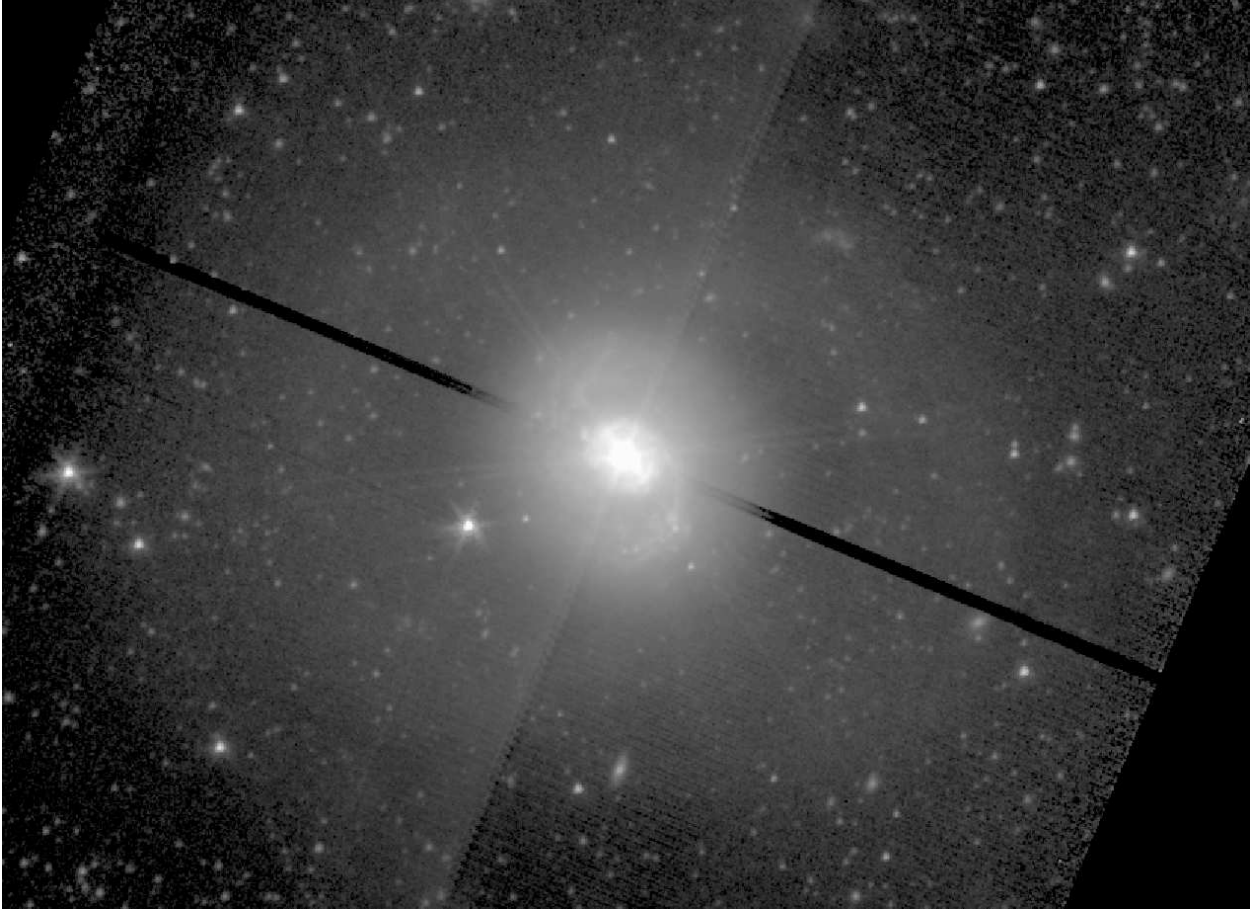


Fig. 1.22.— **NGC 1068** - S⁴G mid-IR classification: (R)SA(s,nr)a ; Filter: IRAC 3.6 μ m; North: up, East: left; Field dimensions: 10.5 \times 7.7 arcmin; Surface brightness range displayed: 11.0–28.0 mag arcsec⁻²



Fig. 1.23.— **NGC 1097** - S⁴G mid-IR classification: (R')SB(rs,rr)ab pec ; Filter: IRAC 3.6 μm; North: up, East: left; Field dimensions: 12.6 × 9.2 arcmin; Surface brightness range displayed: 12.5–28.0 mag arcsec⁻²

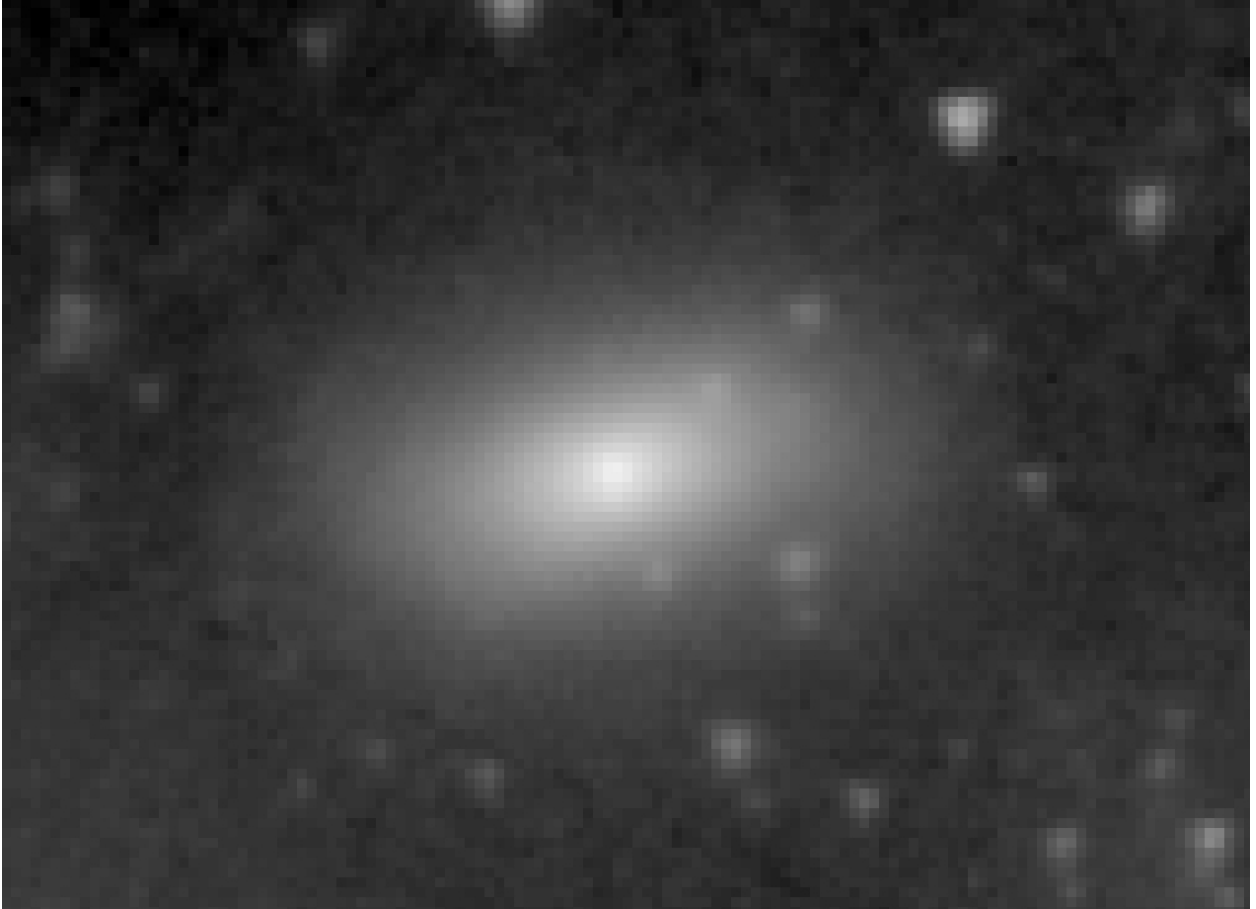


Fig. 1.24.— **NGC 1097A** - S⁴G mid-IR classification: dE5 ; Filter: IRAC 3.6 μ m; North: up, East: left; Field dimensions: 1.6 \times 1.1 arcmin; Surface brightness range displayed: 15.0–28.0 mag arcsec⁻²

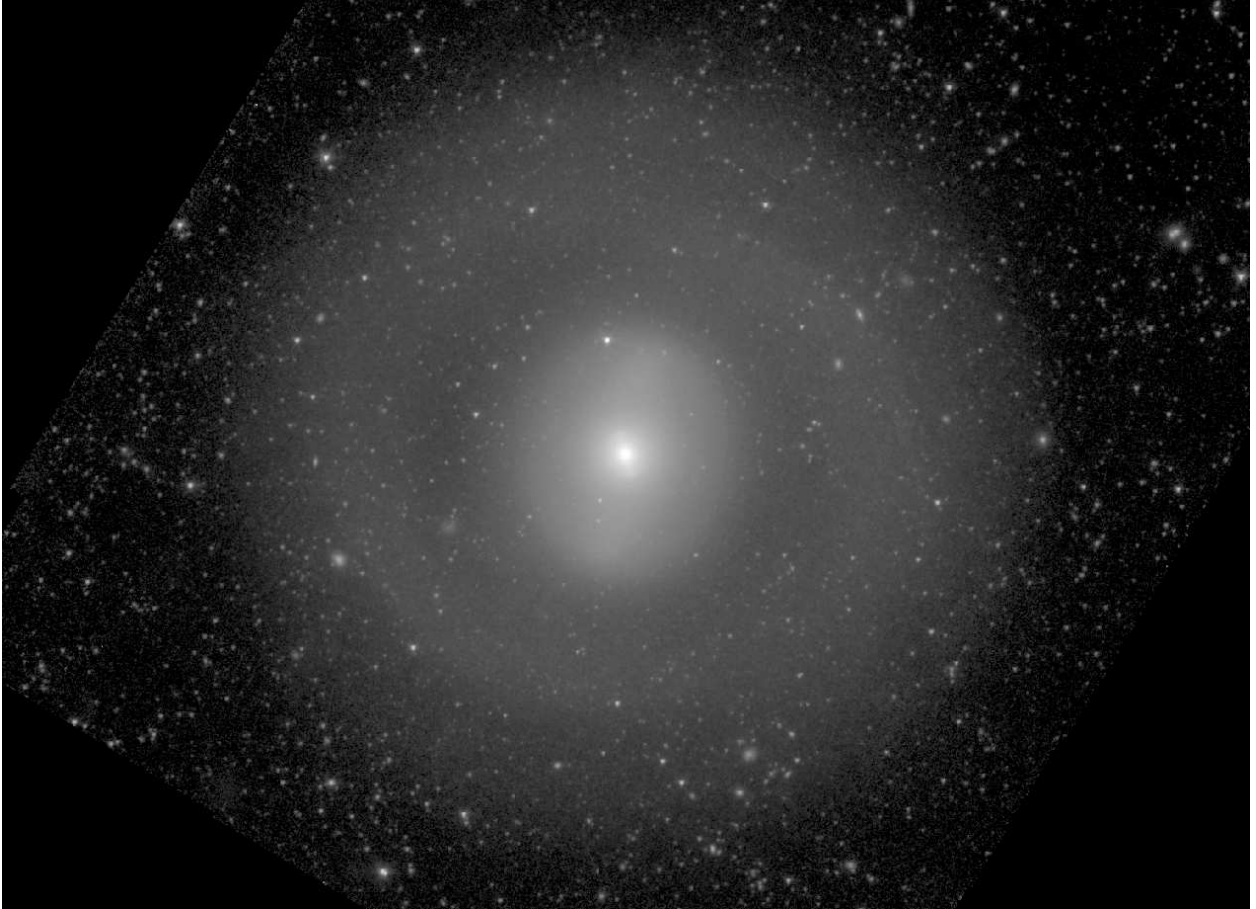


Fig. 1.25.— **NGC 1291** - S⁴G mid-IR classification: (R)SAB(1,nb)0⁺ ; Filter: IRAC 3.6 μ m; North: up, East: left; Field dimensions: 18.5 \times 13.5 arcmin; Surface brightness range displayed: 11.5–28.0 mag arcsec⁻²

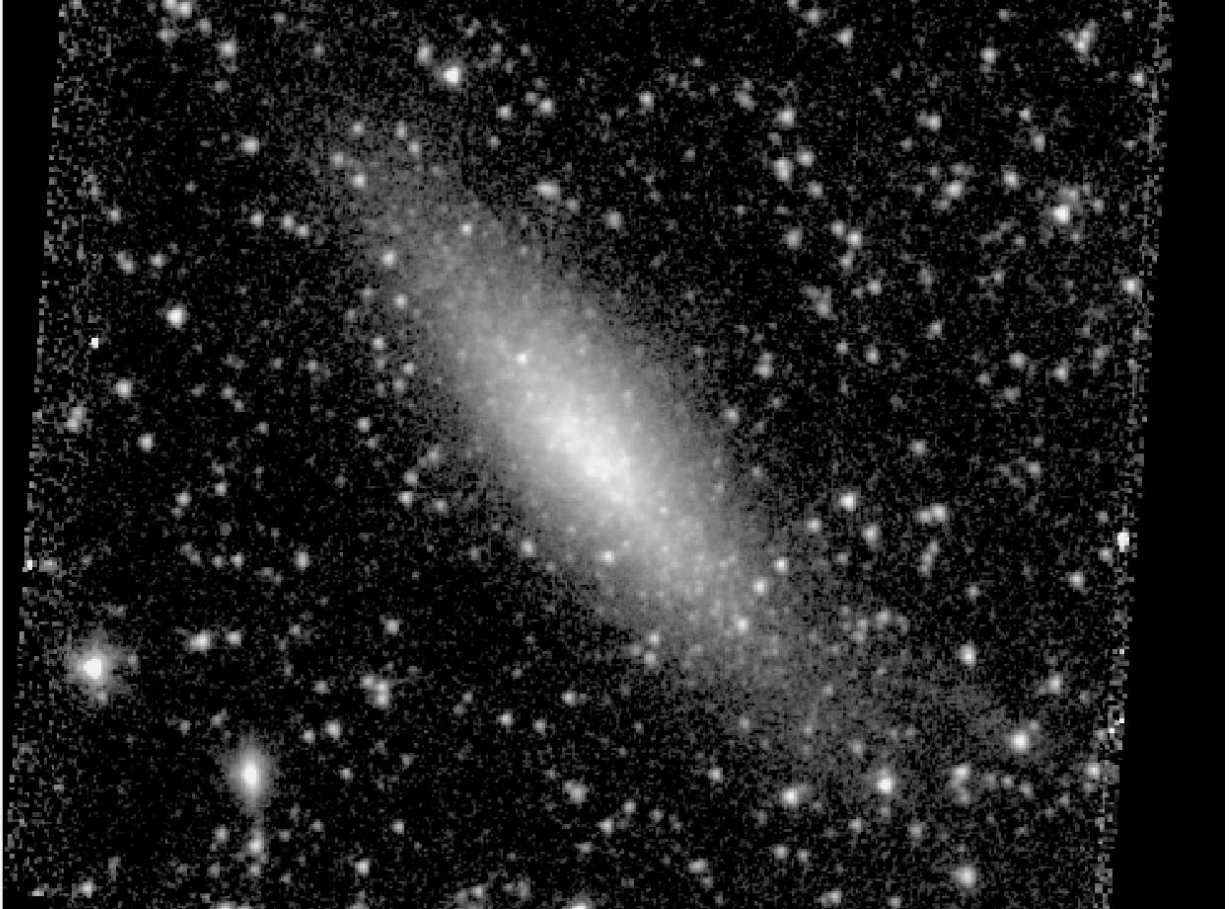


Fig. 1.26.— **NGC 1311** - S⁴G mid-IR classification: SBdm: sp ; Filter: IRAC 3.6 μ m; North: up, East: left; Field dimensions: 6.2 \times 4.5 arcmin; Surface brightness range displayed: 18.0–28.0 mag arcsec⁻²

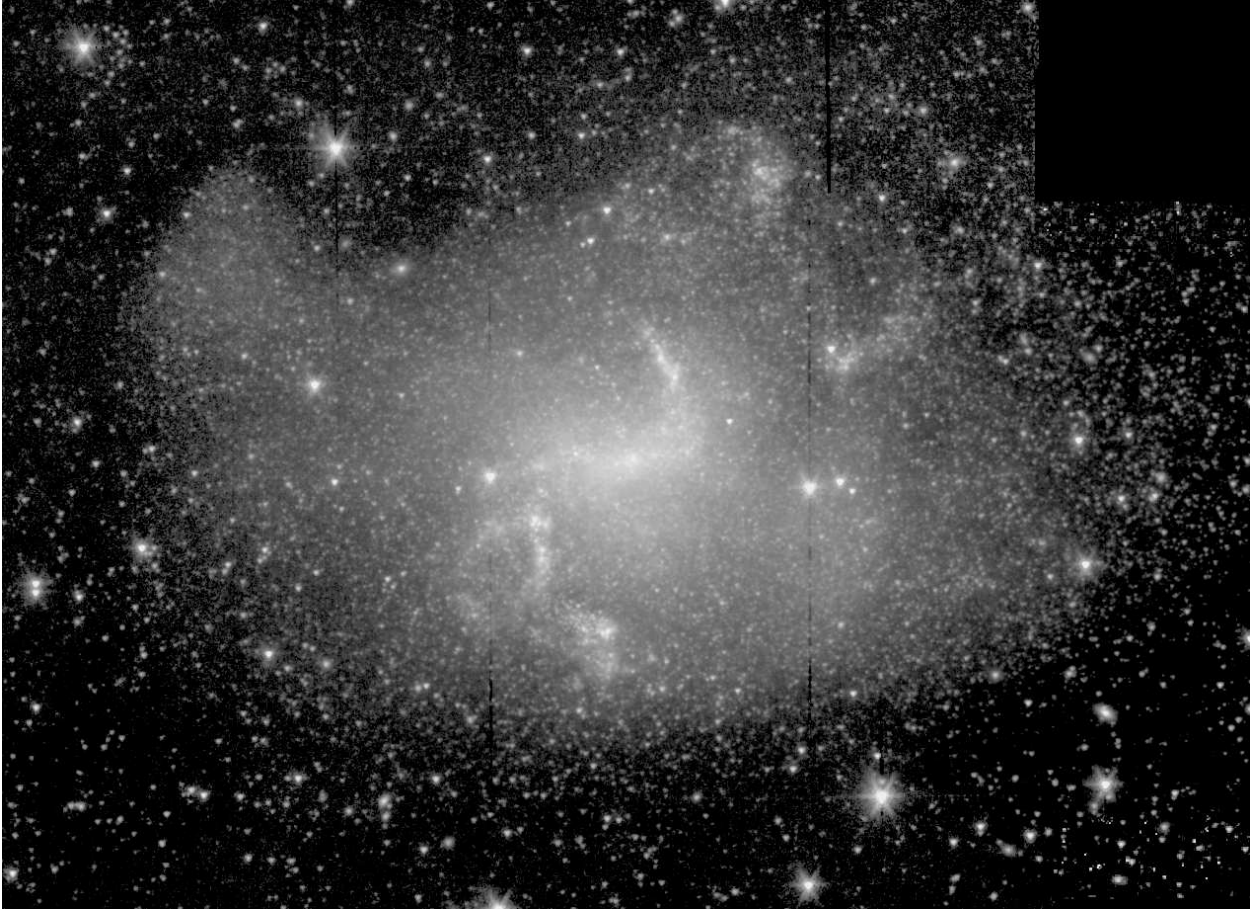


Fig. 1.27.— **NGC 1313** - S⁴G mid-IR classification: SB(s)dm pec ; Filter: IRAC 3.6 μ m; North: left, East: down; Field dimensions: 15.8 \times 11.5 arcmin; Surface brightness range displayed: 16.5–28.0 mag arcsec⁻²

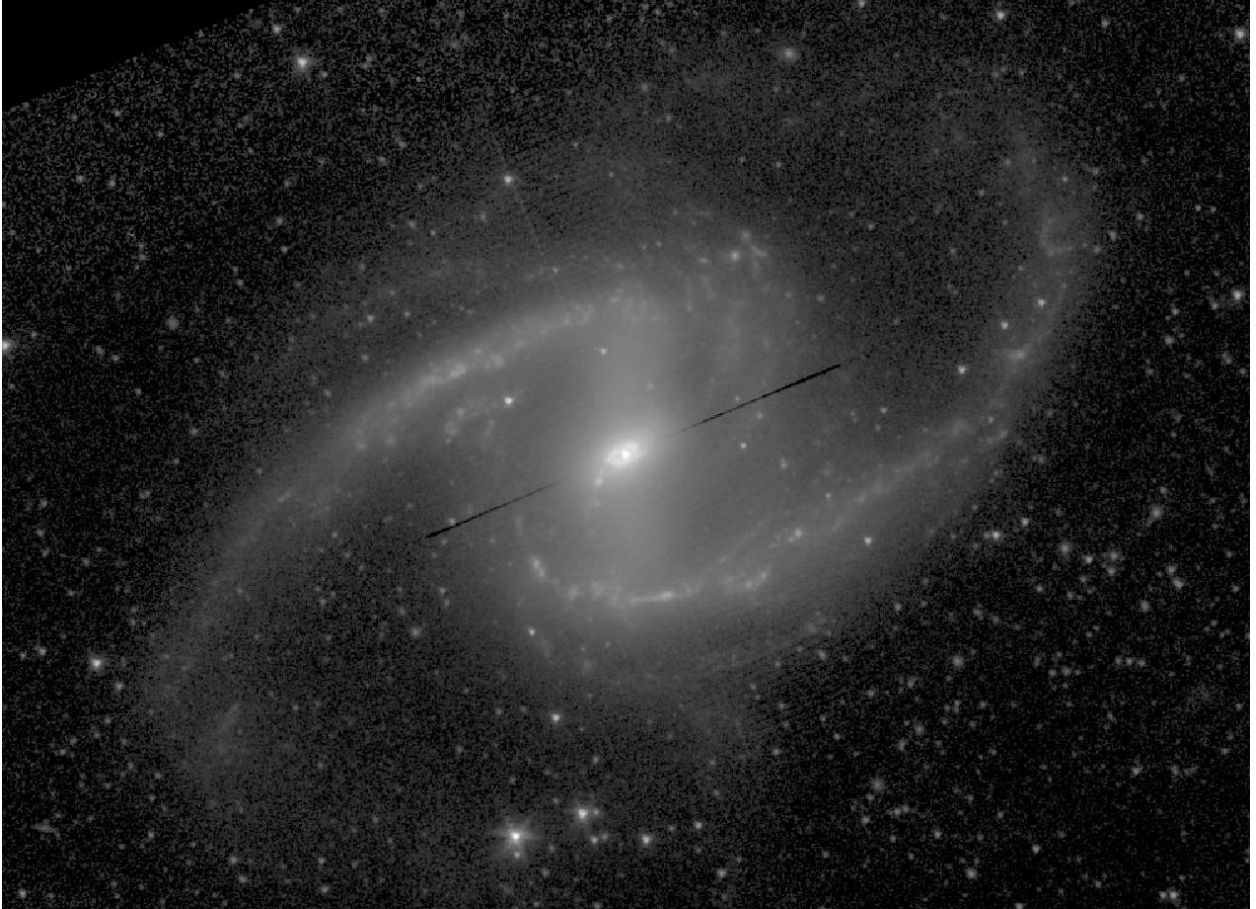


Fig. 1.28.— **NGC 1365** - S⁴G mid-IR classification: SB(r_g,nr)bc ; Filter: IRAC 3.6μm; North: left, East: down; Field dimensions: 12.6× 9.2 arcmin; Surface brightness range displayed: 11.0–28.0 mag arcsec⁻²



Fig. 1.29.— **NGC 1433** - S⁴G mid-IR classification: (R₁')SB(r,nr,nb)a ; Filter: IRAC 3.6 μ m; North: up, East: left; Field dimensions: 10.5 \times 7.6 arcmin; Surface brightness range displayed: 13.0–28.0 mag arcsec⁻²

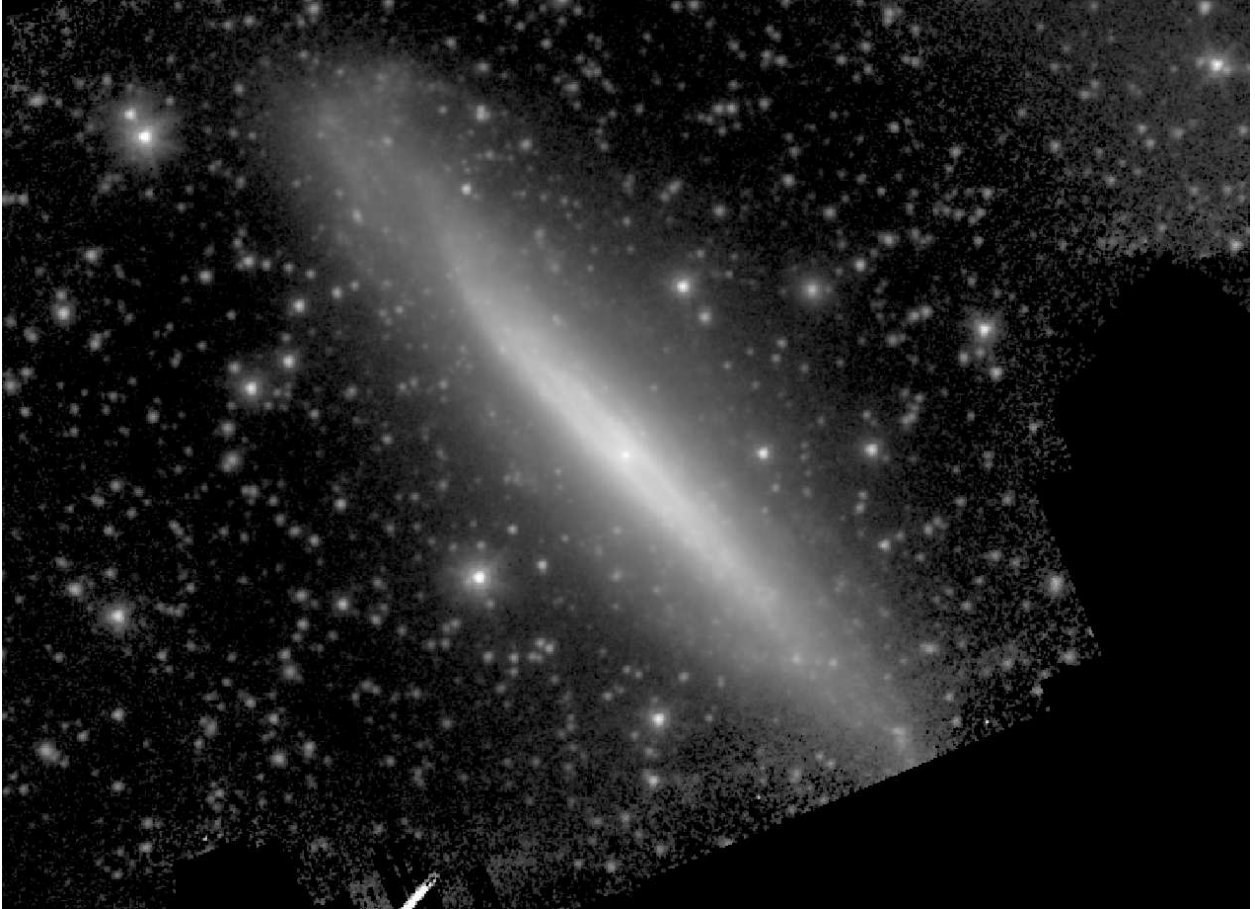


Fig. 1.30.— **NGC 1448** - S⁴G mid-IR classification: SA(rs:)c sp ; Filter: IRAC 3.6 μ m; North: up, East: left; Field dimensions: 9.0 \times 6.6 arcmin; Surface brightness range displayed: 14.0–28.0 mag arcsec⁻²

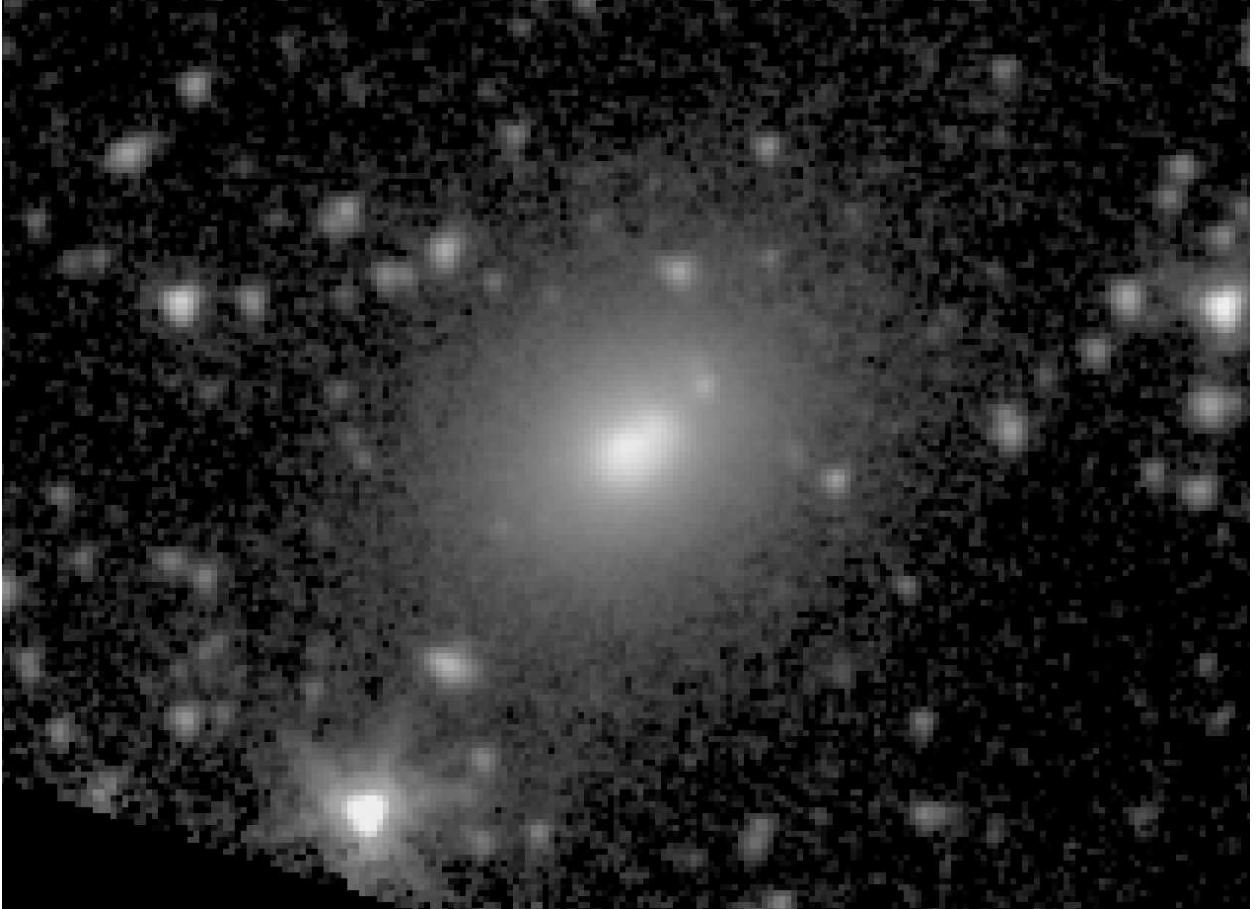


Fig. 1.31.— **NGC 1481** - S⁴G mid-IR classification: SA(l)0⁻: pec ; Filter: IRAC 3.6 μ m;
North: up, East: left; Field dimensions: 2.6 \times 1.9 arcmin; Surface brightness range displayed:
15.5–28.0 mag arcsec⁻²



Fig. 1.32.— **NGC 1482** - S⁴G mid-IR classification: Sa: sp ; Filter: IRAC 3.6 μ m; North: up, East: left; Field dimensions: 5.3 \times 3.8 arcmin; Surface brightness range displayed: 12.0–28.0 mag arcsec⁻²



Fig. 1.33.— **NGC 1487** - S⁴G mid-IR classification: Pec ; Filter: IRAC 3.6 μ m; North: up, East: left; Field dimensions: 5.8 \times 4.2 arcmin; Surface brightness range displayed: 15.5–28.0 mag arcsec⁻²



Fig. 1.34.— **NGC 1510** - S⁴G mid-IR classification: SA0⁺: ; Filter: IRAC 3.6 μ m; North: up, East: left; Field dimensions: 3.2 \times 2.3 arcmin; Surface brightness range displayed: 15.5–28.0 mag arcsec⁻²

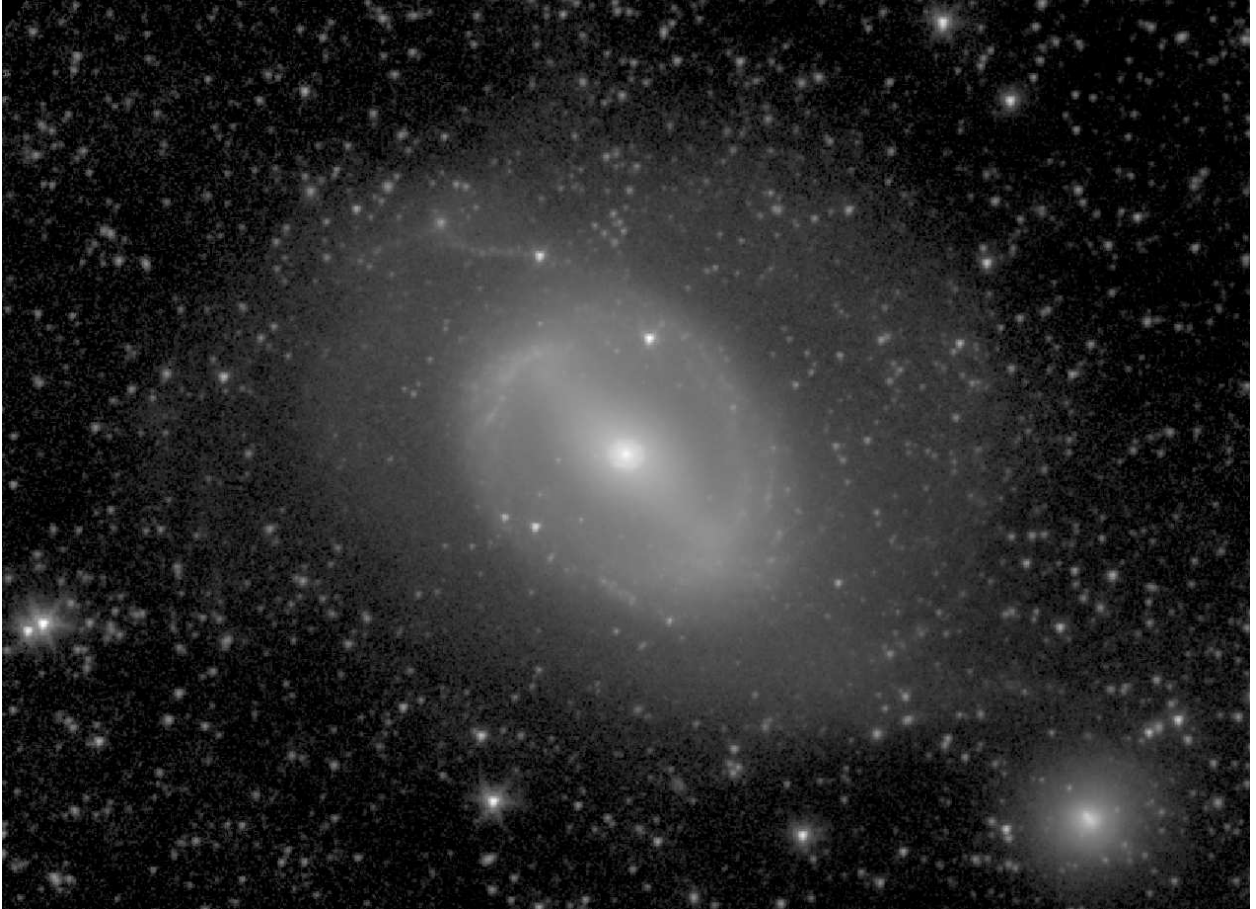


Fig. 1.35.— **NGC 1512** - S⁴G mid-IR classification: (RL)SB(r,nr)a ; Filter: IRAC 3.6 μ m; North: up, East: left; Field dimensions: 10.5 \times 7.7 arcmin; Surface brightness range displayed: 13.5–28.0 mag arcsec⁻²



Fig. 1.36.— **NGC 1559** - S⁴G mid-IR classification: SB(s)cd ; Filter: IRAC 3.6 μ m;
North: up, East: left; Field dimensions: 5.7 \times 4.2 arcmin; Surface brightness range displayed:
15.0–28.0 mag arcsec⁻²



Fig. 1.37.— **NGC 1566** - S⁴G mid-IR classification: (R'₁)SAB(s)b ; Filter: IRAC 3.6μm; North: up, East: left; Field dimensions: 11.5× 8.4 arcmin; Surface brightness range displayed: 12.0–28.0 mag arcsec⁻²

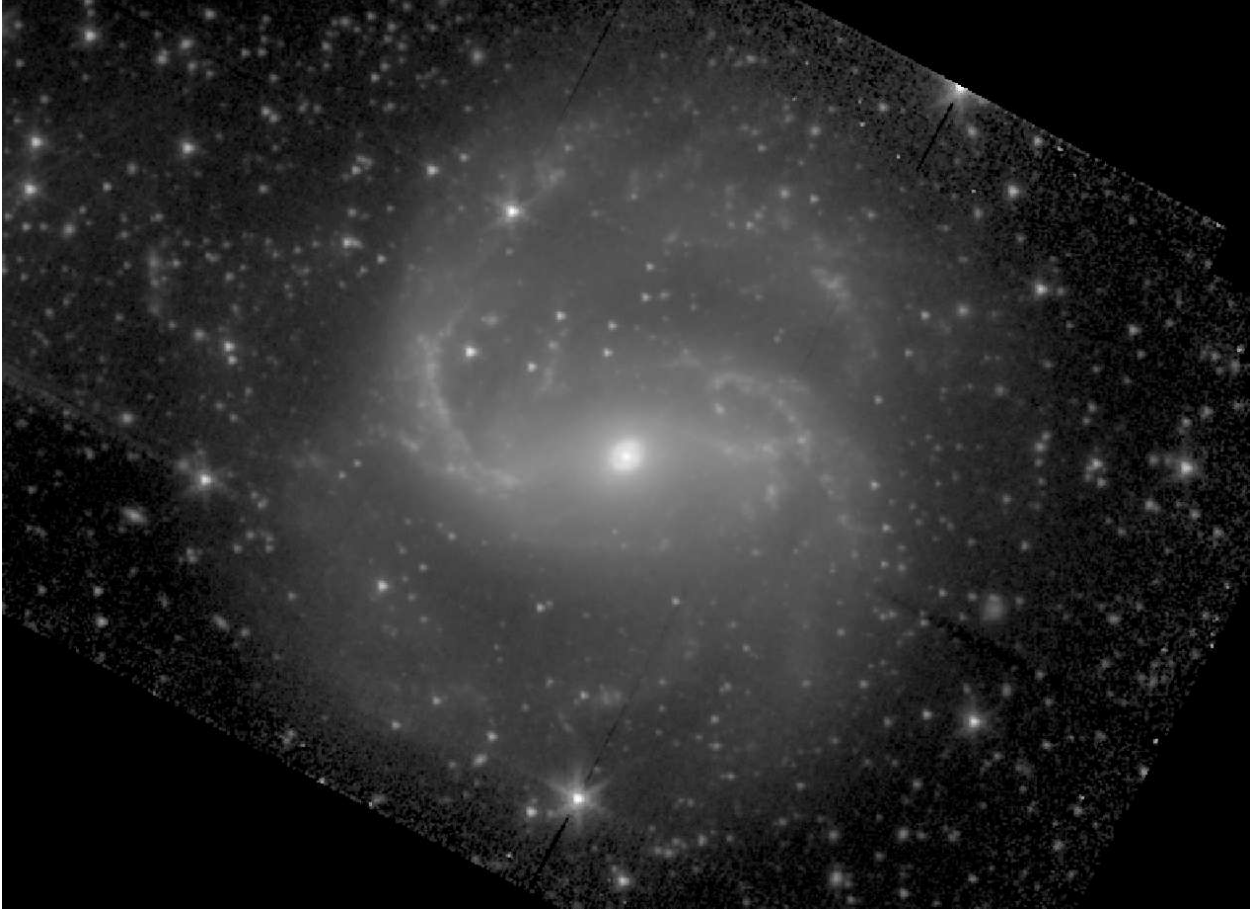


Fig. 1.38.— **NGC 1672** - S⁴G mid-IR classification: (R')SAB(rs,nr)b ; Filter: IRAC 3.6 μ m; North: up, East: left; Field dimensions: 9.9 \times 7.2 arcmin; Surface brightness range displayed: 12.0–28.0 mag arcsec⁻²

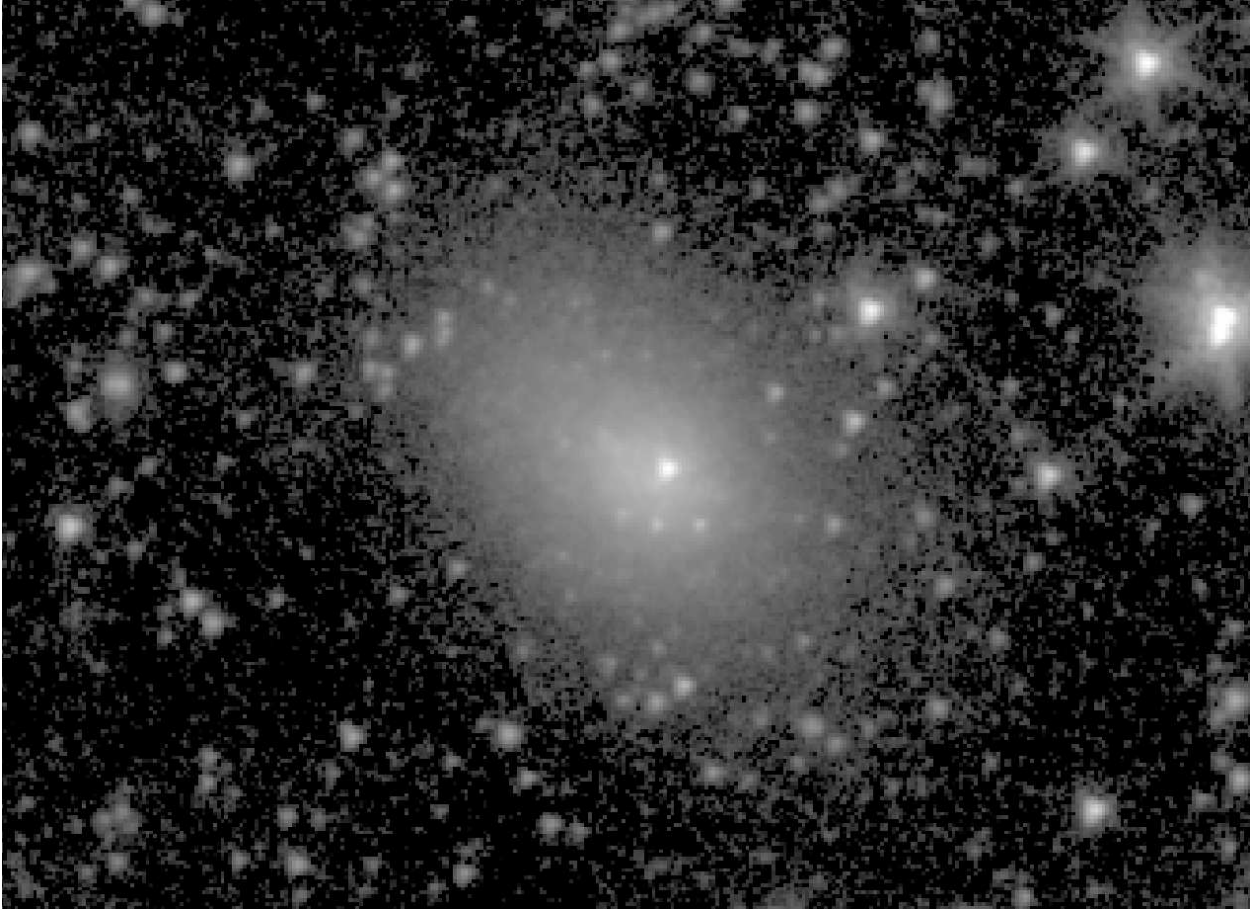


Fig. 1.39.— **NGC 1705** - S⁴G mid-IR classification: dE3,N ; Filter: IRAC 3.6 μ m; North: up, East: left; Field dimensions: 4.2 \times 3.0 arcmin; Surface brightness range displayed: 12.0–28.0 mag arcsec⁻²



Fig. 1.40.— **NGC 1744** - S⁴G mid-IR classification: SB(s)d ; Filter: IRAC 3.6 μ m; North: left, East: down; Field dimensions: 7.9 \times 5.7 arcmin; Surface brightness range displayed: 17.5–28.0 mag arcsec⁻²

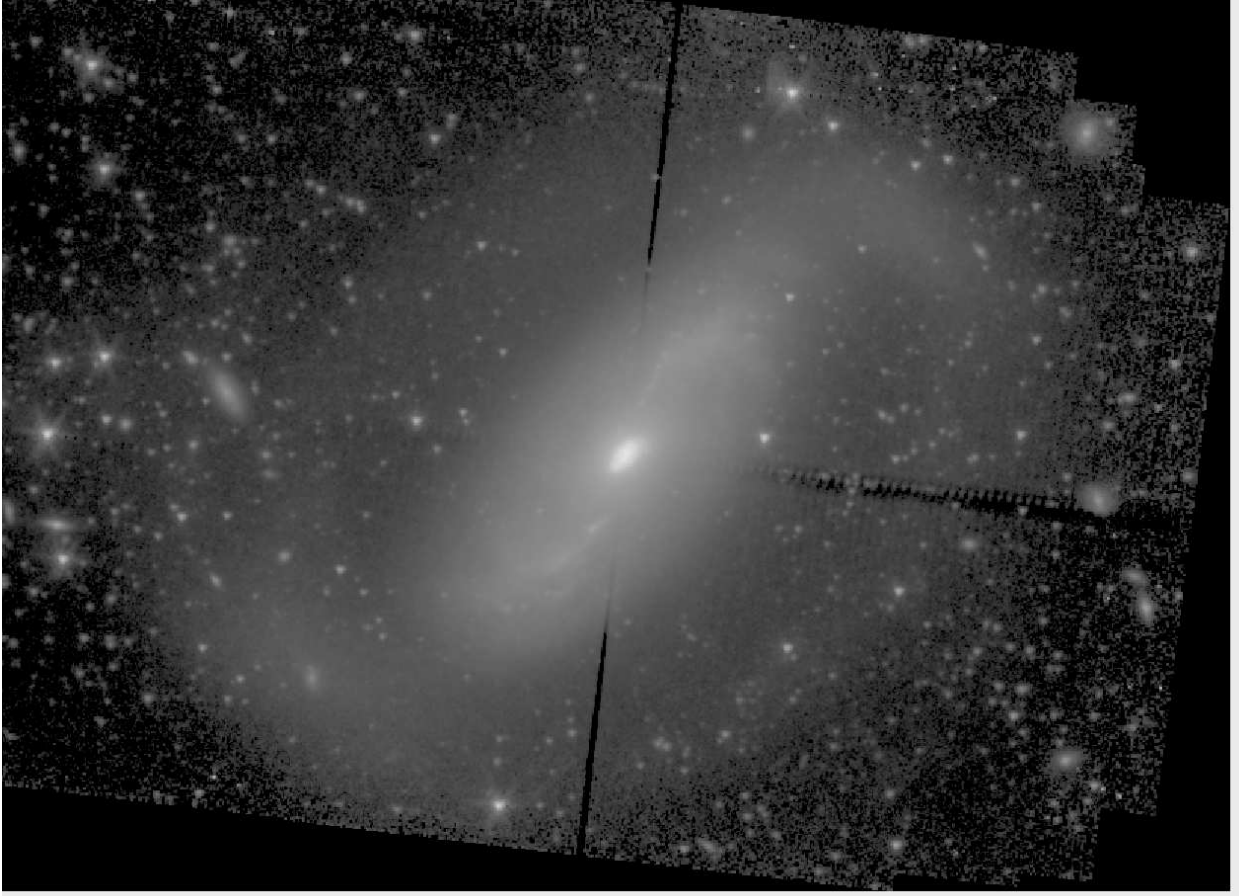


Fig. 1.41.— **NGC 1808** - S⁴G mid-IR classification: (R₁)SAB(s,nr)a ; Filter: IRAC 3.6 μ m; North: up, East: left; Field dimensions: 10.4 \times 7.5 arcmin; Surface brightness range displayed: 11.5–28.0 mag arcsec⁻²



Fig. 1.42.— **NGC 2500** - S⁴G mid-IR classification: SAB(s)d ; Filter: IRAC 3.6 μ m; North: up, East: left; Field dimensions: 5.3 \times 3.8 arcmin; Surface brightness range displayed: 16.5–28.0 mag arcsec⁻²



Fig. 1.43.— **NGC 2552** - S⁴G mid-IR classification: (R')SAB(s)m ; Filter: IRAC 3.6 μ m; North: up, East: left; Field dimensions: 5.3 \times 3.8 arcmin; Surface brightness range displayed: 18.0–28.0 mag arcsec⁻²

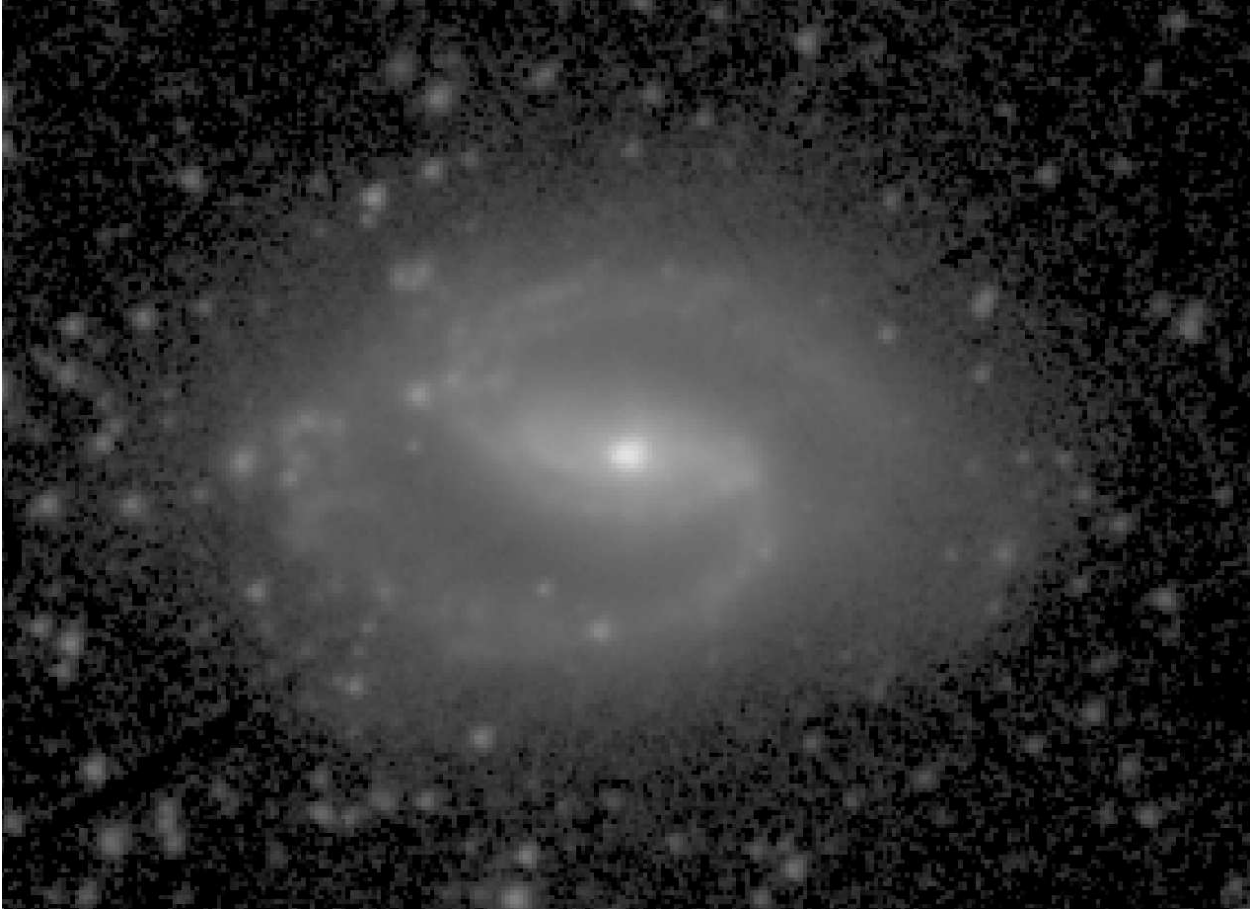


Fig. 1.44.— **NGC 2633** - S^4G mid-IR classification: SAB(rs)b ; Filter: IRAC $3.6\mu\text{m}$; North: left, East: down; Field dimensions: 3.5×2.6 arcmin; Surface brightness range displayed: $12.0\text{--}28.0$ mag arcsec $^{-2}$



Fig. 1.45.— **NGC 2634** - S⁴G mid-IR classification: SA(nl)0⁻ (shells/ripples) ; Filter: IRAC 3.6 μ m; North: left, East: down; Field dimensions: 5.3 \times 3.8 arcmin; Surface brightness range displayed: 13.5–28.0 mag arcsec⁻²

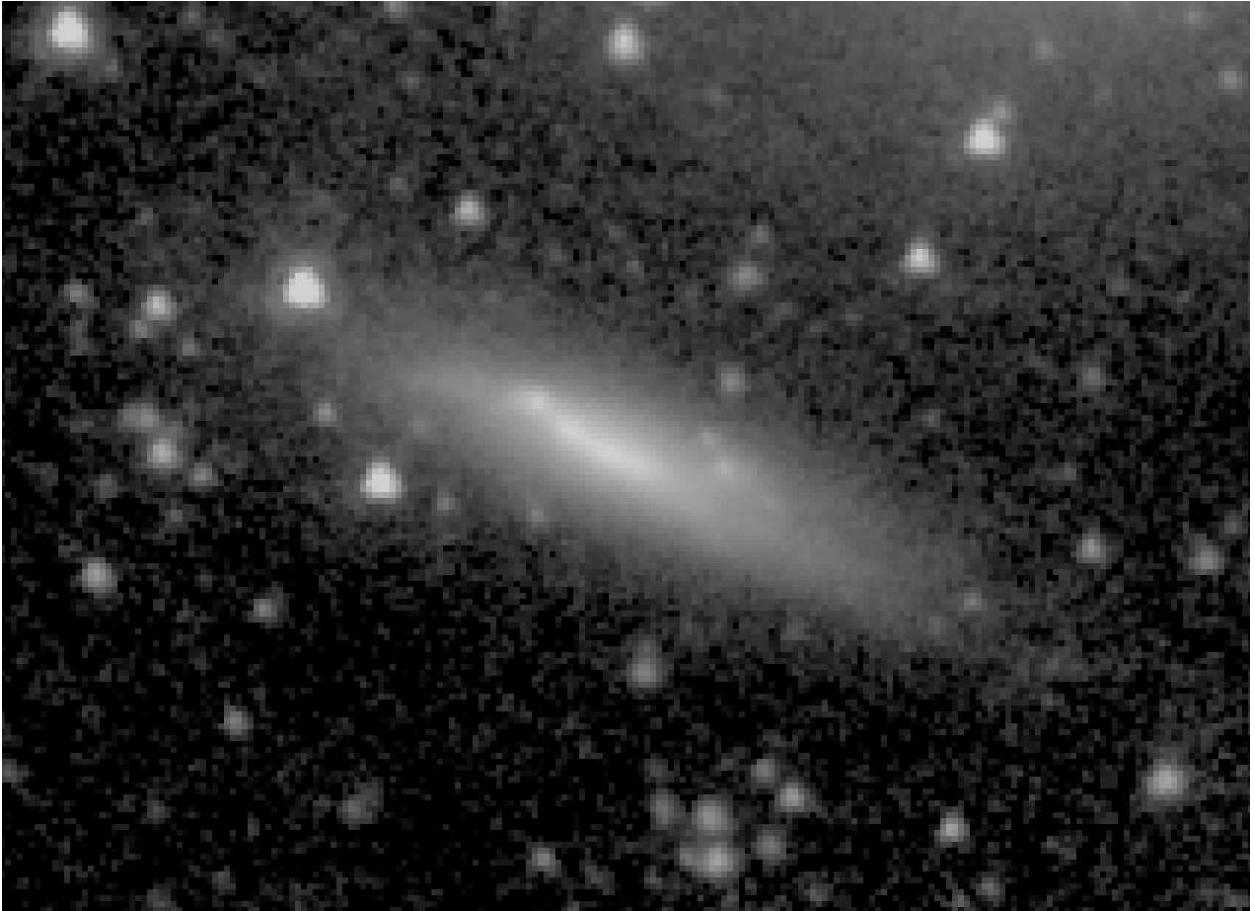


Fig. 1.46.— **NGC 2634A** - S⁴G mid-IR classification: SB(s)m: sp ; Filter: IRAC 3.6 μ m;
North: up, East: left; Field dimensions: 2.6 \times 1.9 arcmin; Surface brightness range displayed:
17.0–28.0 mag arcsec⁻²

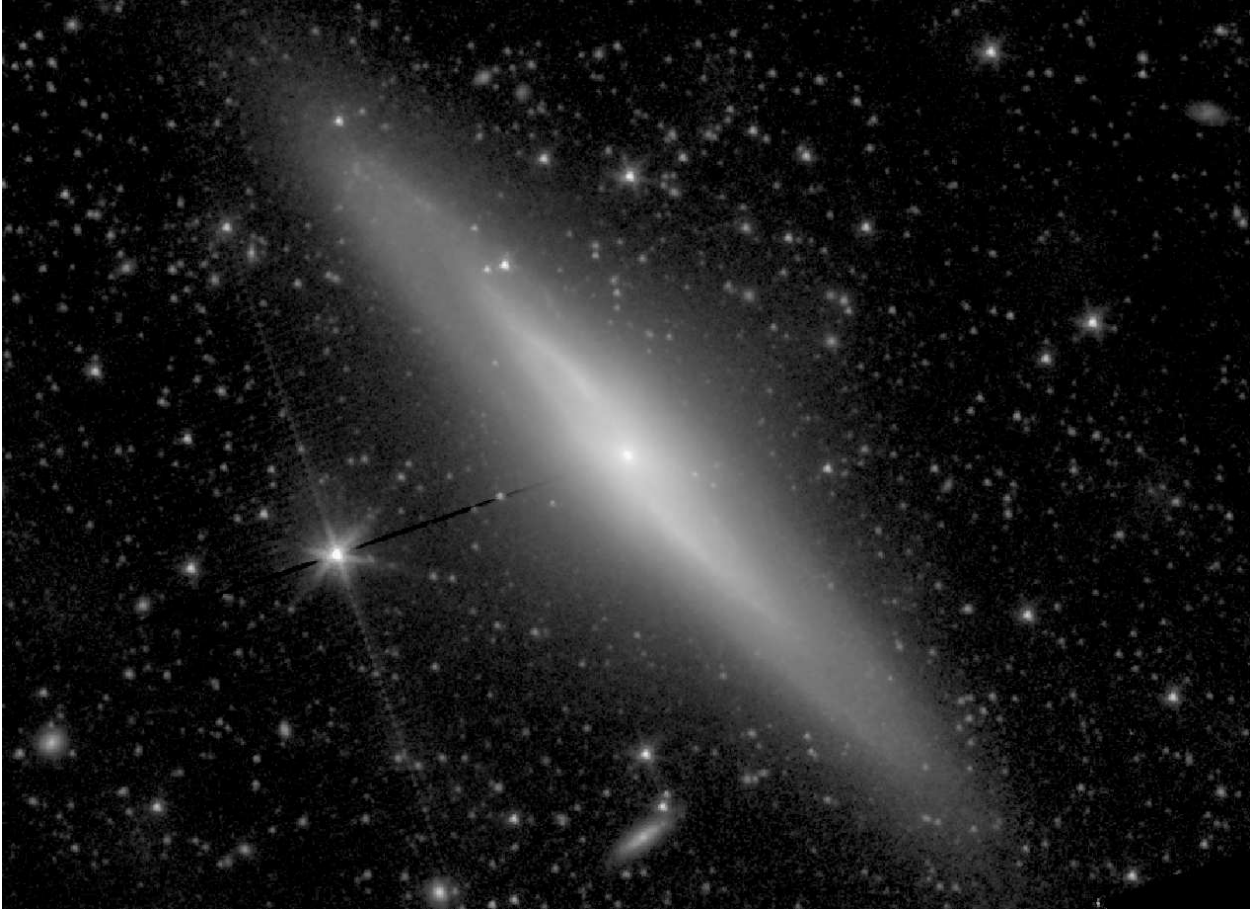


Fig. 1.47.— **NGC 2683** - S⁴G mid-IR classification: (RL)SB_x(rs)0/a sp ; Filter: IRAC 3.6 μ m; North: up, East: left; Field dimensions: 11.3 \times 8.2 arcmin; Surface brightness range displayed: 13.5–28.0 mag arcsec⁻²



Fig. 1.48.— **NGC 2742** - S⁴G mid-IR classification: SA(s)c ; Filter: IRAC 3.6 μ m; North: up, East: left; Field dimensions: 4.5 \times 3.3 arcmin; Surface brightness range displayed: 15.0–28.0 mag arcsec⁻²



Fig. 1.49.— **NGC 2798** (right) and **NGC 2799** (left) - S⁴G mid-IR classifications: SAB(s)a pec, SB(s)dm? pec sp, respectively; Filter: IRAC 3.6 μ m; North: up, East: left; Field dimensions: 4.5 \times 3.3 arcmin; Surface brightness range displayed: 12.0–28.0 mag arcsec⁻²



Fig. 1.50.— **NGC 2805** - S⁴G mid-IR classification: (R)SAB(rs)c pec ; Filter: IRAC 3.6 μ m; North: up, East: left; Field dimensions: 7.9 \times 5.7 arcmin; Surface brightness range displayed: 16.5–28.0 mag arcsec⁻²

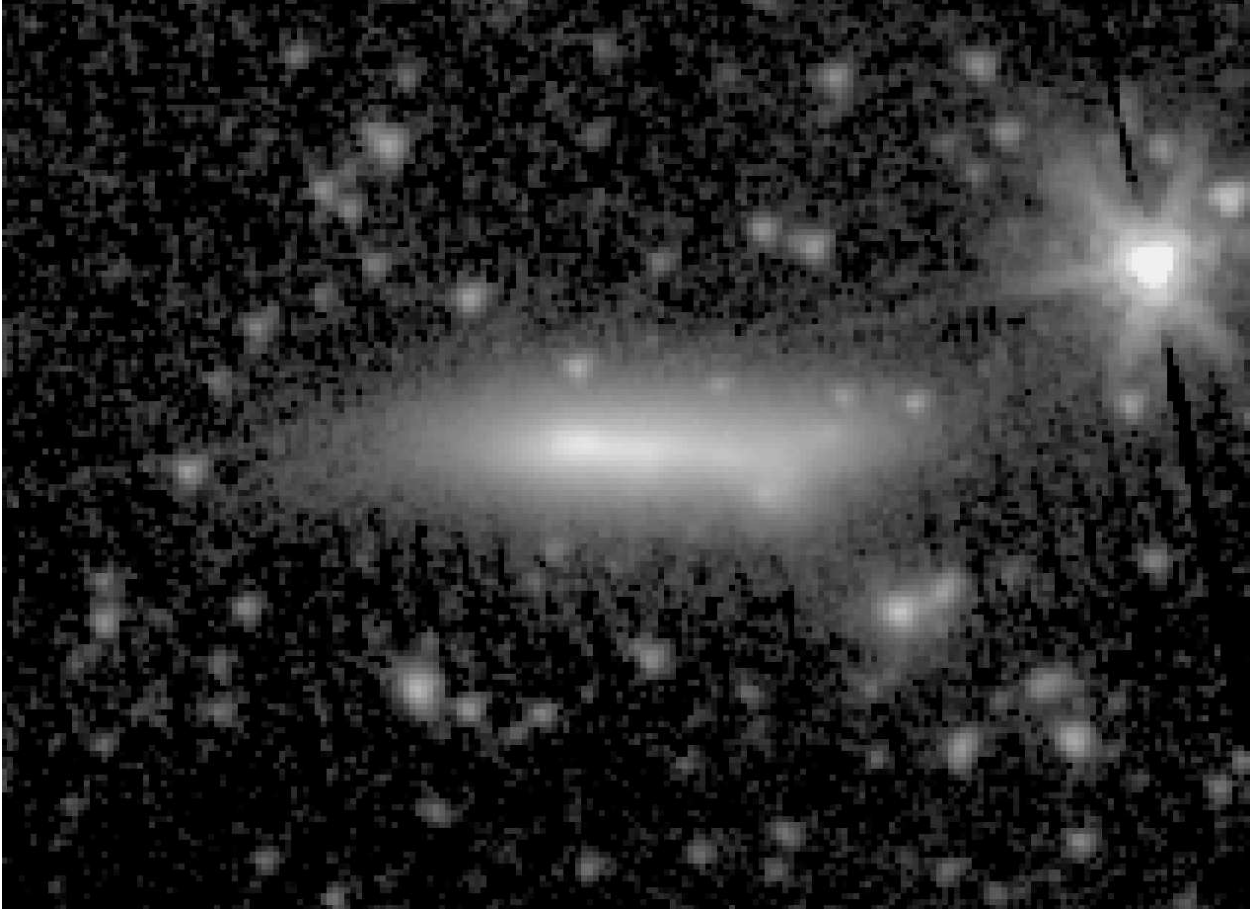


Fig. 1.51.— **NGC 2814** - S⁴G mid-IR classification: S pec sp ; Filter: IRAC 3.6 μ m; North: left, East: down; Field dimensions: 2.6 \times 1.9 arcmin; Surface brightness range displayed: 15.5–28.0 mag arcsec⁻²



Fig. 1.52.— **NGC 2820** - S^4G mid-IR classification: Sc sp ; Filter: IRAC $3.6\mu\text{m}$; North: up, East: left; Field dimensions: 3.9×2.9 arcmin; Surface brightness range displayed: $15.0\text{--}28.0$ mag arcsec $^{-2}$

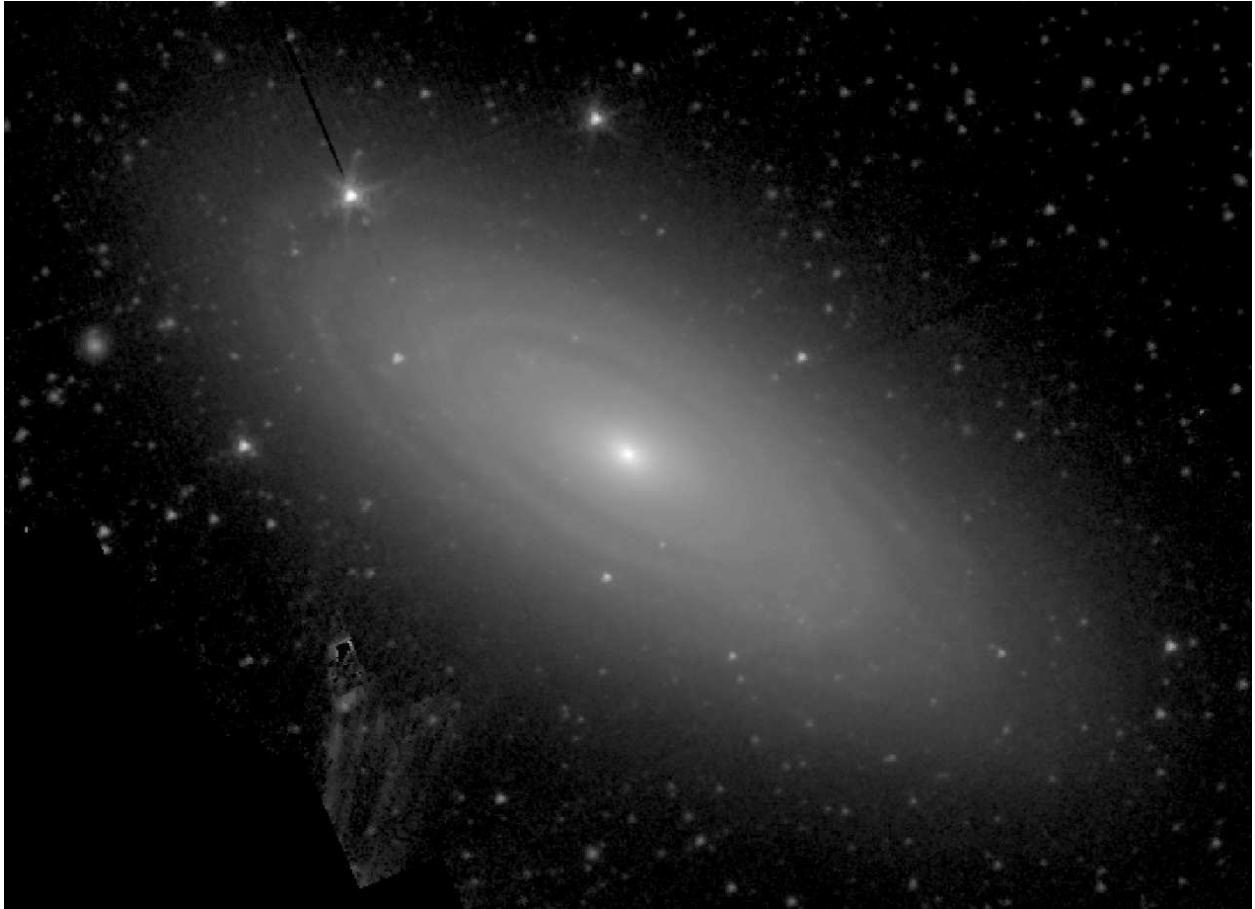


Fig. 1.53.— **NGC 2841** - S⁴G mid-IR classification: S**A**B(r)a ; Filter: IRAC 3.6 μm; North: left, East: down; Field dimensions: 9.6 × 7.0 arcmin; Surface brightness range displayed: 12.0–28.0 mag arcsec⁻²

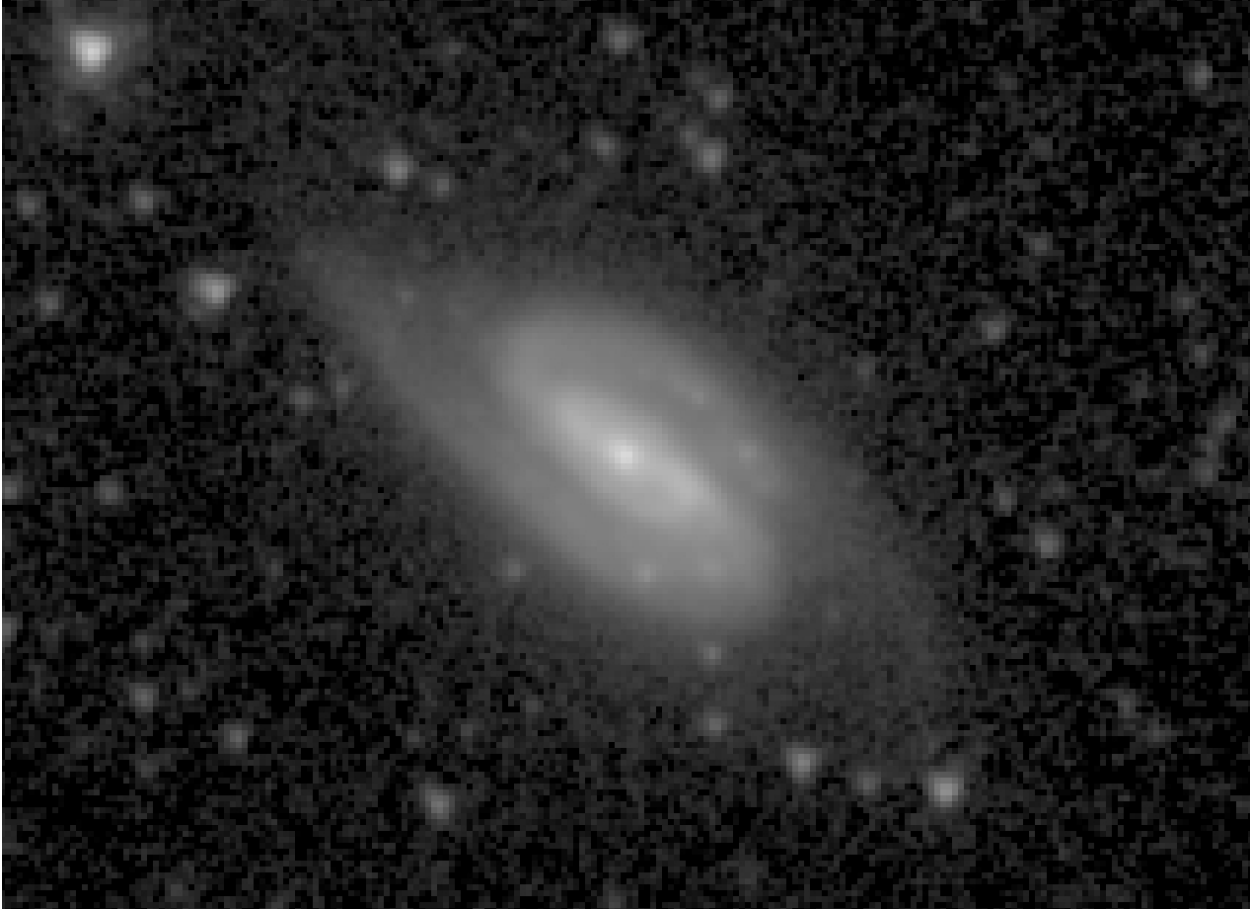


Fig. 1.54.— **NGC 2854** - S⁴G mid-IR classification: SAB(r)a ; Filter: IRAC 3.6μm; North: up, East: left; Field dimensions: 2.6× 1.9 arcmin; Surface brightness range displayed: 14.0–28.0 mag arcsec⁻²

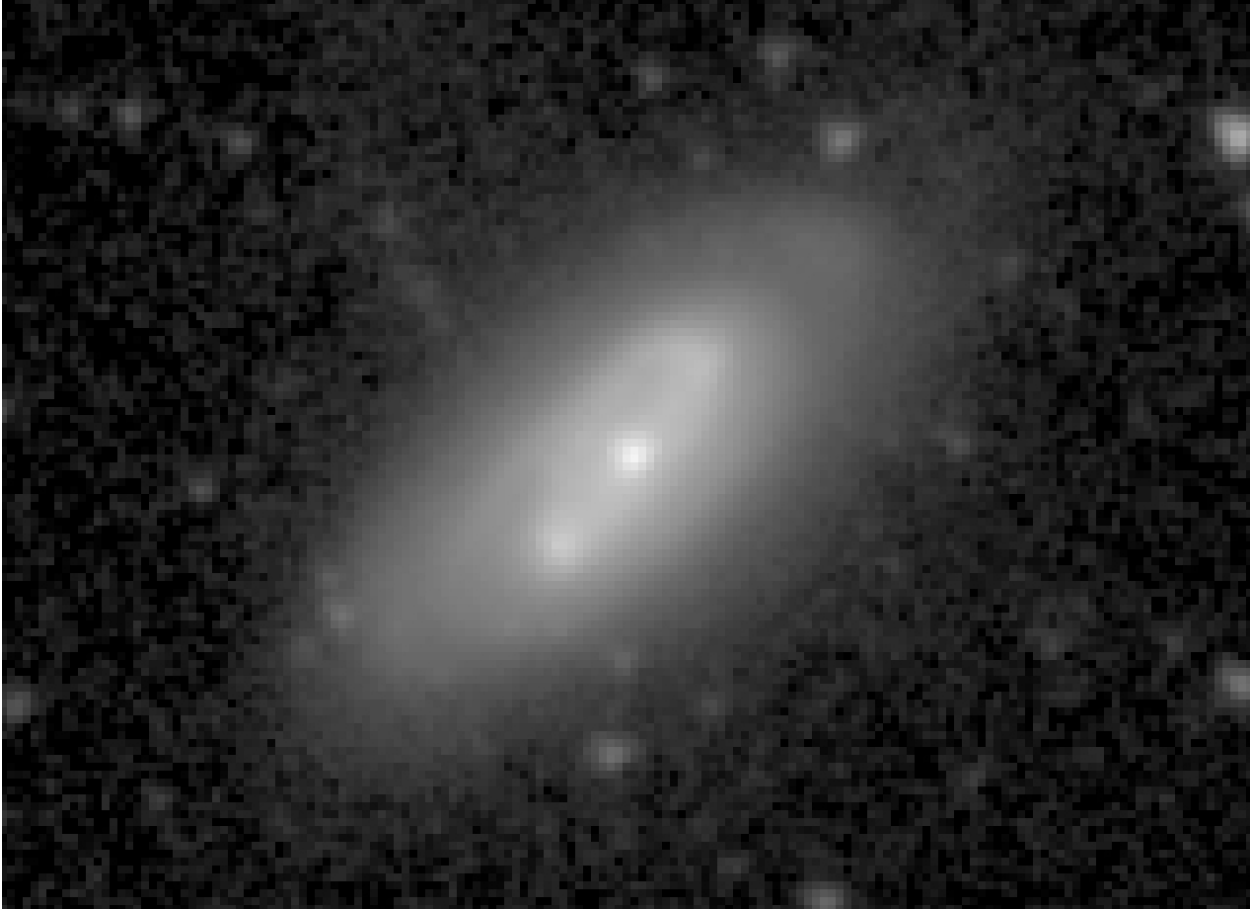


Fig. 1.55.— **NGC 2856** - S⁴G mid-IR classification: SAB(r)a: ; Filter: IRAC 3.6 μ m; North: up, East: left; Field dimensions: 2.0 \times 1.4 arcmin; Surface brightness range displayed: 13.0–28.0 mag arcsec⁻²

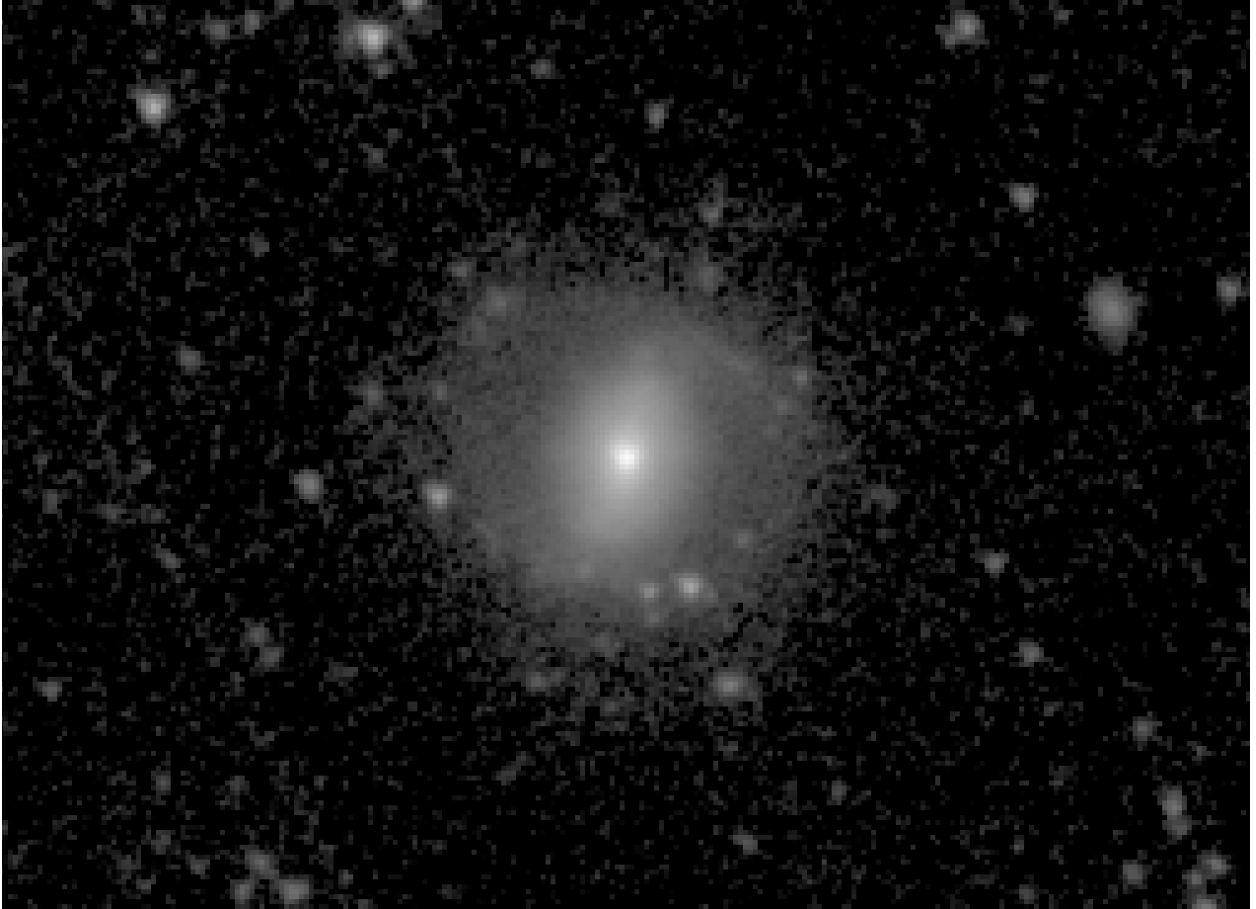


Fig. 1.56.— **NGC 2893** - S⁴G mid-IR classification: (RL)SAB(1)0⁺ ; Filter: IRAC 3.6 μ m;
North: up, East: left; Field dimensions: 3.2 \times 2.3 arcmin; Surface brightness range displayed:
13.0–28.0 mag arcsec⁻²



Fig. 1.57.— **NGC 2903** - S⁴G mid-IR classification: (R')SB(rs,nr)b ; Filter: IRAC 3.6 μ m; North: left, East: down; Field dimensions: 12.6 \times 9.2 arcmin; Surface brightness range displayed: 12.8–28.0 mag arcsec⁻²

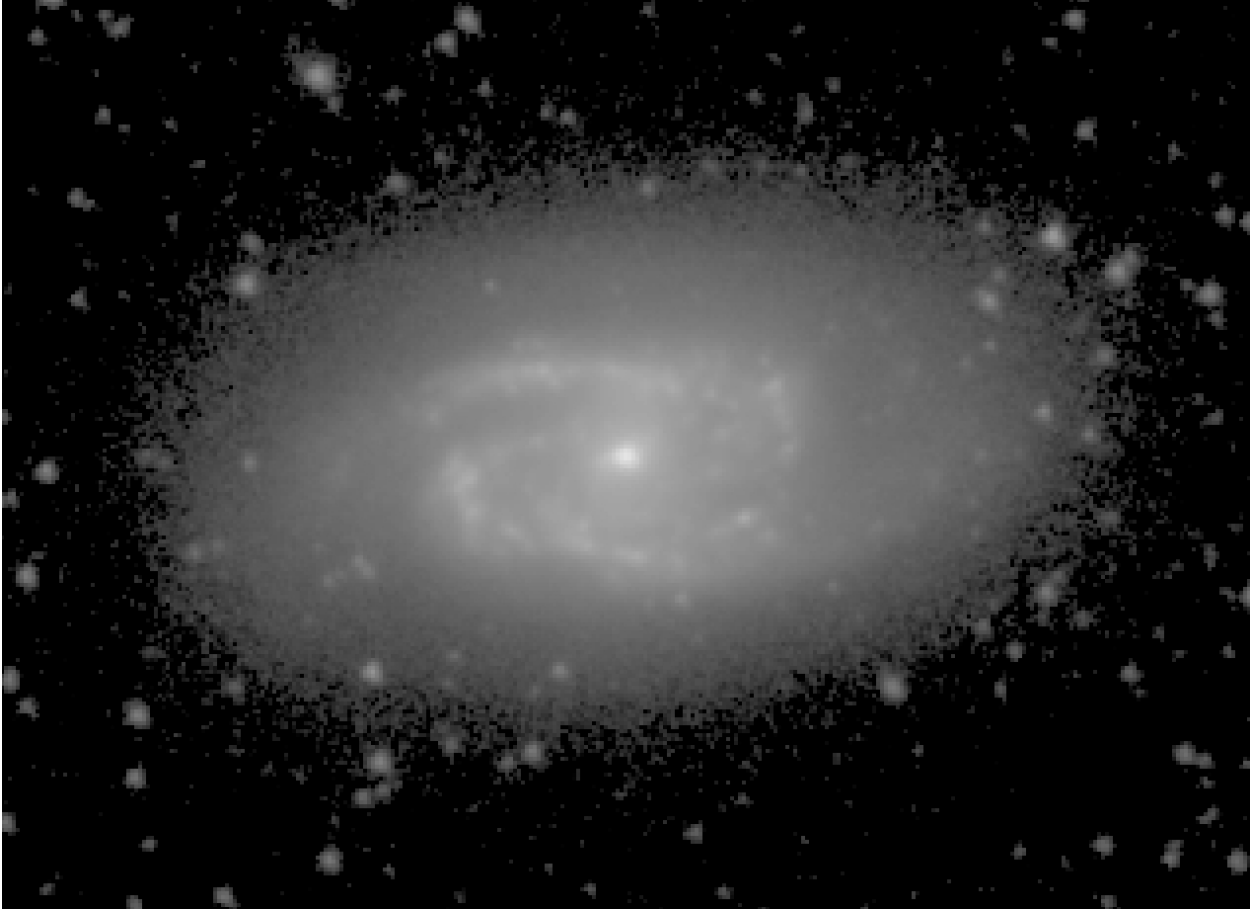


Fig. 1.58.— **NGC 2964** - S⁴G mid-IR classification: SAB(rs)b ; Filter: IRAC 3.6μm;
North: up, East: left; Field dimensions: 4.0× 2.9 arcmin; Surface brightness range displayed:
13.0–28.0 mag arcsec⁻²



Fig. 1.59.— **NGC 2968** - S⁴G mid-IR classification: SB(rs)0⁺ ; Filter: IRAC 3.6 μ m; North: up, East: left; Field dimensions: 5.3 \times 3.8 arcmin; Surface brightness range displayed: 13.0–28.0 mag arcsec⁻²

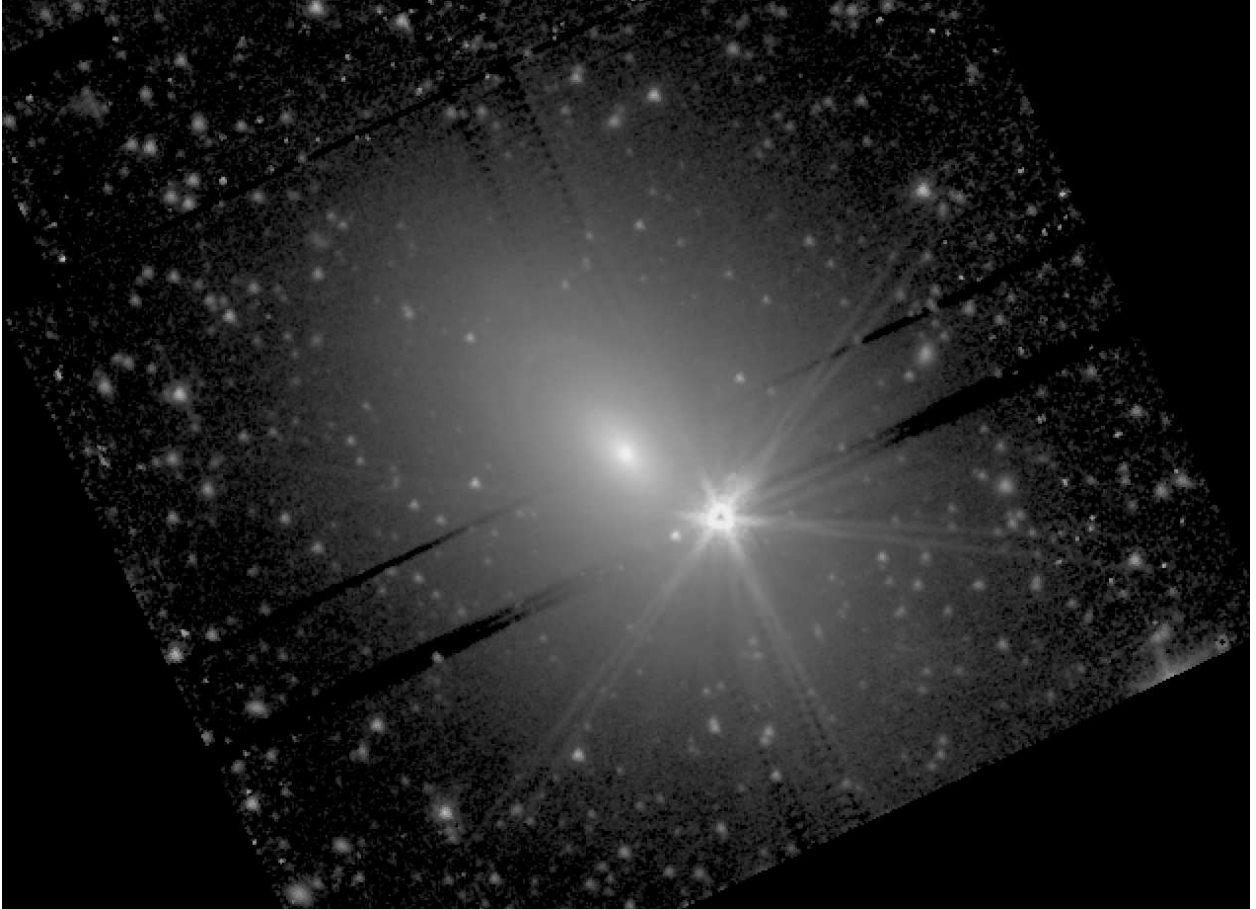


Fig. 1.60.— **NGC 2974** - S⁴G mid-IR classification: SA(r)0/a ; Filter: IRAC 3.6 μ m;
North: up, East: left; Field dimensions: 7.9 \times 5.8 arcmin; Surface brightness range displayed:
13.0–28.0 mag arcsec⁻²

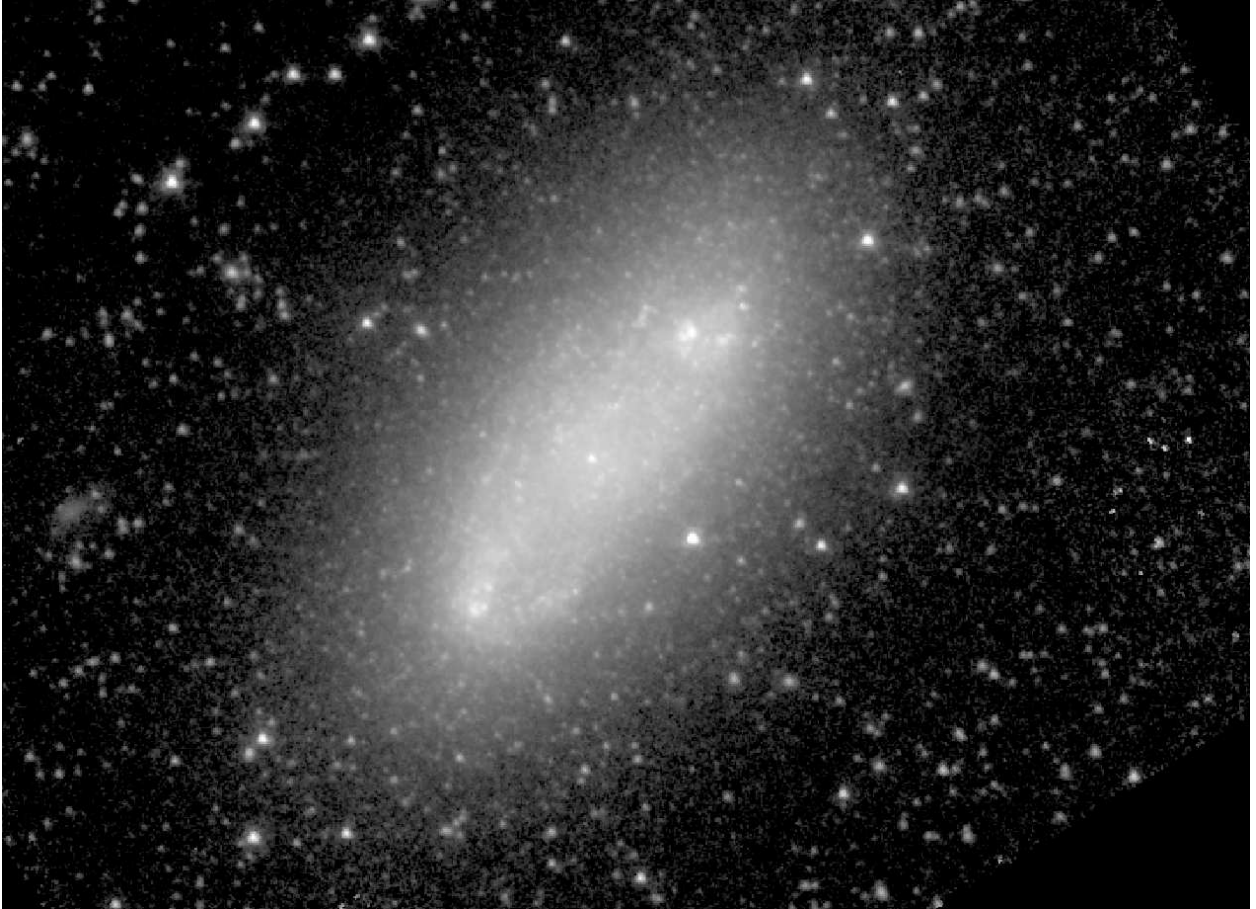


Fig. 1.61.— **NGC 2976** - S⁴G mid-IR classification: SAB(s:)d ; Filter: IRAC 3.6 μ m;
North: up, East: left; Field dimensions: 9.0 \times 6.6 arcmin; Surface brightness range displayed:
15.0–28.0 mag arcsec⁻²

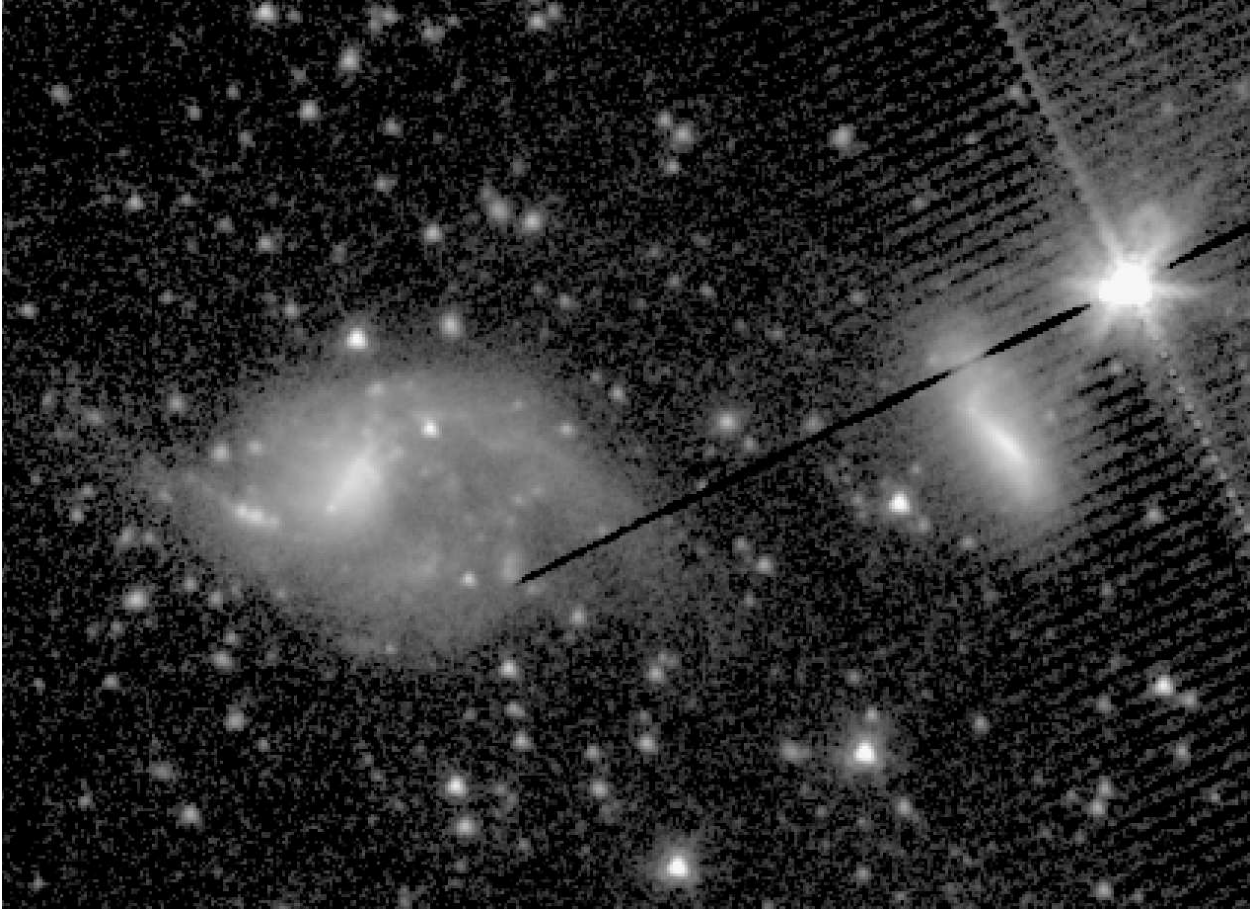


Fig. 1.62.— **NGC 3018** (right) and **NGC 3023** (left) - S⁴G mid-IR classifications: SB(s)d, SB(s)dm, respectively; Filter: IRAC 3.6 μ m; North: up, East: left; Field dimensions: 5.3 \times 3.8 arcmin; Surface brightness range displayed: 16.0–28.0 mag arcsec⁻²

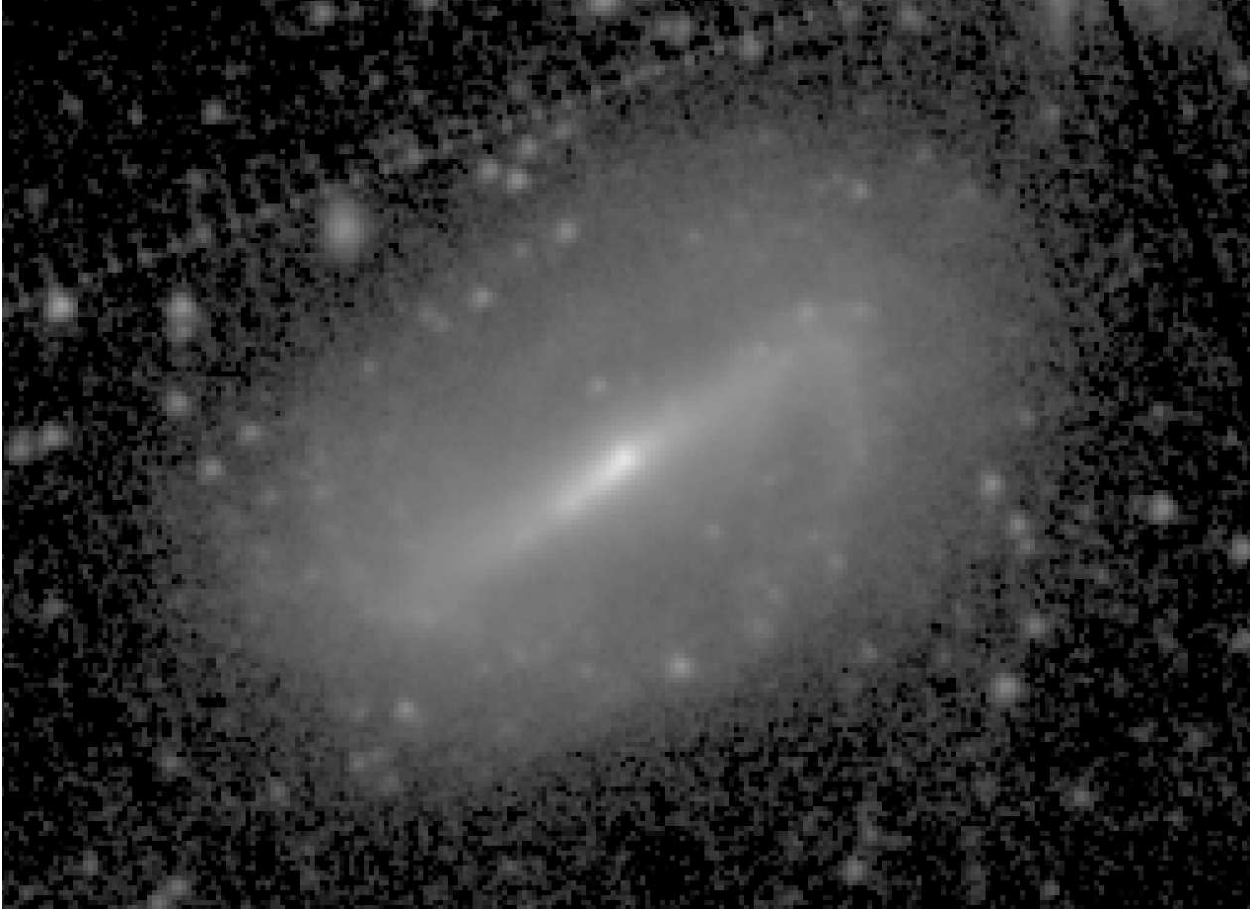


Fig. 1.63.— **NGC 3049** - S⁴G mid-IR classification: SB(s)ab: ; Filter: IRAC 3.6 μ m; North: left, East: down; Field dimensions: 3.2 \times 2.3 arcmin; Surface brightness range displayed: 14.5–28.0 mag arcsec⁻²



Fig. 1.64.— **NGC 3073** - S⁴G mid-IR classification: S0⁻ ; Filter: IRAC 3.6 μ m; North: up, East: left; Field dimensions: 4.0 \times 2.9 arcmin; Surface brightness range displayed: 15.0–28.0 mag arcsec⁻²

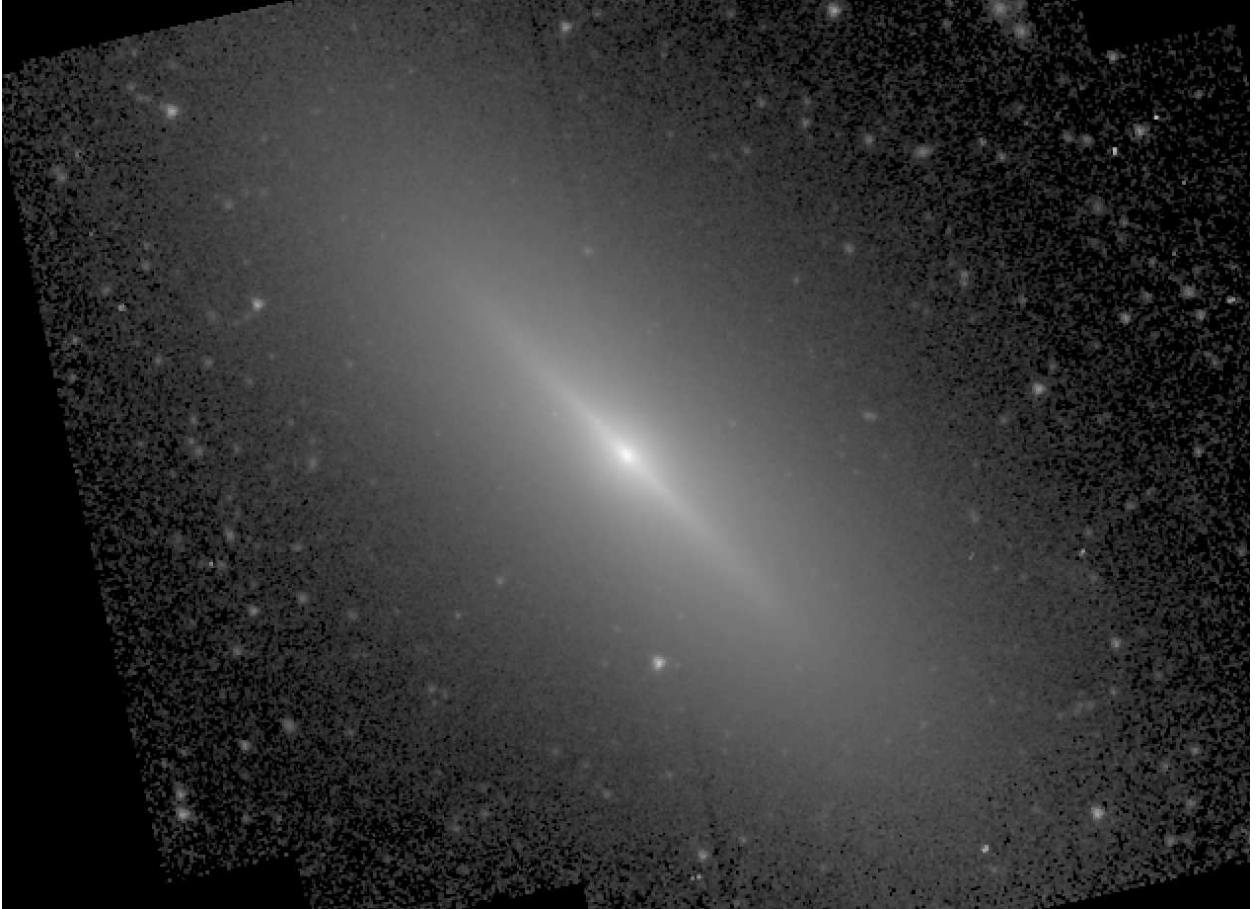


Fig. 1.65.— **NGC 3115** - S⁴G mid-IR classification: S0⁻/E7 sp ; Filter: IRAC 3.6 μ m;
North: up, East: left; Field dimensions: 7.9 \times 5.8 arcmin; Surface brightness range displayed:
11.0–28.0 mag arcsec⁻²



Fig. 1.66.— **NGC 3147** - S^4G mid-IR classification: $S_{\underline{A}B}(r_{\underline{S}})b$; Filter: IRAC $3.6\mu m$; North: left, East: down; Field dimensions: 5.6×4.1 arcmin; Surface brightness range displayed: $12.0-28.0$ mag arcsec $^{-2}$



Fig. 1.67.— **NGC 3184** - S⁴G mid-IR classification: SA(rs)bc ; Filter: IRAC 3.6μm; North: up, East: left; Field dimensions: 11.3× 8.2 arcmin; Surface brightness range displayed: 14.5–28.0 mag arcsec⁻²

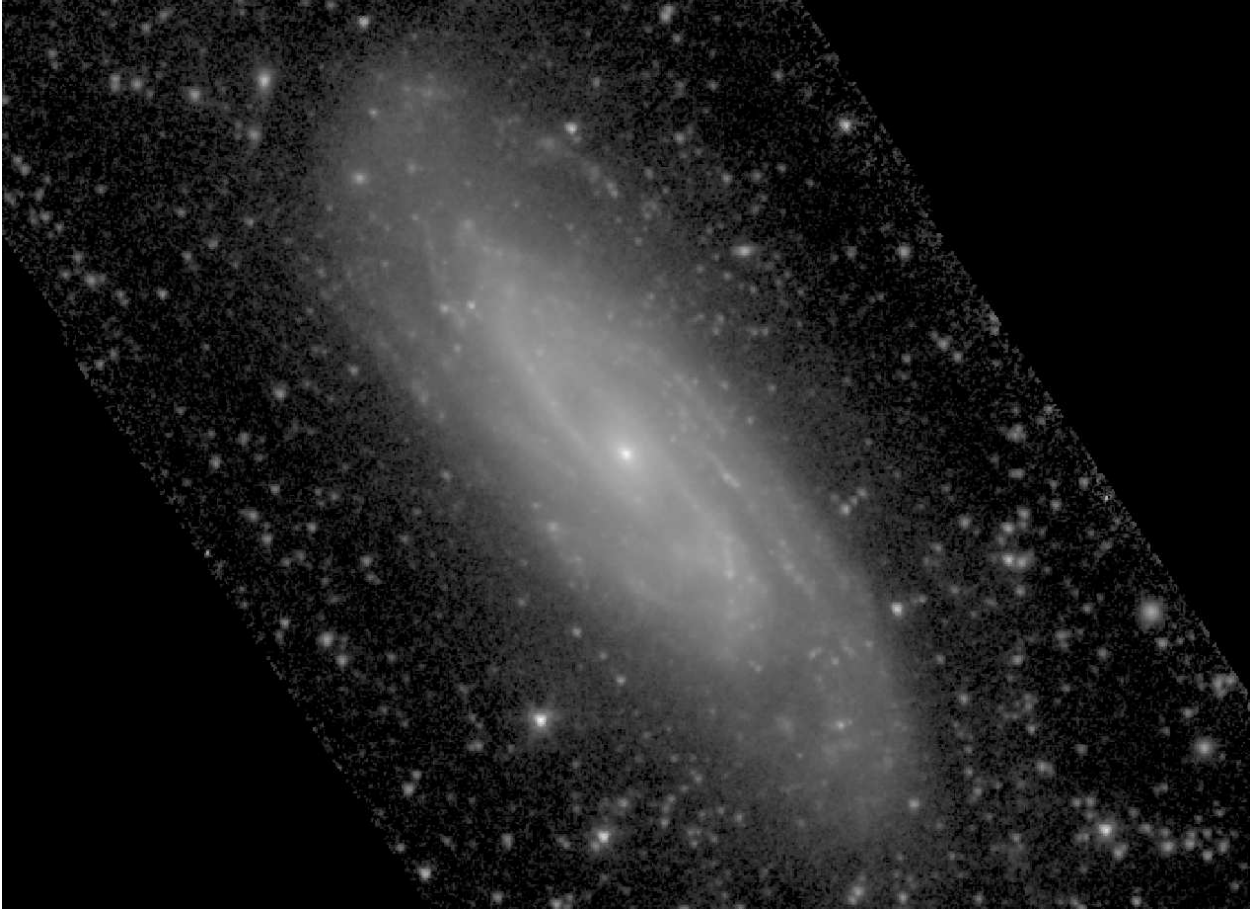


Fig. 1.68.— **NGC 3198** - S⁴G mid-IR classification: SAB(rs)bc ; Filter: IRAC 3.6μm;
North: up, East: left; Field dimensions: 8.8× 6.4 arcmin; Surface brightness range displayed:
14.0–28.0 mag arcsec⁻²

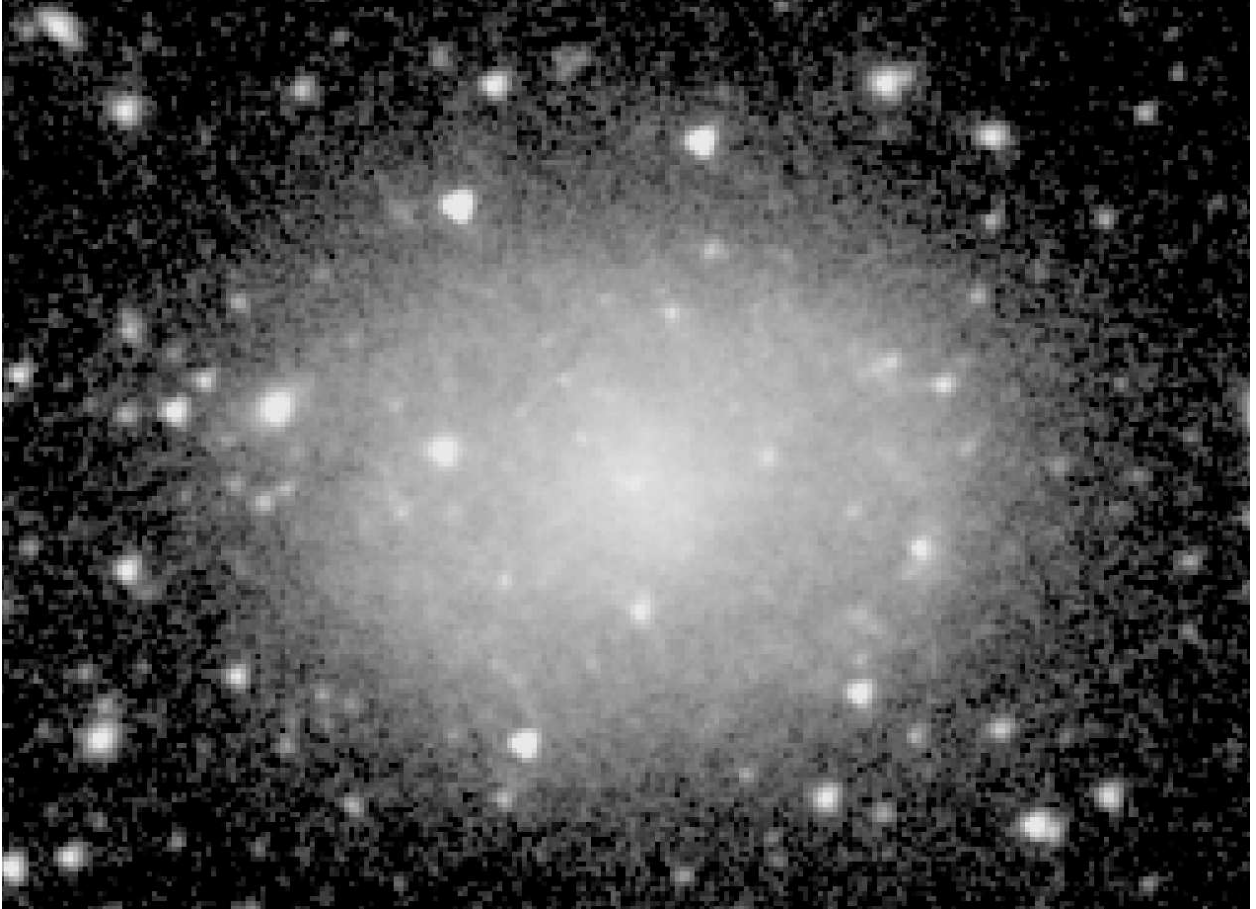


Fig. 1.69.— **NGC 3299** - S⁴G mid-IR classification: SABd; ; Filter: IRAC 3.6 μm; North: left, East: down; Field dimensions: 3.2 × 2.3 arcmin; Surface brightness range displayed: 18.5–28.0 mag arcsec⁻²

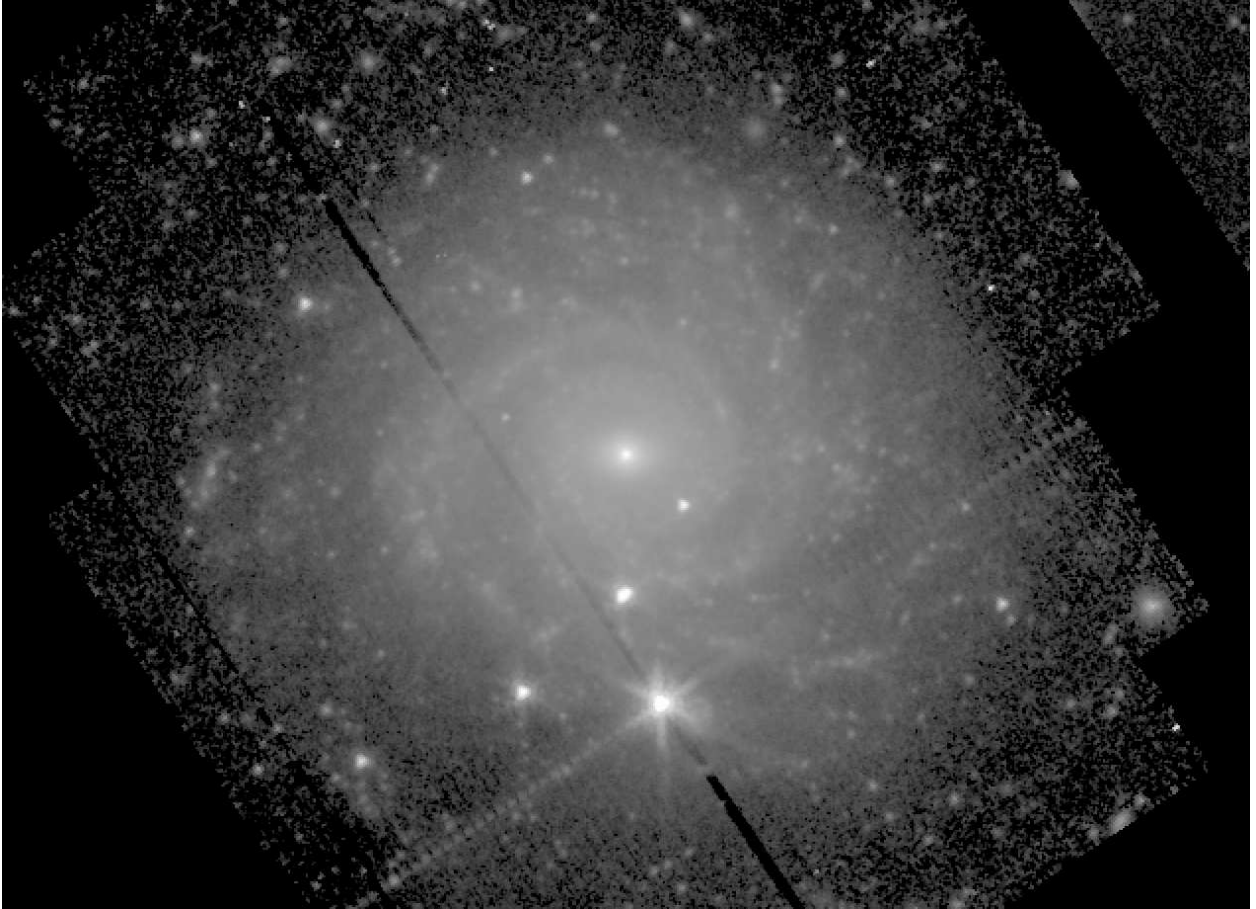


Fig. 1.70.— **NGC 3344** - S⁴G mid-IR classification: SAB(r)bc ; Filter: IRAC 3.6 μ m; North: left, East: down; Field dimensions: 7.9 \times 5.8 arcmin; Surface brightness range displayed: 13.0–28.0 mag arcsec⁻²



Fig. 1.71.— **NGC 3351** - S⁴G mid-IR classification: (R')SB(r,nr)a ; Filter: IRAC 3.6 μ m;
North: left, East: down; Field dimensions: 10.5 \times 7.6 arcmin; Surface brightness range
displayed: 13.5–28.0 mag arcsec⁻²

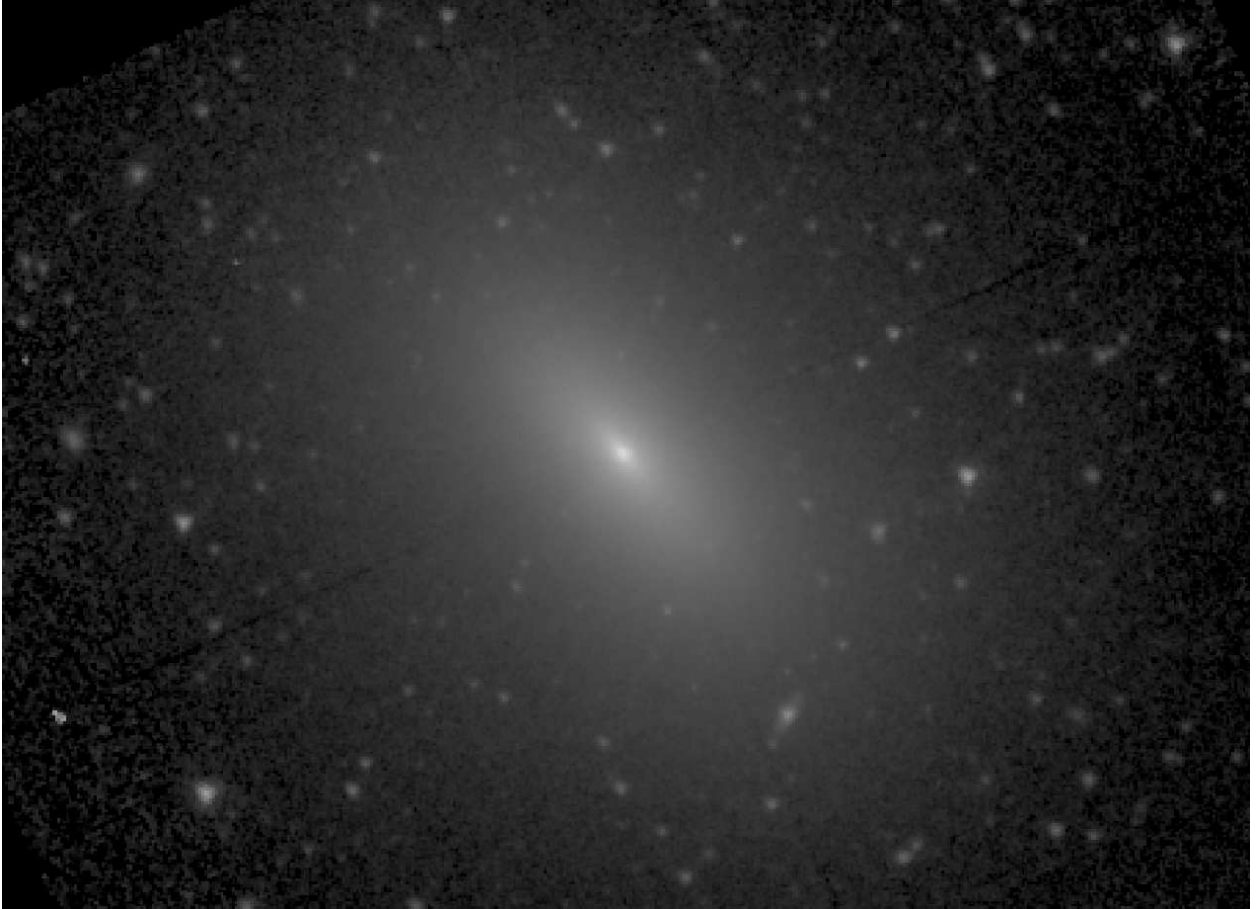


Fig. 1.72.— **NGC 3377** - S⁴G mid-IR classification: E(d)5 ; Filter: IRAC 3.6 μ m; North: up, East: left; Field dimensions: 5.6 \times 4.1 arcmin; Surface brightness range displayed: 12.0–28.0 mag arcsec⁻²

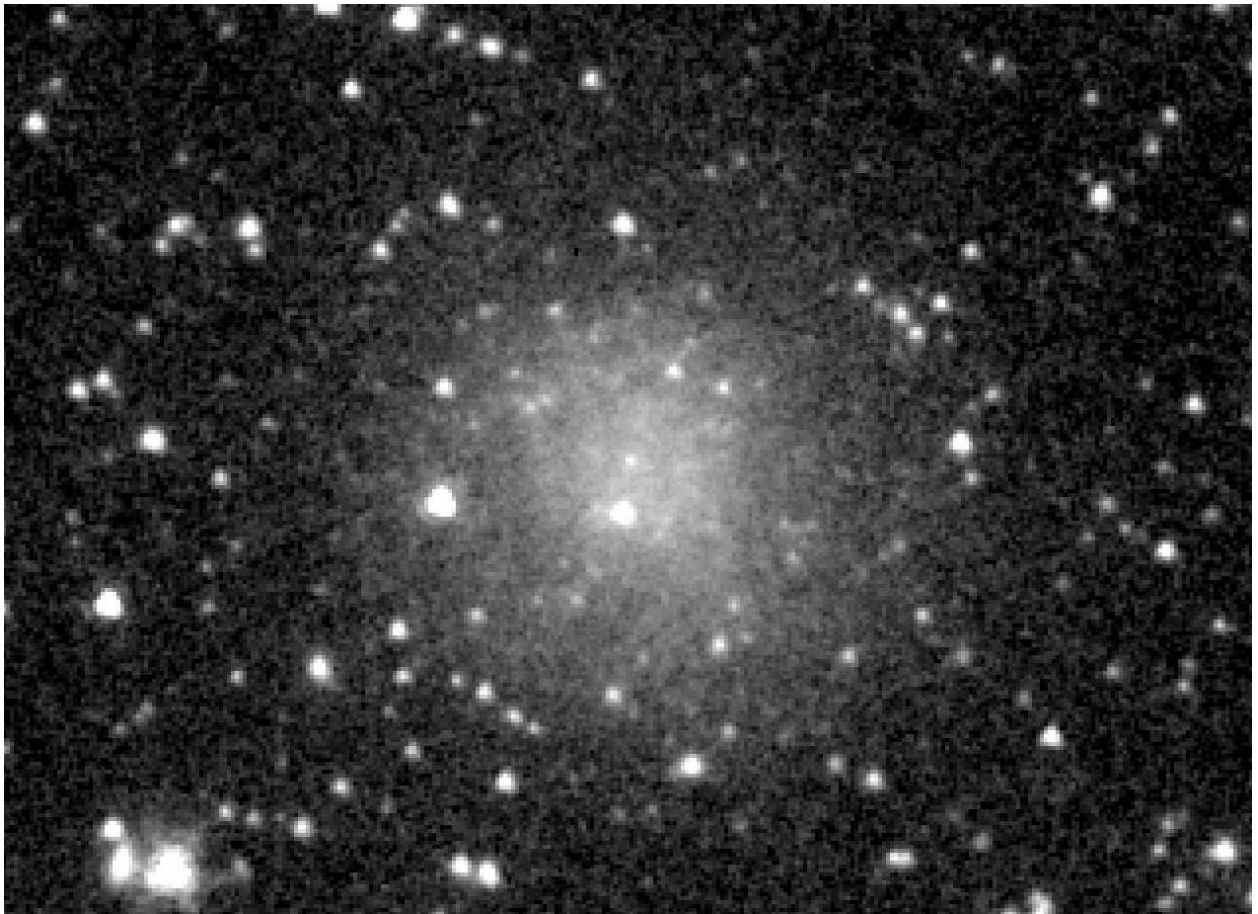


Fig. 1.73.— **NGC 3377A** - S⁴G mid-IR classification: Im ; Filter: IRAC 3.6 μ m; North: up, East: left; Field dimensions: 4.0 \times 2.9 arcmin; Surface brightness range displayed: 18.5–28.0 mag arcsec⁻²



Fig. 1.74.— **NGC 3437** - S⁴G mid-IR classification: SA(rs)c ; Filter: IRAC 3.6μm; North: up, East: left; Field dimensions: 3.5× 2.6 arcmin; Surface brightness range displayed: 13.5–28.0 mag arcsec⁻²

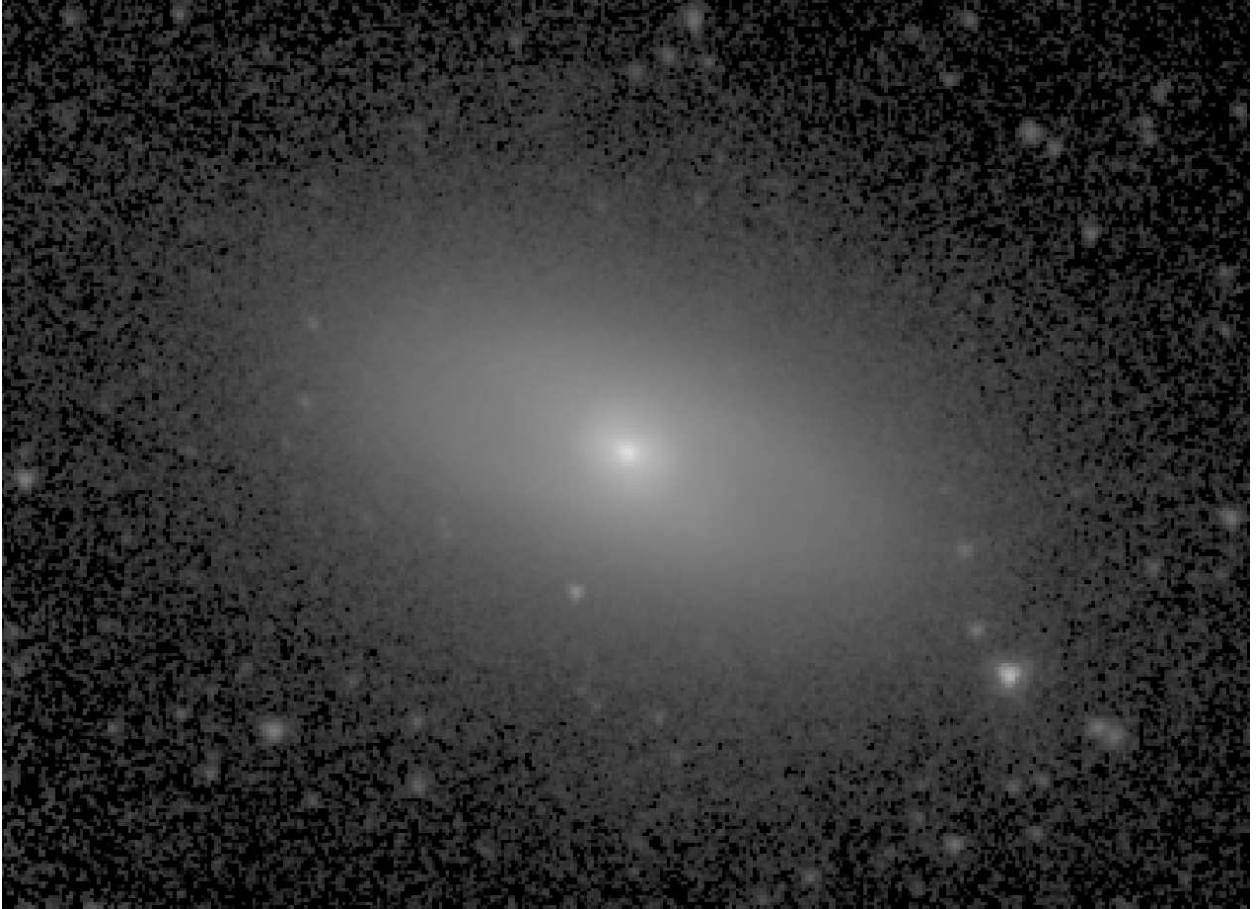


Fig. 1.75.— **NGC 3489** - S⁴G mid-IR classification: (R)SB(r:)0^o ; Filter: IRAC 3.6μm; North: up, East: left; Field dimensions: 4.5× 3.3 arcmin; Surface brightness range displayed: 11.5–28.0 mag arcsec⁻²



Fig. 1.76.— **NGC 3495** - S⁴G mid-IR classification: (R')SB(rs)c: ; Filter: IRAC 3.6 μ m; North: left, East: down; Field dimensions: 5.3 \times 3.8 arcmin; Surface brightness range displayed: 16.0–28.0 mag arcsec⁻²

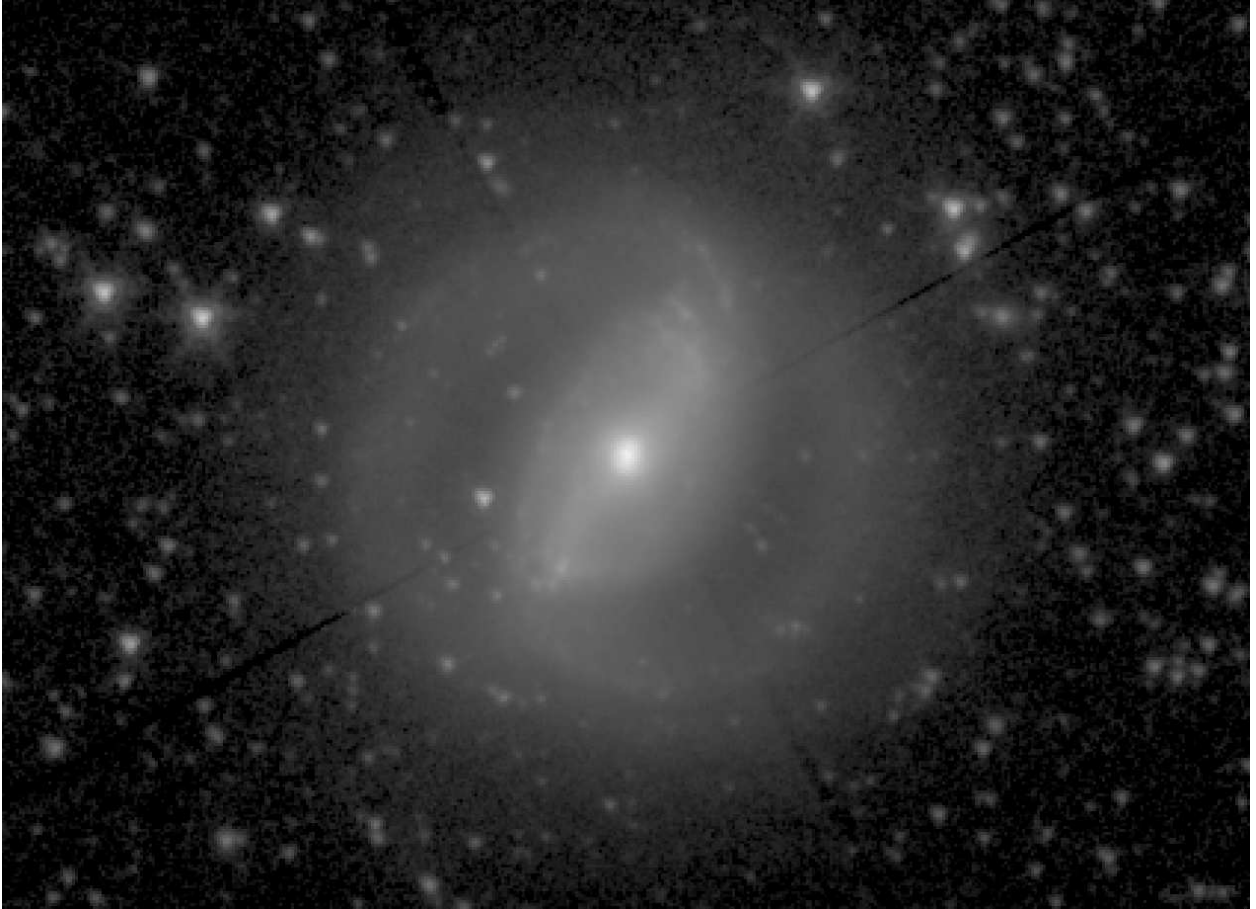


Fig. 1.77.— **NGC 3504** - S⁴G mid-IR classification: (R'₁)SAB(rs,nl)a ; Filter: IRAC 3.6 μm; North: up, East: left; Field dimensions: 5.3 × 3.8 arcmin; Surface brightness range displayed: 12.0–28.0 mag arcsec⁻²

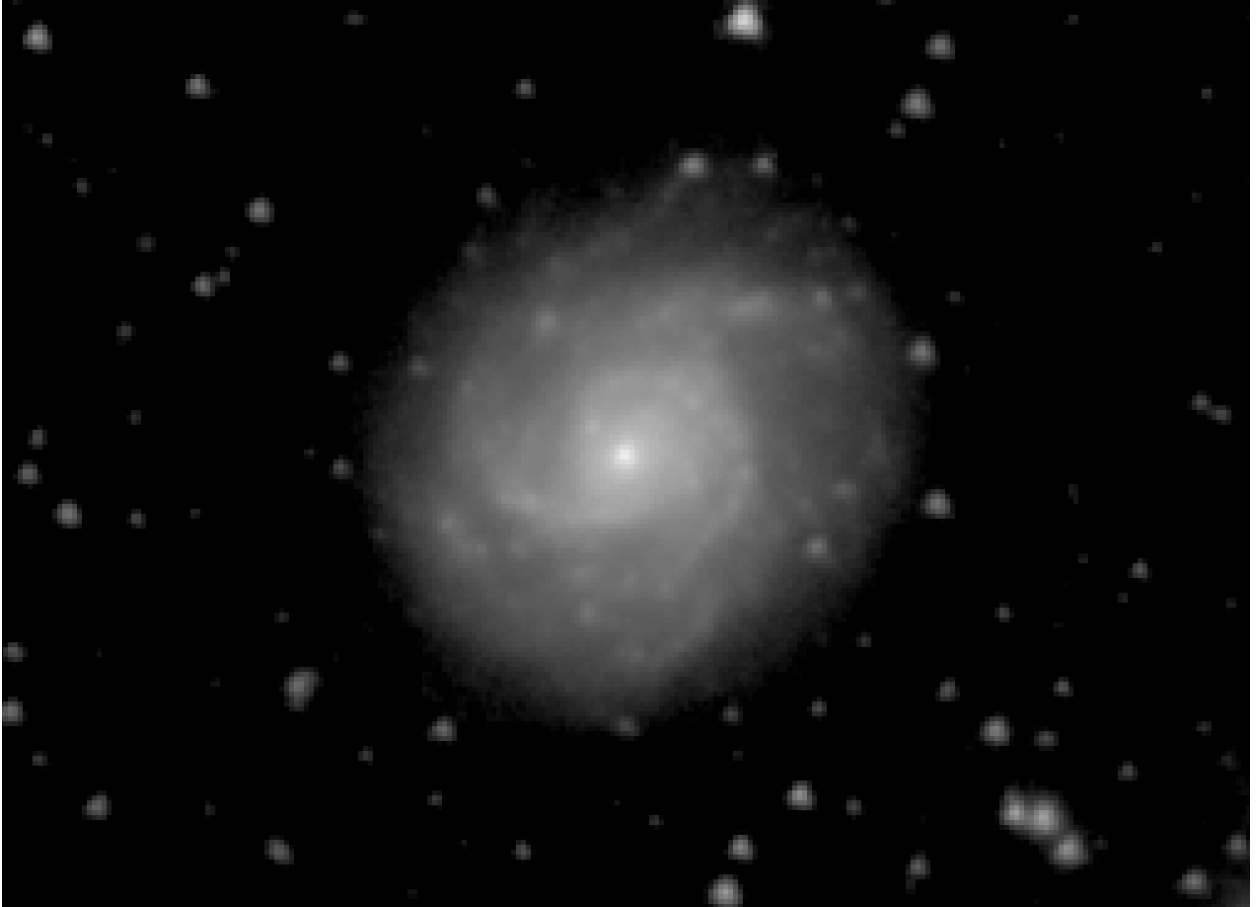


Fig. 1.78.— **NGC 3512** - S⁴G mid-IR classification: SA(s)bc ; Filter: IRAC 3.6μm;
North: up, East: left; Field dimensions: 2.9× 2.1 arcmin; Surface brightness range displayed:
14.5–28.0 mag arcsec⁻²



Fig. 1.79.— **NGC 3608** - S⁴G mid-IR classification: E2 ; Filter: IRAC 3.6 μ m; North: up, East: left; Field dimensions: 7.0 \times 5.1 arcmin; Surface brightness range displayed: 13.0–26.0 mag arcsec⁻²

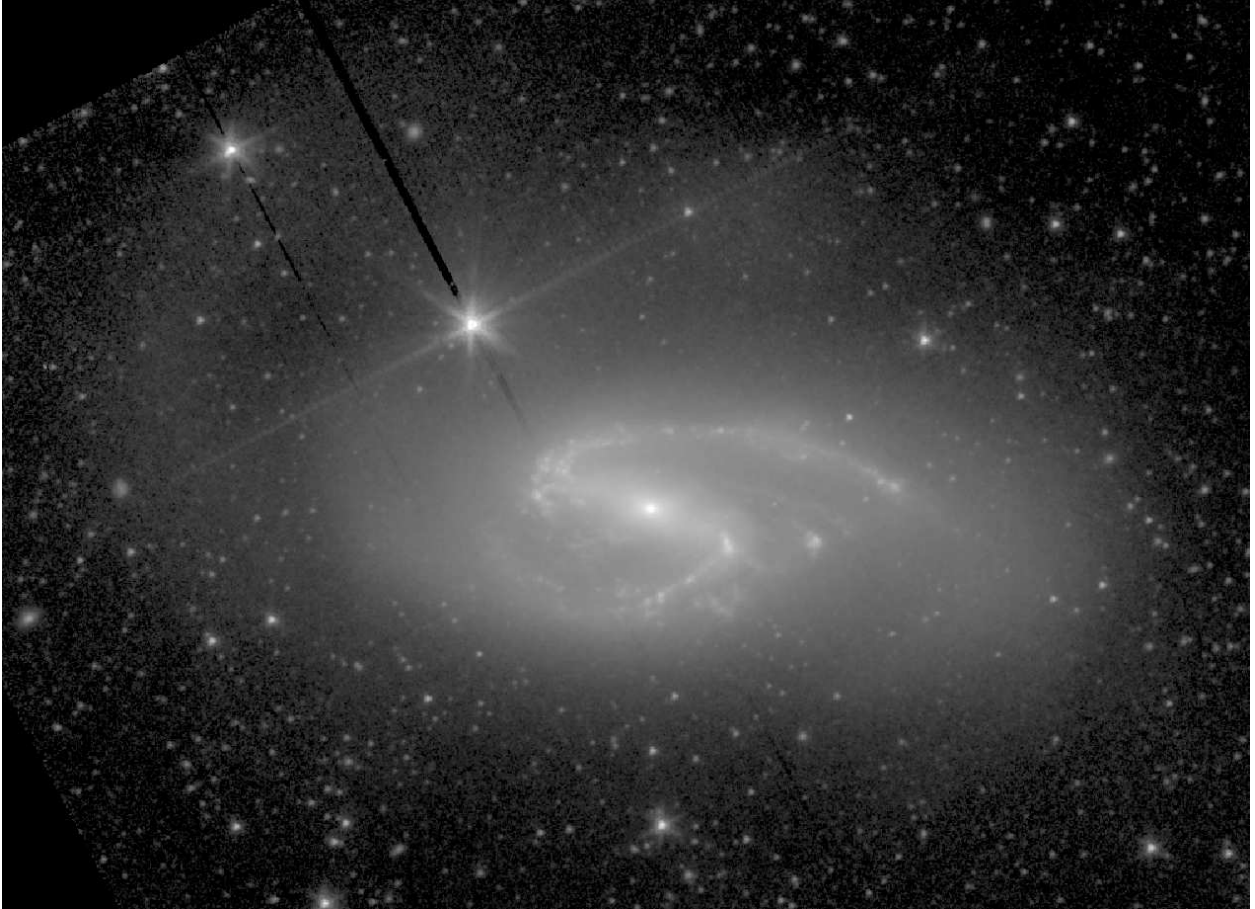


Fig. 1.80.— **NGC 3627** - S⁴G mid-IR classification: SB(s)b pec ; Filter: IRAC 3.6 μ m; North: left, East: down; Field dimensions: 12.6 \times 9.2 arcmin; Surface brightness range displayed: 12.0–28.0 mag arcsec⁻²

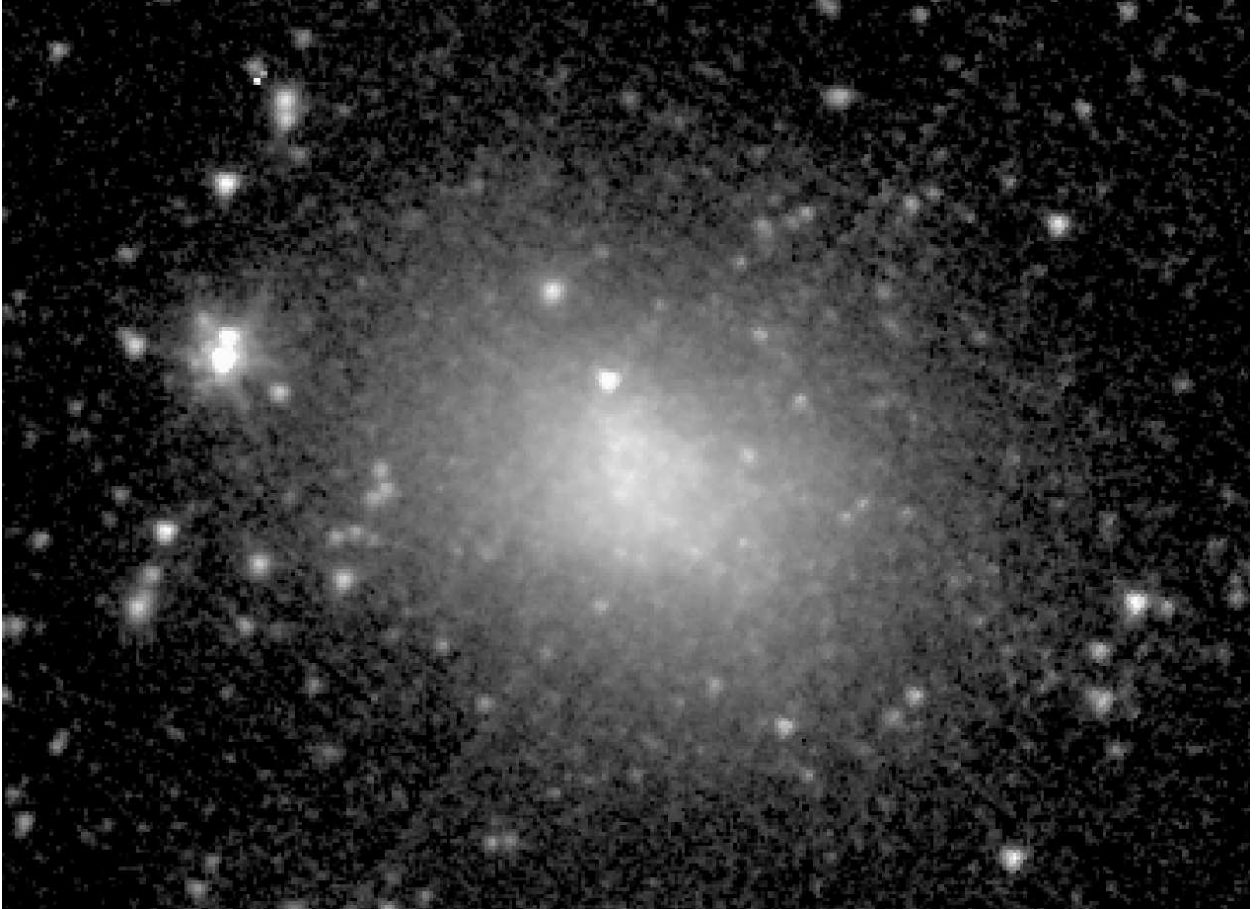


Fig. 1.81.— **NGC 3738** - S⁴G mid-IR classification: dE (Im) ; Filter: IRAC 3.6 μ m; North: left, East: down; Field dimensions: 4.5 \times 3.3 arcmin; Surface brightness range displayed: 16.5–26.0 mag arcsec⁻²



Fig. 1.82.— **NGC 3769** (center) and **MCG8-21-76** (lower right) - S⁴G mid-IR classifications: (R')SB(s)cd, IBm., respectively; Filter: IRAC 3.6 μ m; North: left, East: down; Field dimensions: 4.2 \times 3.1 arcmin; Surface brightness range displayed: 15.5–26.0 mag arcsec⁻²

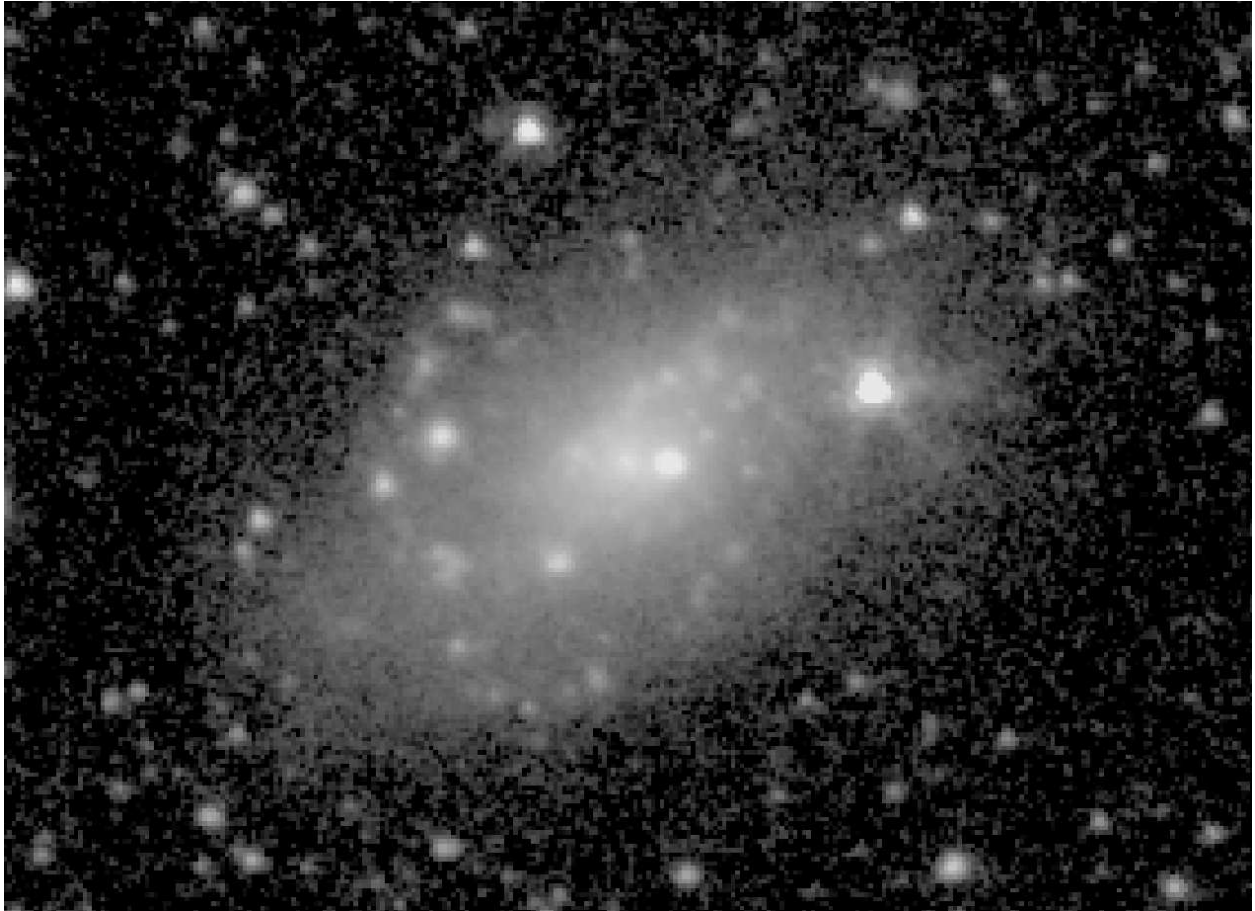


Fig. 1.83.— **NGC 3794** - S⁴G mid-IR classification: SAB(s)dm ; Filter: IRAC 3.6μm;
North: up, East: left; Field dimensions: 3.5× 2.6 arcmin; Surface brightness range displayed:
17.0–26.0 mag arcsec⁻²

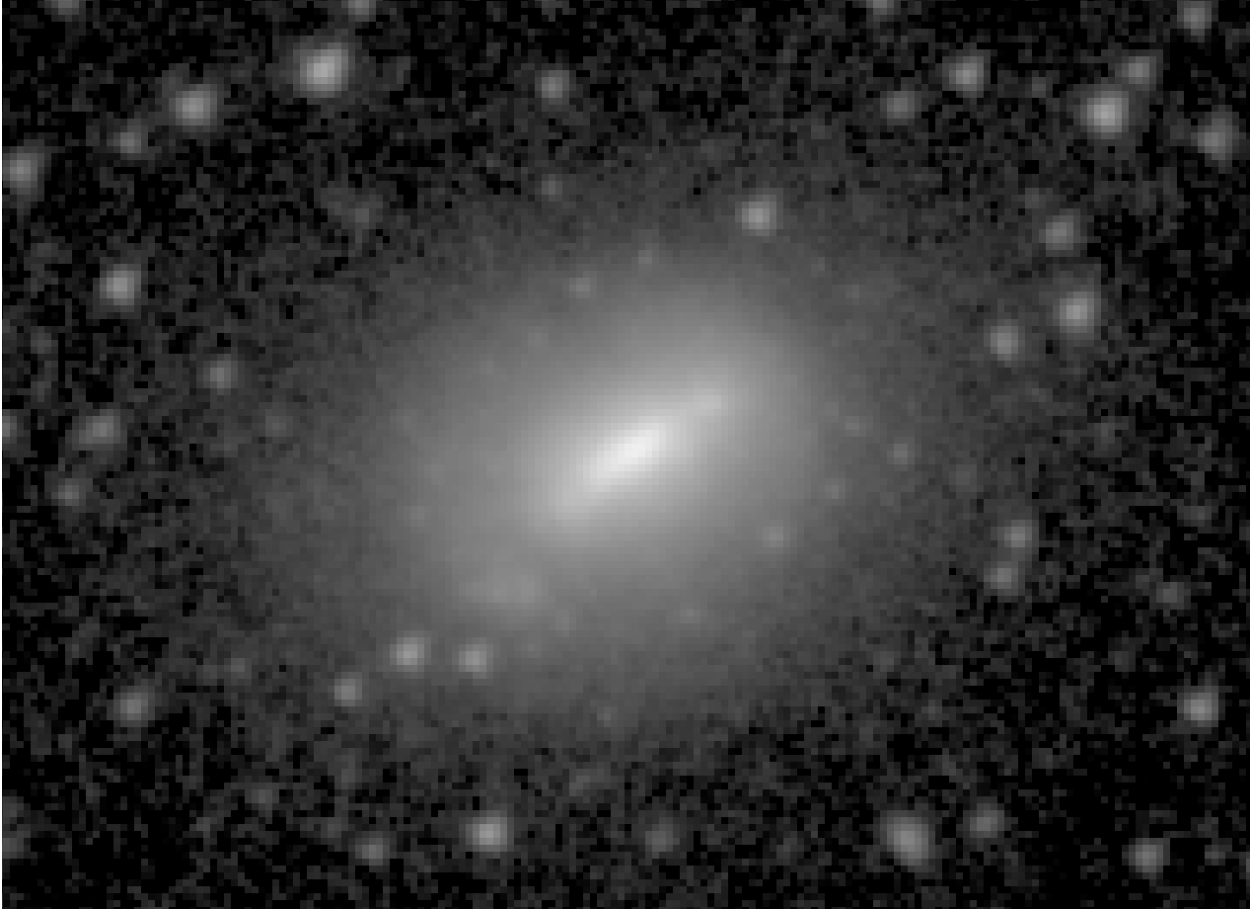


Fig. 1.84.— **NGC 3870** - S⁴G mid-IR classification: SB(rs)0^o? ; Filter: IRAC 3.6 μ m; North: left, East: down; Field dimensions: 4.5 \times 3.3 arcmin; Surface brightness range displayed: 15.0–28.0 mag arcsec⁻²

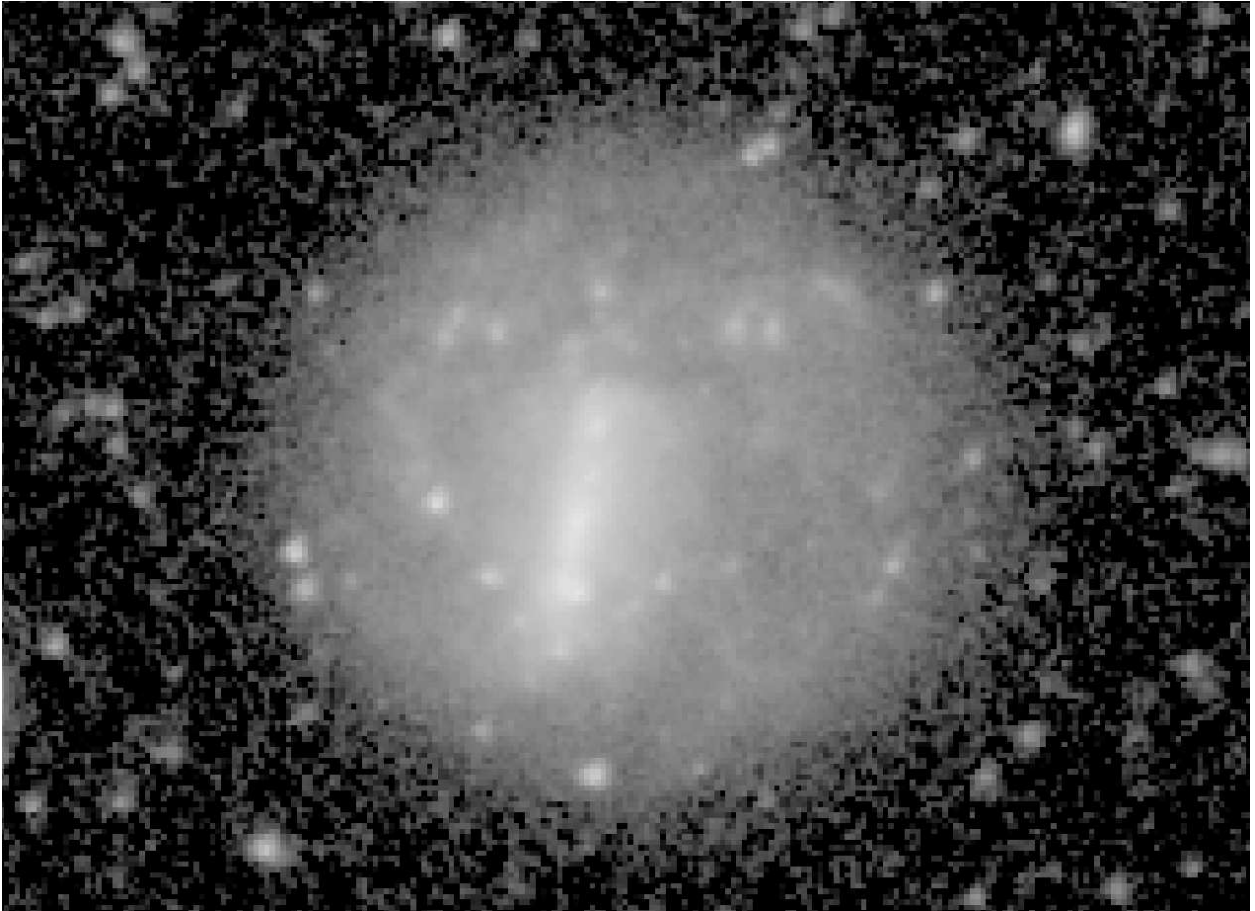


Fig. 1.85.— **NGC 3906** - S⁴G mid-IR classification: SB(l)dm ; Filter: IRAC 3.6 μ m; North: left, East: down; Field dimensions: 2.9 \times 2.1 arcmin; Surface brightness range displayed: 17.0–28.0 mag arcsec⁻²



Fig. 1.86.— **NGC 3938** - S⁴G mid-IR classification: SA(s)c ; Filter: IRAC 3.6μm; North: up, East: left; Field dimensions: 7.9× 5.8 arcmin; Surface brightness range displayed: 14.5–28.0 mag arcsec⁻²

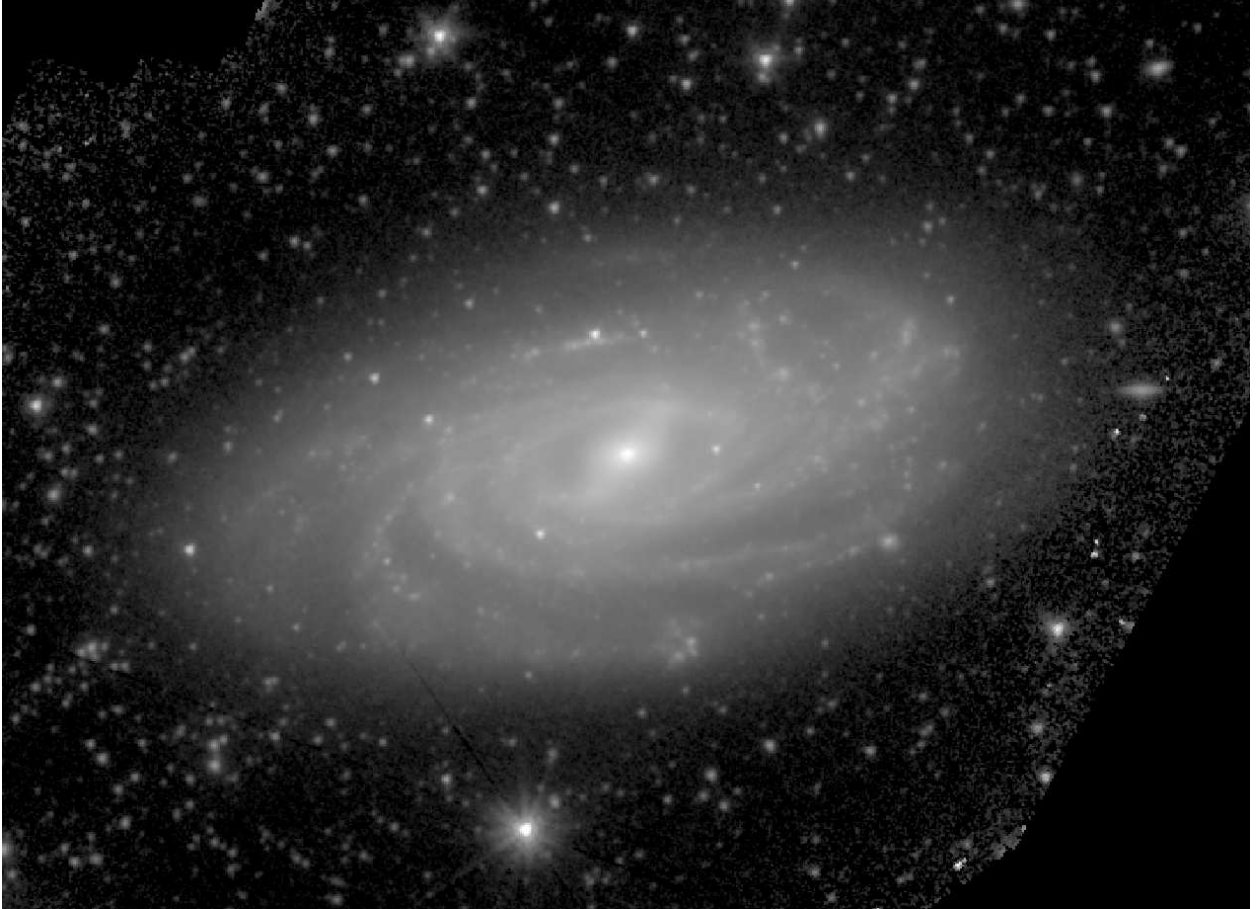


Fig. 1.87.— **NGC 3953** - S⁴G mid-IR classification: SB(r)bc ; Filter: IRAC 3.6 μ m; North: left, East: down; Field dimensions: 9.0 \times 6.6 arcmin; Surface brightness range displayed: 13.0–28.0 mag arcsec⁻²

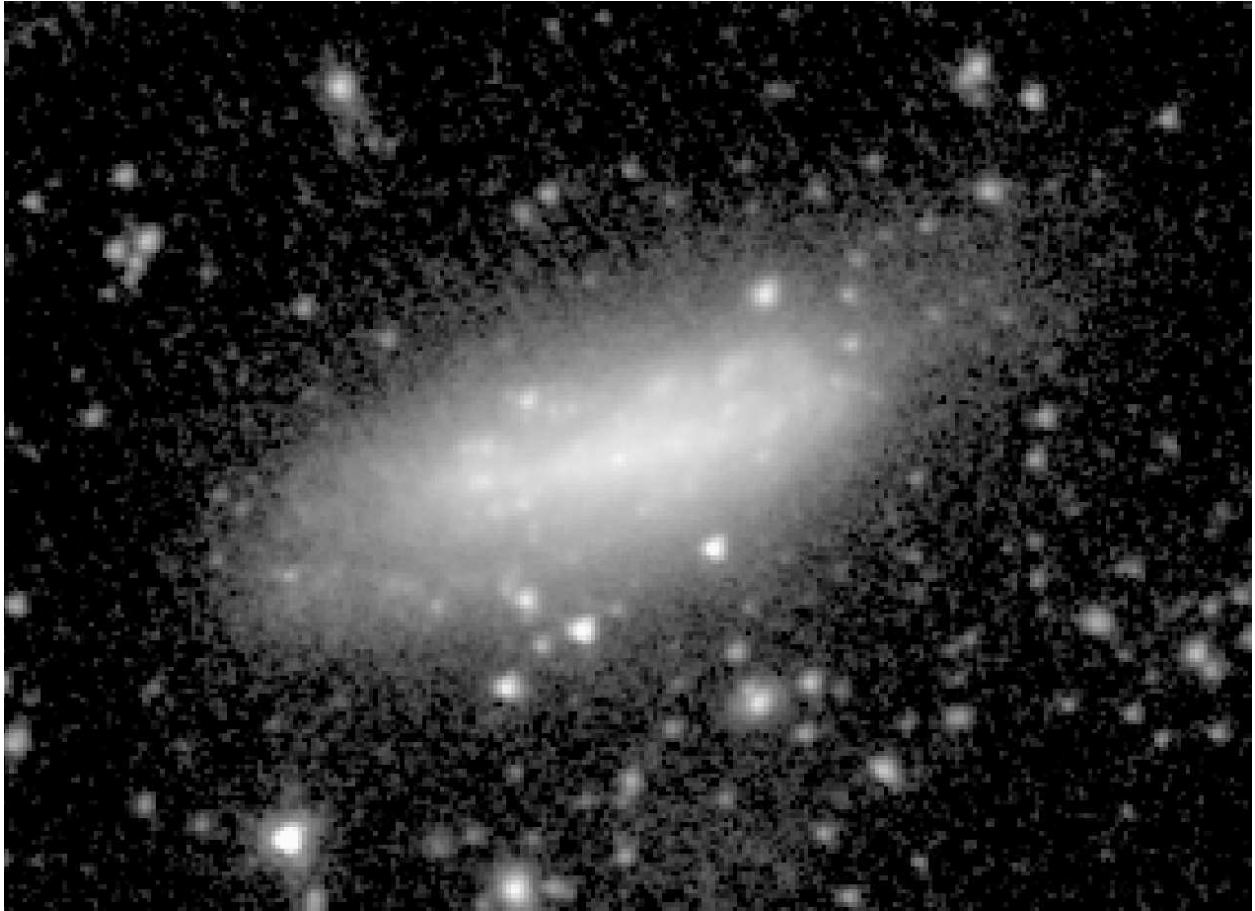


Fig. 1.88.— **NGC 4020** - S⁴G mid-IR classification: SAB(s)d ; Filter: IRAC 3.6 μ m; North: left, East: down; Field dimensions: 3.5 \times 2.6 arcmin; Surface brightness range displayed: 17.0–28.0 mag arcsec⁻²



Fig. 1.89.— **NGC 4068** - S⁴G mid-IR classification: Im ; Filter: IRAC 3.6 μ m; North: up, East: left; Field dimensions: 2.7 \times 2.0 arcmin; Surface brightness range displayed: 16.5–28.0 mag arcsec⁻²

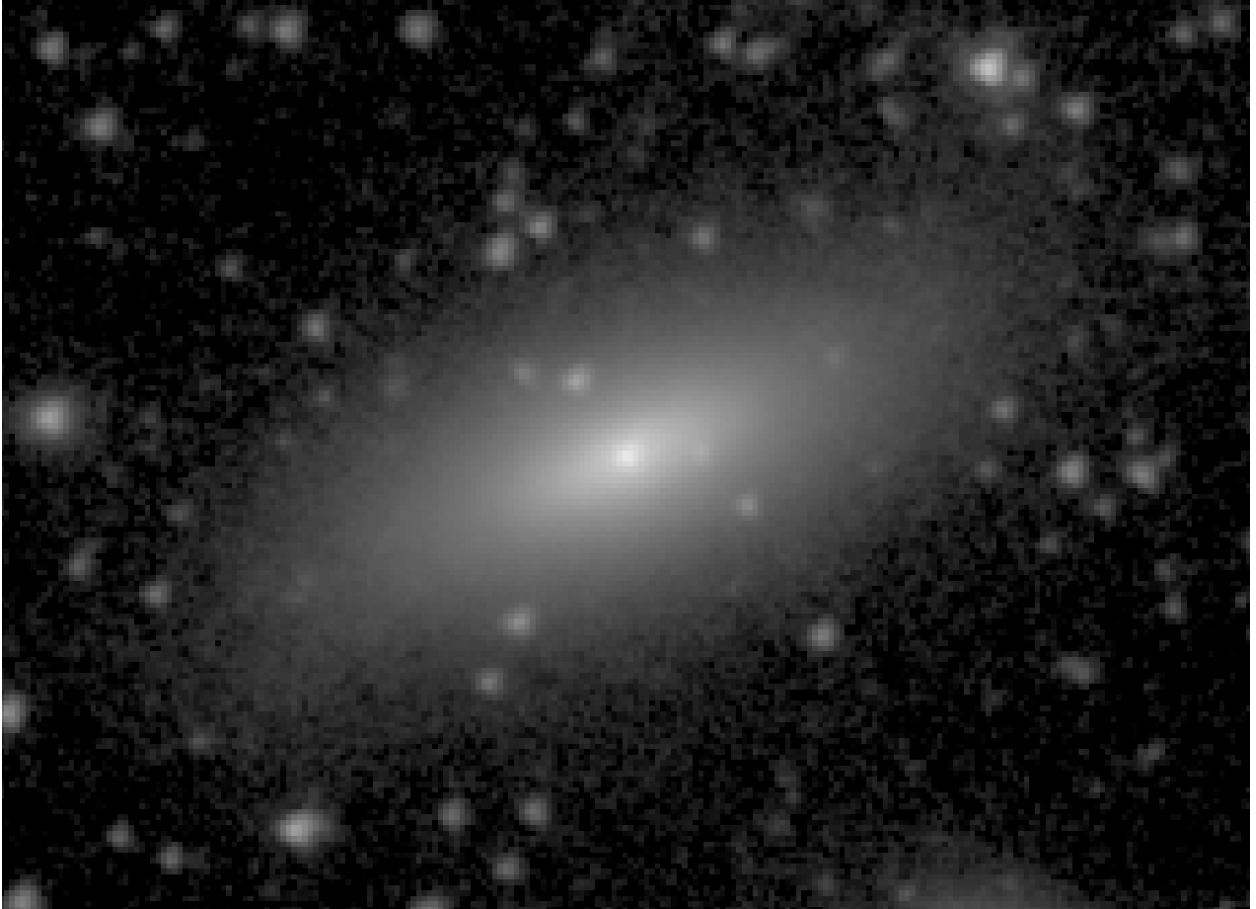


Fig. 1.90.— **NGC 4117** - S⁴G mid-IR classification: S0⁻ sp ; Filter: IRAC 3.6μm; North: left, East: down; Field dimensions: 2.9× 2.1 arcmin; Surface brightness range displayed: 14.0–28.0 mag arcsec⁻²



Fig. 1.91.— **NGC 4118** - S⁴G mid-IR classification: dE3-4: ; Filter: IRAC 3.6 μ m; North: left, East: down; Field dimensions: 1.4 \times 1.0 arcmin; Surface brightness range displayed: 17.0–28.0 mag arcsec⁻²

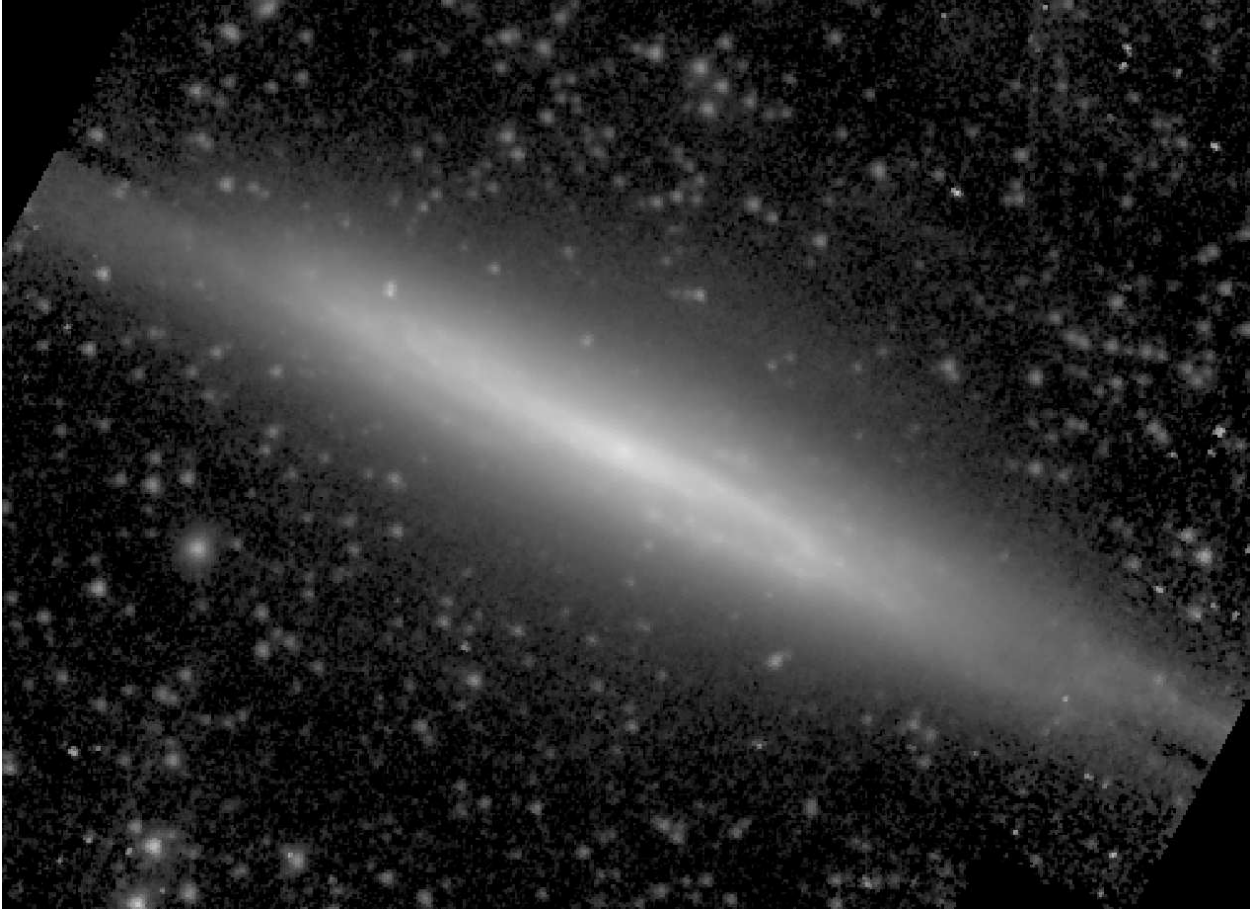


Fig. 1.92.— **NGC 4157** - S⁴G mid-IR classification: SAB(s)c: ; Filter: IRAC 3.6μm; North: up, East: left; Field dimensions: 6.3× 4.6 arcmin; Surface brightness range displayed: 14.0–28.0 mag arcsec⁻²

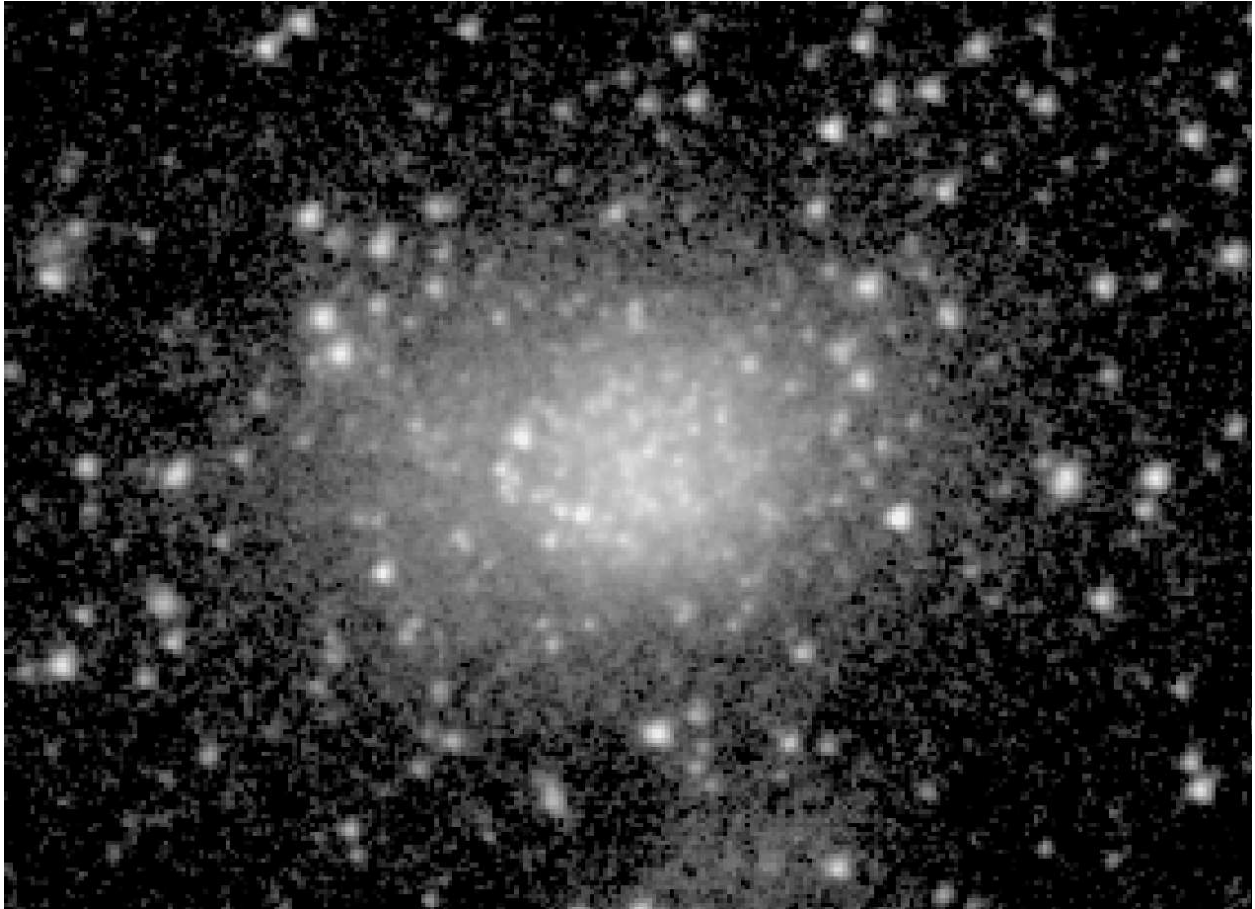


Fig. 1.93.— **NGC 4163** - S⁴G mid-IR classification: dE (Im) ; Filter: IRAC 3.6 μ m; North: left, East: down; Field dimensions: 3.5 \times 2.6 arcmin; Surface brightness range displayed: 18.0–28.0 mag arcsec⁻²

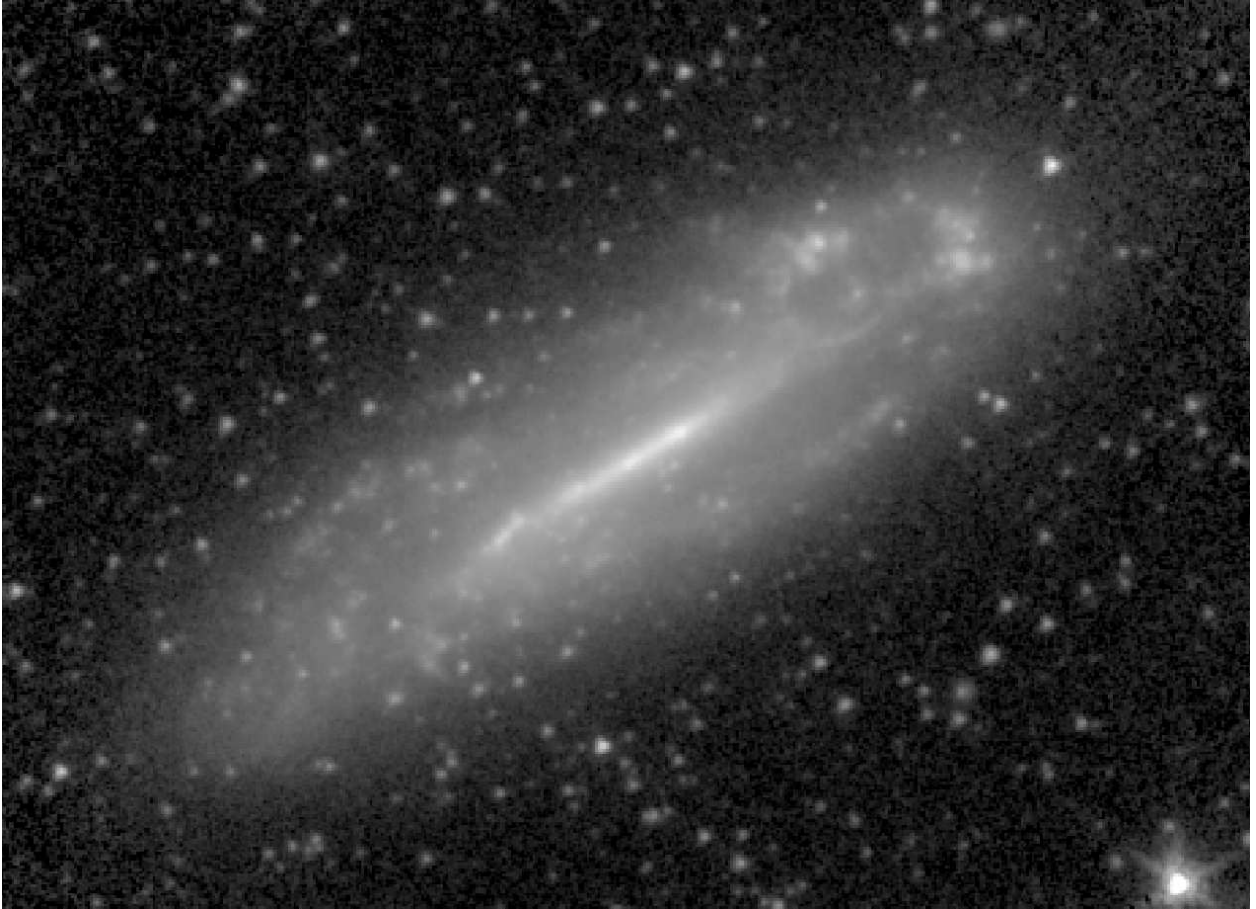


Fig. 1.94.— **NGC 4178** - S⁴G mid-IR classification: (R'₂)SB(s)d ; Filter: IRAC 3.6μm; North: left, East: down; Field dimensions: 5.8× 4.2 arcmin; Surface brightness range displayed: 15.5–28.0 mag arcsec⁻²

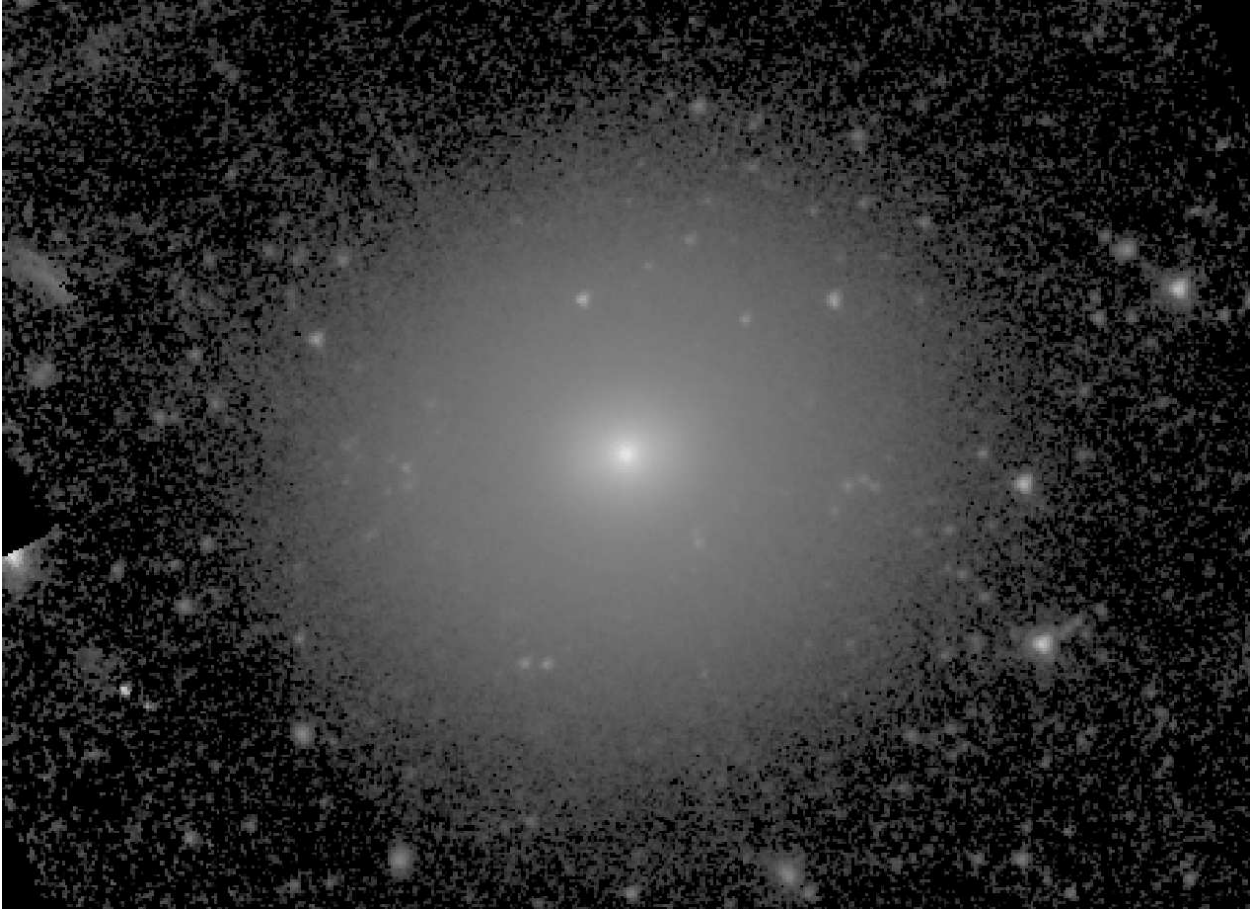


Fig. 1.95.— **NGC 4203** - S⁴G mid-IR classification: SAB0⁻ ; Filter: IRAC 3.6μm; North: left, East: down; Field dimensions: 5.7× 4.2 arcmin; Surface brightness range displayed: 12.5–28.0 mag arcsec⁻²



Fig. 1.96.— **NGC 4244** - S⁴G mid-IR classification: Sd sp ; Filter: IRAC 3.6 μ m; North: up, East: left; Field dimensions: 15.8 \times 11.5 arcmin; Surface brightness range displayed: 15.0–28.0 mag arcsec⁻²

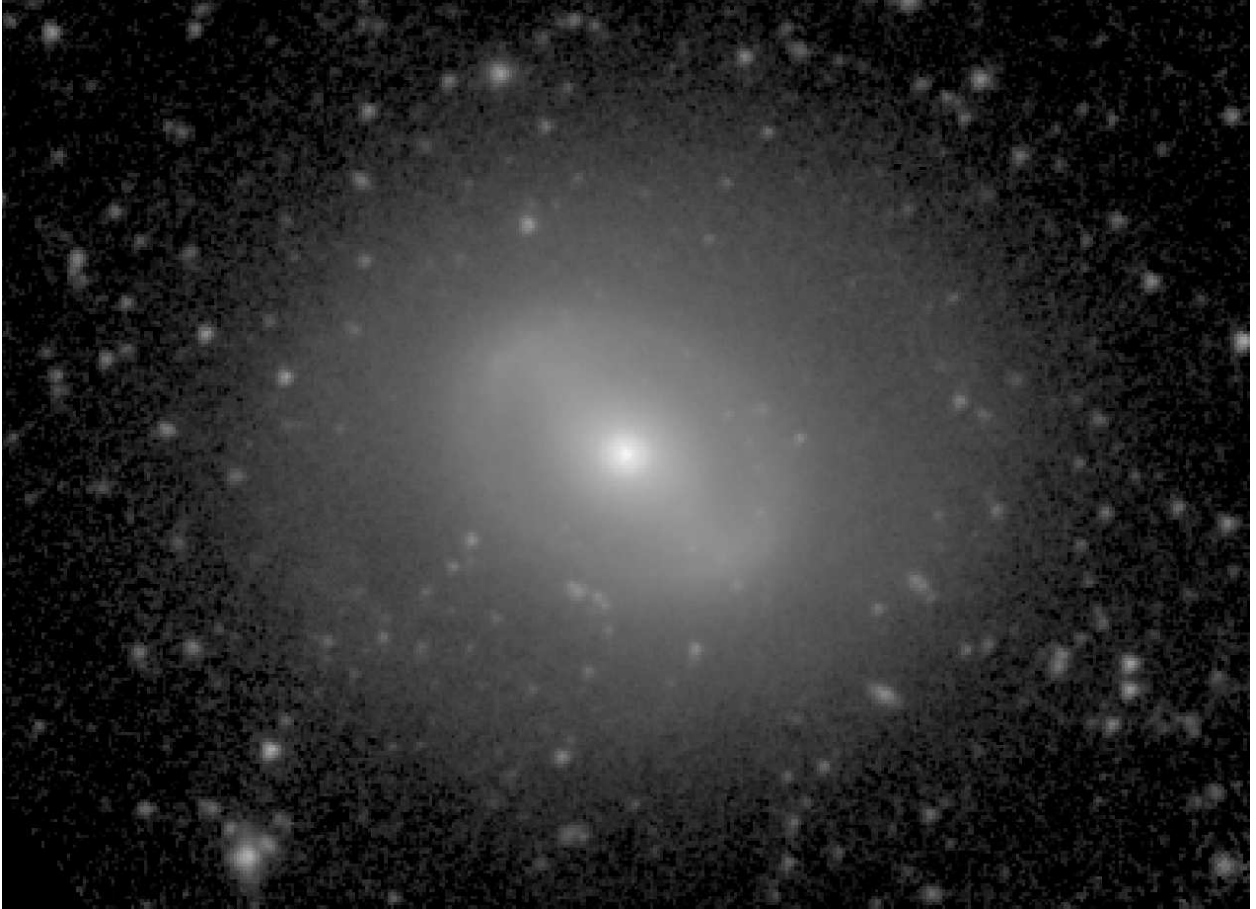


Fig. 1.97.— **NGC 4245** - S⁴G mid-IR classification: (RL)SB(r,nr)0⁺ ; Filter: IRAC 3.6 μ m; North: left, East: down; Field dimensions: 4.8 \times 3.5 arcmin; Surface brightness range displayed: 13.5–28.0 mag arcsec⁻²



Fig. 1.98.— **NGC 4254** - S⁴G mid-IR classification: SA(s)c pec ; Filter: IRAC 3.6 μ m;
North: up, East: left; Field dimensions: 7.0 \times 5.1 arcmin; Surface brightness range displayed:
14.0–28.0 mag arcsec⁻²

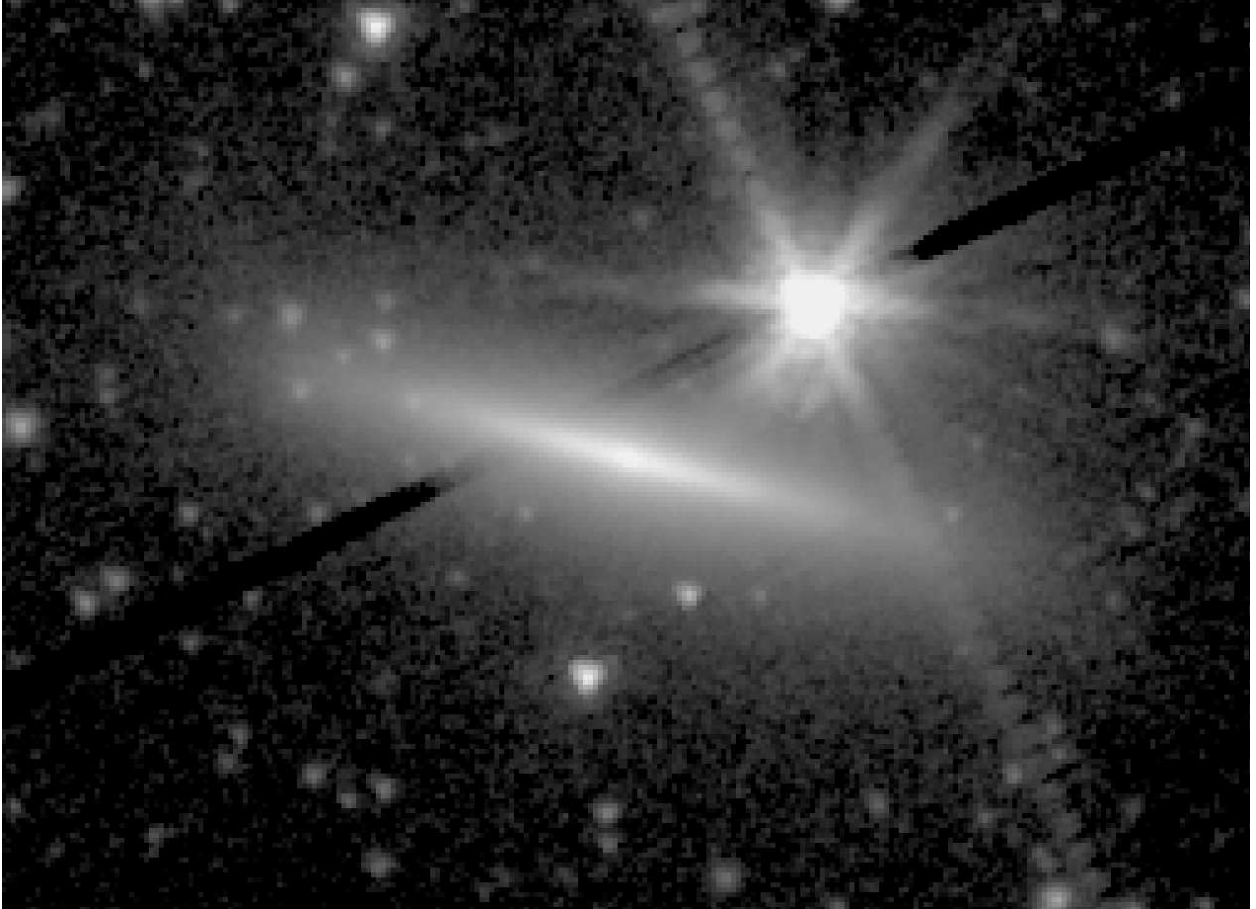


Fig. 1.99.— **NGC 4266** - S⁴G mid-IR classification: S0^o sp ; Filter: IRAC 3.6 μ m; North: up, East: left; Field dimensions: 3.2 \times 2.3 arcmin; Surface brightness range displayed: 15.0–28.0 mag arcsec⁻²

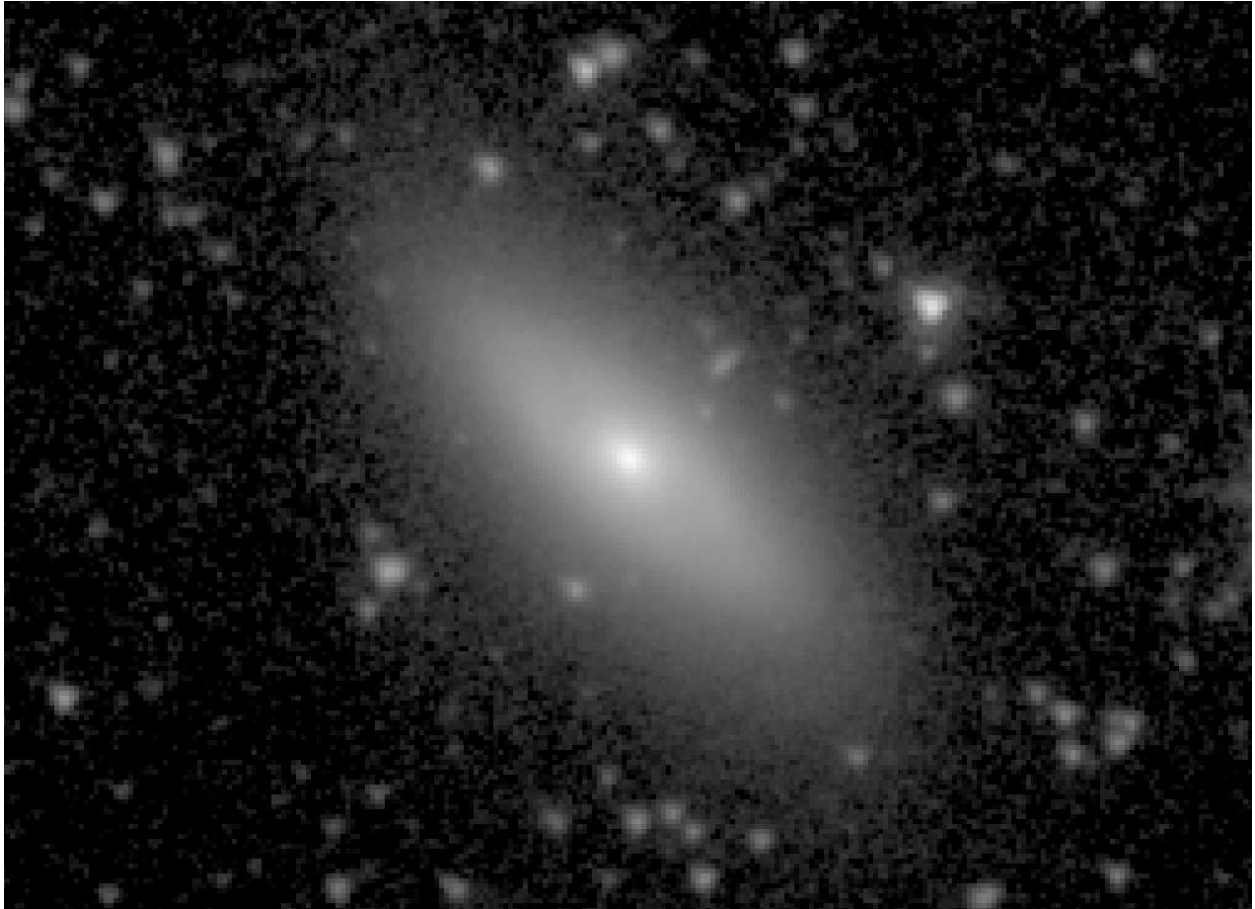


Fig. 1.100.— **NGC 4268** - S⁴G mid-IR classification: SA:(rs)0⁺ sp ; Filter: IRAC 3.6μm;
North: up, East: left; Field dimensions: 3.2× 2.3 arcmin; Surface brightness range displayed:
13.5–28.0 mag arcsec⁻²

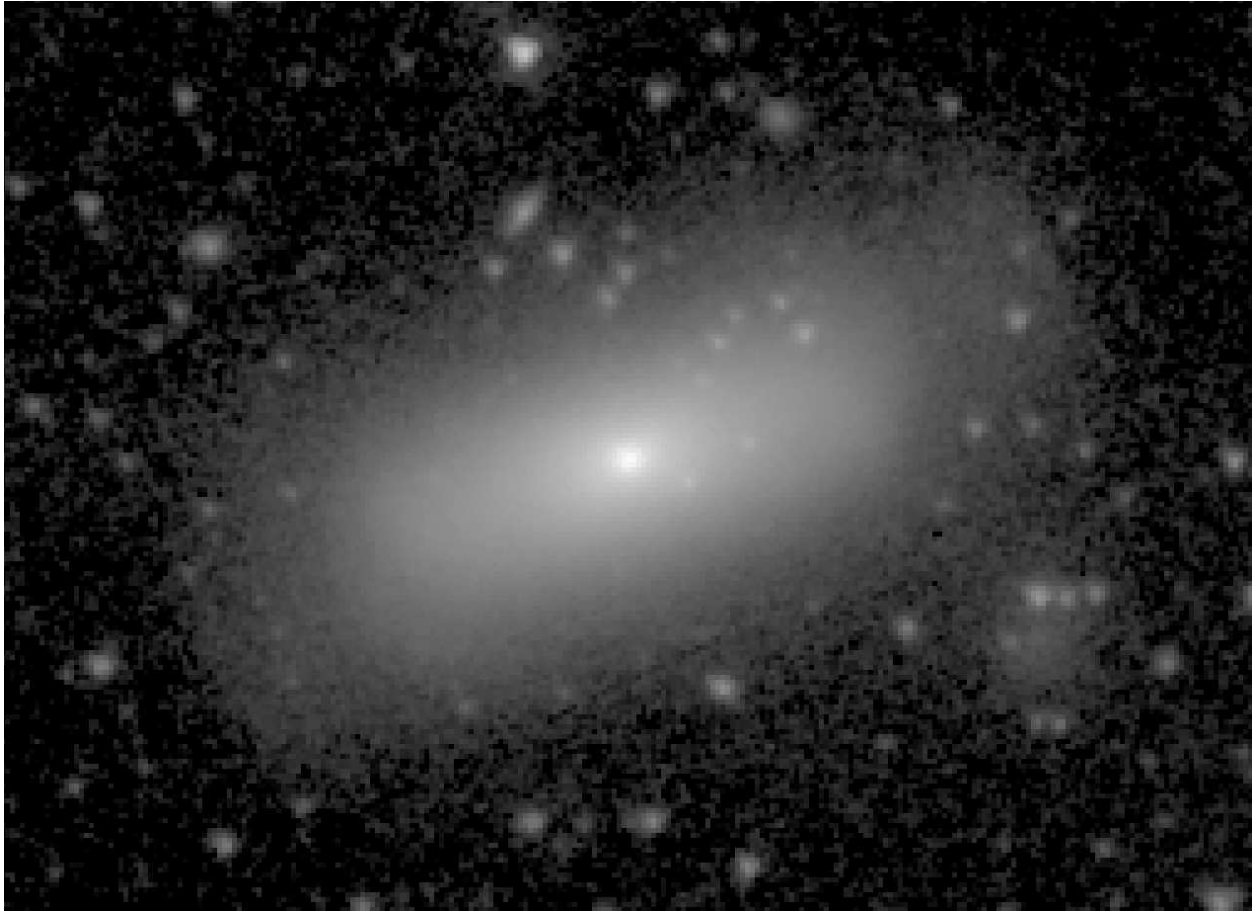


Fig. 1.101.— **NGC 4270** - S⁴G mid-IR classification: S0⁺ sp? ; Filter: IRAC 3.6μm; North: up, East: left; Field dimensions: 5.3× 3.8 arcmin; Surface brightness range displayed: 13.5–28.0 mag arcsec⁻²



Fig. 1.102.— **NGC 4273** - S⁴G mid-IR classification: SAB(s)c pec ; Filter: IRAC 3.6μm; North: left, East: down; Field dimensions: 3.2× 2.3 arcmin; Surface brightness range displayed: 13.5–28.0 mag arcsec⁻²

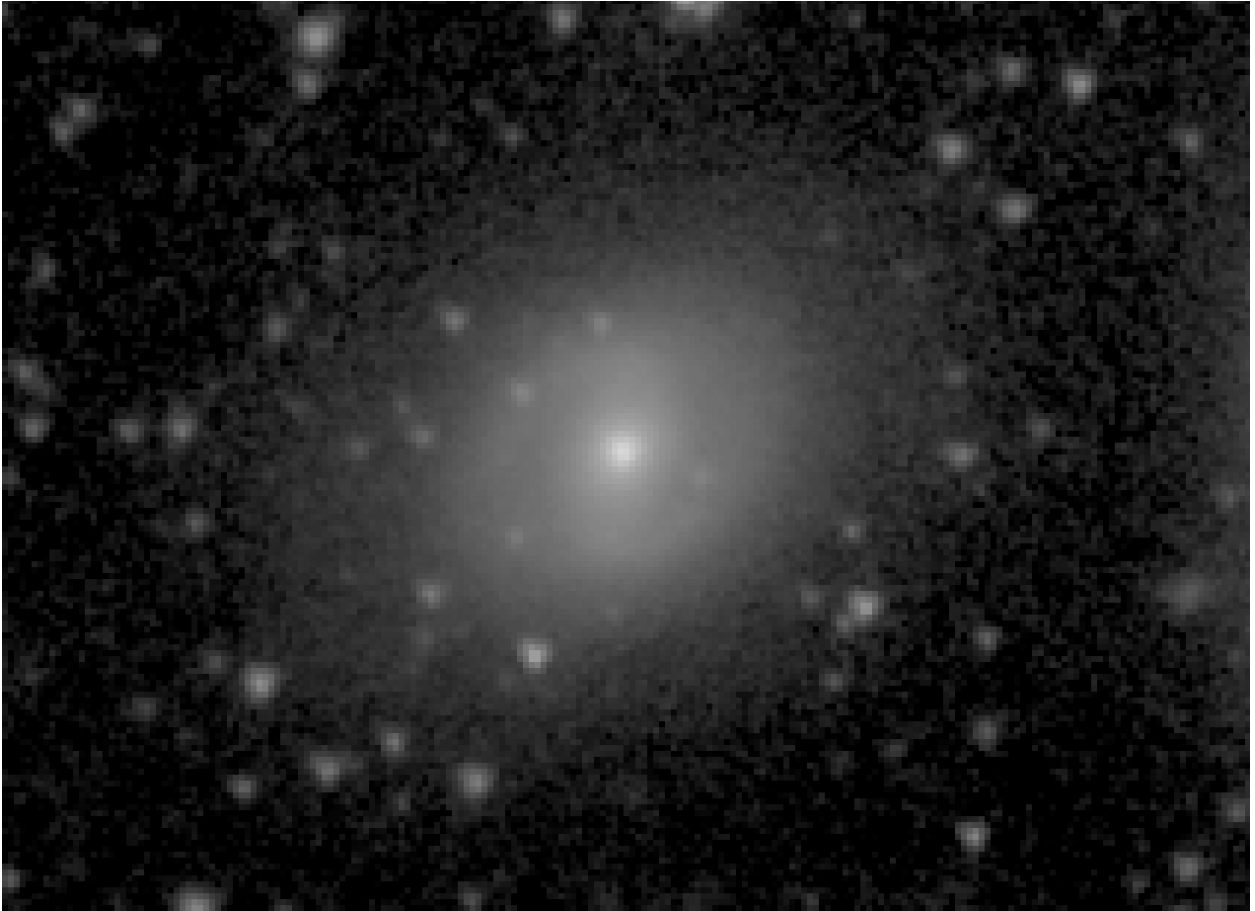


Fig. 1.103.— **NGC 4277** - S⁴G mid-IR classification: SAB(rs)0⁺ ; Filter: IRAC 3.6μm;
North: up, East: left; Field dimensions: 2.6× 1.9 arcmin; Surface brightness range displayed:
13.5–28.0 mag arcsec⁻²

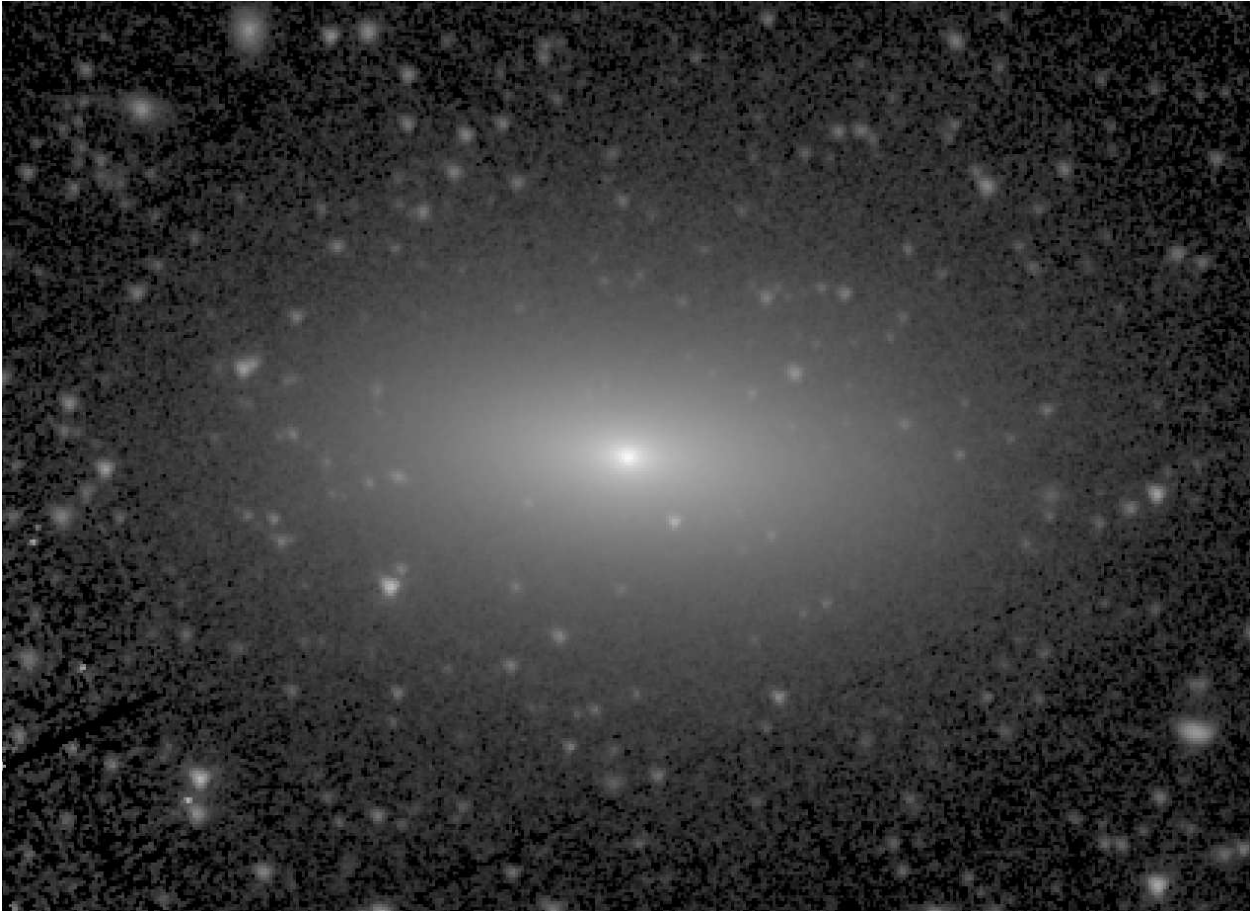


Fig. 1.104.— **NGC 4281** - S⁴G mid-IR classification: E(d)5 ; Filter: IRAC 3.6 μ m; North: up, East: left; Field dimensions: 5.3 \times 3.8 arcmin; Surface brightness range displayed: 12.5–28.0 mag arcsec⁻²



Fig. 1.105.— **NGC 4294** - S⁴G mid-IR classification: SB(s)d ; Filter: IRAC 3.6 μ m; North: left, East: down; Field dimensions: 4.0 \times 2.9 arcmin; Surface brightness range displayed: 16.0–28.0 mag arcsec⁻²

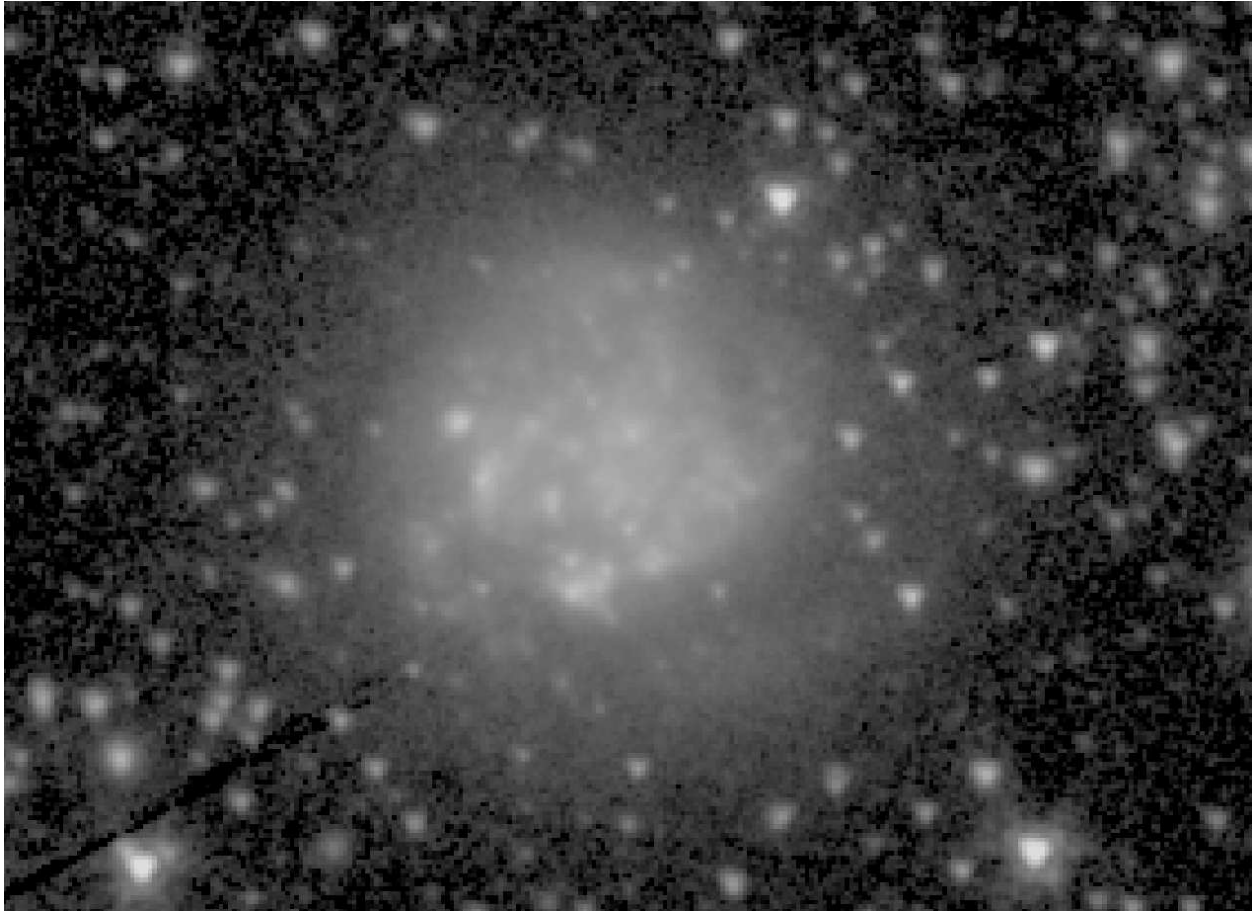


Fig. 1.106.— **NGC 4299** - S⁴G mid-IR classification: SA(s)dm ; Filter: IRAC 3.6 μ m;
North: up, East: left; Field dimensions: 3.5 \times 2.6 arcmin; Surface brightness range displayed:
17.0–28.0 mag arcsec⁻²

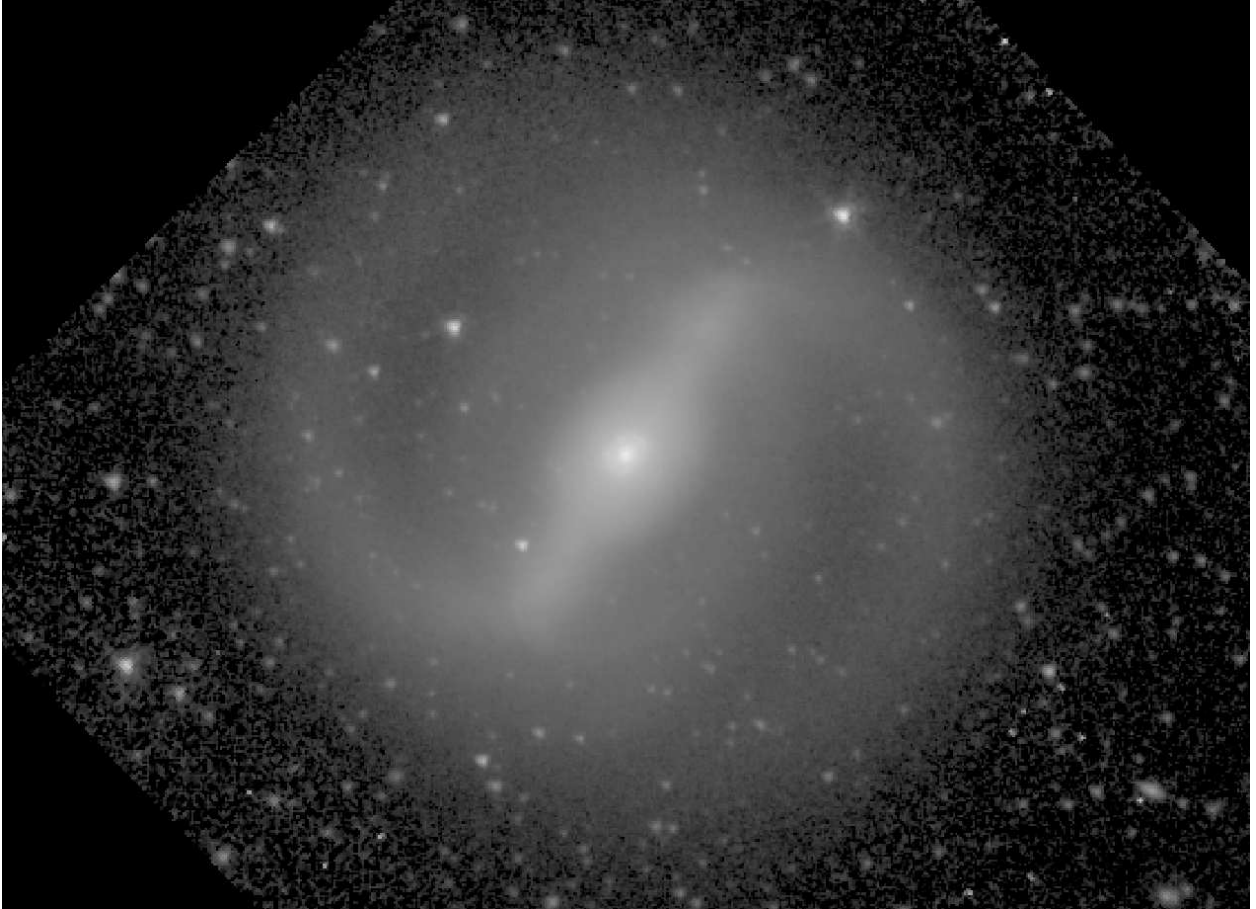


Fig. 1.107.— **NGC 4314** - S⁴G mid-IR classification: (R'₁)SB(rl,nr)a ; Filter: IRAC 3.6 μ m; North: up, East: left; Field dimensions: 7.0 \times 5.1 arcmin; Surface brightness range displayed: 13.0–28.0 mag arcsec⁻²



Fig. 1.108.— **NGC 4321** - S⁴G mid-IR classification: SAB(rs, nr)bc ; Filter: IRAC 3.6 μm; North: left, East: down; Field dimensions: 12.1 × 8.9 arcmin; Surface brightness range displayed: 13.0–28.0 mag arcsec⁻²

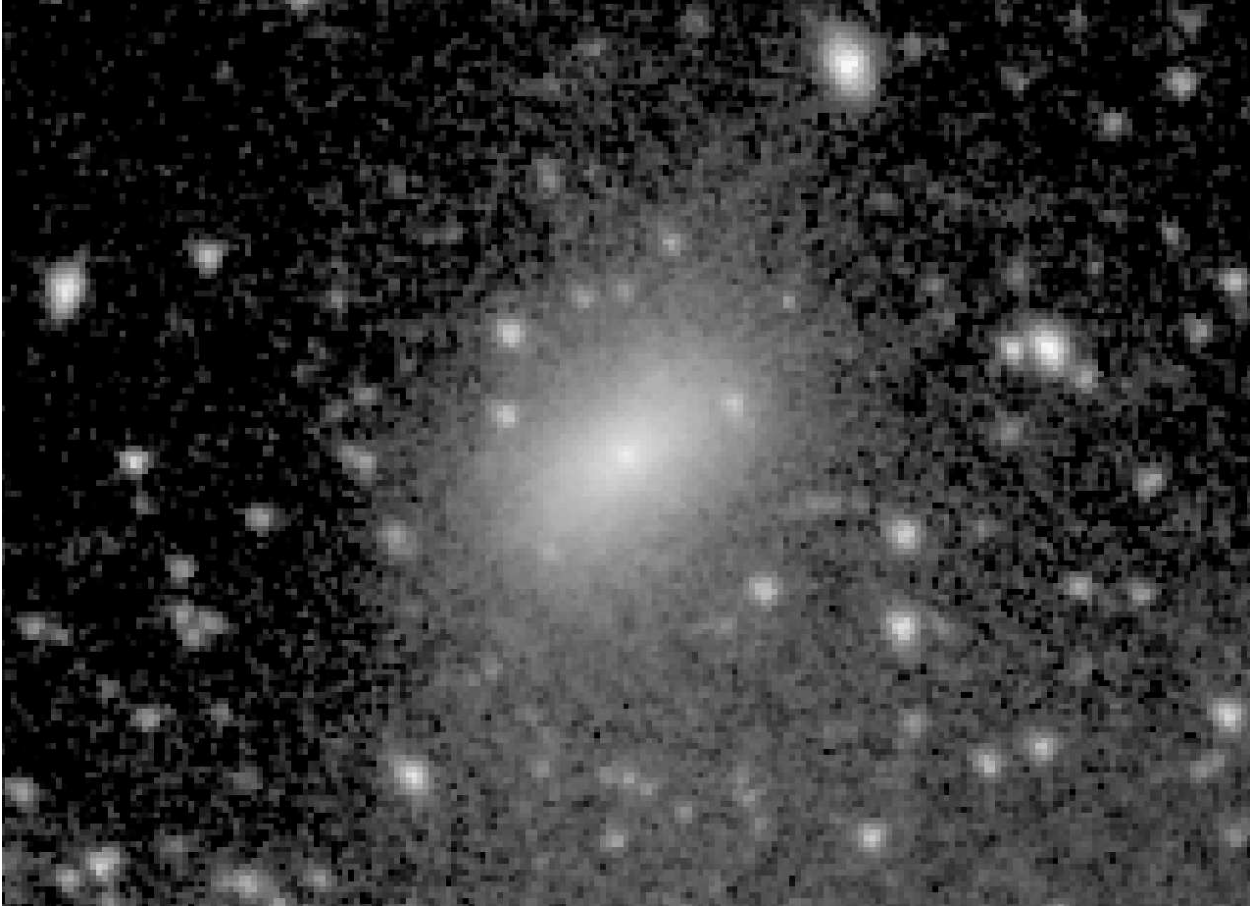


Fig. 1.109.— **NGC 4323** - S⁴G mid-IR classification: dE3,N ; Filter: IRAC 3.6 μ m; North: up, East: left; Field dimensions: 2.7 \times 2.0 arcmin; Surface brightness range displayed: 17.5–28.0 mag arcsec⁻²

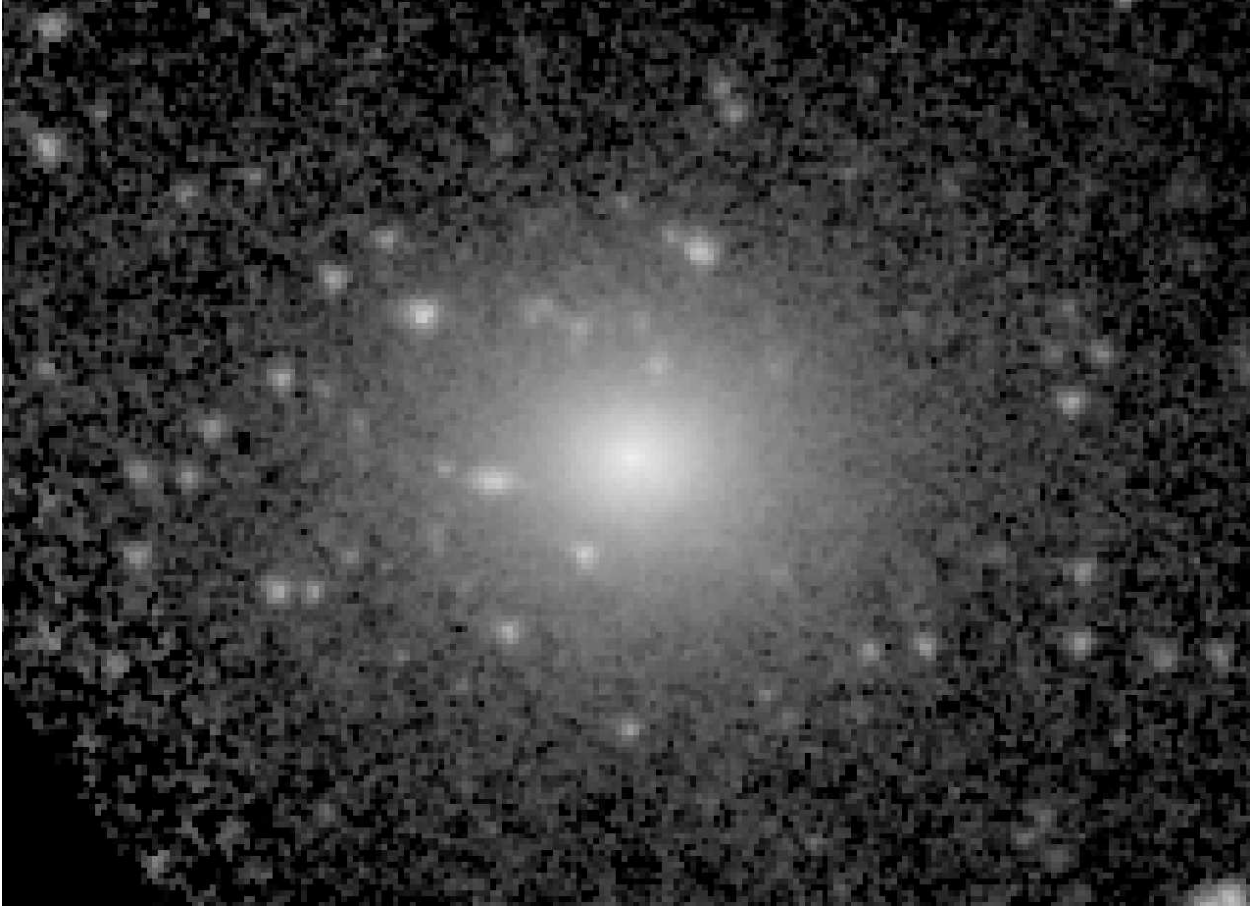


Fig. 1.110.— **NGC 4328** - S⁴G mid-IR classification: dSA(1)0⁻ ; Filter: IRAC 3.6 μ m; North: up, East: left; Field dimensions: 2.7 \times 2.0 arcmin; Surface brightness range displayed: 17.0–28.0 mag arcsec⁻²



Fig. 1.111.— **NGC 4369** - S⁴G mid-IR classification: (R)SB(rs)0/a: pec ; Filter: IRAC 3.6 μ m; North: up, East: left; Field dimensions: 4.5 \times 3.3 arcmin; Surface brightness range displayed: 14.0–28.0 mag arcsec⁻²



Fig. 1.112.— **NGC 4383** - S⁴G mid-IR classification: E(twist?)/SAB0⁻; ; Filter: IRAC 3.6 μ m; North: left, East: down; Field dimensions: 4.0 \times 2.9 arcmin; Surface brightness range displayed: 13.0–28.0 mag arcsec⁻²

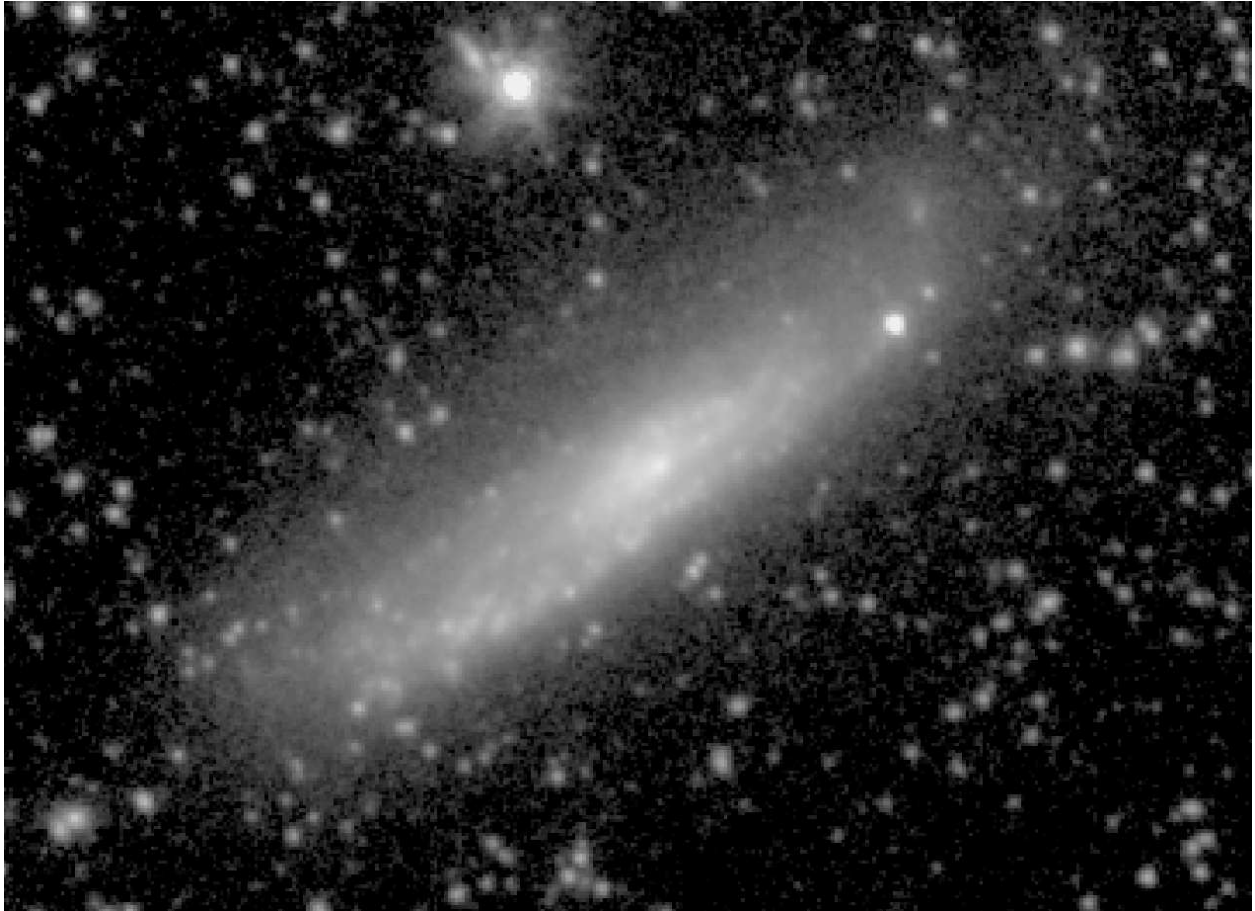


Fig. 1.113.— **NGC 4396** - S⁴G mid-IR classification: Scd: pec sp ; Filter: IRAC 3.6 μ m;
North: up, East: left; Field dimensions: 4.5 \times 3.3 arcmin; Surface brightness range displayed:
16.5–28.0 mag arcsec⁻²



Fig. 1.114.— **NGC 4437** - S⁴G mid-IR classification: Sc sp ; Filter: IRAC 3.6 μ m; North: up, East: left; Field dimensions: 12.6 \times 9.2 arcmin; Surface brightness range displayed: 14.5–28.0 mag arcsec⁻²

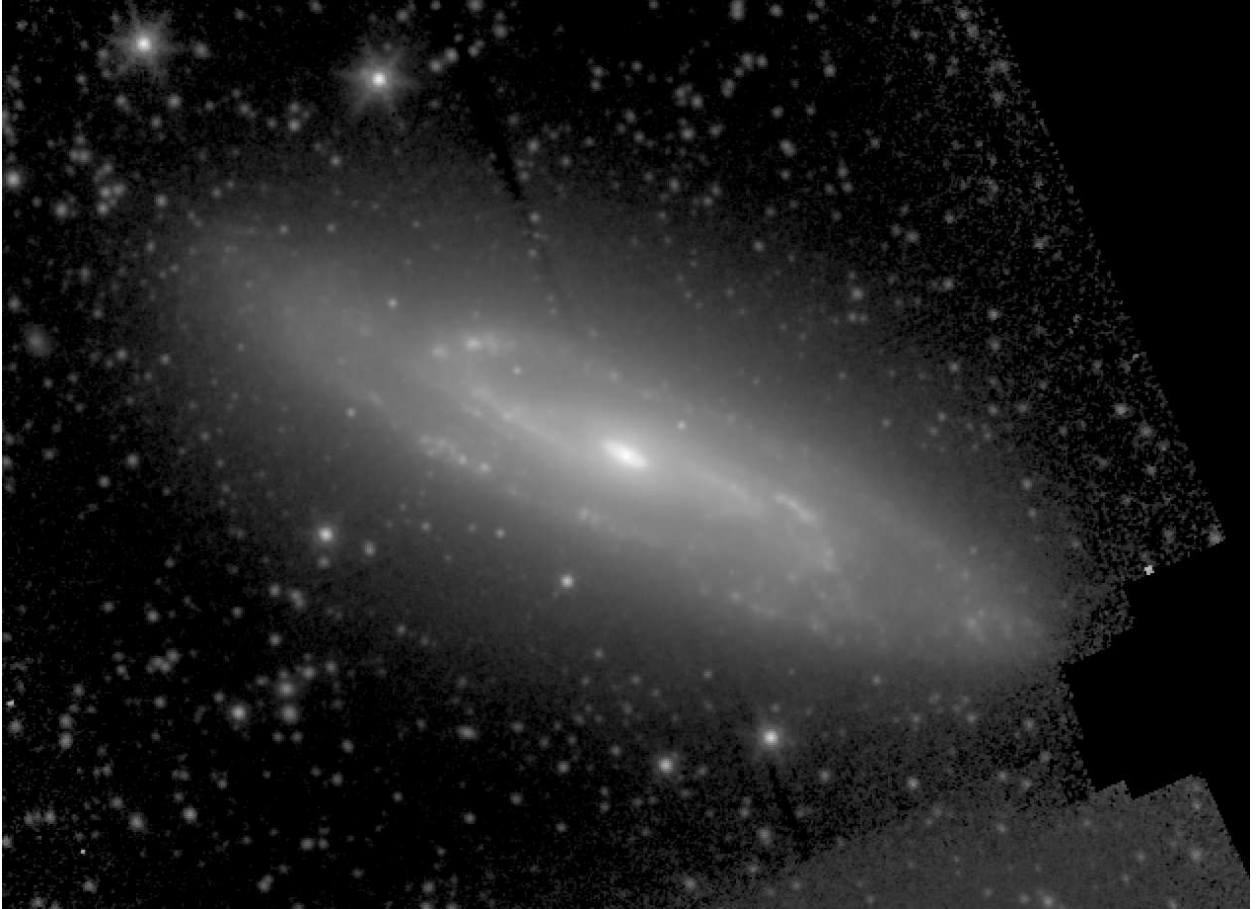


Fig. 1.115.— **NGC 4527** - S⁴G mid-IR classification: (R'₂)SAB(rs,nr)b_⊥ ; Filter: IRAC 3.6 μm; North: up, East: left; Field dimensions: 7.9 × 5.7 arcmin; Surface brightness range displayed: 12.0–28.0 mag arcsec⁻²

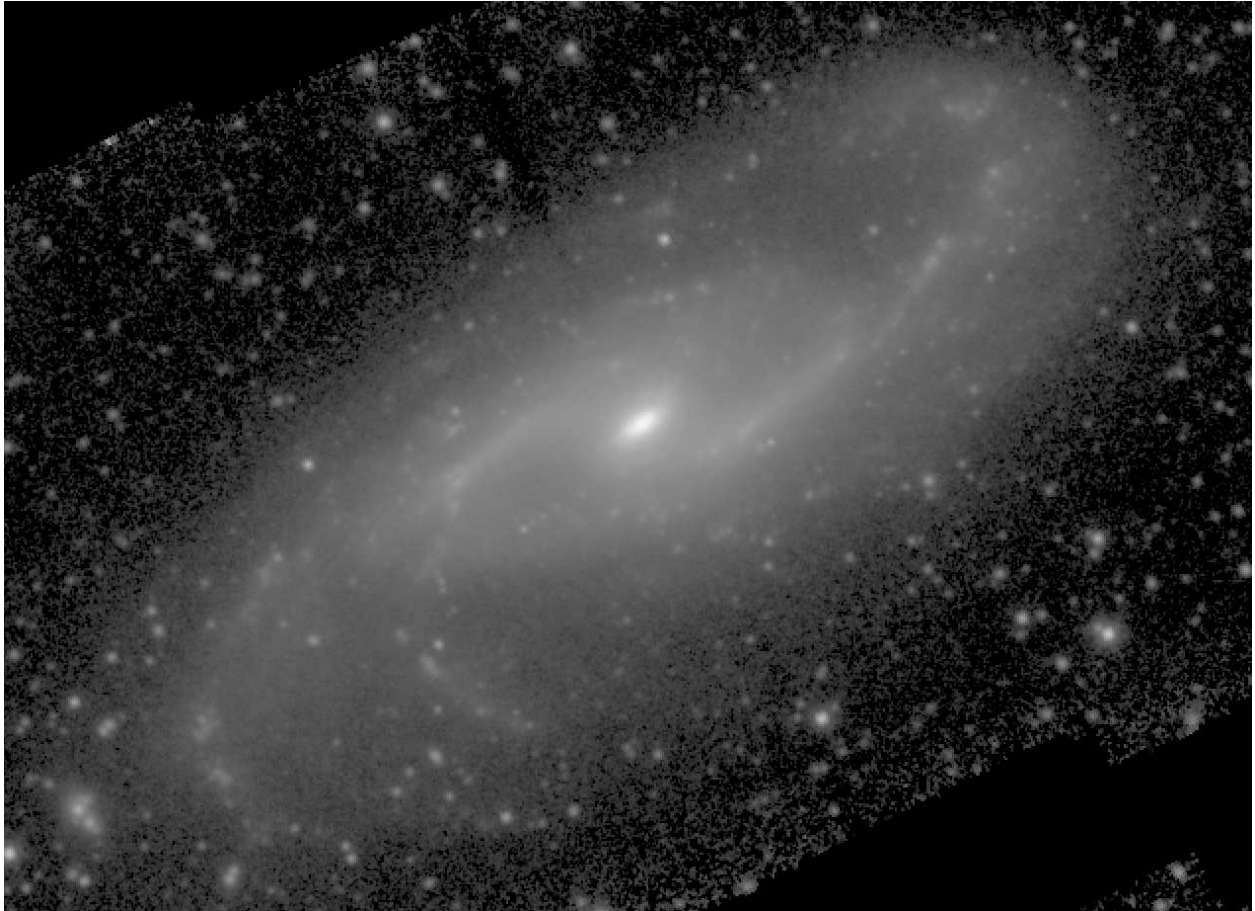


Fig. 1.116.— **NGC 4536** - S⁴G mid-IR classification: SAB(rs)bc ; Filter: IRAC 3.6 μ m; North: up, East: left; Field dimensions: 7.9 \times 5.8 arcmin; Surface brightness range displayed: 12.5–28.0 mag arcsec⁻²

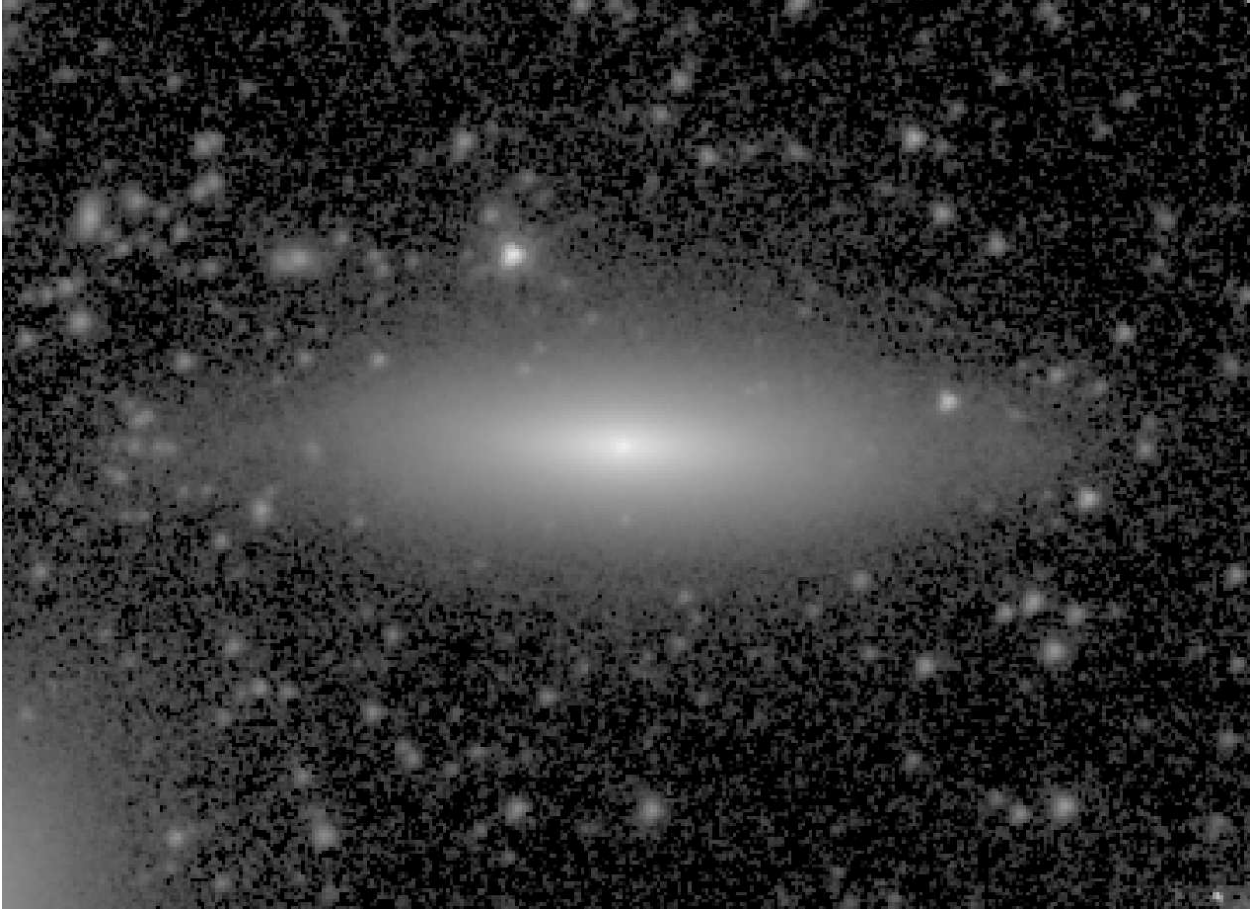


Fig. 1.117.— **NGC 4550** - S⁴G mid-IR classification: S0⁻ sp ; Filter: IRAC 3.6 μ m; North: left, East: down; Field dimensions: 4.5 \times 3.3 arcmin; Surface brightness range displayed: 13.5–28.0 mag arcsec⁻²

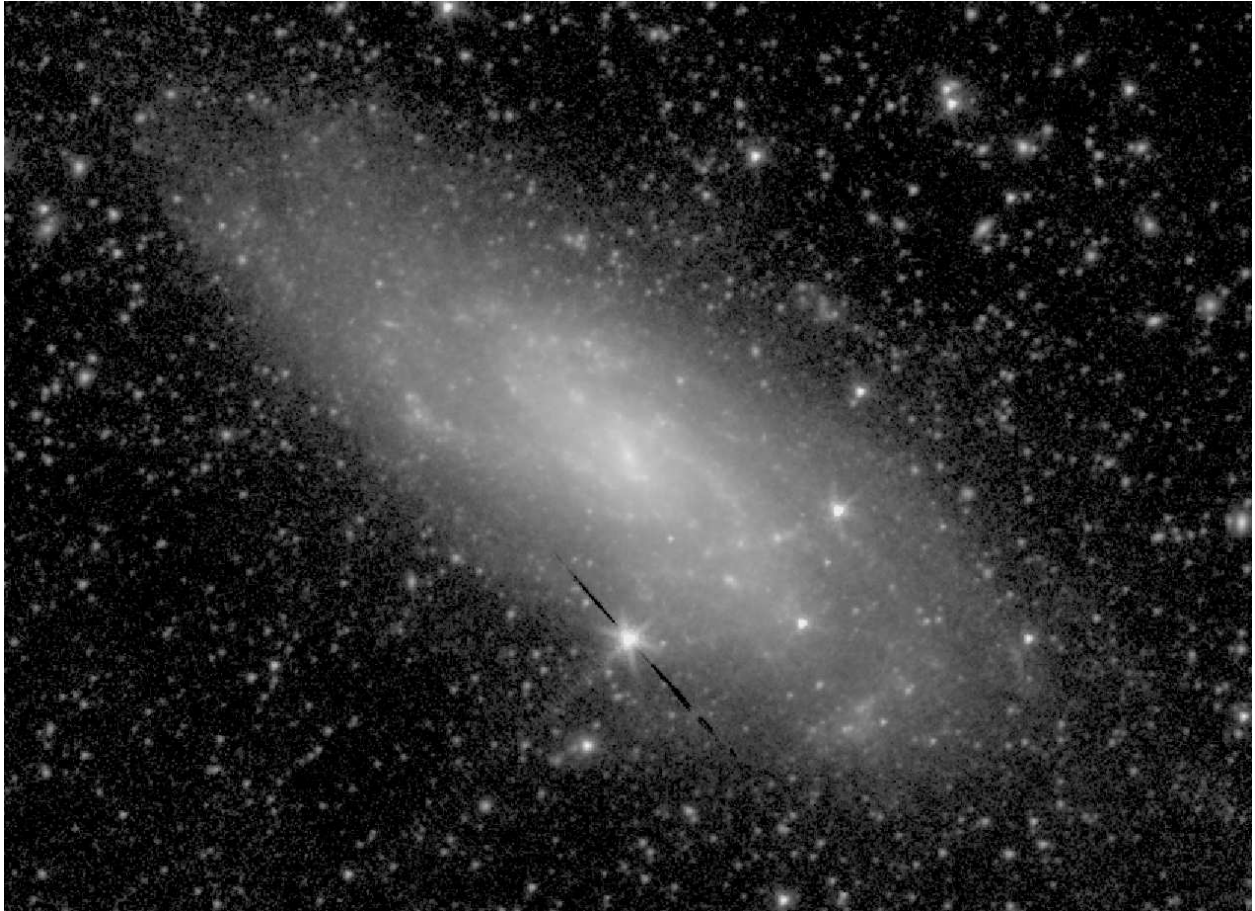


Fig. 1.118.— **NGC 4559** - S^4G mid-IR classification: SB(s)cd ; Filter: IRAC $3.6\mu\text{m}$; North: left, East: down; Field dimensions: 10.5×7.7 arcmin; Surface brightness range displayed: $15.5\text{--}28.0$ mag arcsec $^{-2}$



Fig. 1.119.— **NGC 4567** (left) and **NGC 4568** (right) - S⁴G mid-IR classifications: SA(rs)bc, SA(rs)bc, respectively; Filter: IRAC 3.6 μ m; North: left, East: down; Field dimensions: 6.3 \times 4.6 arcmin; Surface brightness range displayed: 13.0–28.0 mag arcsec⁻²



Fig. 1.120.— **NGC 4579** - S⁴G mid-IR classification: (R)SB(rs)a ; Filter: IRAC 3.6μm;
North: up, East: left; Field dimensions: 7.9× 5.7 arcmin; Surface brightness range displayed:
12.0–28.0 mag arcsec⁻²

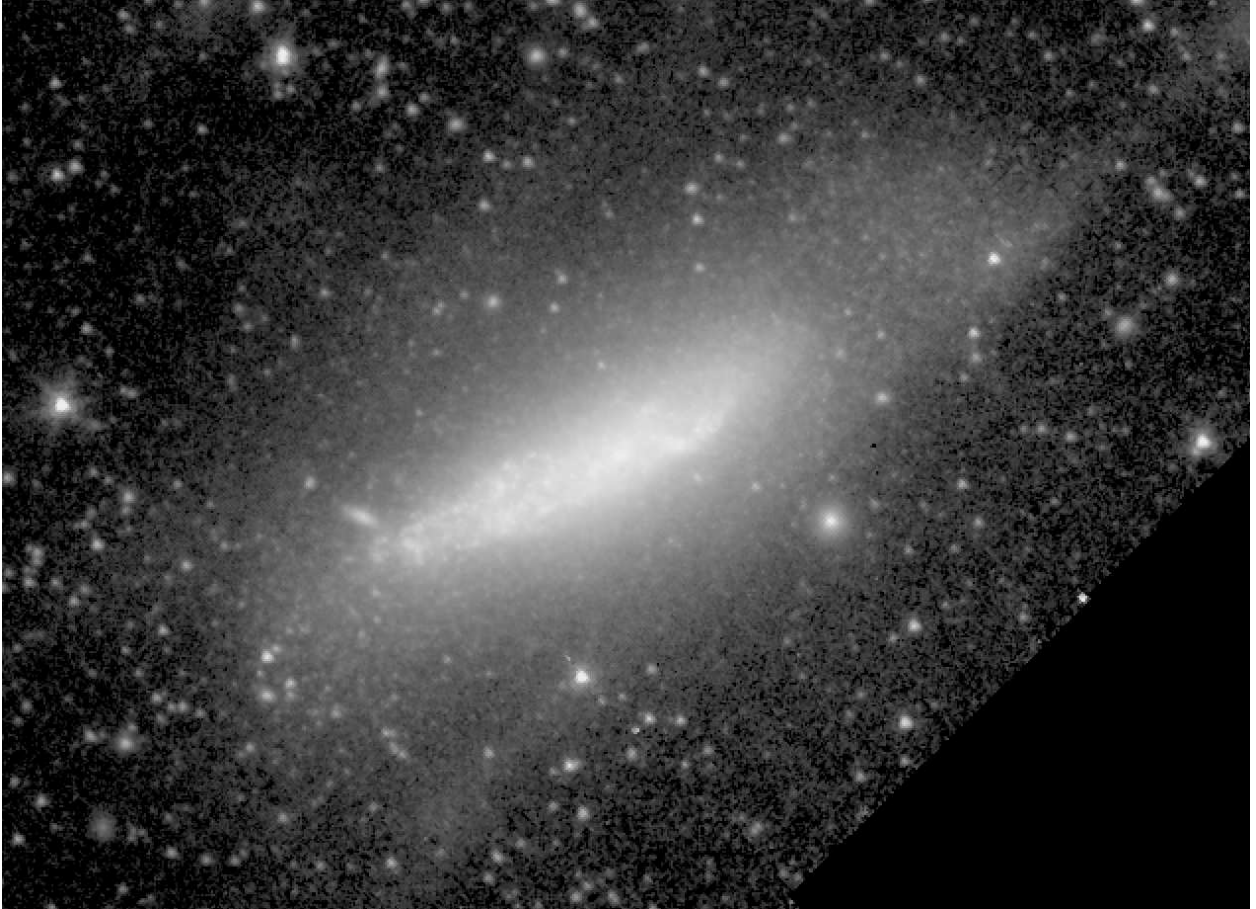


Fig. 1.121.— **NGC 4605** - S⁴G mid-IR classification: IB(s)m sp ; Filter: IRAC 3.6 μ m;
North: up, East: left; Field dimensions: 7.9 \times 5.7 arcmin; Surface brightness range displayed:
16.0–28.0 mag arcsec⁻²

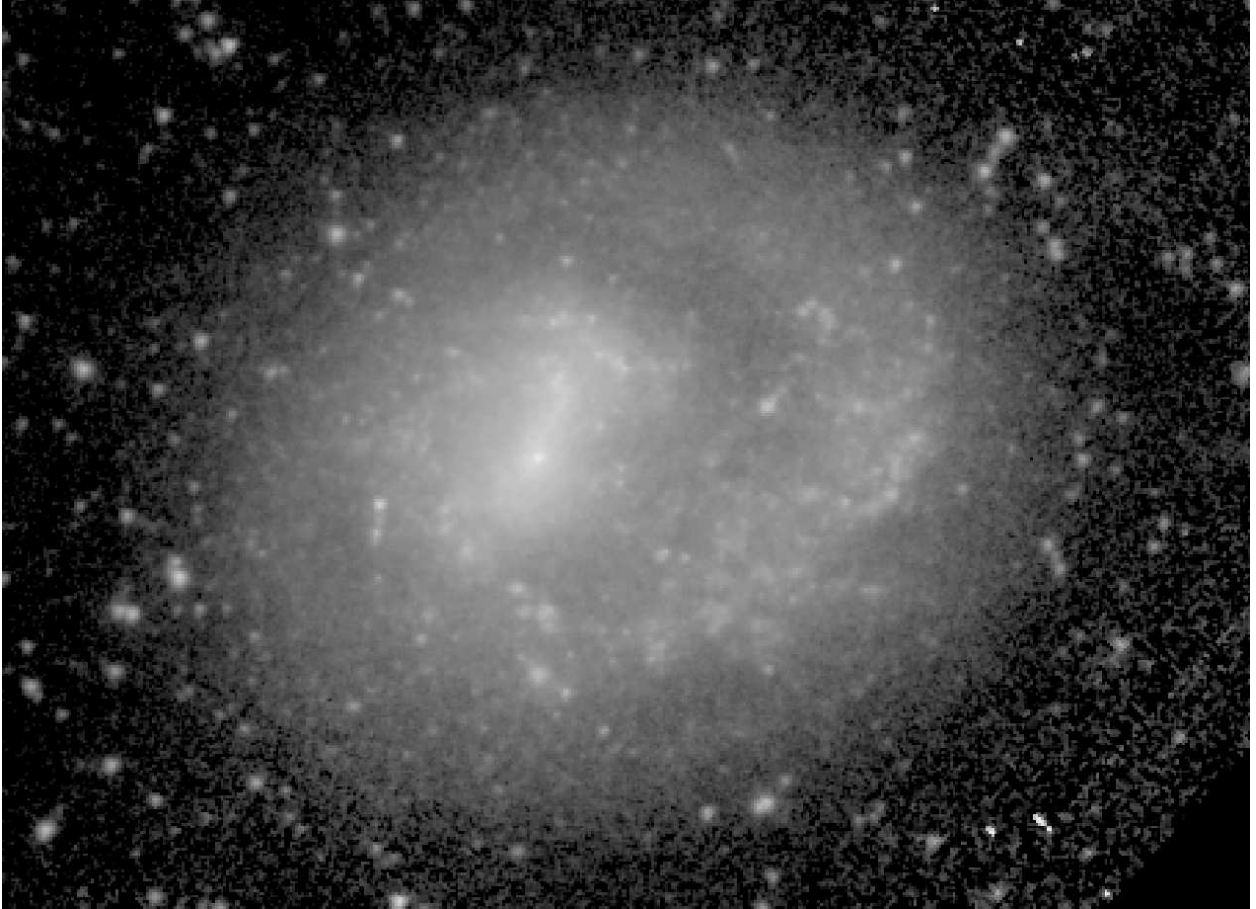


Fig. 1.122.— **NGC 4618** - S⁴G mid-IR classification: (R')SB(rs)m ; Filter: IRAC 3.6μm; North: left, East: down; Field dimensions: 5.7× 4.1 arcmin; Surface brightness range displayed: 16.0–28.0 mag arcsec⁻²

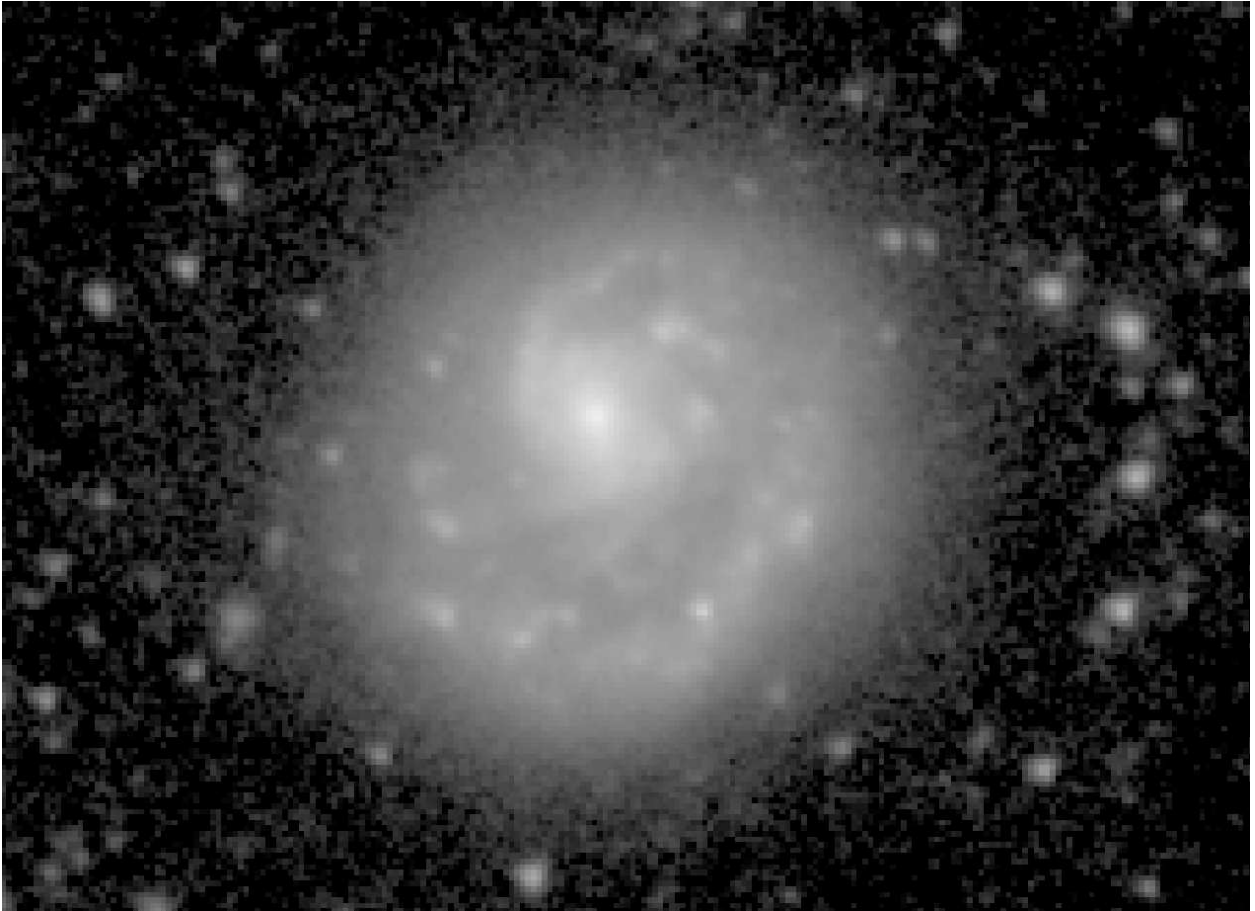


Fig. 1.123.— **NGC 4625** - S⁴G mid-IR classification: (R')SAB(rs)m ; Filter: IRAC 3.6 μ m;
North: up, East: left; Field dimensions: 2.8 \times 2.1 arcmin; Surface brightness range displayed:
16.0–28.0 mag arcsec⁻²

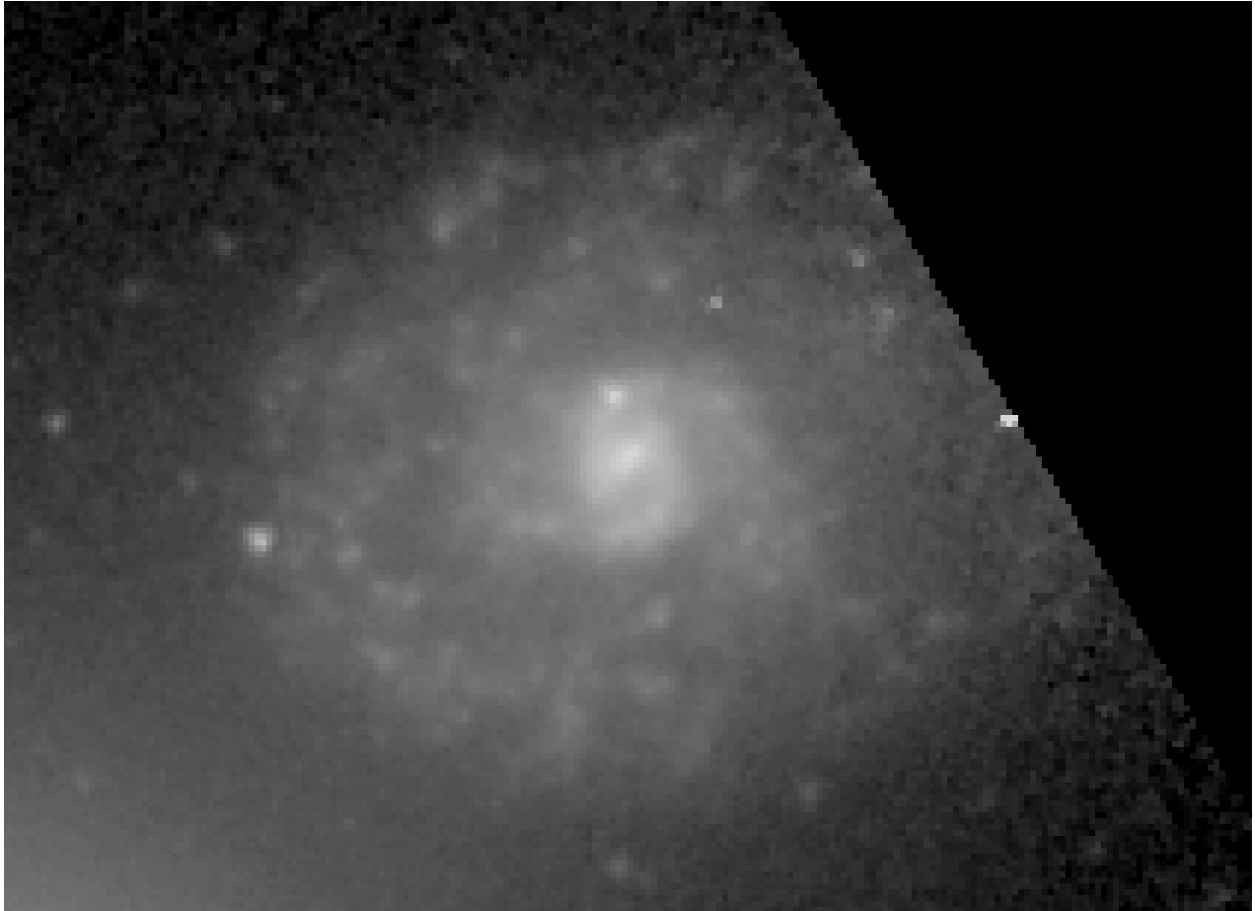


Fig. 1.124.— **NGC 4647** - S⁴G mid-IR classification: SAB(rs)cd ; Filter: IRAC 3.6 μ m;
North: up, East: left; Field dimensions: 2.6 \times 1.9 arcmin; Surface brightness range displayed:
15.0–28.0 mag arcsec⁻²

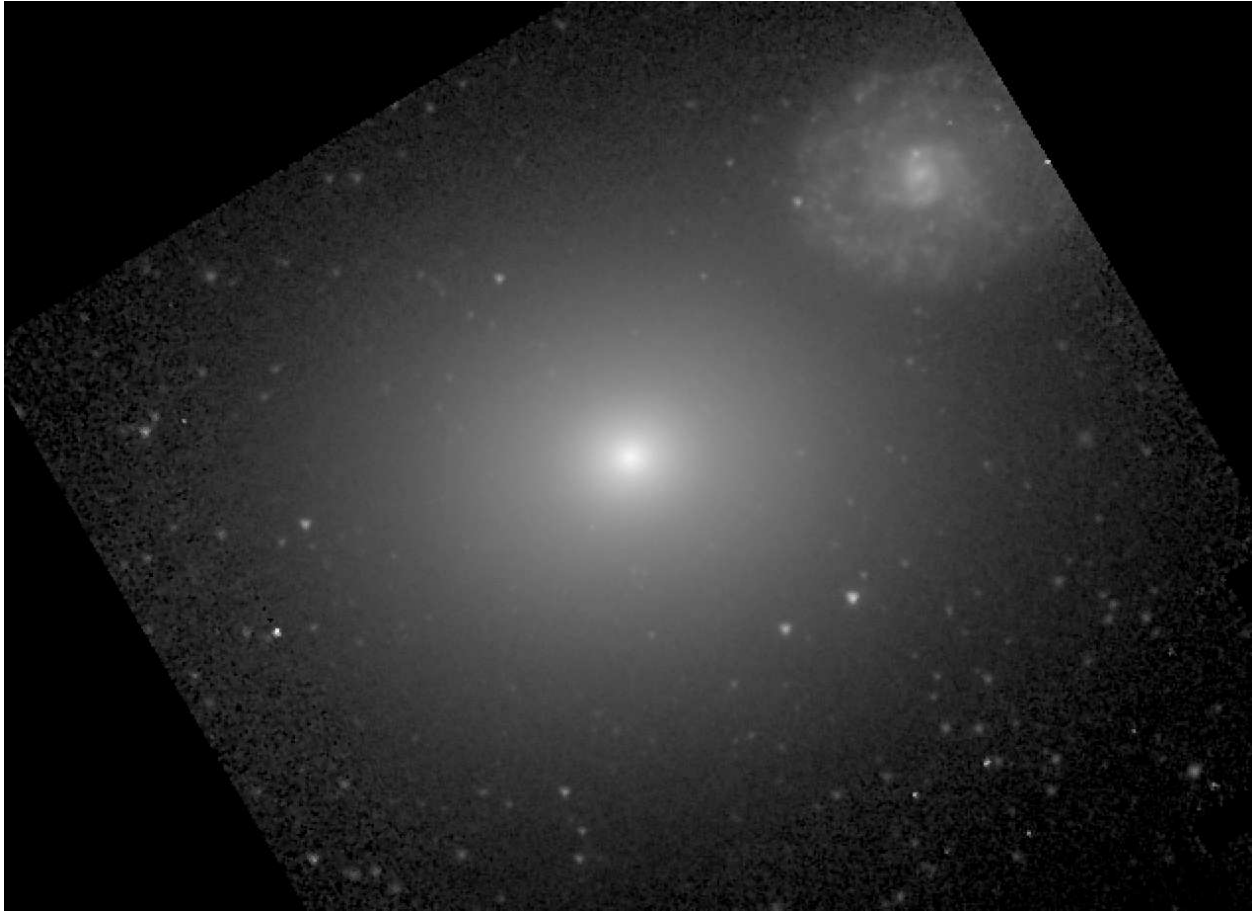


Fig. 1.125.— **NGC 4649** - S⁴G mid-IR classification: SA0⁻ ; Filter: IRAC 3.6μm; North: up, East: left; Field dimensions: 7.9× 5.7 arcmin; Surface brightness range displayed: 12.5–28.0 mag arcsec⁻²



Fig. 1.126.— **NGC 4707** - S⁴G mid-IR classification: Im ; Filter: IRAC 3.6 μ m; North: up, East: left; Field dimensions: 5.6 \times 4.1 arcmin; Surface brightness range displayed: 18.5–28.0 mag arcsec⁻²



Fig. 1.127.— **NGC 4725** - S⁴G mid-IR classification: SAB(r,nb)a ; Filter: IRAC 3.6 μ m; North: up, East: left; Field dimensions: 14.3 \times 10.4 arcmin; Surface brightness range displayed: 12.5–28.0 mag arcsec⁻²

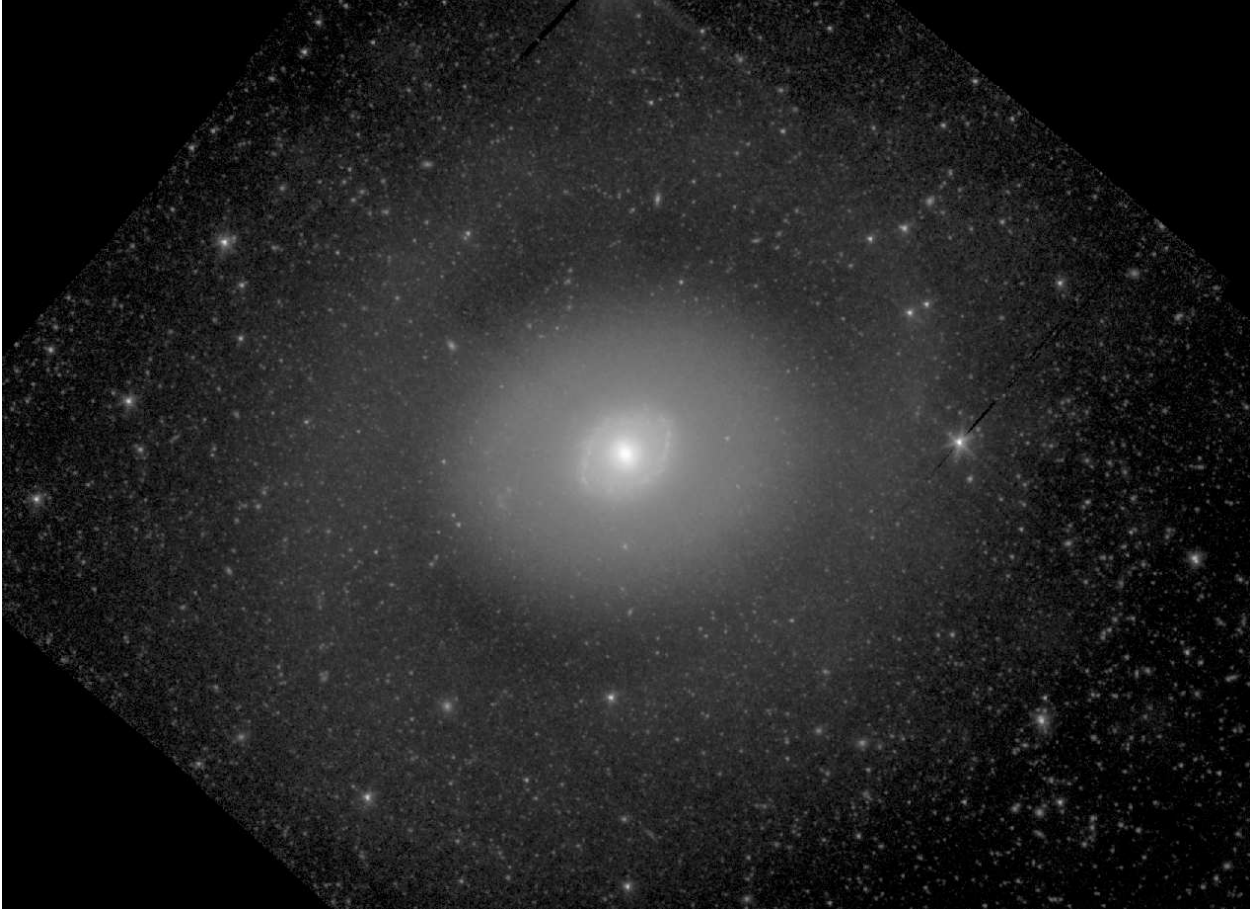


Fig. 1.128.— **NGC 4736** - S⁴G mid-IR classification: (R)SAB(rl,nr',nl,nb)a ; Filter: IRAC 3.6 μ m; North: up, East: left; Field dimensions: 21.0 \times 15.3 arcmin; Surface brightness range displayed: 12.0–28.0 mag arcsec⁻²



Fig. 1.129.— **NGC 4750** - S⁴G mid-IR classification: (R')SA(rs)a ; Filter: IRAC 3.6 μ m; North: left, East: down; Field dimensions: 6.7 \times 4.9 arcmin; Surface brightness range displayed: 13.0–28.0 mag arcsec⁻²

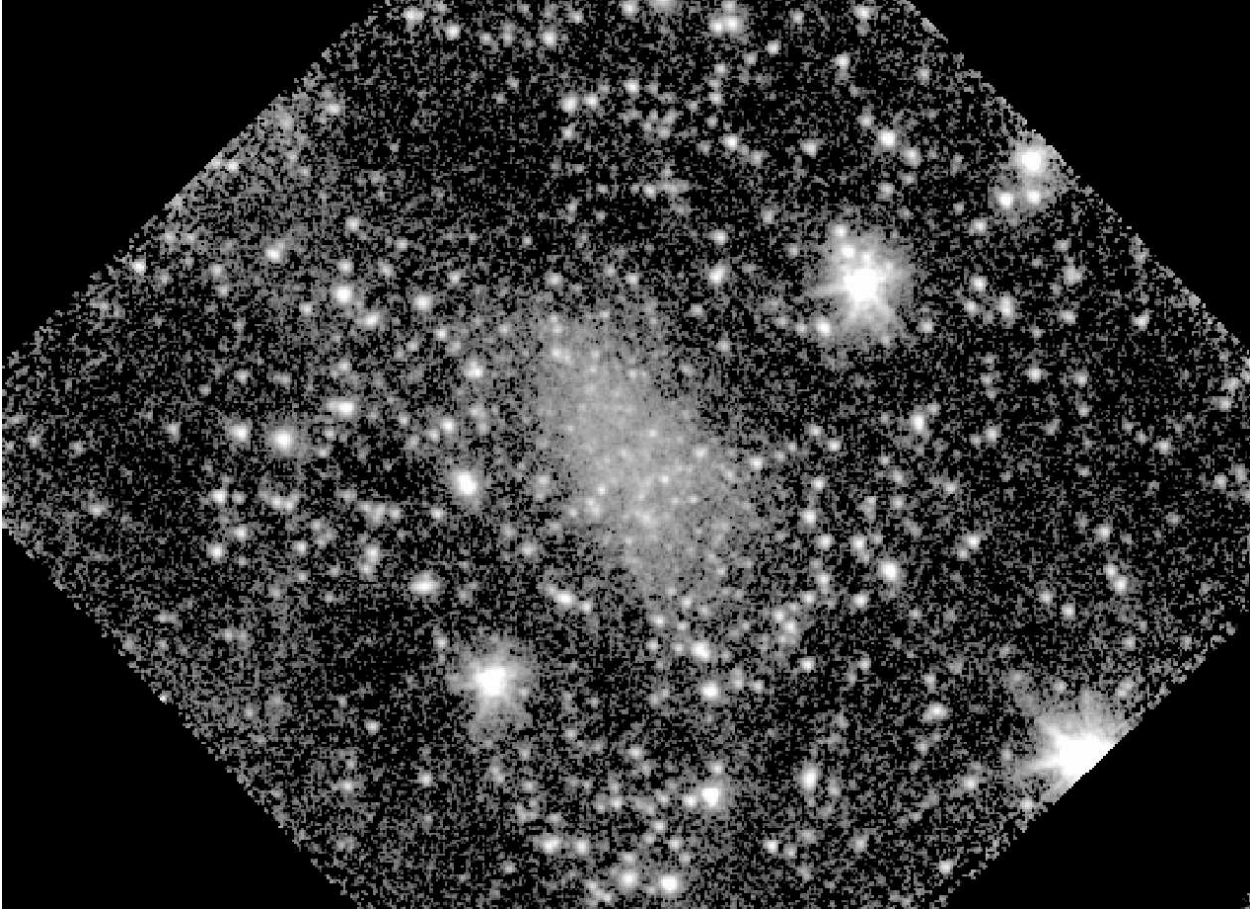


Fig. 1.130.— **NGC 4789A** - S⁴G mid-IR classification: Im ; Filter: IRAC 3.6 μ m; North: up, East: left; Field dimensions: 6.7 \times 4.9 arcmin; Surface brightness range displayed: 18.5–28.0 mag arcsec⁻²



Fig. 1.131.— **NGC 5018** - S⁴G mid-IR classification: SAB0⁻ (shells/ripples) pec ; Filter: IRAC 3.6 μ m; North: up, East: left; Field dimensions: 6.7 \times 4.9 arcmin; Surface brightness range displayed: 12.0–28.0 mag arcsec⁻²

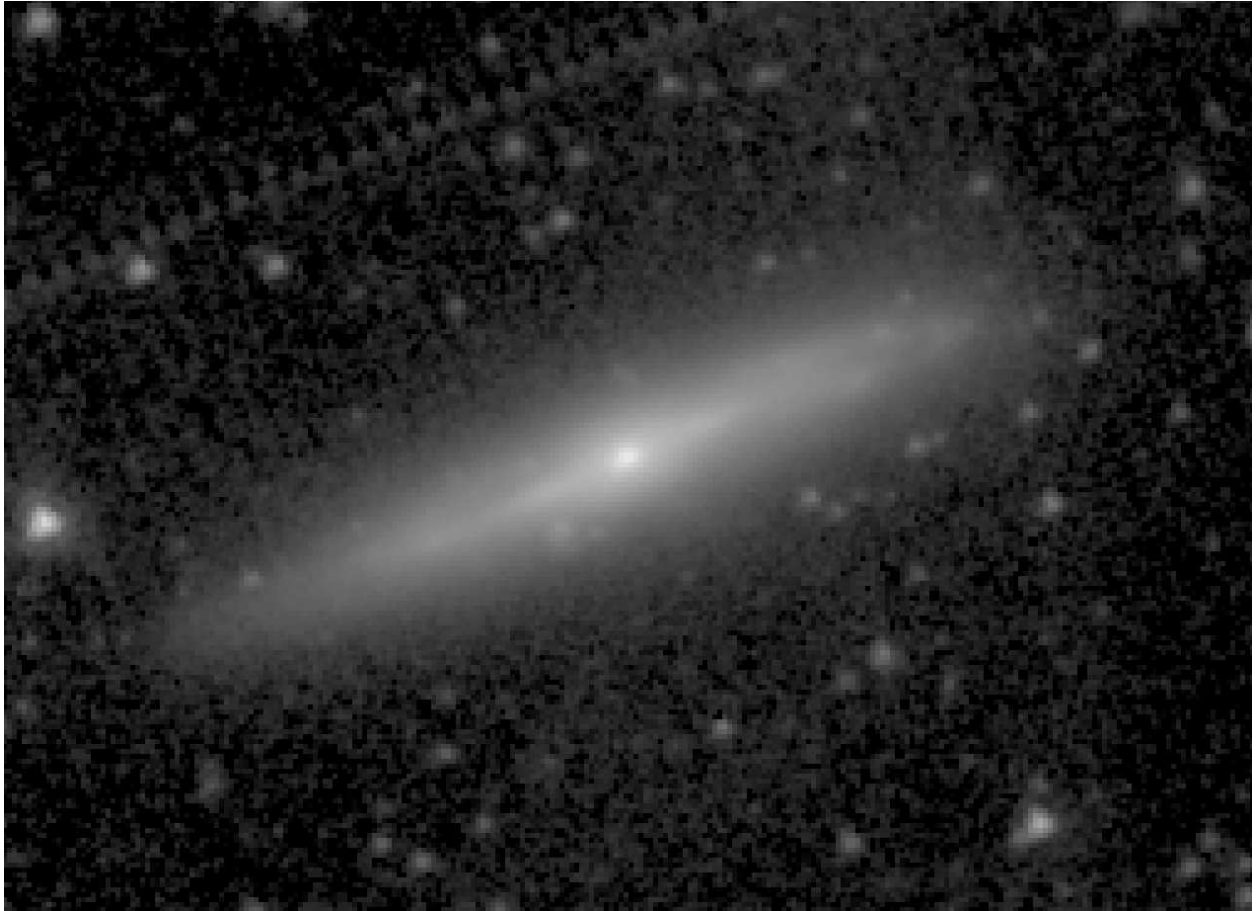


Fig. 1.132.— **NGC 5022** - S⁴G mid-IR classification: Sab sp ; Filter: IRAC 3.6 μ m; North: left, East: down; Field dimensions: 3.2 \times 2.3 arcmin; Surface brightness range displayed: 13.5–28.0 mag arcsec⁻²



Fig. 1.133.— **NGC 5055** - S⁴G mid-IR classification: SA(rs,rl)bc ; Filter: IRAC 3.6μm; North: up, East: left; Field dimensions: 12.6× 9.2 arcmin; Surface brightness range displayed: 12.0–28.0 mag arcsec⁻²



Fig. 1.134.— **NGC 5068** - S⁴G mid-IR classification: SB(rs)d ; Filter: IRAC 3.6 μ m; North: up, East: left; Field dimensions: 10.5 \times 7.7 arcmin; Surface brightness range displayed: 16.0–28.0 mag arcsec⁻²



Fig. 1.135.— **NGC 5173** - S⁴G mid-IR classification: E⁺1 ; Filter: IRAC 3.6 μ m; North: up, East: left; Field dimensions: 4.4 \times 3.2 arcmin; Surface brightness range displayed: 13.5–28.0 mag arcsec⁻²



Fig. 1.136.— **NGC 5194** (right) and **NGC 5195** (left) - S⁴G mid-IR classification: SAB(rs, nr)bc, SAB(r)0/a; Filter: IRAC 3.6 μm; North: left, East: down; Field dimensions: 17.5 × 12.8 arcmin; Surface brightness range displayed: 12.5–28.0 mag arcsec⁻²



Fig. 1.137.— **NGC 5216** (right) and **NGC 5218** (left) - S⁴G mid-IR classifications: E0(shells?) pec, SB(rs)a pec, respectively; Filter: IRAC 3.6 μ m; North: left, East: down; Field dimensions: 7.9 \times 5.7 arcmin; Surface brightness range displayed: 14.0–28.0 mag arcsec⁻²



Fig. 1.138.— **NGC 5248** - S⁴G mid-IR classification: SAB(s,nr)b_c ; Filter: IRAC 3.6 μ m; North: up, East: left; Field dimensions: 7.0 \times 5.1 arcmin; Surface brightness range displayed: 13.5–28.0 mag arcsec⁻²



Fig. 1.139.— **NGC 5338** - S⁴G mid-IR classification: SB(rs)0^o ; Filter: IRAC 3.6 μ m;
North: up, East: left; Field dimensions: 3.5 \times 2.6 arcmin; Surface brightness range displayed:
15.0–28.0 mag arcsec⁻²



Fig. 1.140.— **NGC 5350** - S⁴G mid-IR classification: SB(rs)ab ; Filter: IRAC 3.6μm; North: up, East: left; Field dimensions: 3.5× 2.6 arcmin; Surface brightness range displayed: 14.0–28.0 mag arcsec⁻²

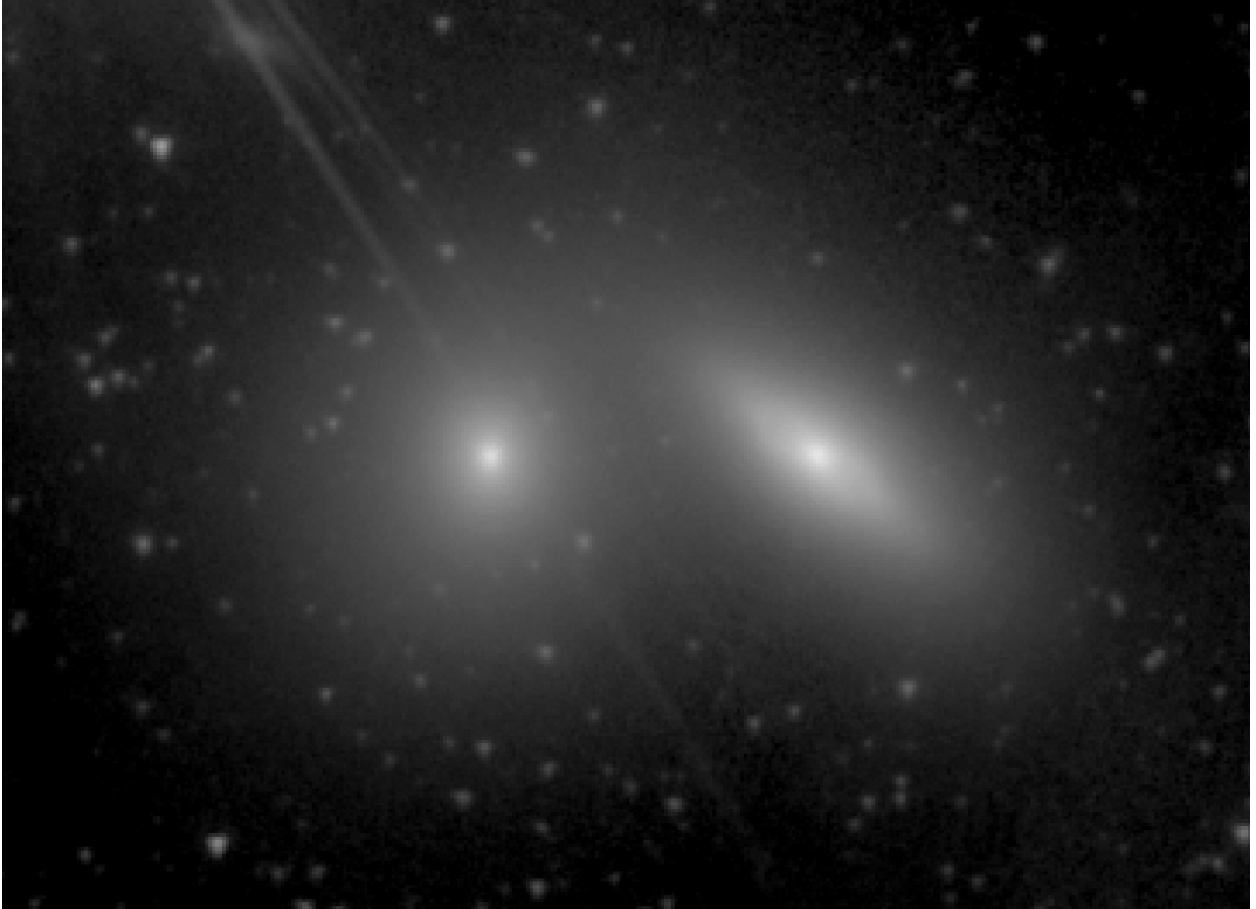


Fig. 1.141.— **NGC 5353** (right) and **NGC 5354** (left) - S⁴G mid-IR classifications: S0⁺ sp, SA0⁻, respectively; Filter: IRAC 3.6 μ m; North: left, East: down; Field dimensions: 4.5 \times 3.3 arcmin; Surface brightness range displayed: 12.5–28.0 mag arcsec⁻²



Fig. 1.142.— **NGC 5355** - S⁴G mid-IR classification: SAB(s)0^o ; Filter: IRAC 3.6μm;
North: up, East: left; Field dimensions: 2.6× 1.9 arcmin; Surface brightness range displayed:
14.0–28.0 mag arcsec⁻²

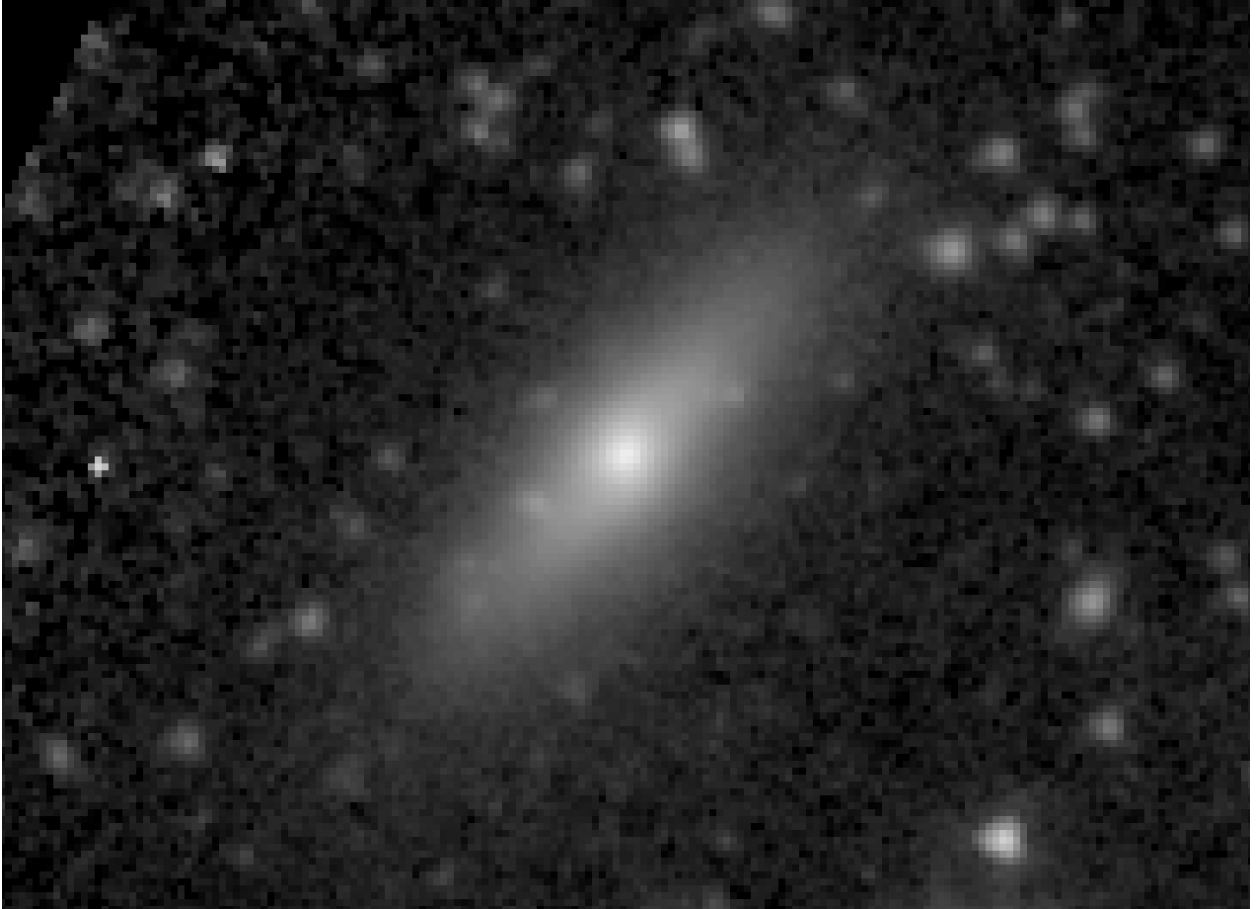


Fig. 1.143.— **NGC 5358** - S⁴G mid-IR classification: S0^o sp ; Filter: IRAC 3.6 μ m;
North: up, East: left; Field dimensions: 2.3 \times 1.6 arcmin; Surface brightness range displayed:
15.0–28.0 mag arcsec⁻²

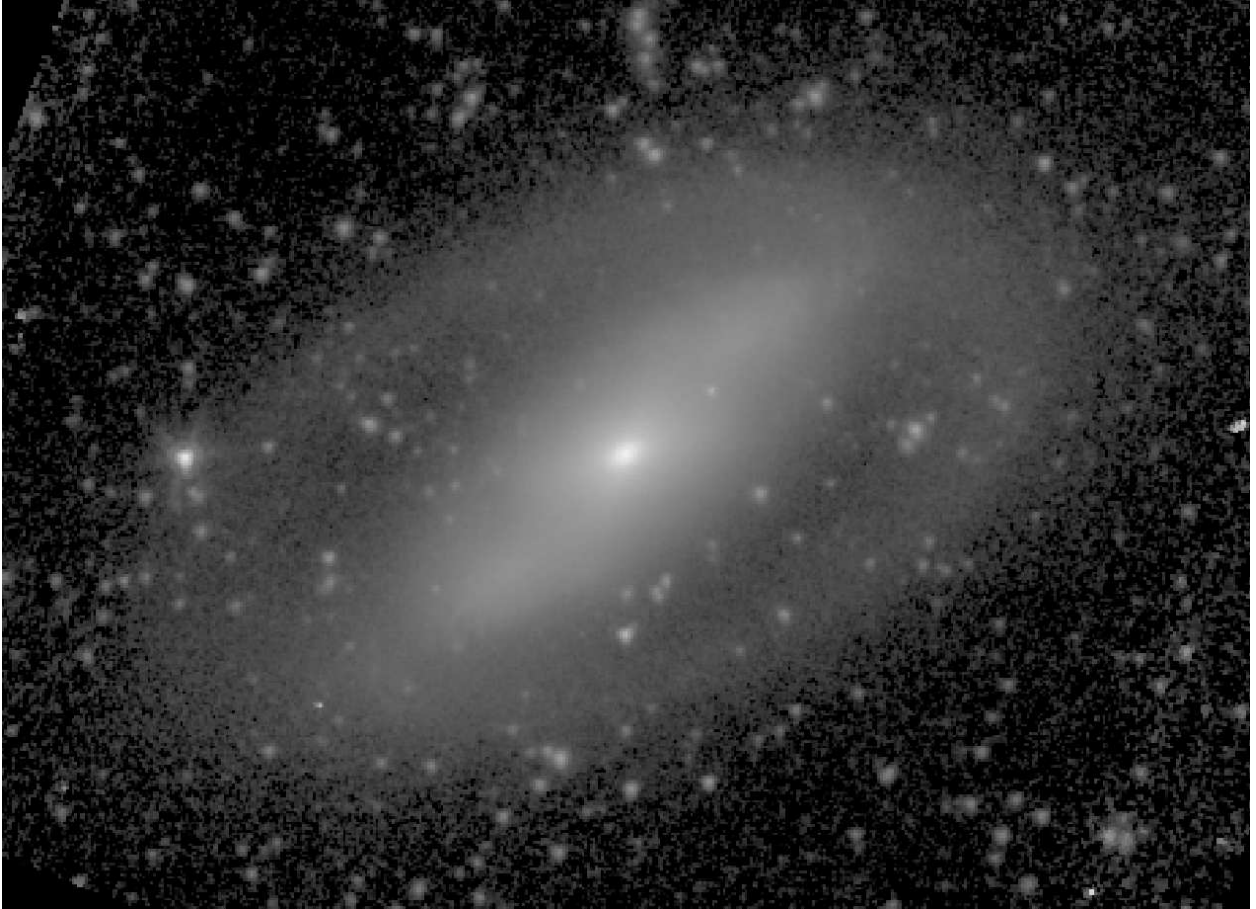


Fig. 1.144.— **NGC 5377** - S⁴G mid-IR classification: (R₁)SAB(s)0/a ; Filter: IRAC 3.6 μ m; North: left, East: down; Field dimensions: 5.8 \times 4.2 arcmin; Surface brightness range displayed: 13.0–28.0 mag arcsec⁻²



Fig. 1.145.— **NGC 5426** (right) and **NGC 5427** (left) - S⁴G mid-IR classifications: S**A**(rs)c, SA(r)bc, respectively; Filter: IRAC 3.6 μ m; North: left, East: down; Field dimensions: 6.3 \times 4.6 arcmin; Surface brightness range displayed: 13.5–28.0 mag arcsec⁻²

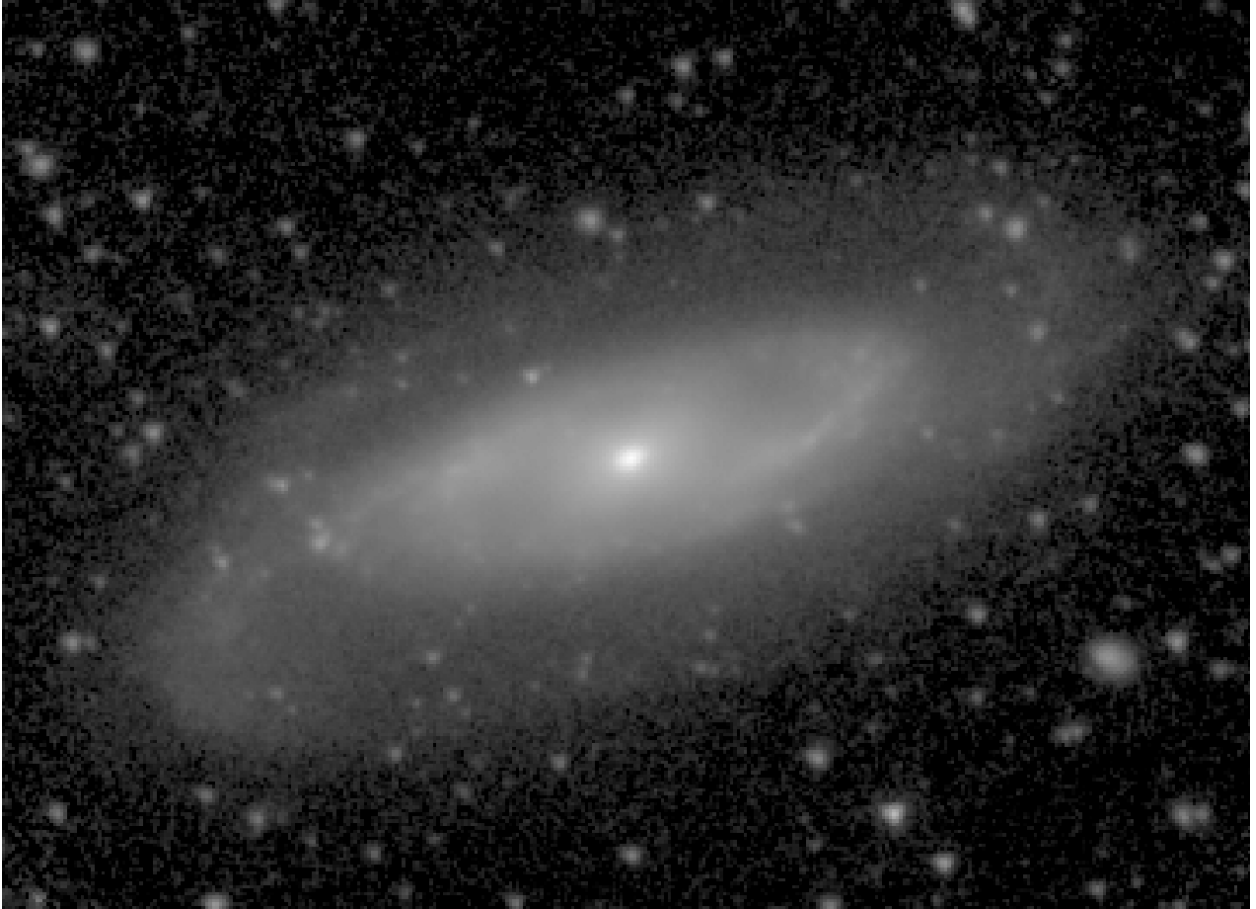


Fig. 1.146.— **NGC 5448** - S⁴G mid-IR classification: (R₁)SAB(rs)a ; Filter: IRAC 3.6μm; North: up, East: left; Field dimensions: 4.5 × 3.3 arcmin; Surface brightness range displayed: 13.0–28.0 mag arcsec⁻²

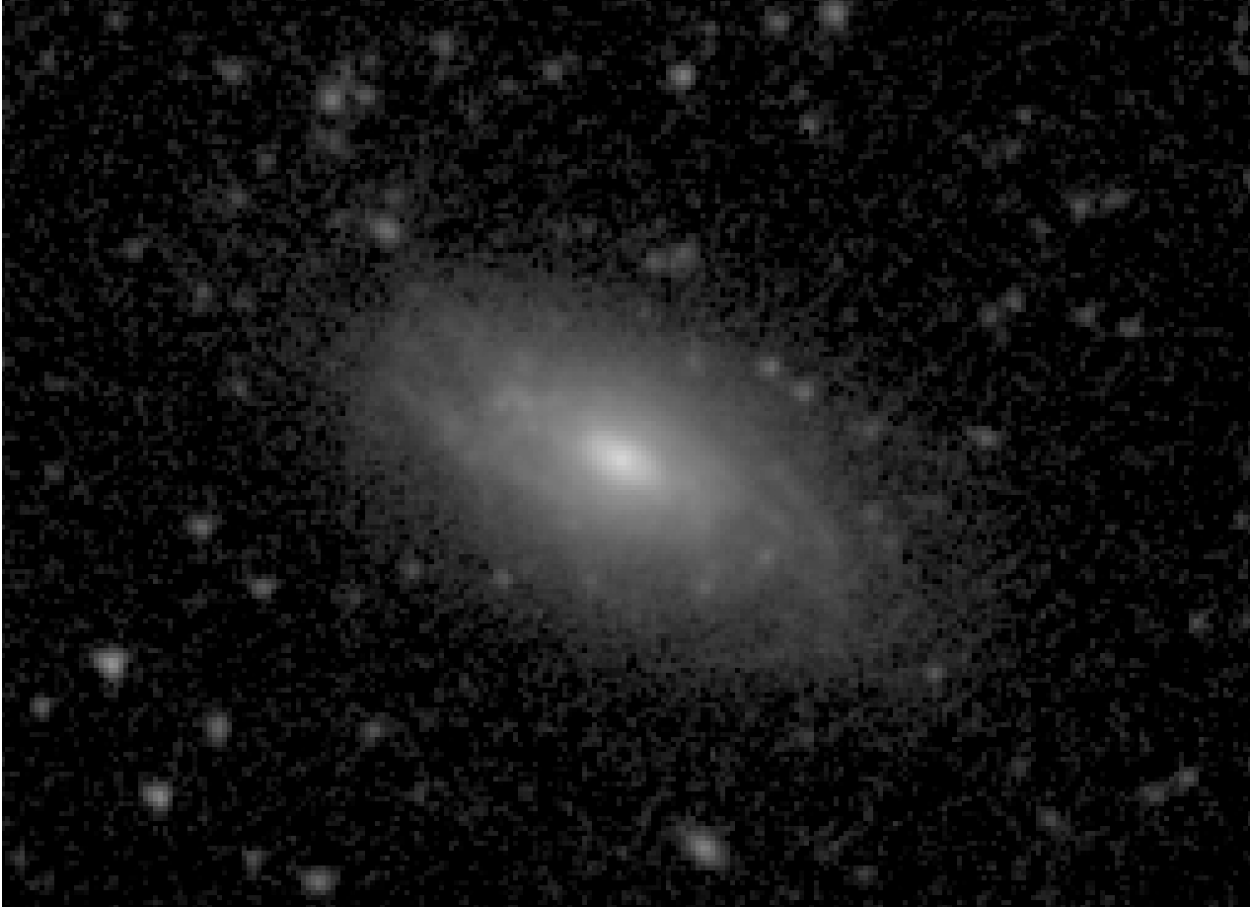


Fig. 1.147.— **NGC 5520** - S⁴G mid-IR classification: SA(l)bc ; Filter: IRAC 3.6 μ m;
North: up, East: left; Field dimensions: 2.3 \times 1.6 arcmin; Surface brightness range displayed:
14.0–28.0 mag arcsec⁻²

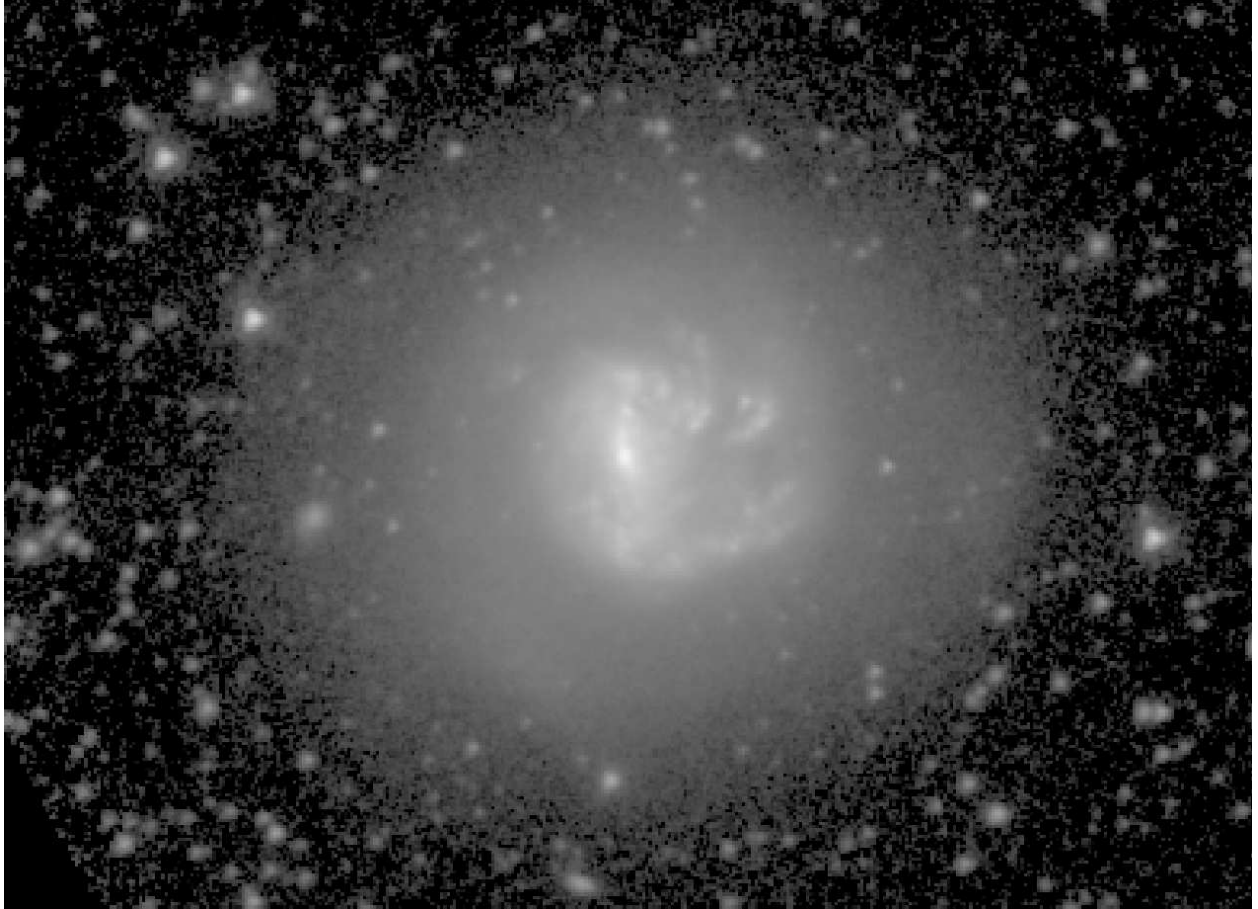


Fig. 1.148.— **NGC 5713** - S⁴G mid-IR classification: (R')SB(rs)ab: pec ; Filter: IRAC 3.6 μ m; North: left, East: down; Field dimensions: 4.9 \times 3.5 arcmin; Surface brightness range displayed: 13.0–28.0 mag arcsec⁻²

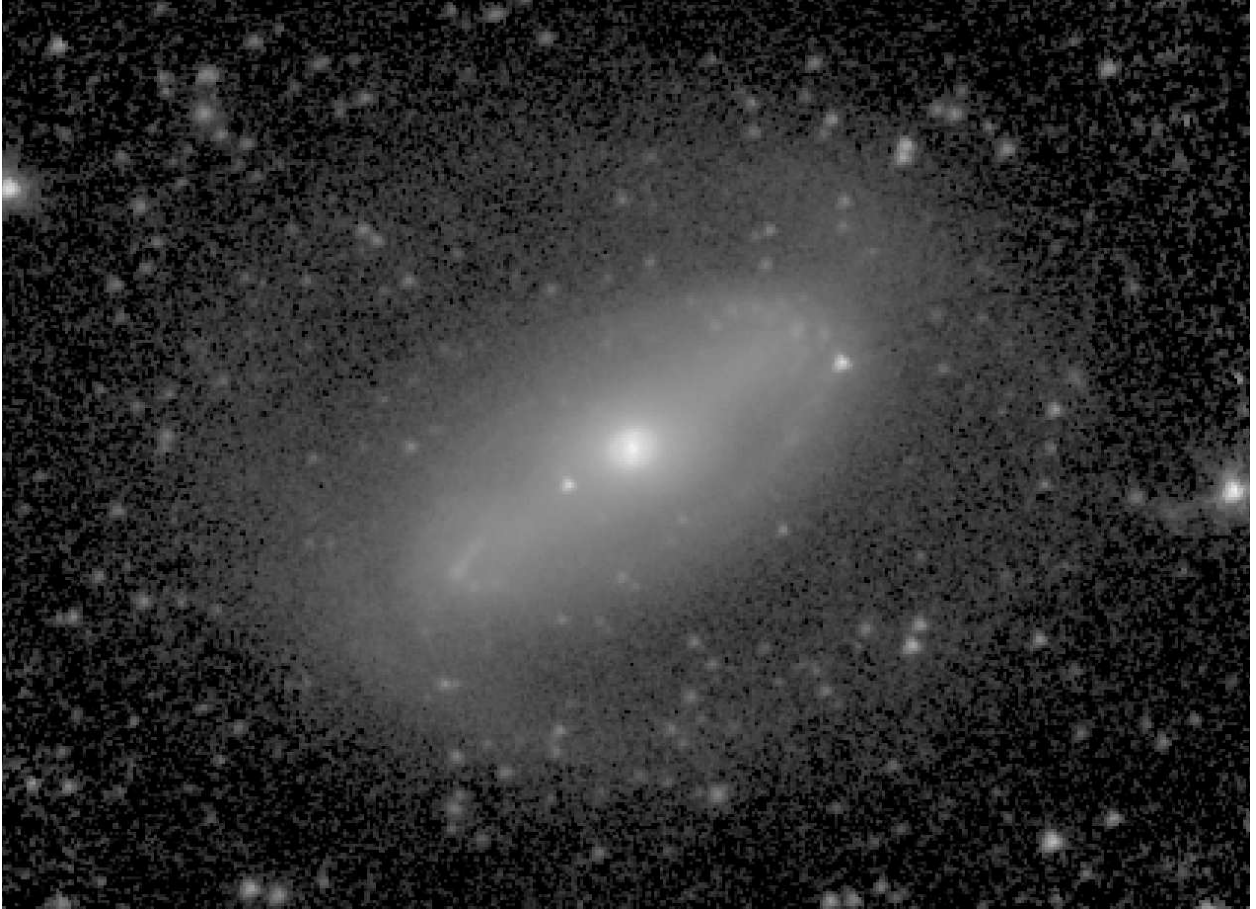


Fig. 1.149.— **NGC 5728** - S⁴G mid-IR classification: (R₁)SB(rs,nr,nb)0/a ; Filter: IRAC 3.6 μ m; North: left, East: down; Field dimensions: 5.3 \times 3.8 arcmin; Surface brightness range displayed: 13.0–28.0 mag arcsec⁻²

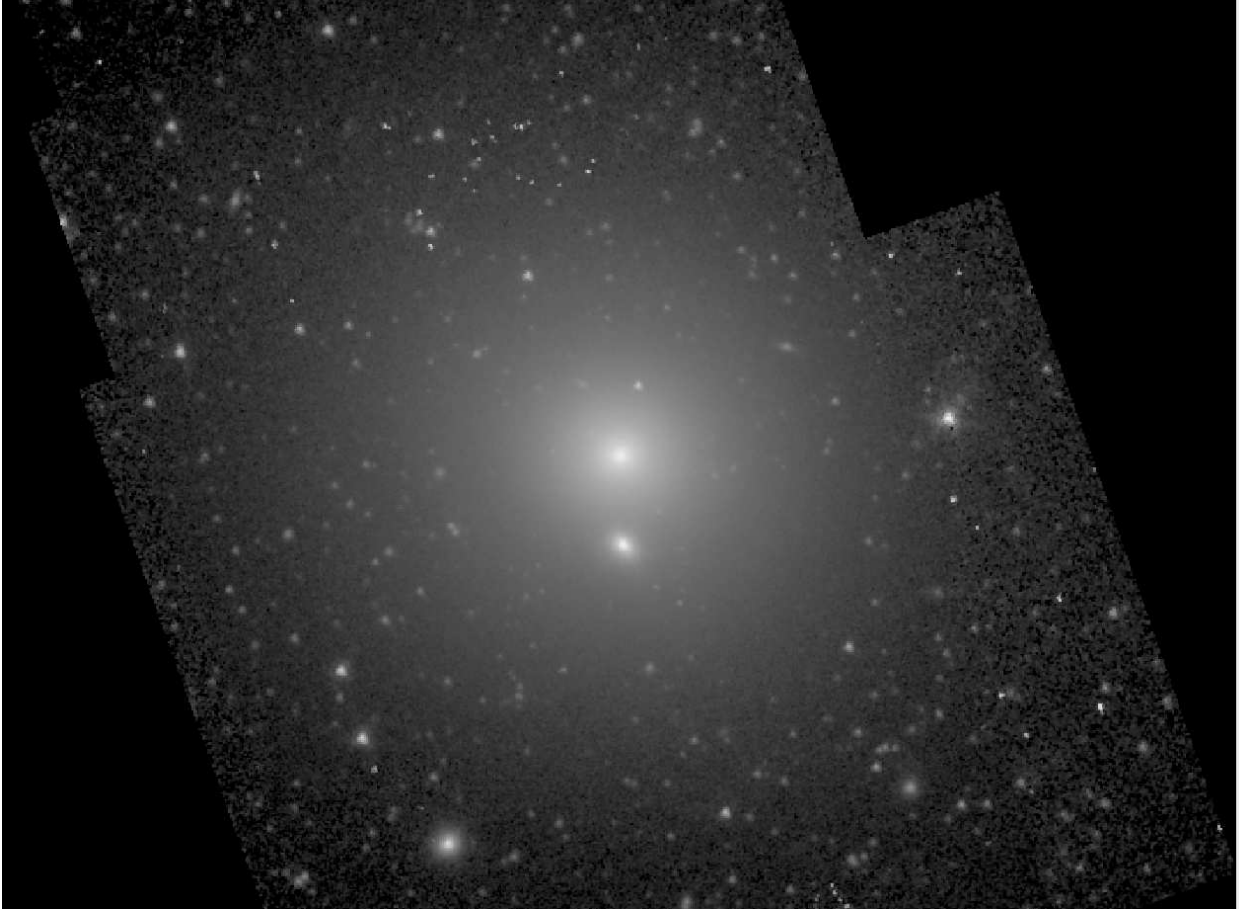


Fig. 1.150.— **NGC 5846** - S⁴G mid-IR classification: E⁺⁰/SA0⁻ ; Filter: IRAC 3.6μm;
North: up, East: left; Field dimensions: 8.9× 6.5 arcmin; Surface brightness range displayed:
13.5–28.0 mag arcsec⁻²



Fig. 1.151.— **NGC 5850** - S⁴G mid-IR classification: (R')SB(r,nr,nb)ab ; Filter: IRAC 3.6 μ m; North: left, East: down; Field dimensions: 7.0 \times 5.1 arcmin; Surface brightness range displayed: 13.5–28.0 mag arcsec⁻²

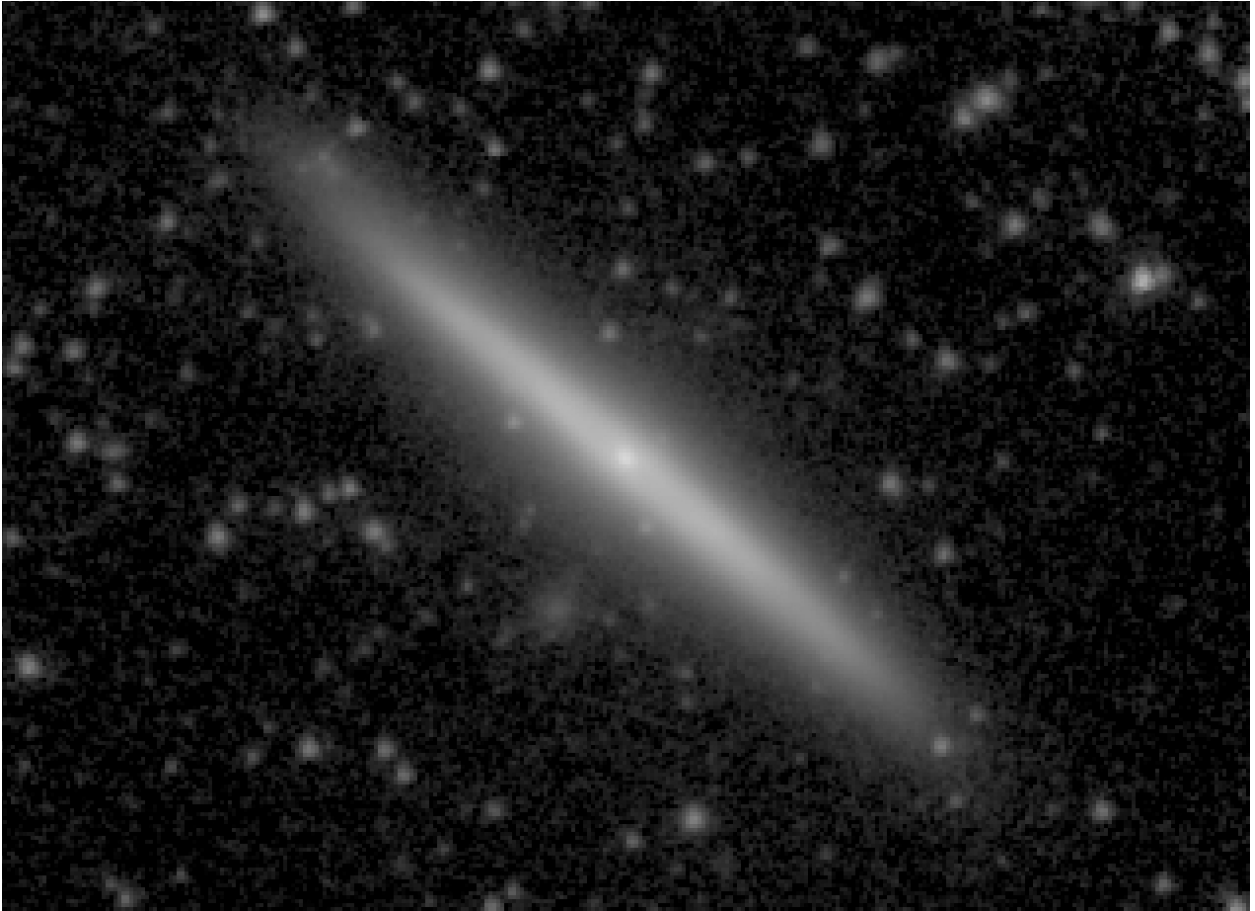


Fig. 1.152.— **NGC 5981** - S⁴G mid-IR classification: S0⁺ sp ; Filter: IRAC 3.6 μ m; North: left, East: down; Field dimensions: 4.0 \times 2.9 arcmin; Surface brightness range displayed: 14.5–28.0 mag arcsec⁻²



Fig. 1.153.— **NGC 5982** - S⁴G mid-IR classification: E2 ; Filter: IRAC 3.6 μ m; North: up, East: left; Field dimensions: 7.0 \times 5.1 arcmin; Surface brightness range displayed: 13.0–28.0 mag arcsec⁻²

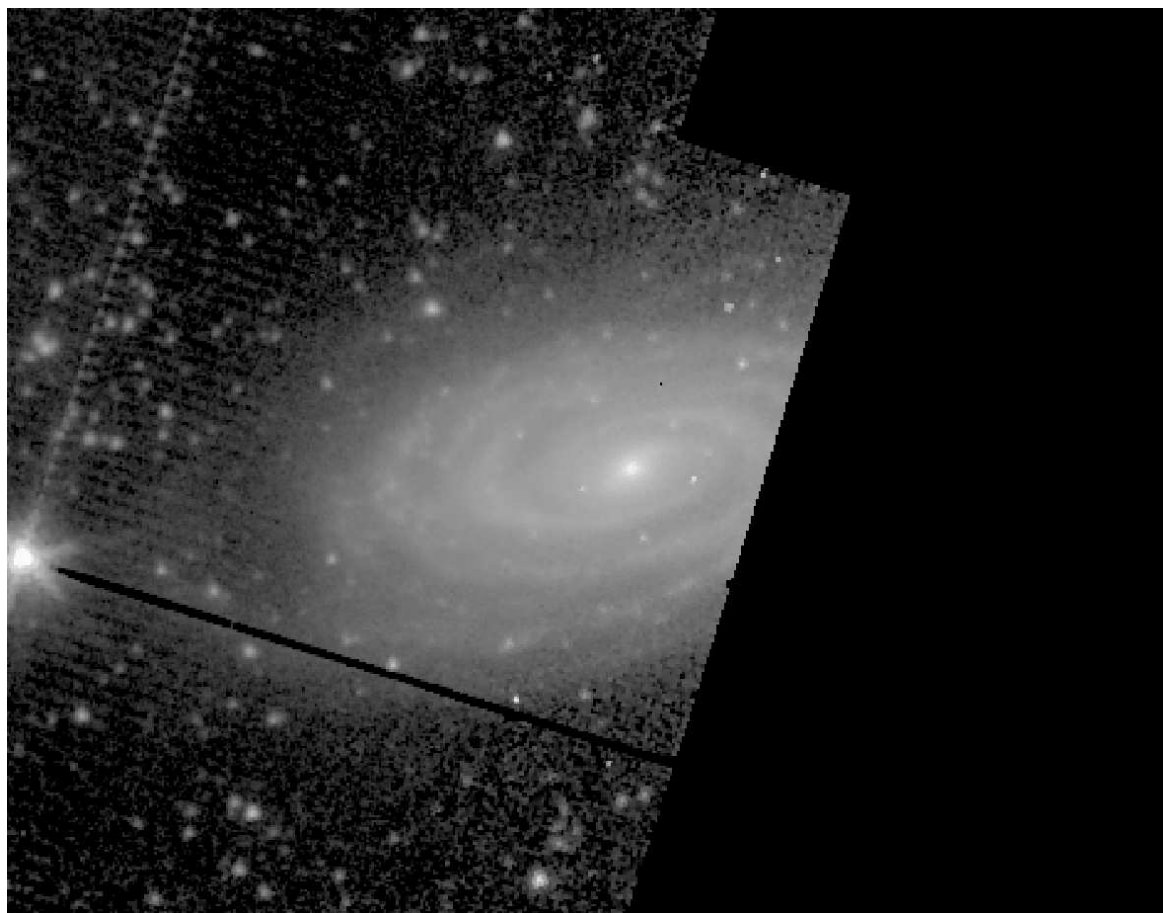


Fig. 1.154.— **NGC 5985** - S⁴G mid-IR classification: SAB(s)ab ; Filter: IRAC 3.6 μ m;
North: left, East: down; Field dimensions: 5.9 \times 4.3 arcmin; Surface brightness range displayed: 14.5–28.0 mag arcsec⁻²

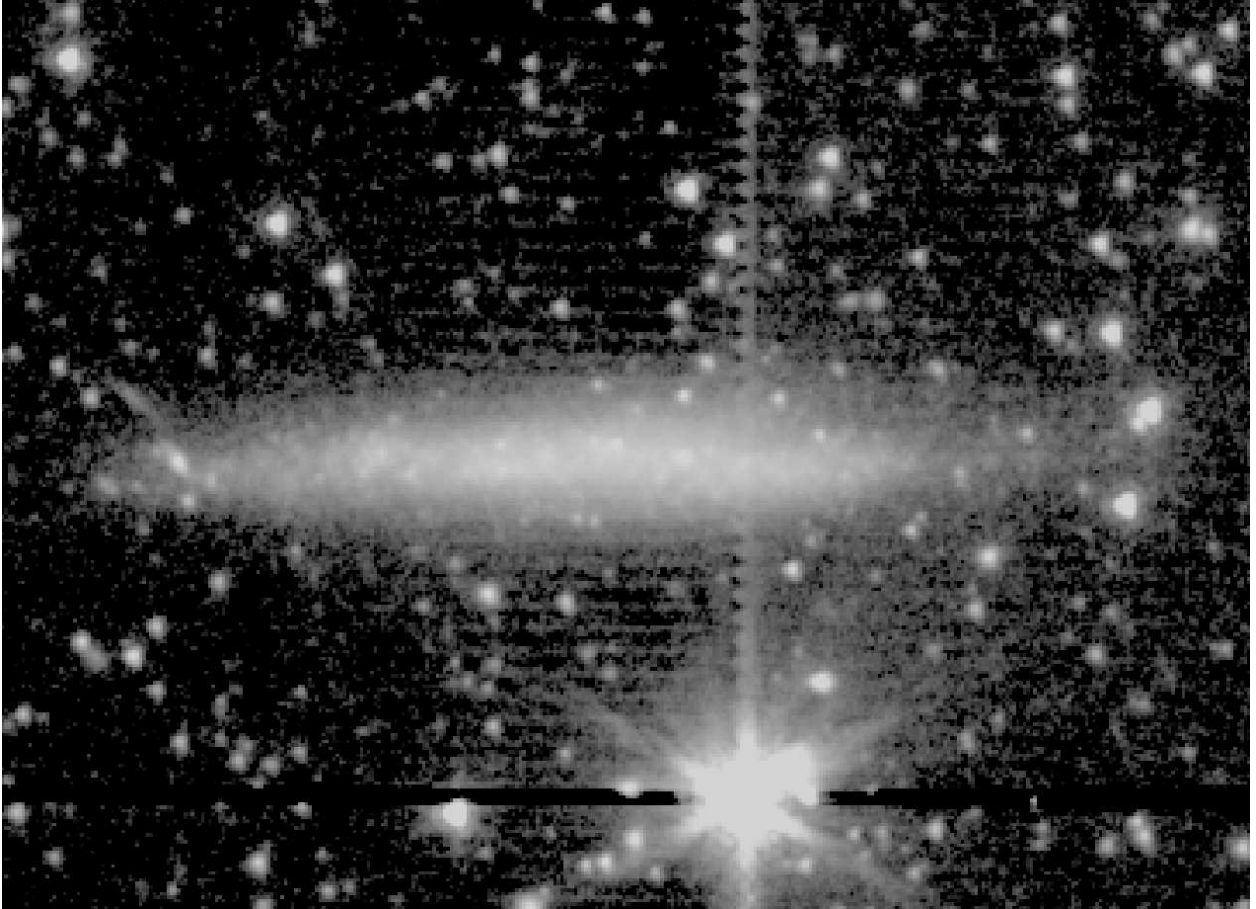


Fig. 1.155.— **NGC 7064** - S⁴G mid-IR classification: Sd sp ; Filter: IRAC 3.6 μ m; North: up, East: left; Field dimensions: 4.5 \times 3.3 arcmin; Surface brightness range displayed: 18.0–28.0 mag arcsec⁻²



Fig. 1.156.— **NGC 7479** - S⁴G mid-IR classification: (R')SB(s)b ; Filter: IRAC 3.6 μ m; North: left, East: down; Field dimensions: 5.8 \times 4.2 arcmin; Surface brightness range displayed: 12.0–28.0 mag arcsec⁻²

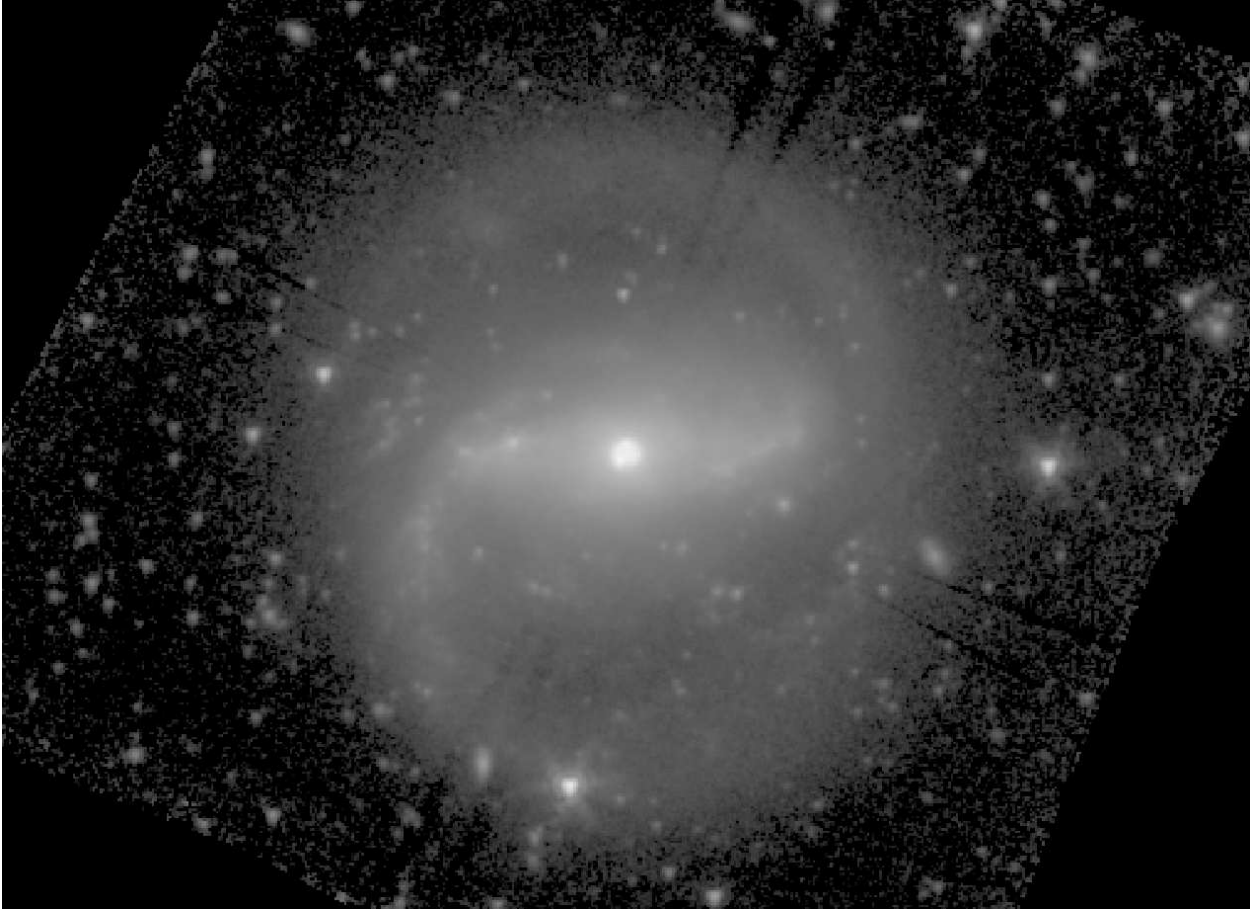


Fig. 1.157.— **NGC 7552** - S⁴G mid-IR classification: (R₁')SB(r₂,nr)a ; Filter: IRAC 3.6 μ m;
North: up, East: left; Field dimensions: 6.3 \times 4.6 arcmin; Surface brightness range displayed:
12.0–28.0 mag arcsec⁻²

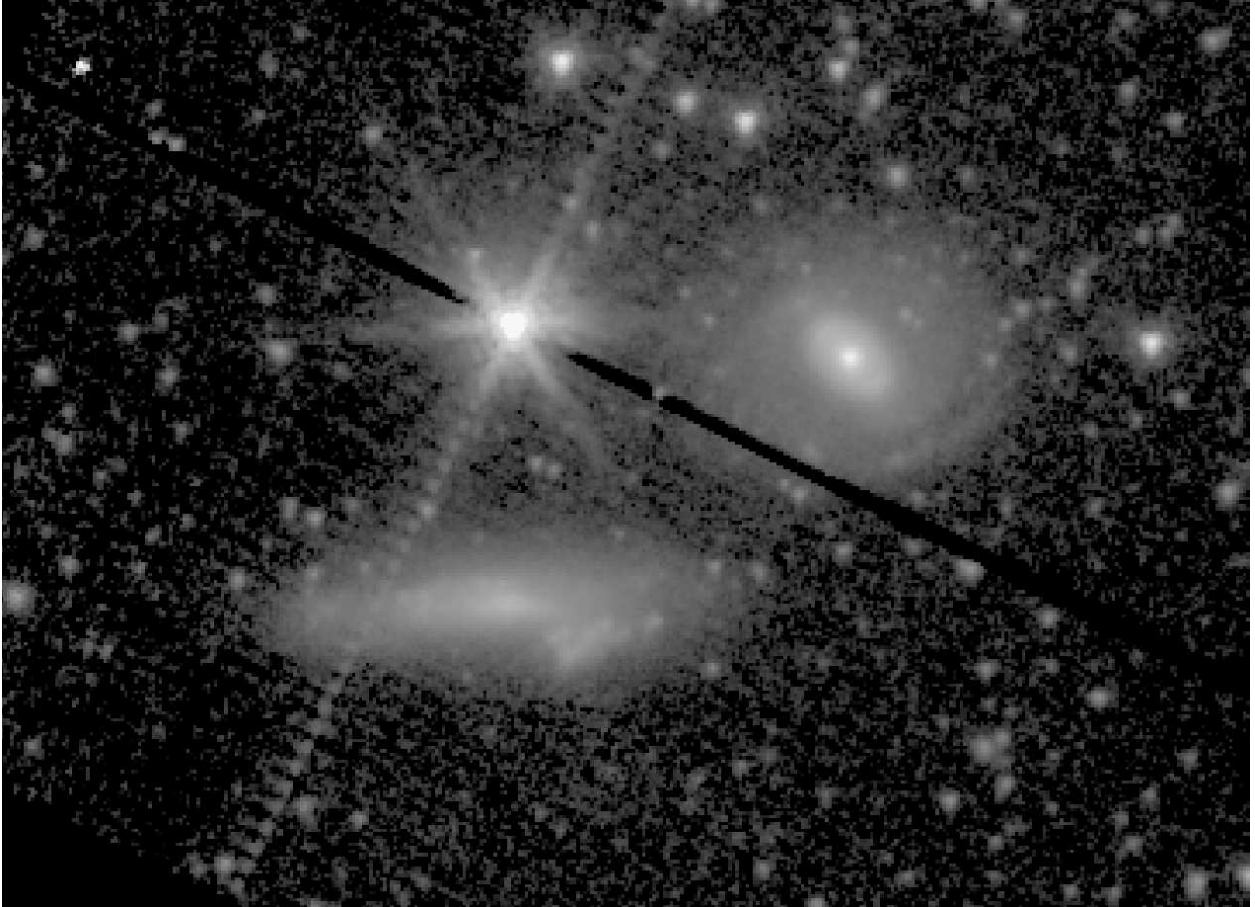


Fig. 1.158.— **NGC 7731** (upper right) and **NGC 7732** (lower left) - S⁴G mid-IR classifications: (R₁R'₂)SAB(r)a, SBd: sp, respectively; Filter: IRAC 3.6 μ m; North: up, East: left; Field dimensions: 4.5 \times 3.3 arcmin; Surface brightness range displayed: 14.0–28.0 mag arcsec⁻²

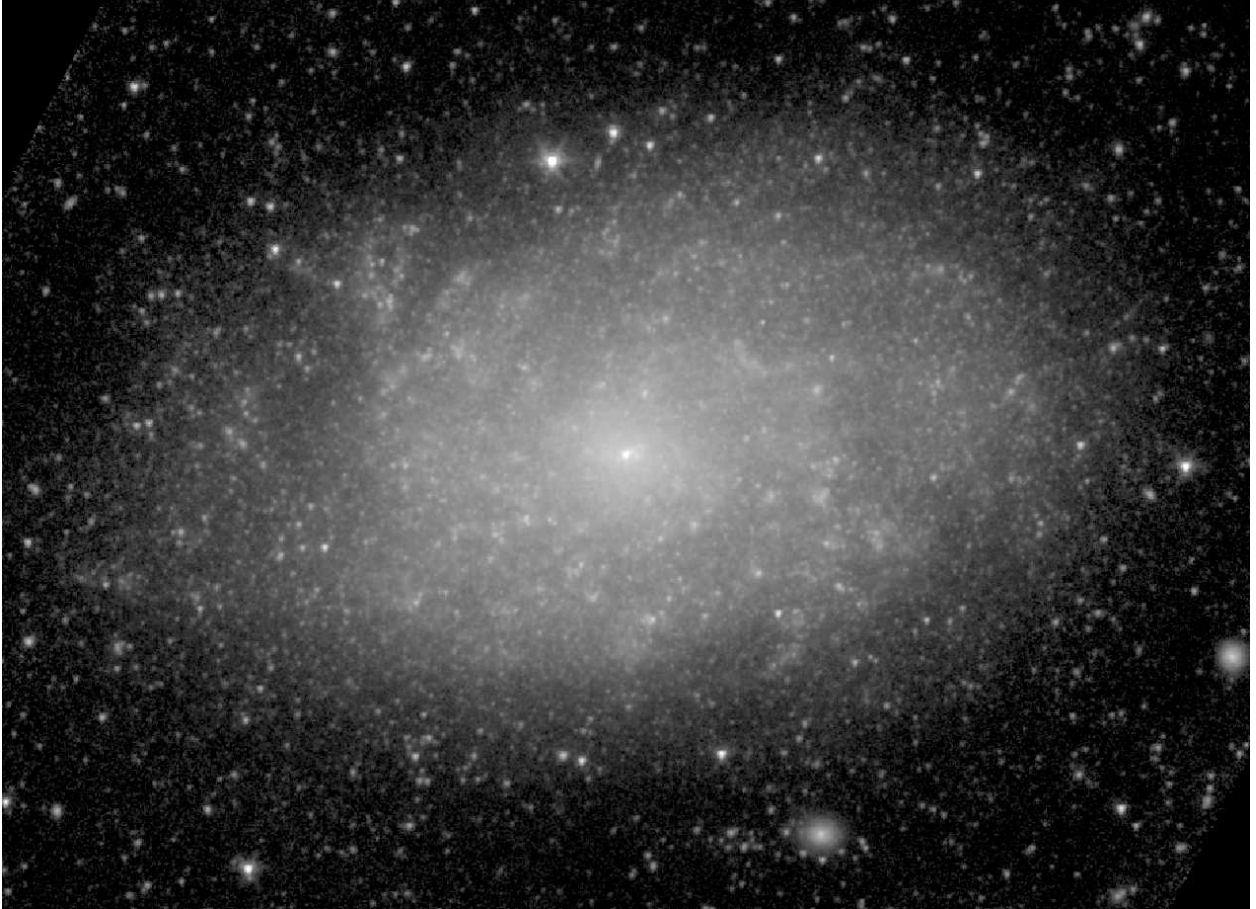


Fig. 1.159.— **NGC 7793** - S⁴G mid-IR classification: SA(s)c ; Filter: IRAC 3.6 μ m; North: up, East: left; Field dimensions: 11.7 \times 8.5 arcmin; Surface brightness range displayed: 14.0–28.0 mag arcsec⁻²

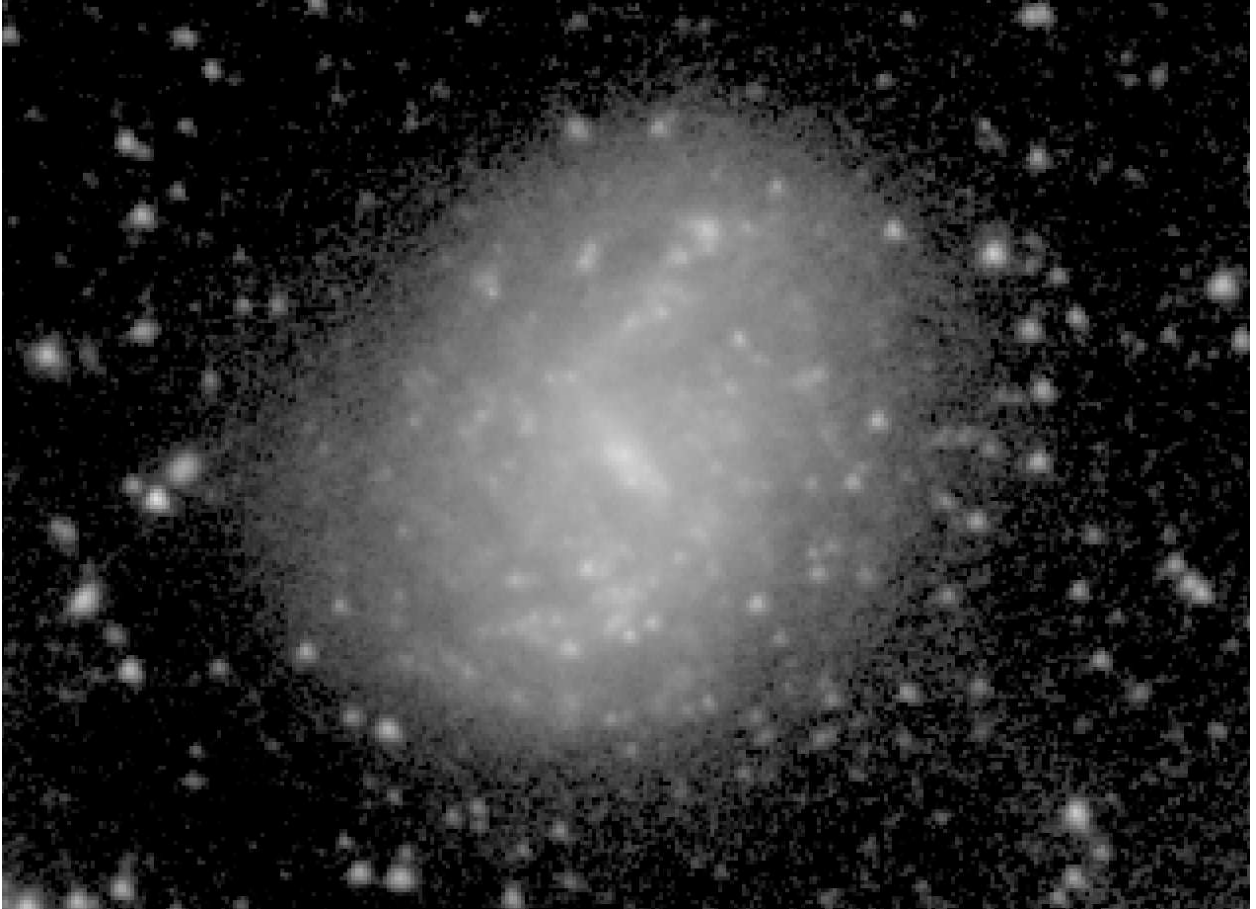


Fig. 1.160.— **IC 749** - S⁴G mid-IR classification: SB(rs)cd ; Filter: IRAC 3.6 μ m; North: up, East: left; Field dimensions: 4.0 \times 2.9 arcmin; Surface brightness range displayed: 16.5–28.0 mag arcsec⁻²

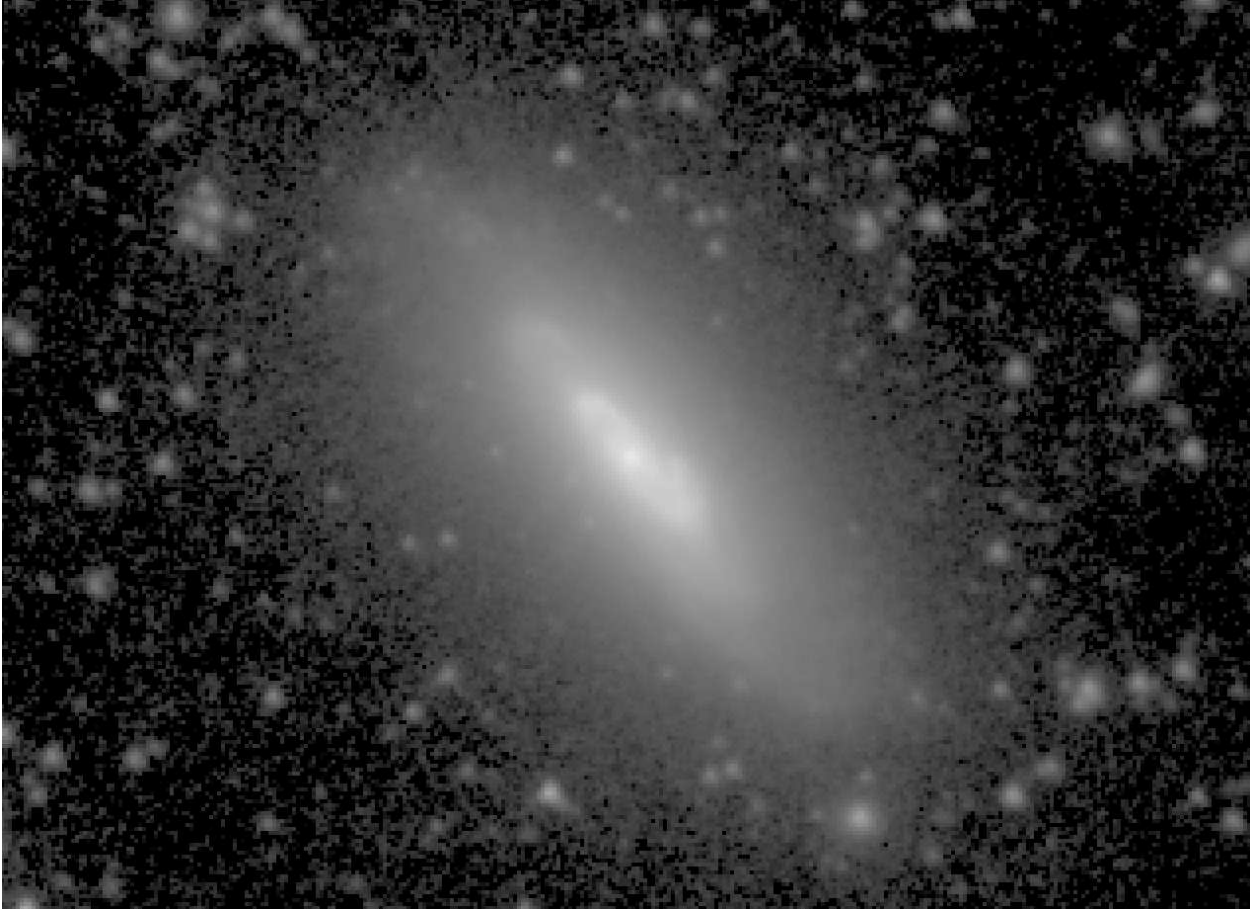


Fig. 1.161.— **IC 750** - S⁴G mid-IR classification: SA(s)a ; Filter: IRAC 3.6 μ m; North: up, East: left; Field dimensions: 4.0 \times 2.9 arcmin; Surface brightness range displayed: 13.0–28.0 mag arcsec⁻²

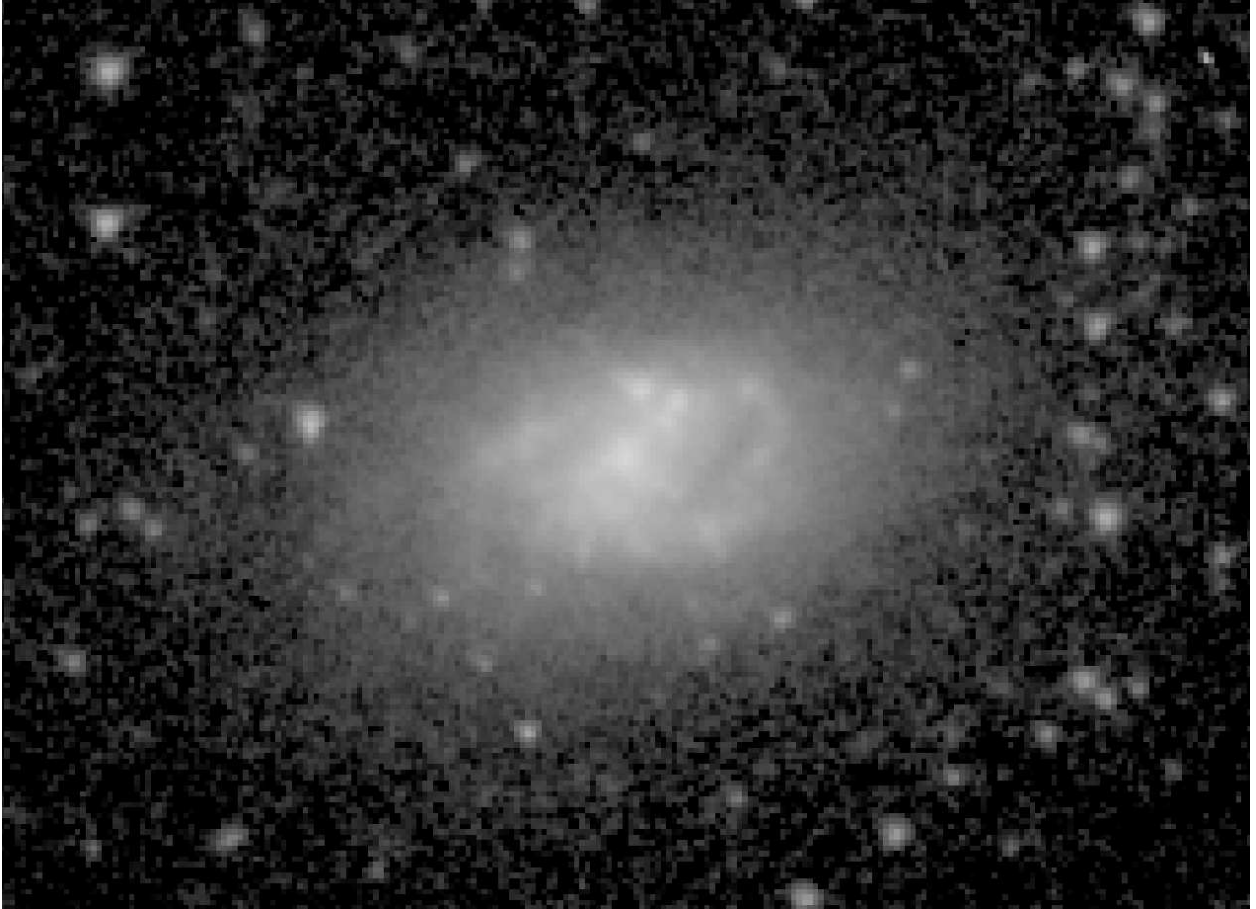


Fig. 1.162.— **IC 797** - S⁴G mid-IR classification: SAB(s)dm: ; Filter: IRAC 3.6μm; North: up, East: left; Field dimensions: 2.9× 2.1 arcmin; Surface brightness range displayed: 17.0–28.0 mag arcsec⁻²

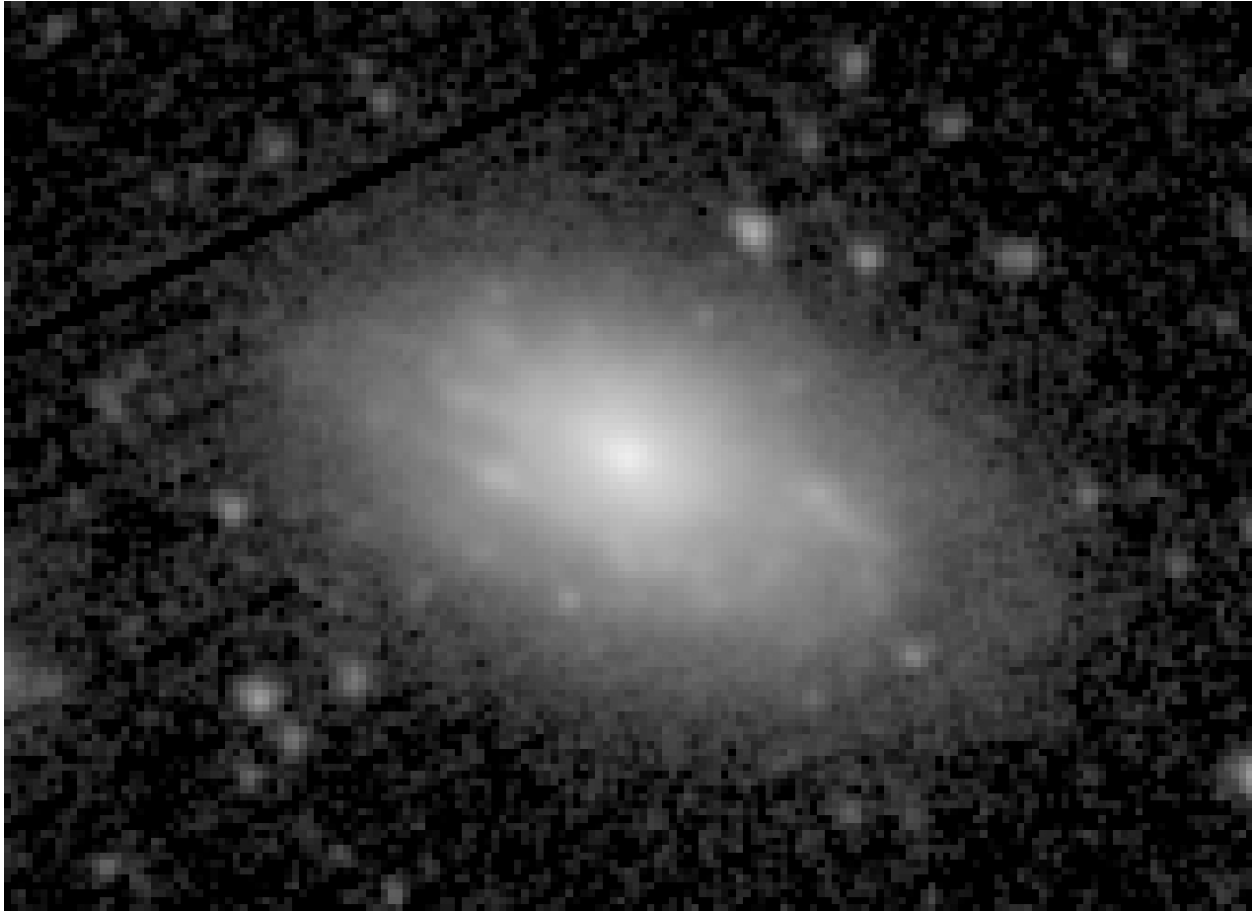


Fig. 1.163.— **IC 1066** - S⁴G mid-IR classification: SAbc: ; Filter: IRAC 3.6 μ m; North: up, East: left; Field dimensions: 2.1 \times 1.5 arcmin; Surface brightness range displayed: 16.0–28.0 mag arcsec⁻²

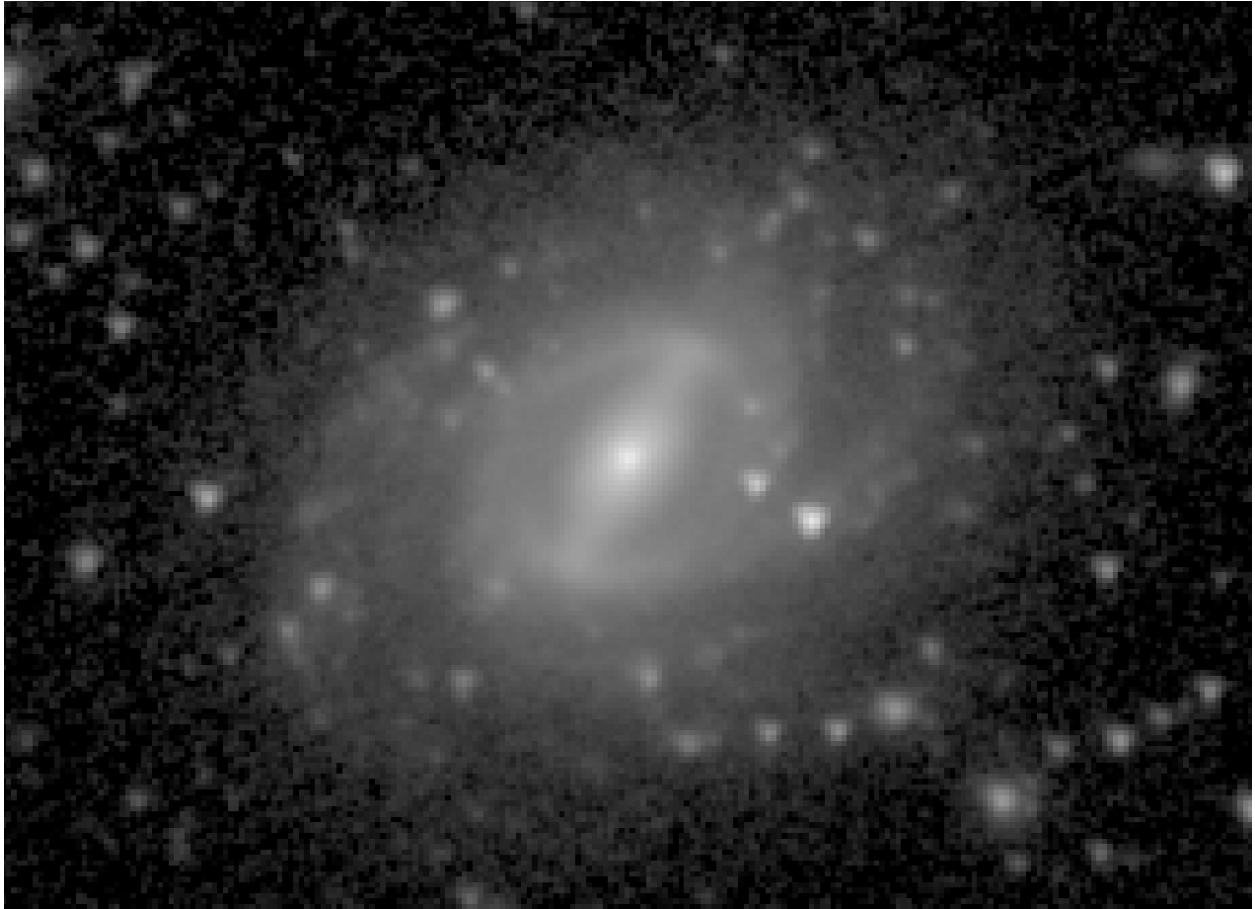


Fig. 1.164.— **IC 1067** - S⁴G mid-IR classification: SB(r)b ; Filter: IRAC 3.6 μ m; North: up, East: left; Field dimensions: 2.9 \times 2.1 arcmin; Surface brightness range displayed: 14.5–28.0 mag arcsec⁻²

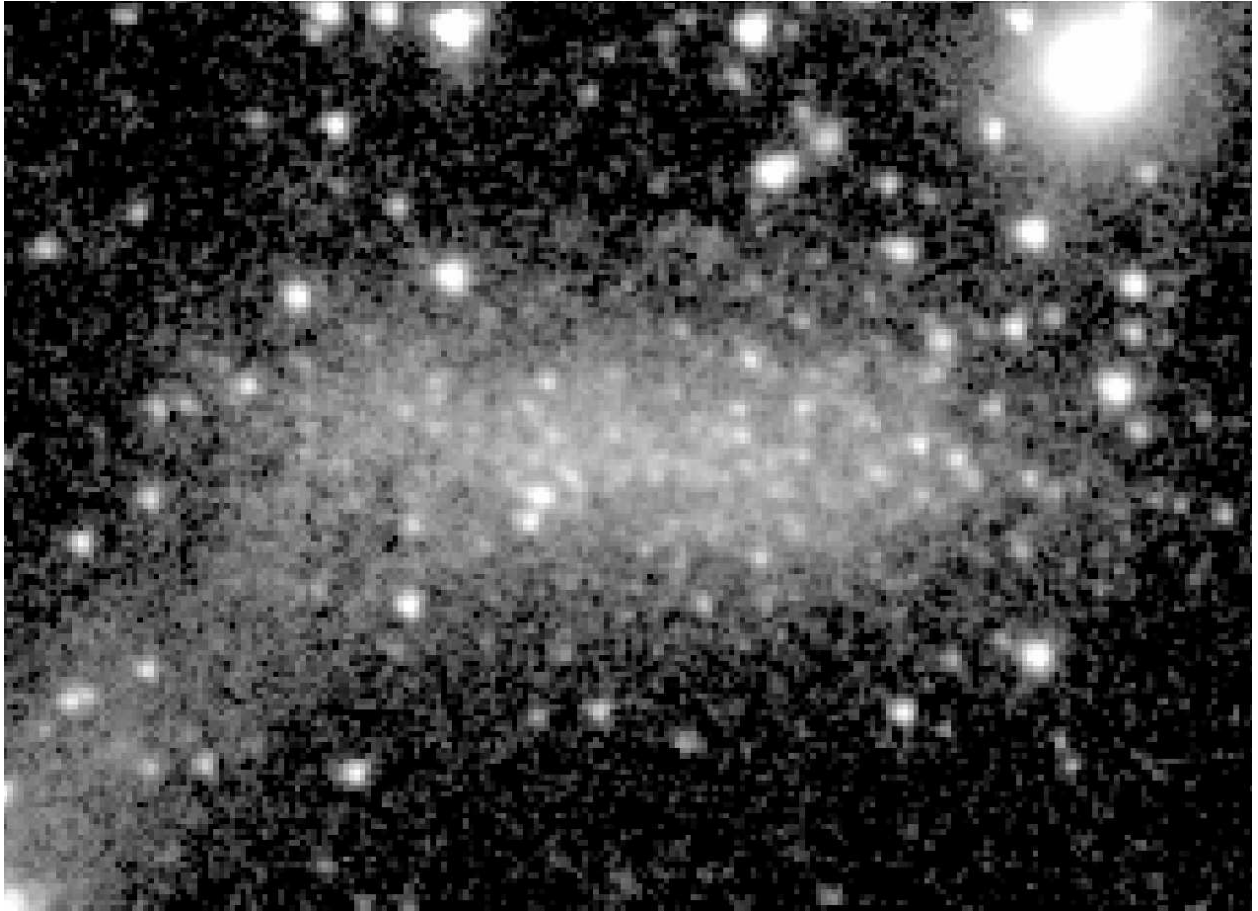


Fig. 1.165.— **IC 1574** - S⁴G mid-IR classification: IBm sp? ; Filter: IRAC 3.6 μ m; North: left, East: down; Field dimensions: 2.9 \times 2.1 arcmin; Surface brightness range displayed: 18.5–28.0 mag arcsec⁻²



Fig. 1.166.— **IC 1727** - S⁴G mid-IR classification: SB(s)m ; Filter: IRAC 3.6 μ m; North: left, East: down; Field dimensions: 7.2 \times 5.2 arcmin; Surface brightness range displayed: 18.5–28.0 mag arcsec⁻²



Fig. 1.167.— **IC 1959** - S⁴G mid-IR classification: SBd sp ; Filter: IRAC 3.6 μ m; North: left, East: down; Field dimensions: 3.5 \times 2.6 arcmin; Surface brightness range displayed: 17.5–27.0 mag arcsec⁻²



Fig. 1.168.— **IC 2233** - S⁴G mid-IR classification: SBdm sp ; Filter: IRAC 3.6 μ m; North: left, East: down; Field dimensions: 5.7 \times 4.2 arcmin; Surface brightness range displayed: 17.5–28.0 mag arcsec⁻²



Fig. 1.169.— **IC 2574** - S⁴G mid-IR classification: IB(s)m ; Filter: IRAC 3.6 μ m; North: up, East: left; Field dimensions: 15.8 \times 11.5 arcmin; Surface brightness range displayed: 18.5–28.0 mag arcsec⁻²

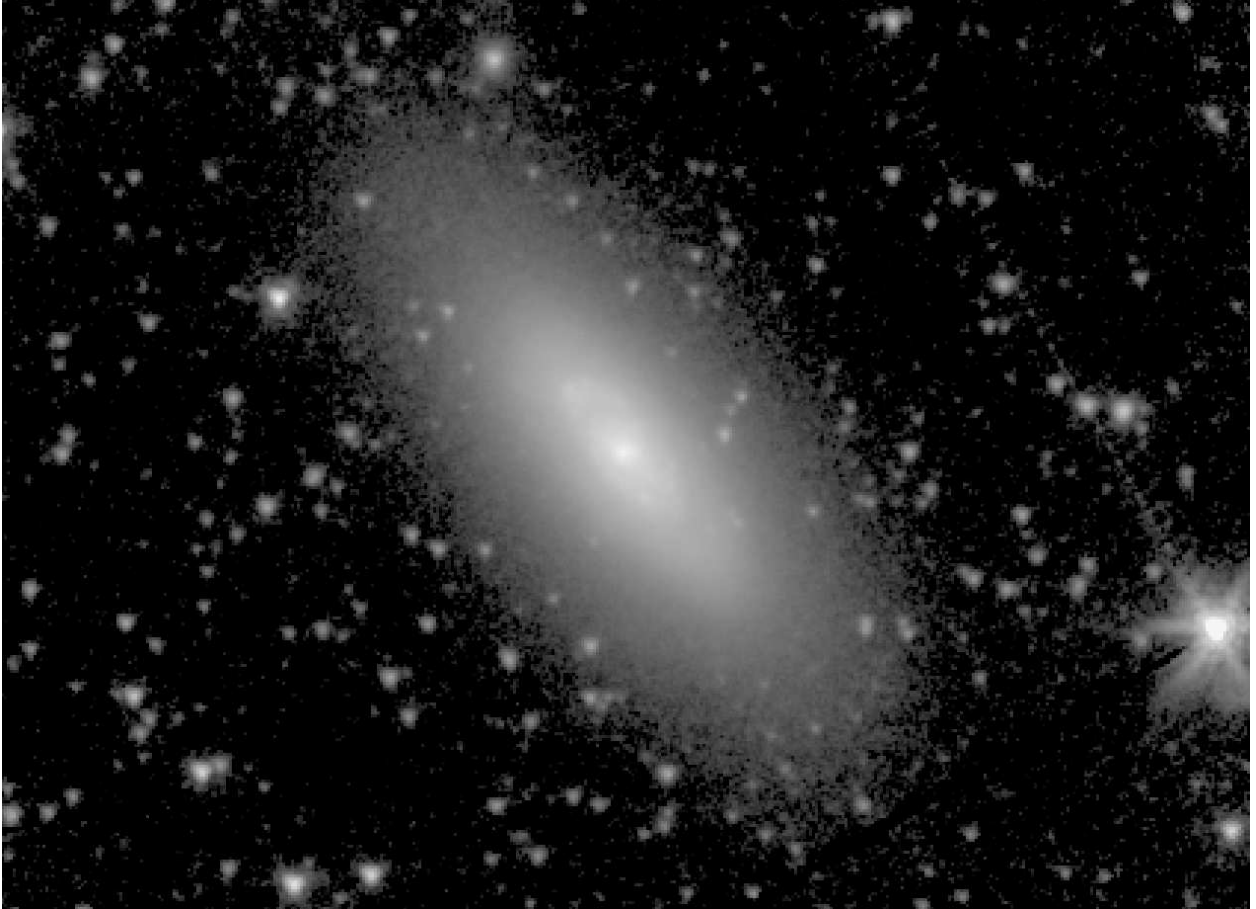


Fig. 1.170.— **IC 3392** - S⁴G mid-IR classification: SA(rs)ab ; Filter: IRAC 3.6 μ m; North: up, East: left; Field dimensions: 5.3 \times 3.8 arcmin; Surface brightness range displayed: 15.0–28.0 mag arcsec⁻²



Fig. 1.171.— **IC 4182** - S⁴G mid-IR classification: SA(s)m ; Filter: IRAC 3.6 μ m; North: up, East: left; Field dimensions: 7.9 \times 5.8 arcmin; Surface brightness range displayed: 18.5–28.0 mag arcsec⁻²



Fig. 1.172.— **IC 4951** - S⁴G mid-IR classification: SB(s)dm: sp ; Filter: IRAC 3.6 μ m;
North: left, East: down; Field dimensions: 3.5 \times 2.6 arcmin; Surface brightness range displayed: 18.0–28.0 mag arcsec⁻²



Fig. 1.173.— **IC 5052** - S⁴G mid-IR classification: Sd sp ; Filter: IRAC 3.6 μ m; North: left, East: down; Field dimensions: 7.0 \times 5.1 arcmin; Surface brightness range displayed: 16.5–28.0 mag arcsec⁻²



Fig. 1.174.— **IC 5332** - S⁴G mid-IR classification: SAB(s)cd ; Filter: IRAC 3.6μm; North: up, East: left; Field dimensions: 10.5× 7.7 arcmin; Surface brightness range displayed: 17.0–28.0 mag arcsec⁻²



Fig. 1.175.— **PGC 6667** - S⁴G mid-IR classification: SB(s)dm ; Filter: IRAC 3.6 μ m;
North: up, East: left; Field dimensions: 4.0 \times 2.9 arcmin; Surface brightness range displayed:
17.5–28.0 mag arcsec⁻²

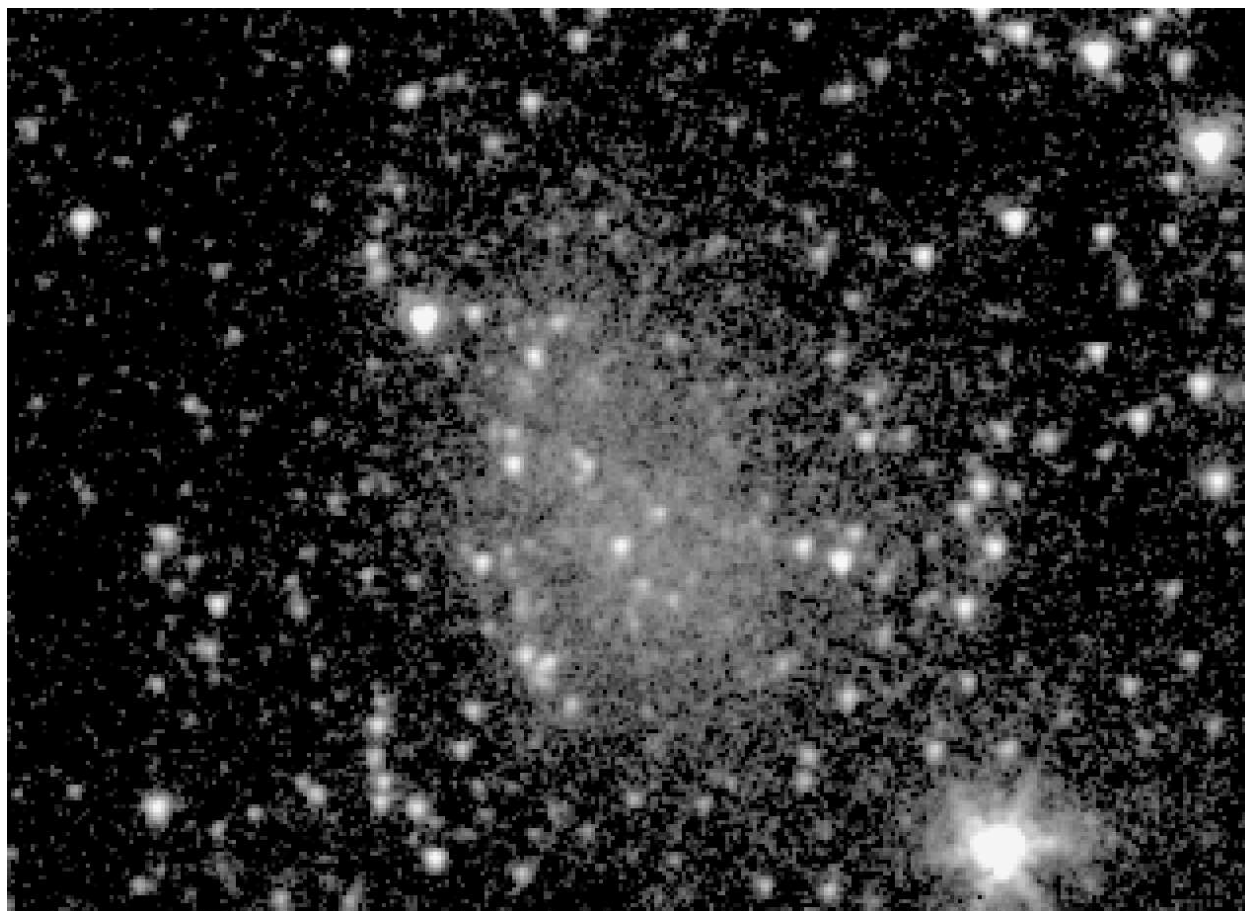


Fig. 1.176.— **UGC 1176** - S⁴G mid-IR classification: Im ; Filter: IRAC 3.6 μ m; North: up, East: left; Field dimensions: 4.0 \times 2.9 arcmin; Surface brightness range displayed: 18.5–28.0 mag arcsec⁻²



Fig. 1.177.— **UGC 4305** - S⁴G mid-IR classification: Im ; Filter: IRAC 3.6 μ m; North: up, East: left; Field dimensions: 10.5 \times 7.7 arcmin; Surface brightness range displayed: 18.5–28.0 mag arcsec⁻²

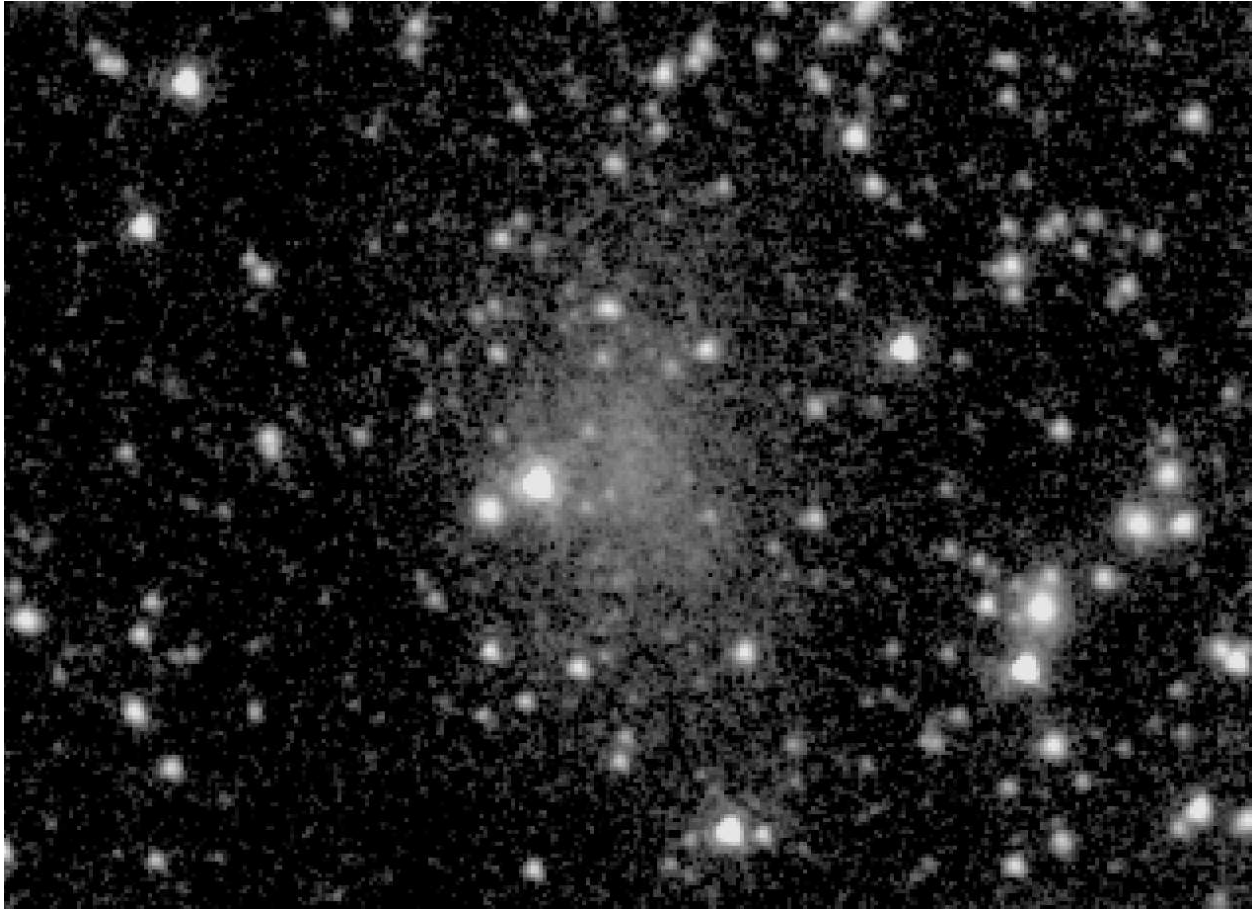


Fig. 1.178.— **UGC 4426** - S⁴G mid-IR classification: Im ; Filter: IRAC 3.6 μ m; North: up, East: left; Field dimensions: 3.9 \times 2.9 arcmin; Surface brightness range displayed: 18.5–28.0 mag arcsec⁻²



Fig. 1.179.— **UGC 5139** - S⁴G mid-IR classification: Im ; Filter: IRAC 3.6 μ m; North: up, East: left; Field dimensions: 5.3 \times 3.8 arcmin; Surface brightness range displayed: 18.0–28.0 mag arcsec⁻²

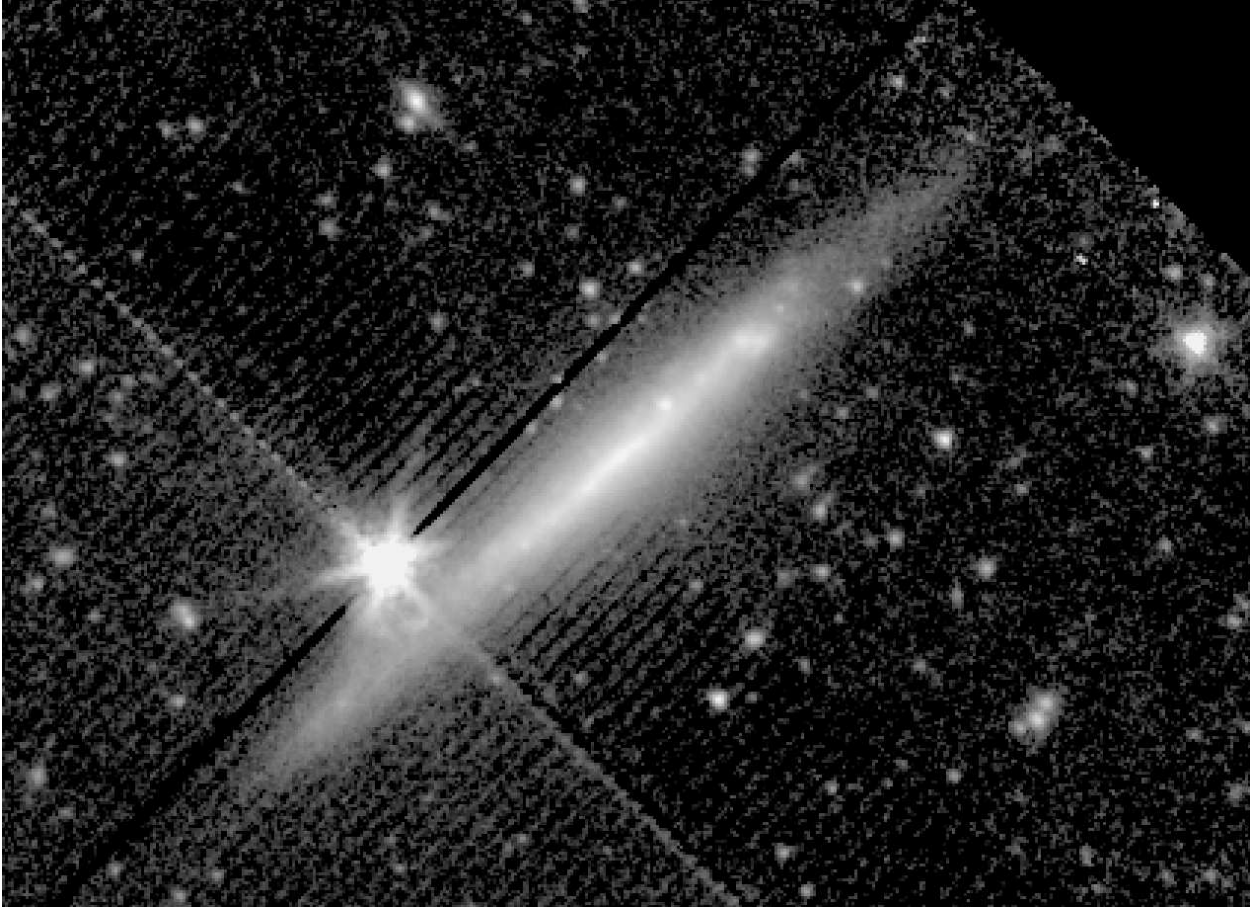


Fig. 1.180.— **UGC 5459** - S⁴G mid-IR classification: SBdm sp ; Filter: IRAC 3.6 μ m;
North: up, East: left; Field dimensions: 5.3 \times 3.8 arcmin; Surface brightness range displayed:
16.5–28.0 mag arcsec⁻²

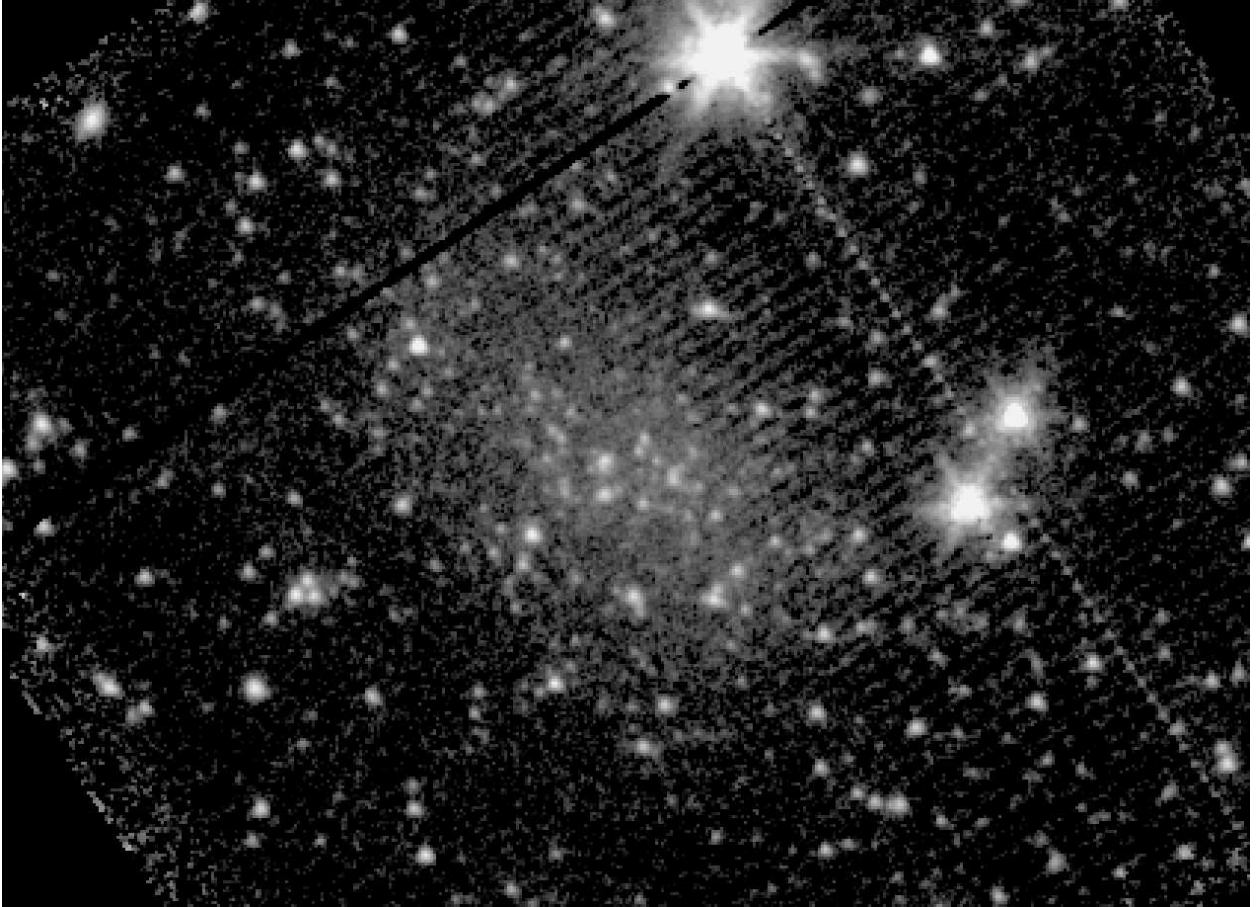


Fig. 1.181.— **UGC 6817** - S⁴G mid-IR classification: Im ; Filter: IRAC 3.6 μ m; North: up, East: left; Field dimensions: 5.3 \times 3.8 arcmin; Surface brightness range displayed: 18.0–28.0 mag arcsec⁻²



Fig. 1.182.— **UGC 6956** - S⁴G mid-IR classification: SB(s)dm: ; Filter: IRAC 3.6μm;
North: up, East: left; Field dimensions: 3.5× 2.6 arcmin; Surface brightness range displayed:
18.5–28.0 mag arcsec⁻²



Fig. 1.183.— **UGC 7504** - S⁴G mid-IR classification: S0⁻ ; Filter: IRAC 3.6 μ m; North: left, East: down; Field dimensions: 3.2 \times 2.3 arcmin; Surface brightness range displayed: 18.0–28.0 mag arcsec⁻²

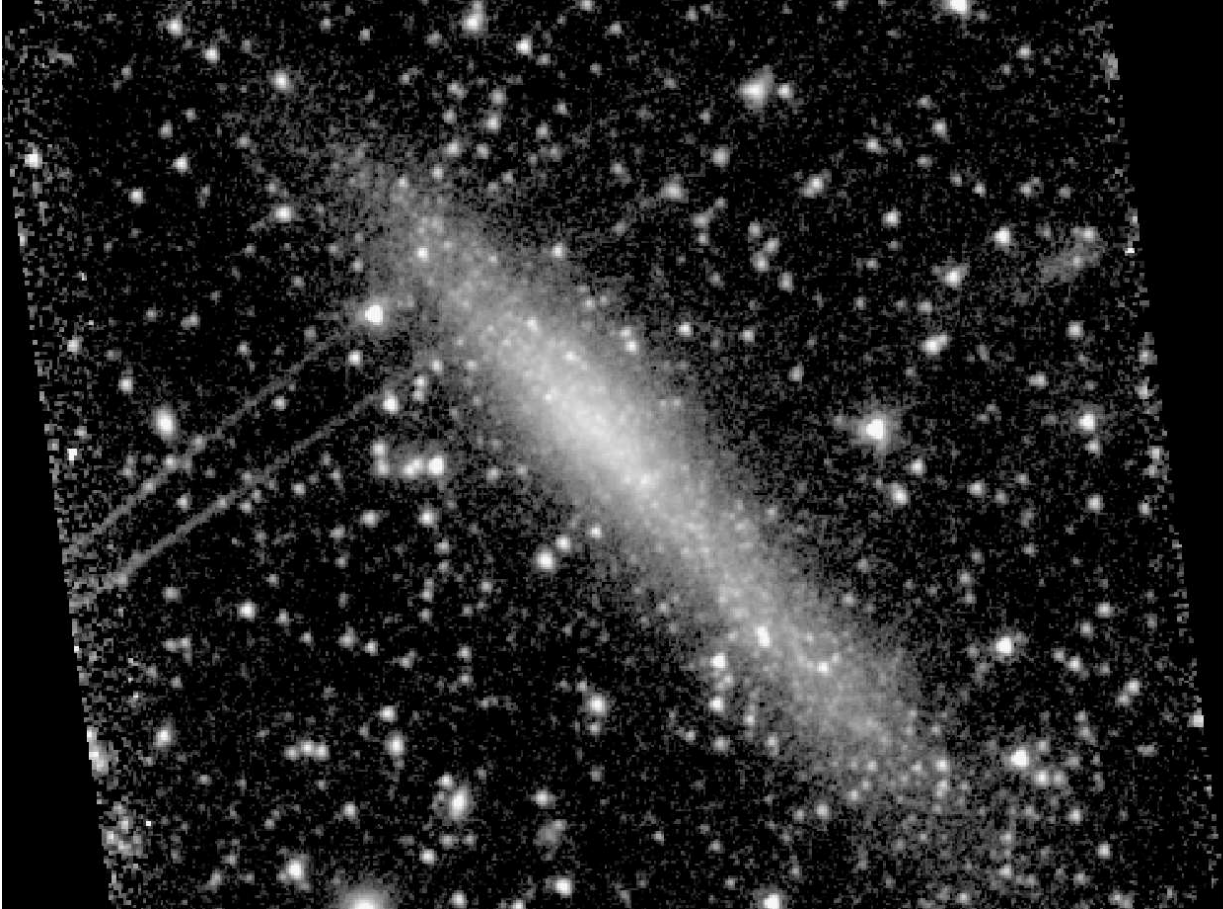


Fig. 1.184.— **ESO 115- 21** - S⁴G mid-IR classification: SB(s)m sp ; Filter: IRAC 3.6 μ m;
North: up, East: left; Field dimensions: 6.2 \times 4.5 arcmin; Surface brightness range displayed:
18.5–28.0 mag arcsec⁻²



Fig. 1.185.— **ESO 119- 16** - S⁴G mid-IR classification: (R')SAB(s)dm: ; Filter: IRAC 3.6 μ m; North: up, East: left; Field dimensions: 3.5 \times 2.6 arcmin; Surface brightness range displayed: 18.5–28.0 mag arcsec⁻²



Fig. 1.186.— **ESO 149- 3** - S⁴G mid-IR classification: IBm: sp ; Filter: IRAC 3.6 μ m;
North: up, East: left; Field dimensions: 3.5 \times 2.6 arcmin; Surface brightness range displayed:
18.5–28.0 mag arcsec⁻²



Fig. 1.187.— **ESO 154- 23** - S⁴G mid-IR classification: SB(s)d sp ; Filter: IRAC 3.6 μ m;
North: up, East: left; Field dimensions: 9.0 \times 6.6 arcmin; Surface brightness range displayed:
18.5–28.0 mag arcsec⁻²

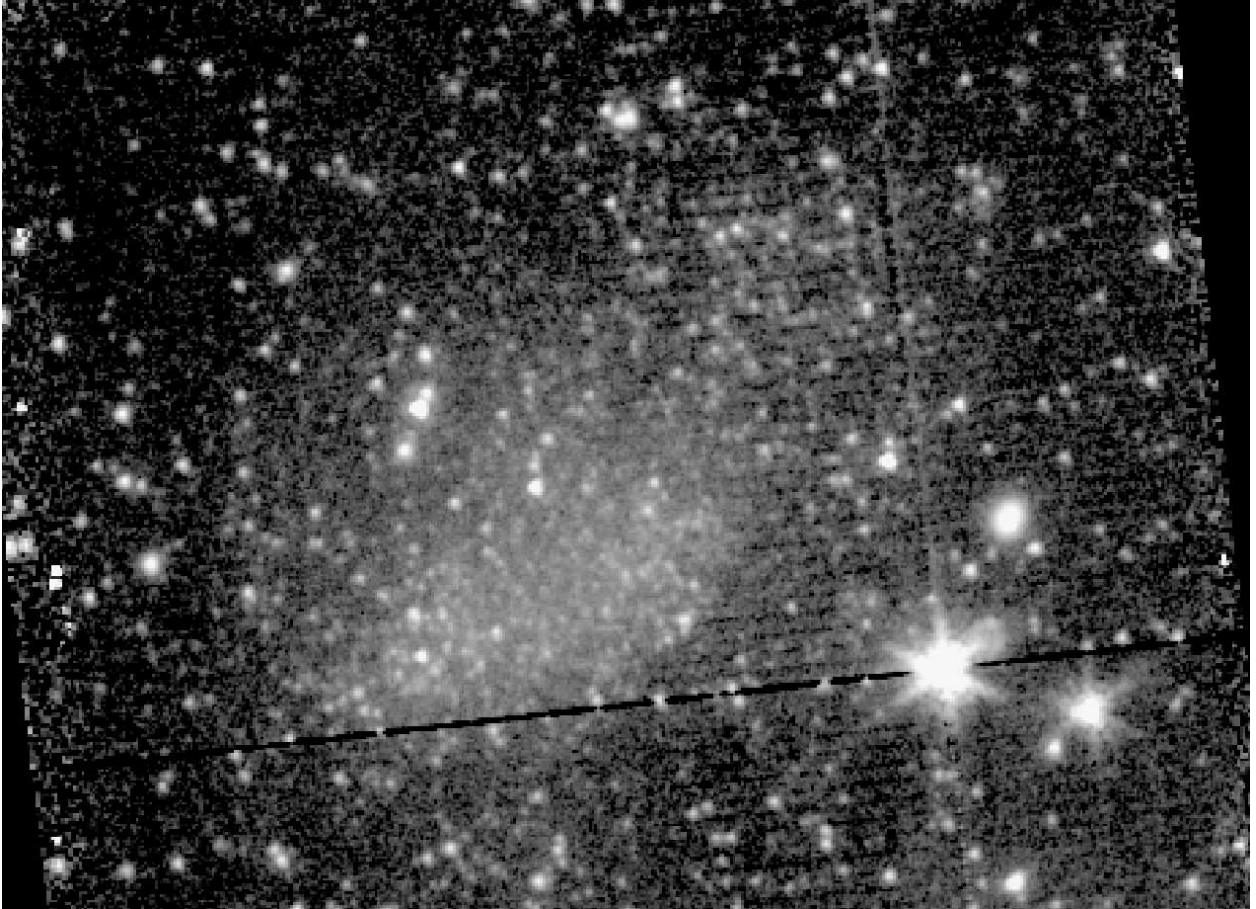


Fig. 1.188.— **ESO 245- 5** - S⁴G mid-IR classification: IAB(s)m ; Filter: IRAC 3.6 μ m;
North: up, East: left; Field dimensions: 5.7 \times 4.2 arcmin; Surface brightness range displayed:
18.5–28.0 mag arcsec⁻²



Fig. 1.189.— **ESO 245- 7** - S⁴G mid-IR classification: Im ; Filter: IRAC 3.6 μ m; North: up, East: left; Field dimensions: 6.6 \times 4.8 arcmin; Surface brightness range displayed: 18.5–28.0 mag arcsec⁻²



Fig. 1.190.— **ESO 362- 9** - S⁴G mid-IR classification: SAB(s)dm ; Filter: IRAC 3.6μm;
North: up, East: left; Field dimensions: 5.8× 4.2 arcmin; Surface brightness range displayed:
18.5–28.0 mag arcsec⁻²

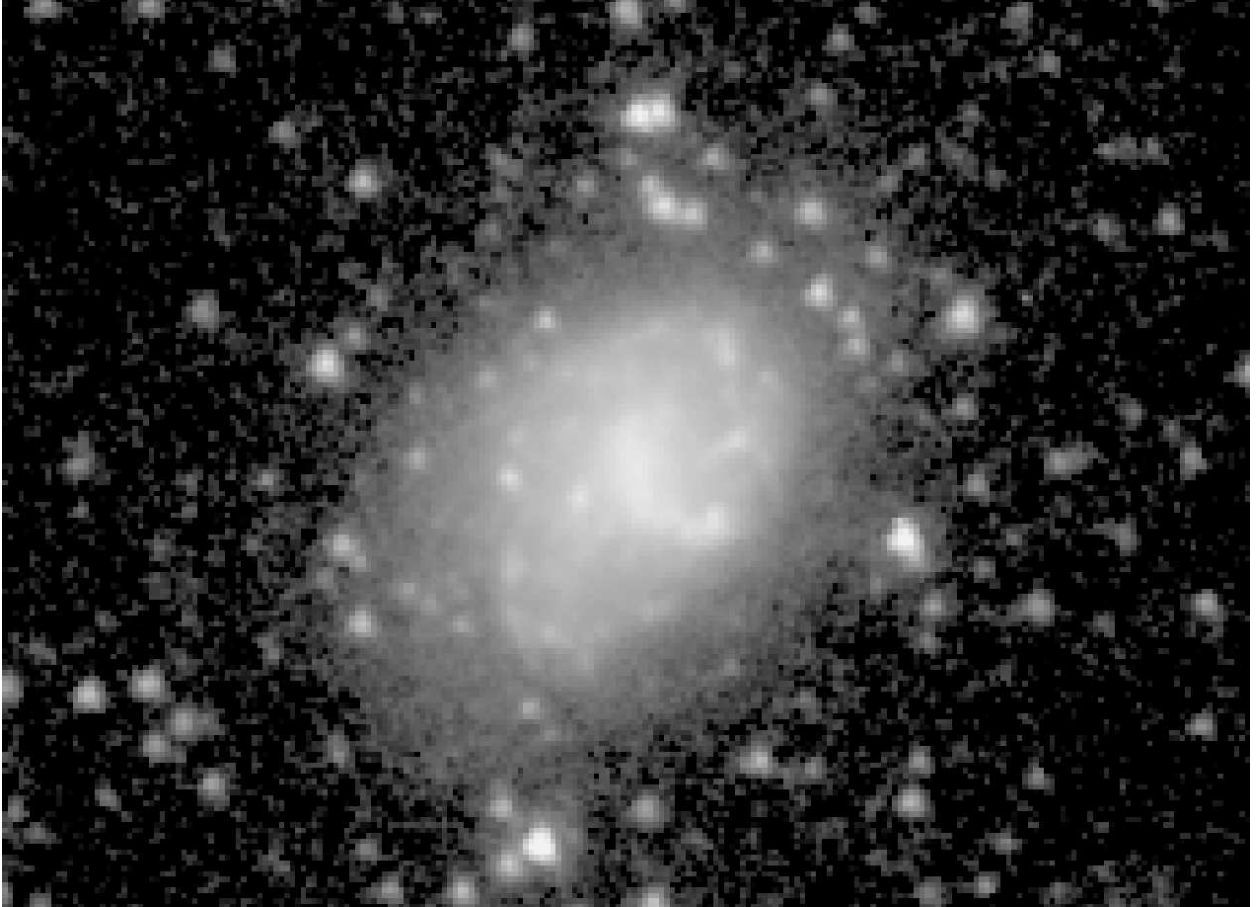


Fig. 1.191.— **ESO 418- 8** - S⁴G mid-IR classification: (R')SB(s)dm: ; Filter: IRAC 3.6μm;
North: up, East: left; Field dimensions: 2.9× 2.1 arcmin; Surface brightness range displayed:
17.5–28.0 mag arcsec⁻²

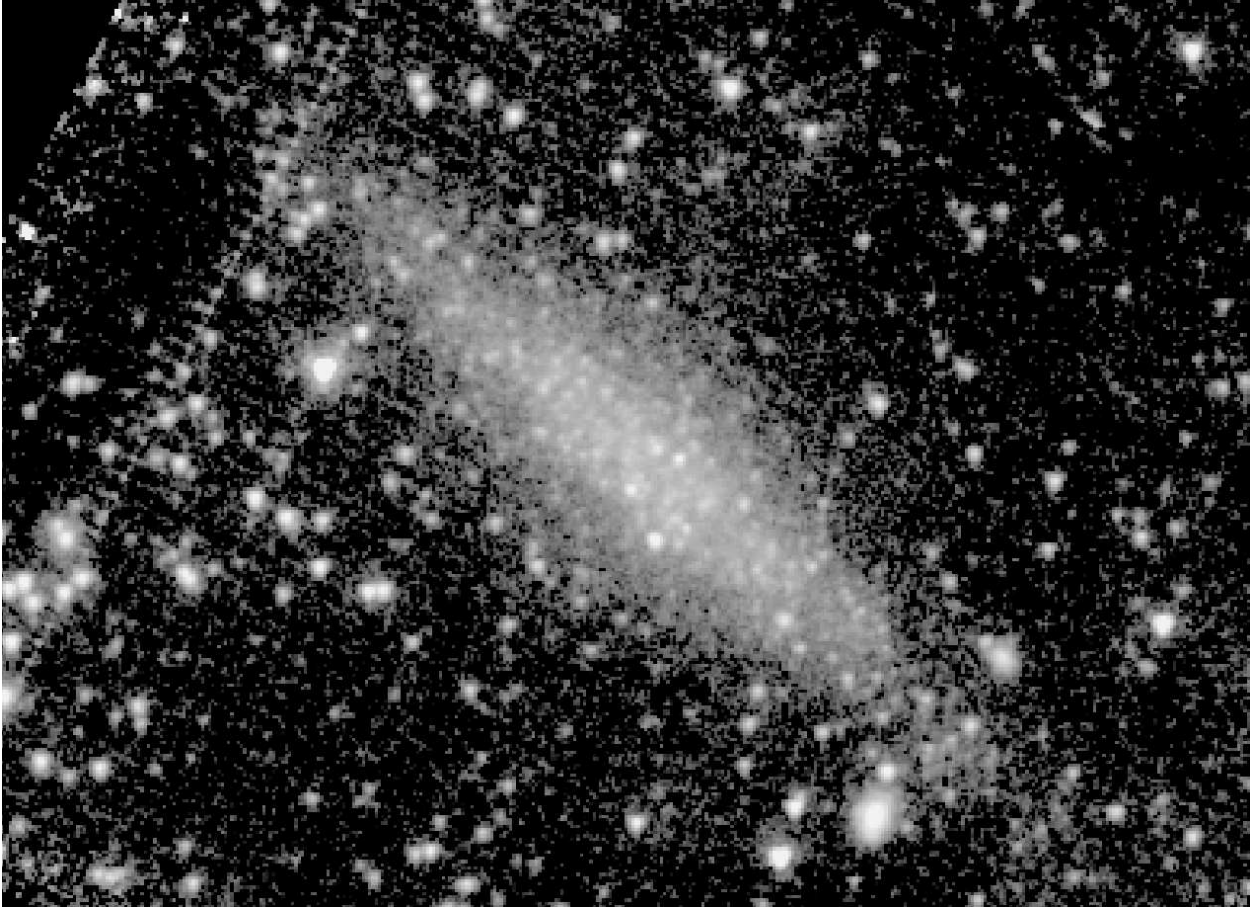


Fig. 1.192.— **ESO 471- 6** - S⁴G mid-IR classification: SBd: sp ; Filter: IRAC 3.6 μ m;
North: up, East: left; Field dimensions: 4.9 \times 3.6 arcmin; Surface brightness range displayed:
18.5–28.0 mag arcsec⁻²

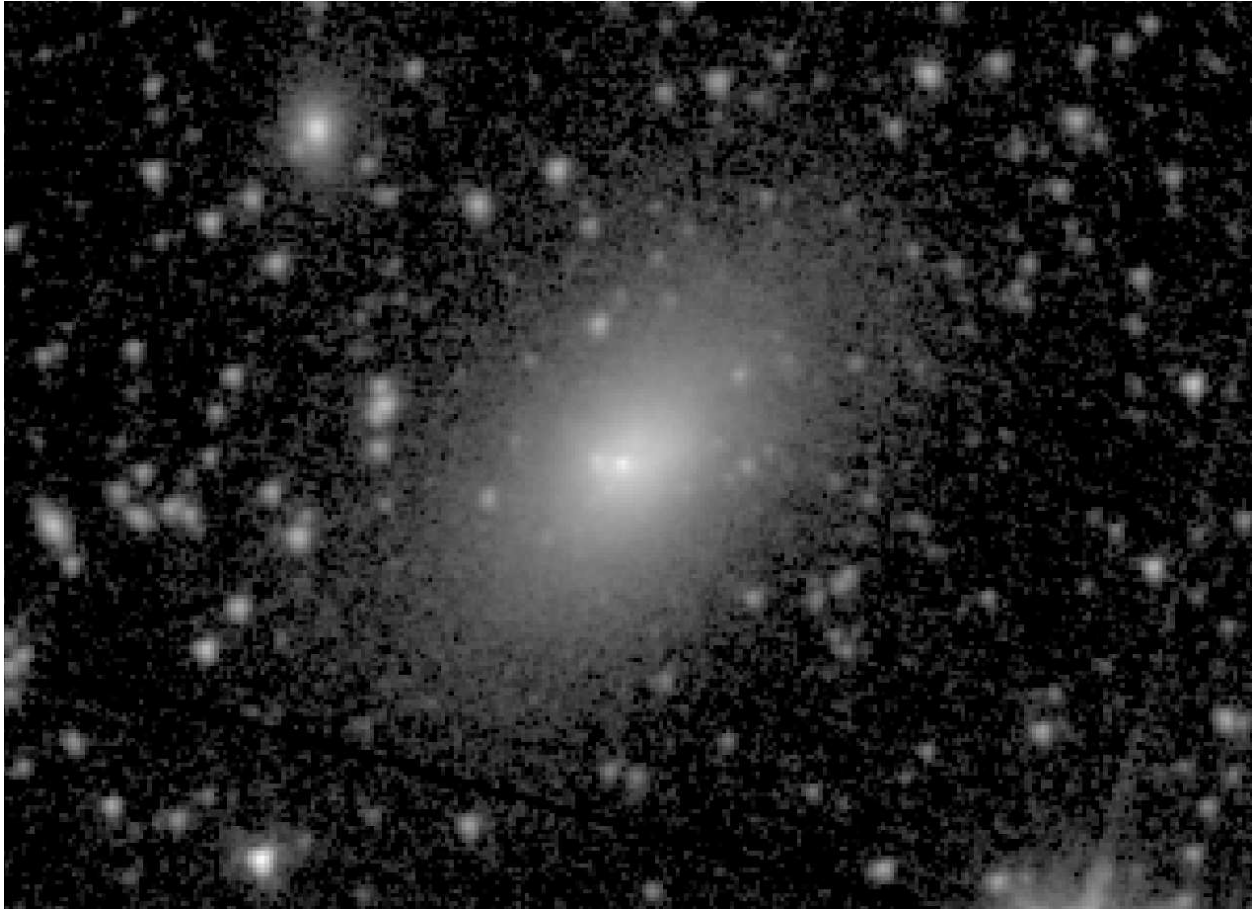


Fig. 1.193.— **ESO 483- 13** - S⁴G mid-IR classification: dE4,N/SA0⁻ ; Filter: IRAC 3.6μm; North: up, East: left; Field dimensions: 3.7× 2.7 arcmin; Surface brightness range displayed: 15.5–28.0 mag arcsec⁻²

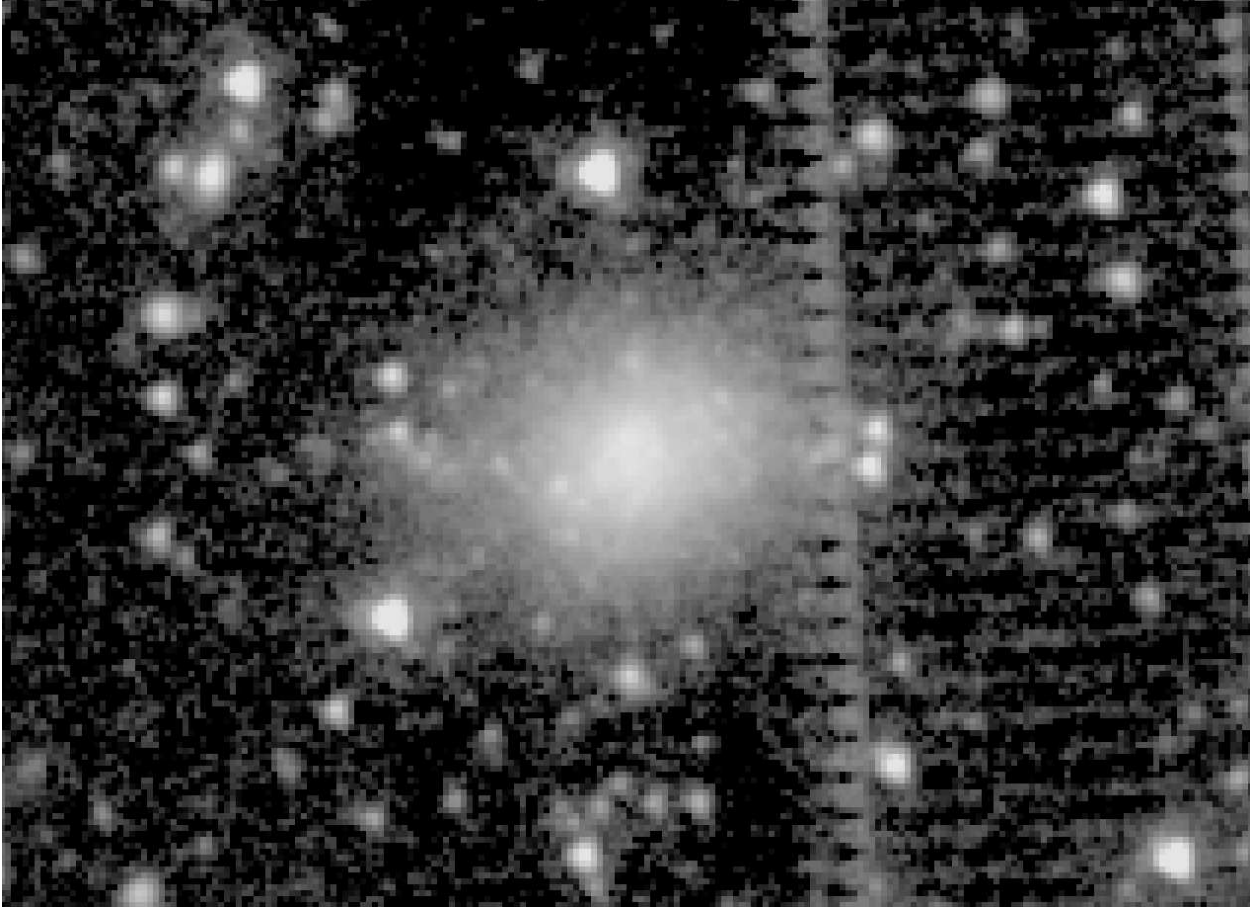


Fig. 1.194.— **ESO 486- 21** - S⁴G mid-IR classification: dE (Im) ; Filter: IRAC 3.6 μ m; North: up, East: left; Field dimensions: 2.6 \times 1.9 arcmin; Surface brightness range displayed: 18.0–26.0 mag arcsec⁻²

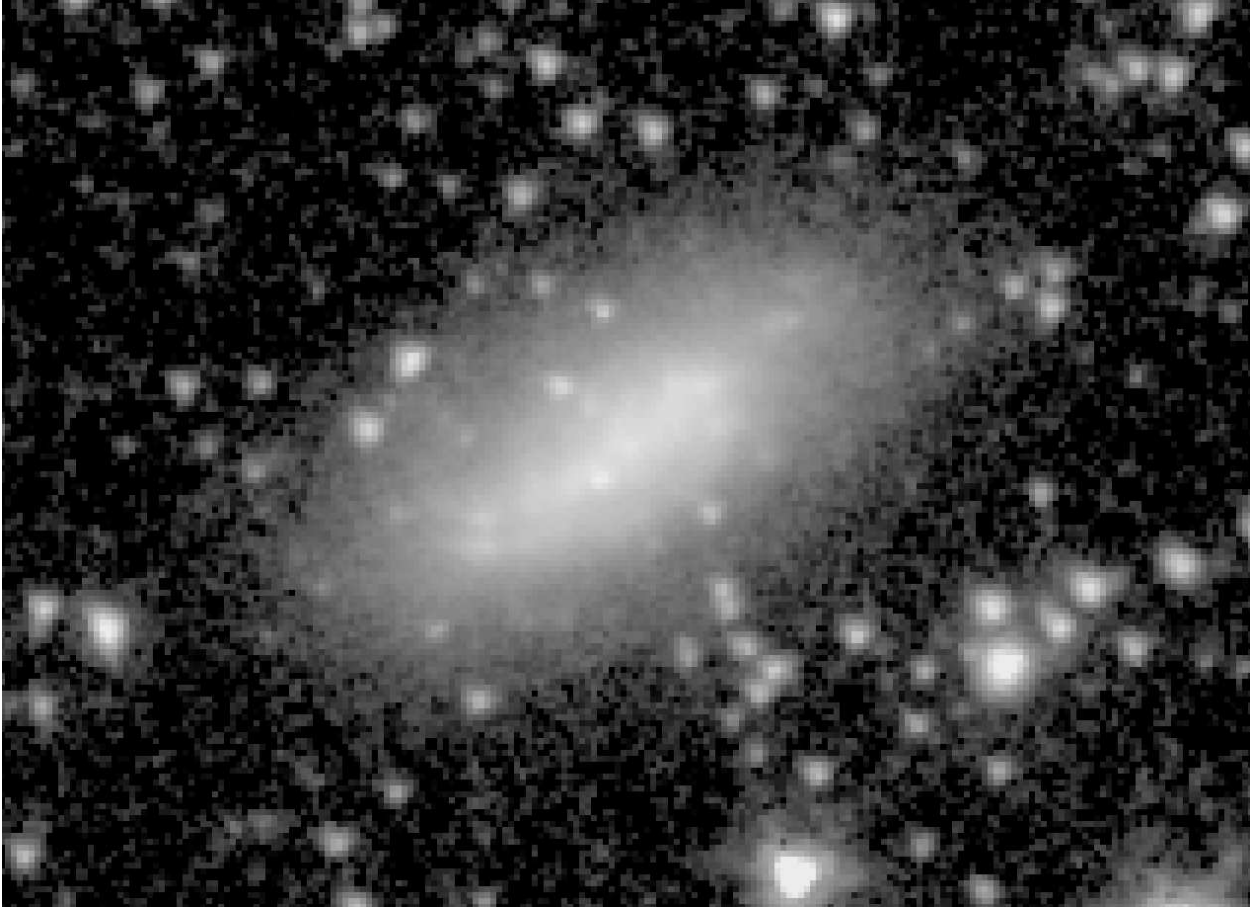


Fig. 1.195.— **ESO 503- 22** - S⁴G mid-IR classification: SB(s)m: ; Filter: IRAC 3.6 μ m;
North: up, East: left; Field dimensions: 2.6 \times 1.9 arcmin; Surface brightness range displayed:
18.0–28.0 mag arcsec⁻²

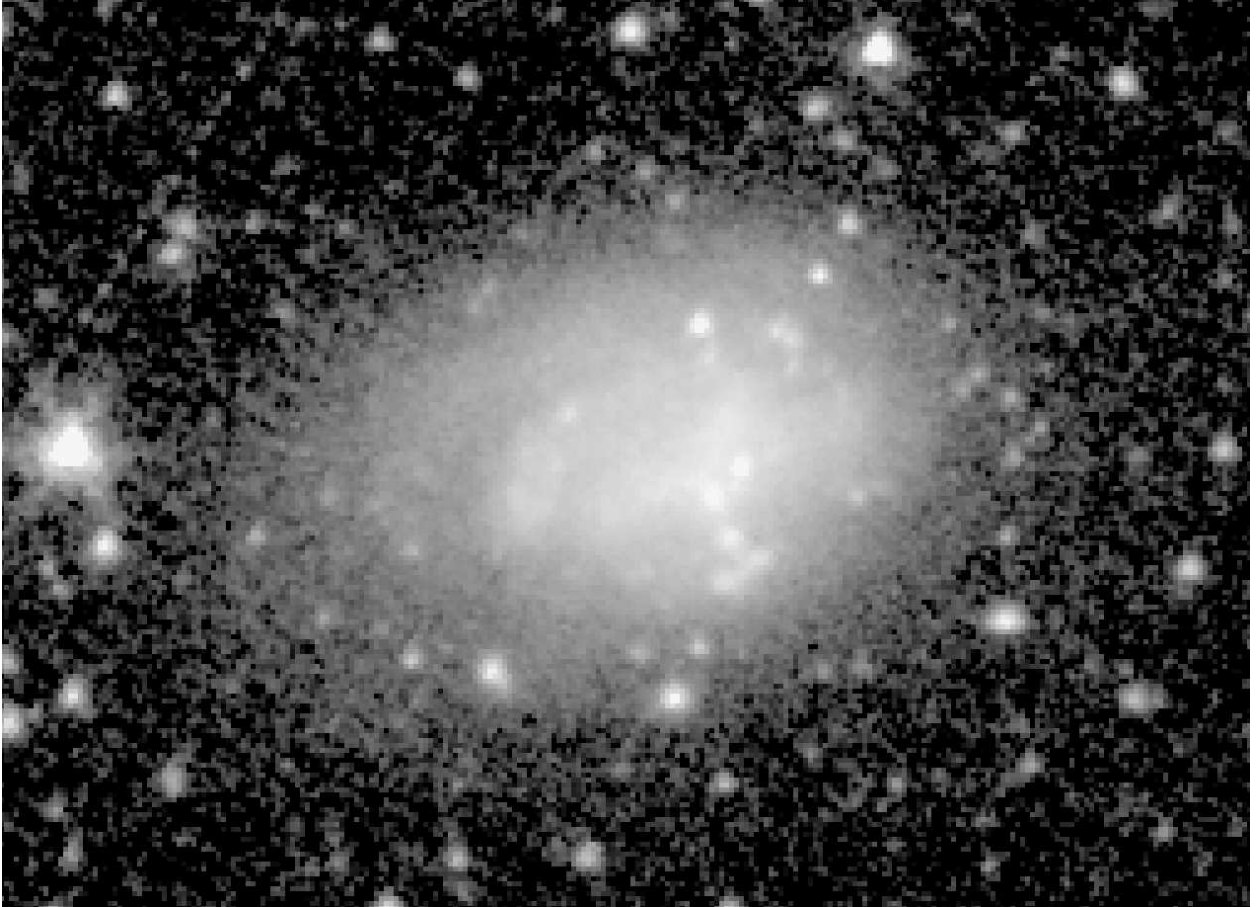


Fig. 1.196.— **ESO 544- 30** - S⁴G mid-IR classification: SAB(s)m ; Filter: IRAC 3.6μm; North: up, East: left; Field dimensions: 3.2× 2.3 arcmin; Surface brightness range displayed: 18.0–28.0 mag arcsec⁻²

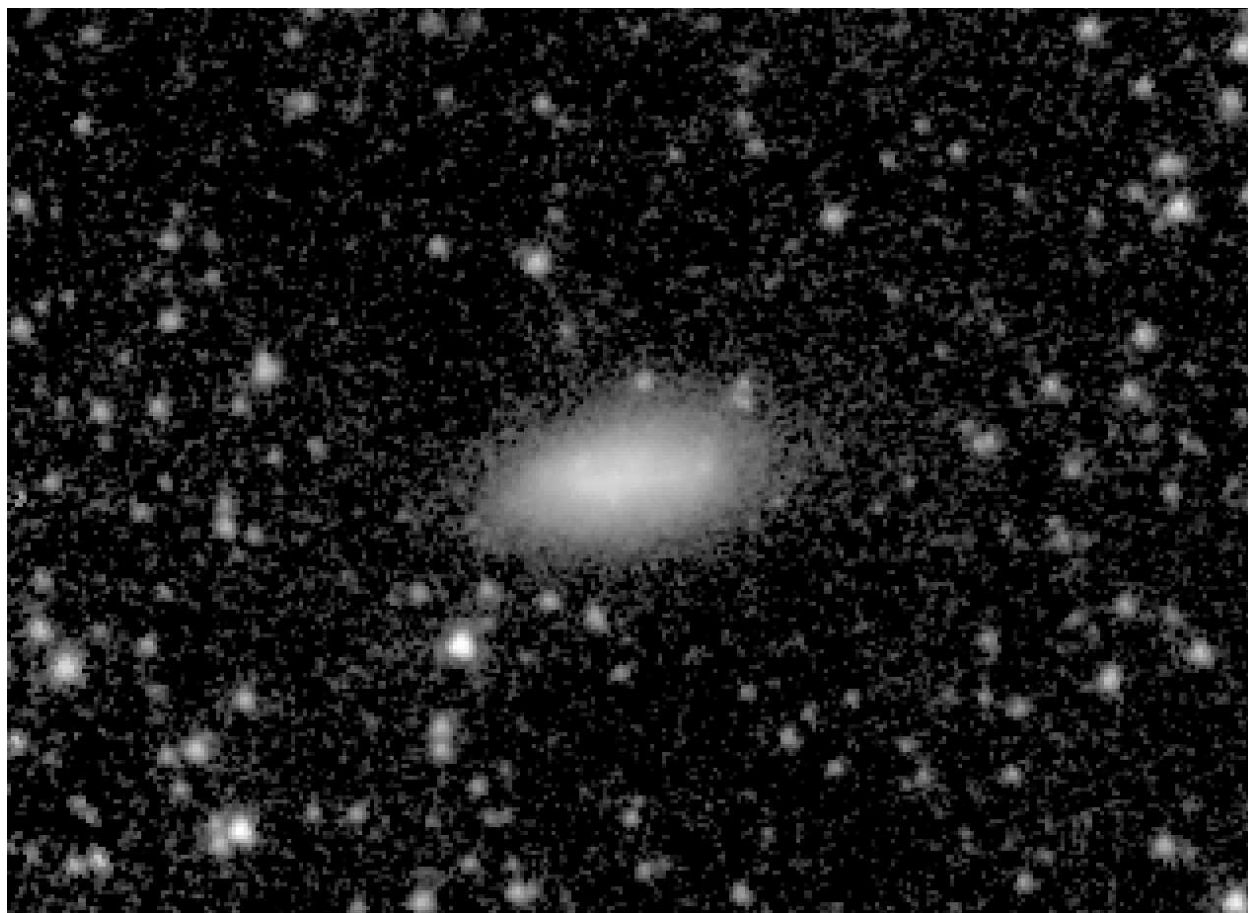


Fig. 1.197.— **CGCG265-55** - S⁴G mid-IR classification: dE (Im) ; Filter: IRAC 3.6 μ m;
North: up, East: left; Field dimensions: 4.0 \times 2.9 arcmin; Surface brightness range displayed:
16.5–28.0 mag arcsec⁻²

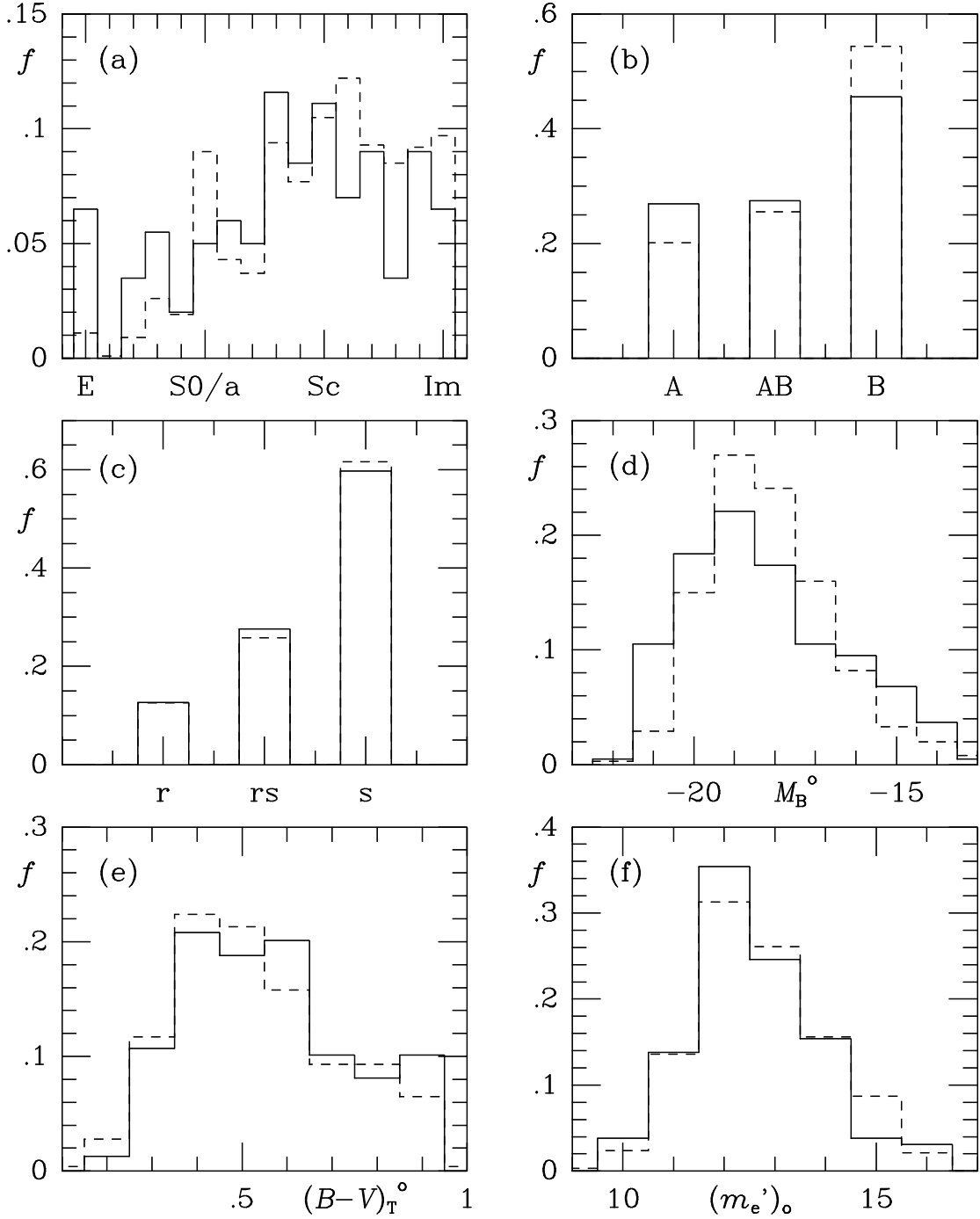


Fig. 2.— Histograms of the relative numbers of galaxies in our subset (solid lines) and the full S⁴G sample (dashed lines) versus RC3 (a) stage; (b) family classification; (c) variety classification; (d) absolute blue magnitude (based on the corrected RC3 total magnitude, a distance derived from the radial velocity relative to the Galactic Standard of rest, and a Hubble constant of 73 km s⁻¹ Mpc⁻¹); (e) total extinction-corrected $B - V$ color index; and (f) extinction-corrected mean effective blue light surface brightness (mag arcmin⁻²).

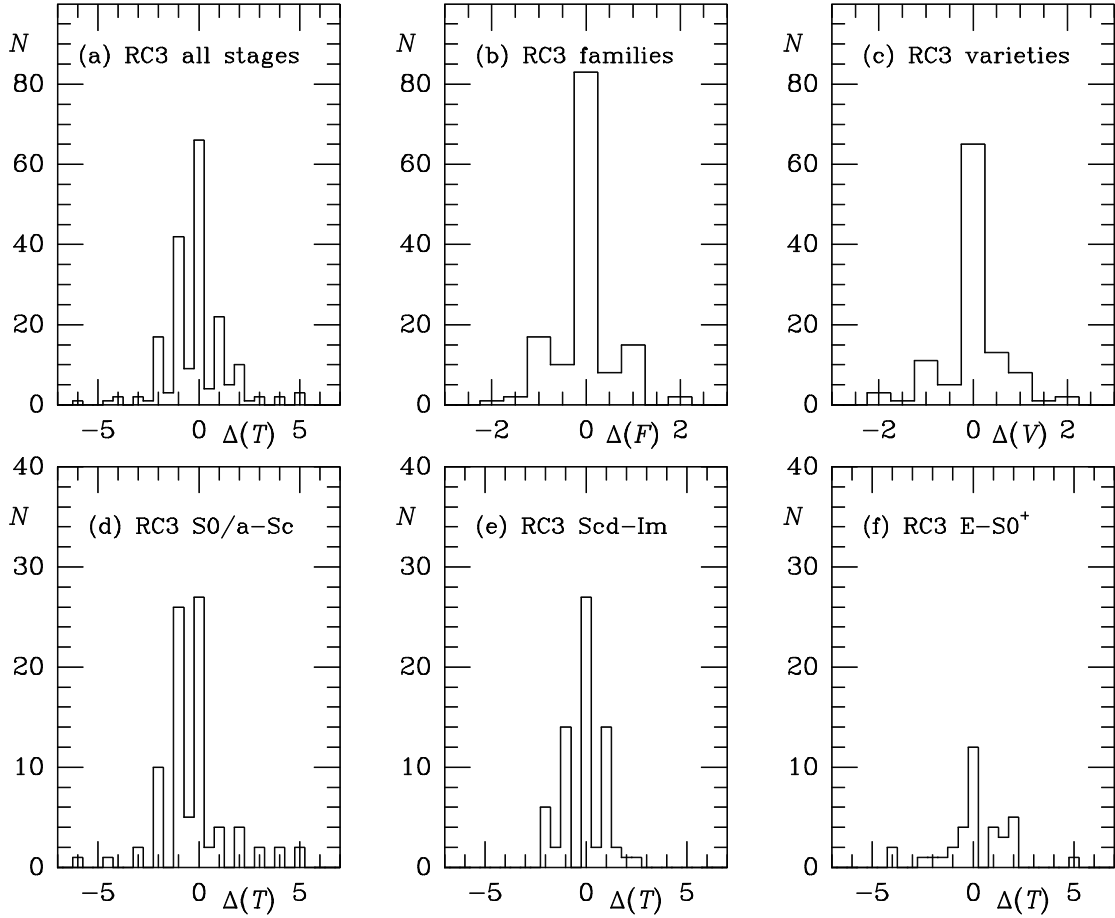


Fig. 3.— Histograms of morphological index differences $\Delta(T, F, V) = T, F, V(S^4G) - T, F, V(RC3)$, where T is the numerical stage index, F is the numerical family index, and V is the numerical variety index. The stage index ranges from $T=-5$ for E galaxies to $+10$ for magellanic irregulars, Im. The family index is $F=-1$ for SA galaxies, 0 for SAB galaxies, and $+1$ for SB galaxies. The variety index is $V=-1$ for (r), 0 for (rs), and $+1$ for (s) galaxies. Types with underlines (e.g., Sbc, SAB, (rs), etc.) are assigned half steps. Varieties like (r1) or (l) are not assigned numerical indices.

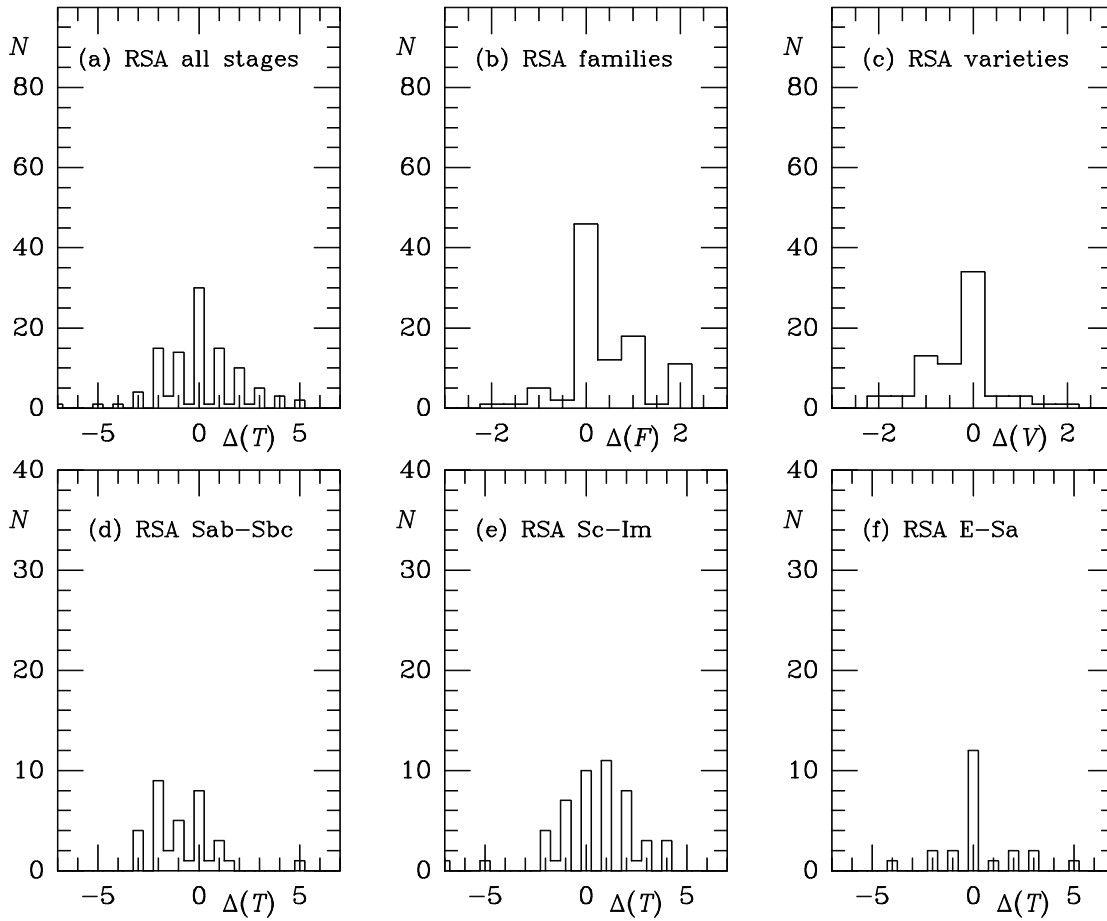


Fig. 4.— Same as Figure 3, but for RSA types, families, and varieties.

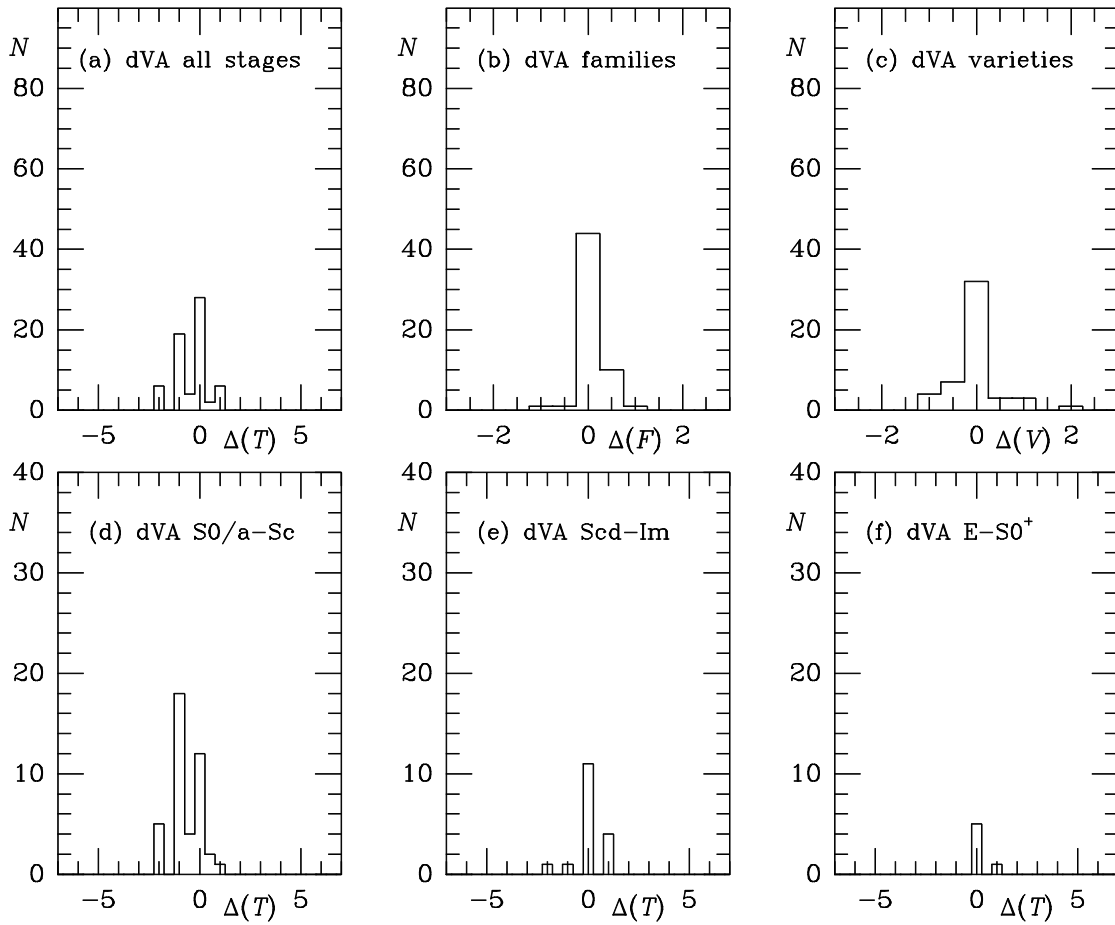


Fig. 5.— Same as Figure 3, but for dVA types, families, and varieties.

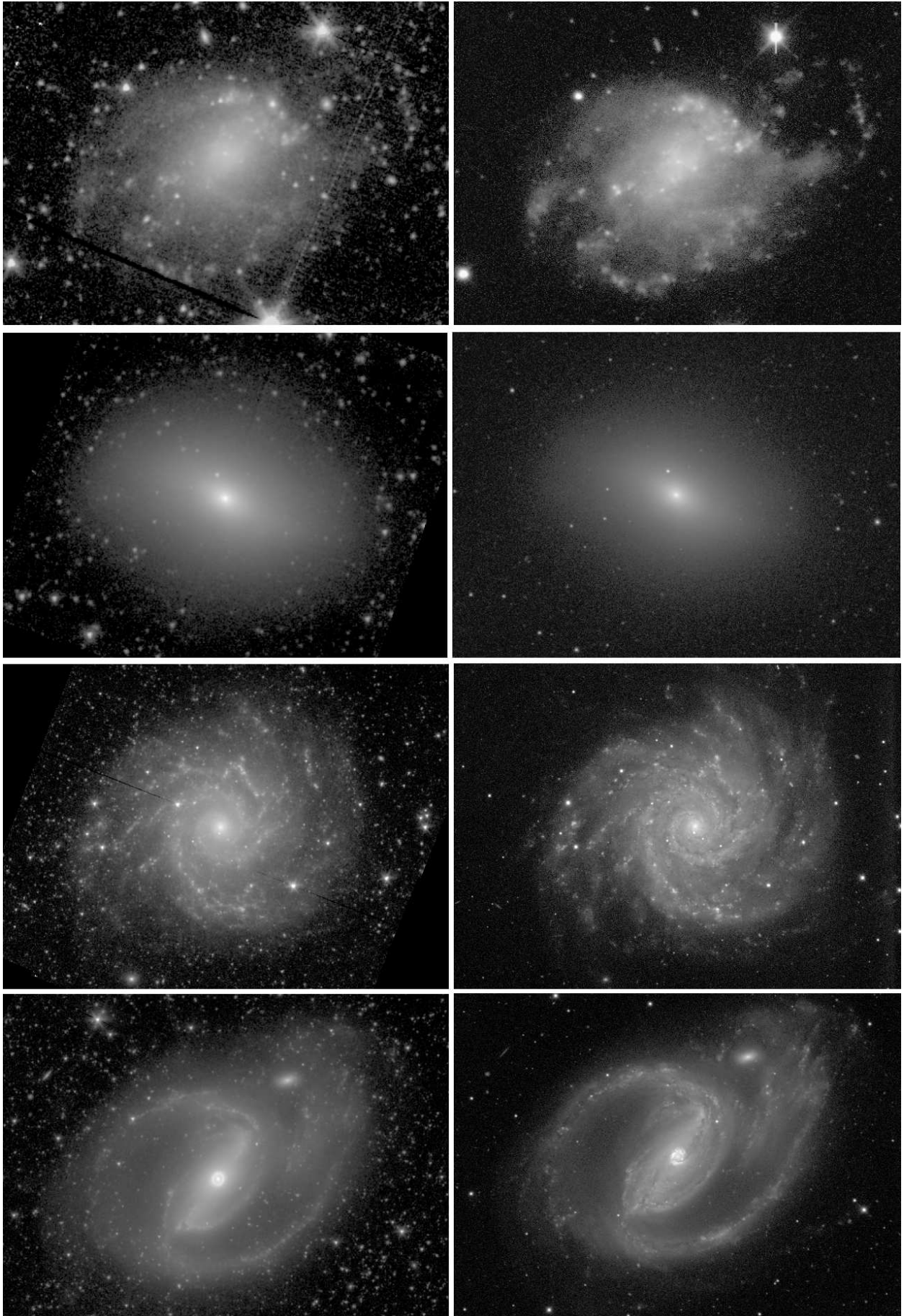


Fig. 6 (cont.).— Comparison between $3.6\mu\text{m}$ images (left) and B -band images (right) for (top-to-bottom) NGC 428, NGC 584, NGC 628, and NGC 1097. All of the images are in units of mag arcsec^{-2} , and the B -band images are from the dVA.

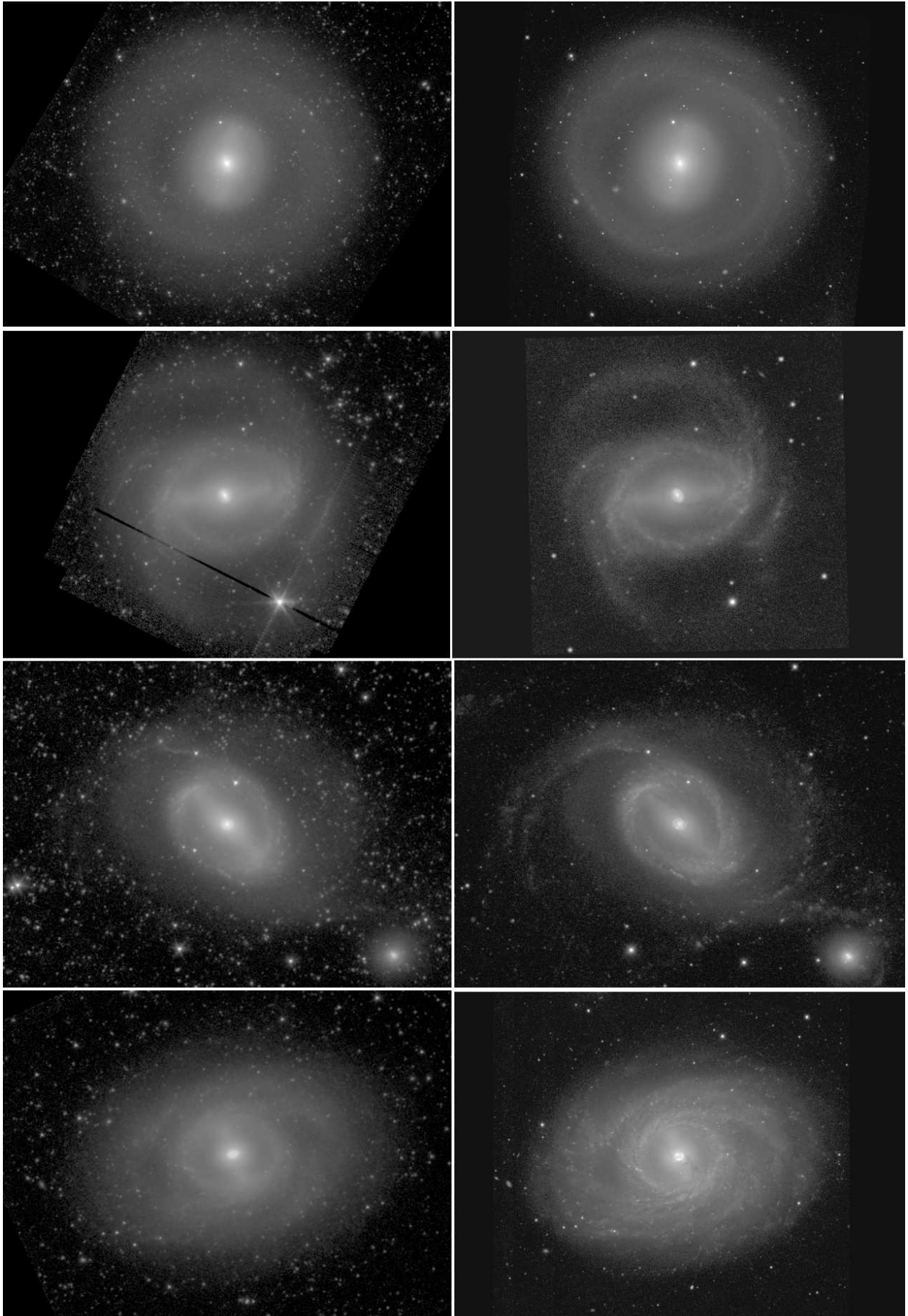


Fig. 7 (cont.).— Comparison between $3.6\mu\text{m}$ images (left) and B -band images (right) for four ringed galaxies (top-to-bottom): NGC 1291, NGC 1433, NGC 1512, and NGC 3351. All of the images are in units of mag arcsec^{-2} , and the B -band images are from the dVA.

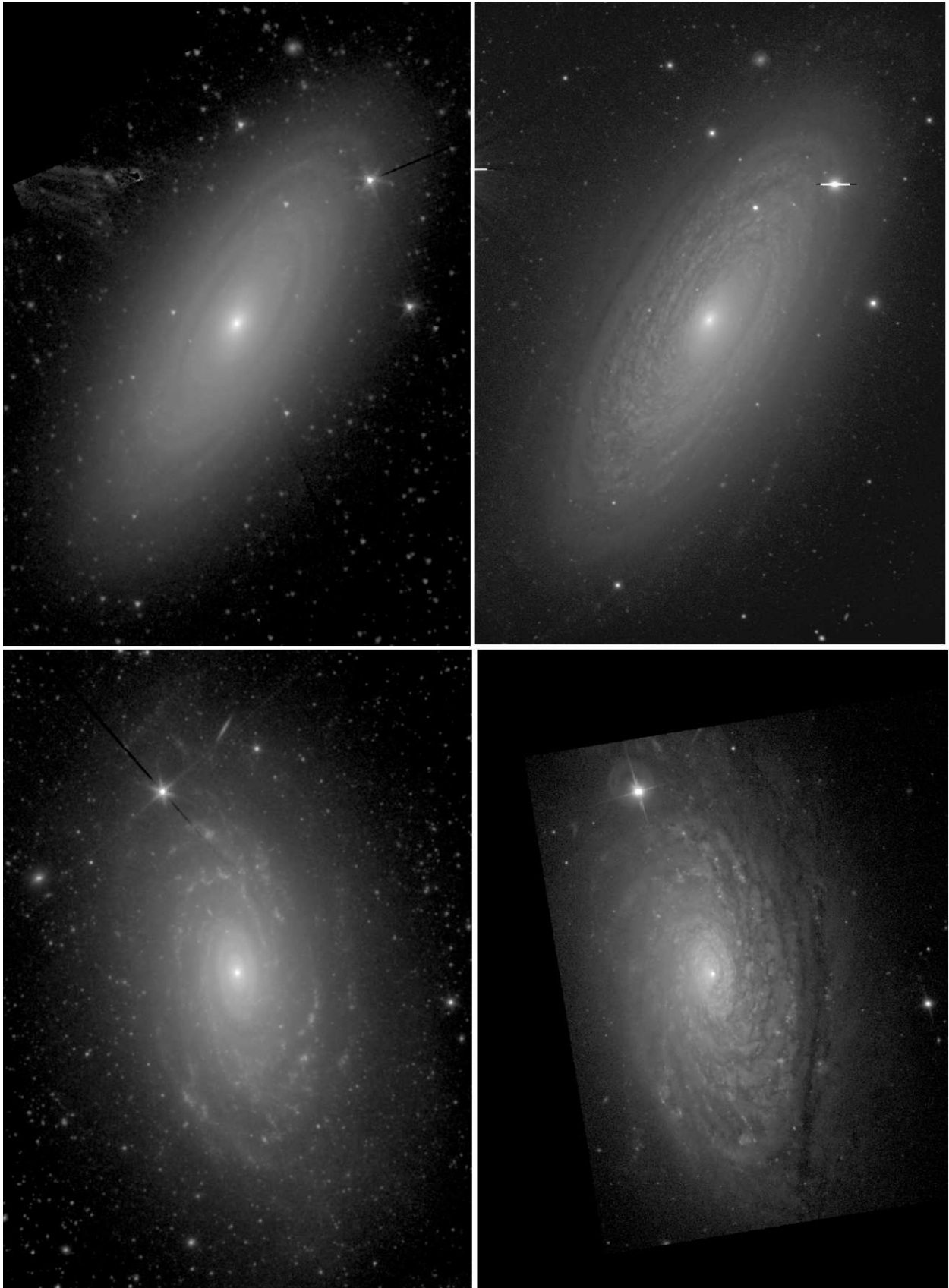


Fig. 8.—

Fig. 8 (cont.).— Comparison between $3.6\mu\text{m}$ images (left) and optical images (right) for two flocculent spirals (top-to-bottom): NGC 2841, NGC 5055. All of the images are in units of mag arcsec^{-2} . The optical image of NGC 2841 is B -band and is from the dVA. The optical image of NGC 5055 is g -band and is from the SDSS.

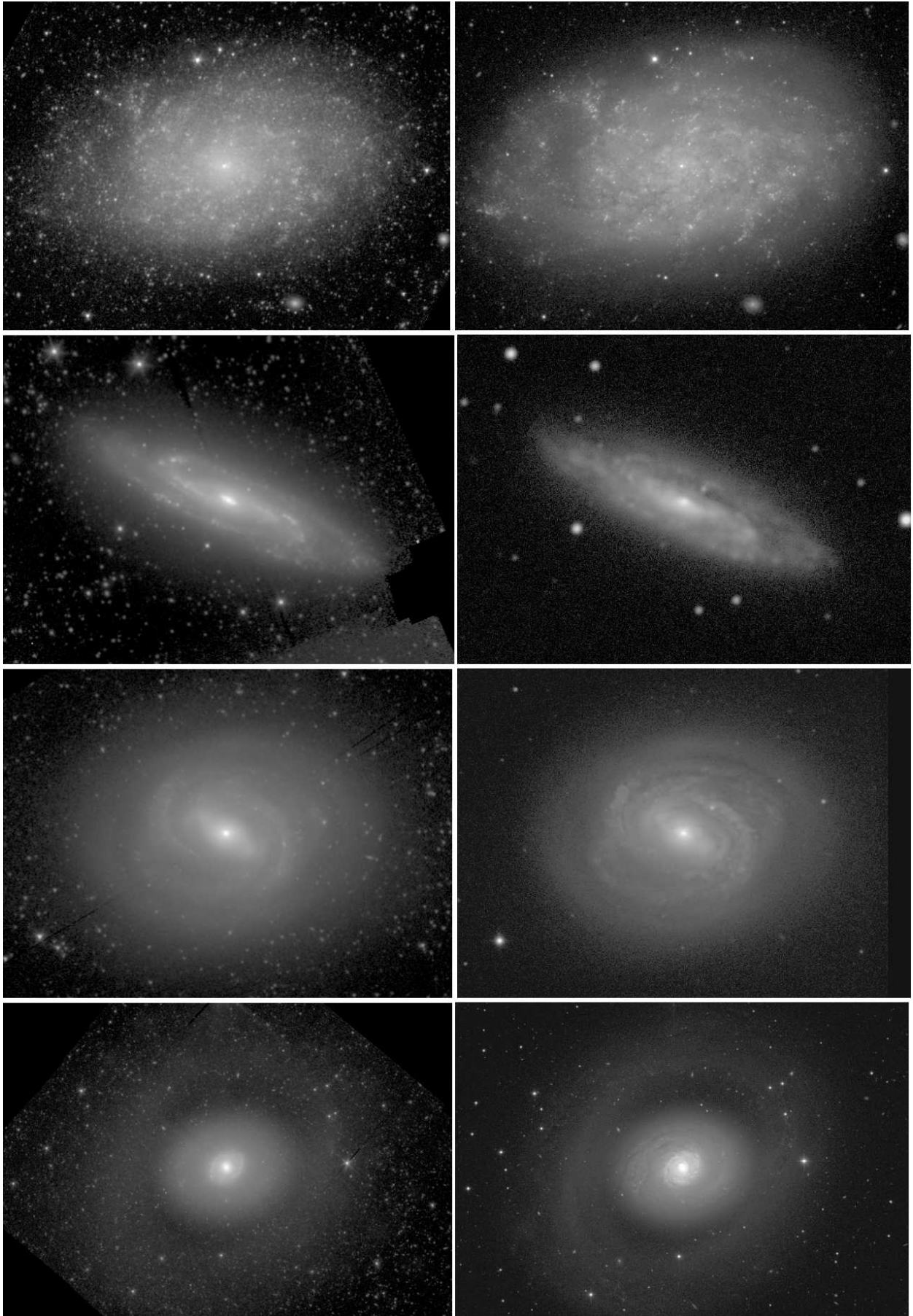


Fig. 9 (cont.).— Comparison between $3.6\mu\text{m}$ images (left) and B -band images (right) for four late to early-type galaxies (top-to-bottom): NGC 7793, NGC 4527, NGC 4579, and NGC 4736. All of the images are in units of mag arcsec^{-2} . The B -band images are from the dVA.

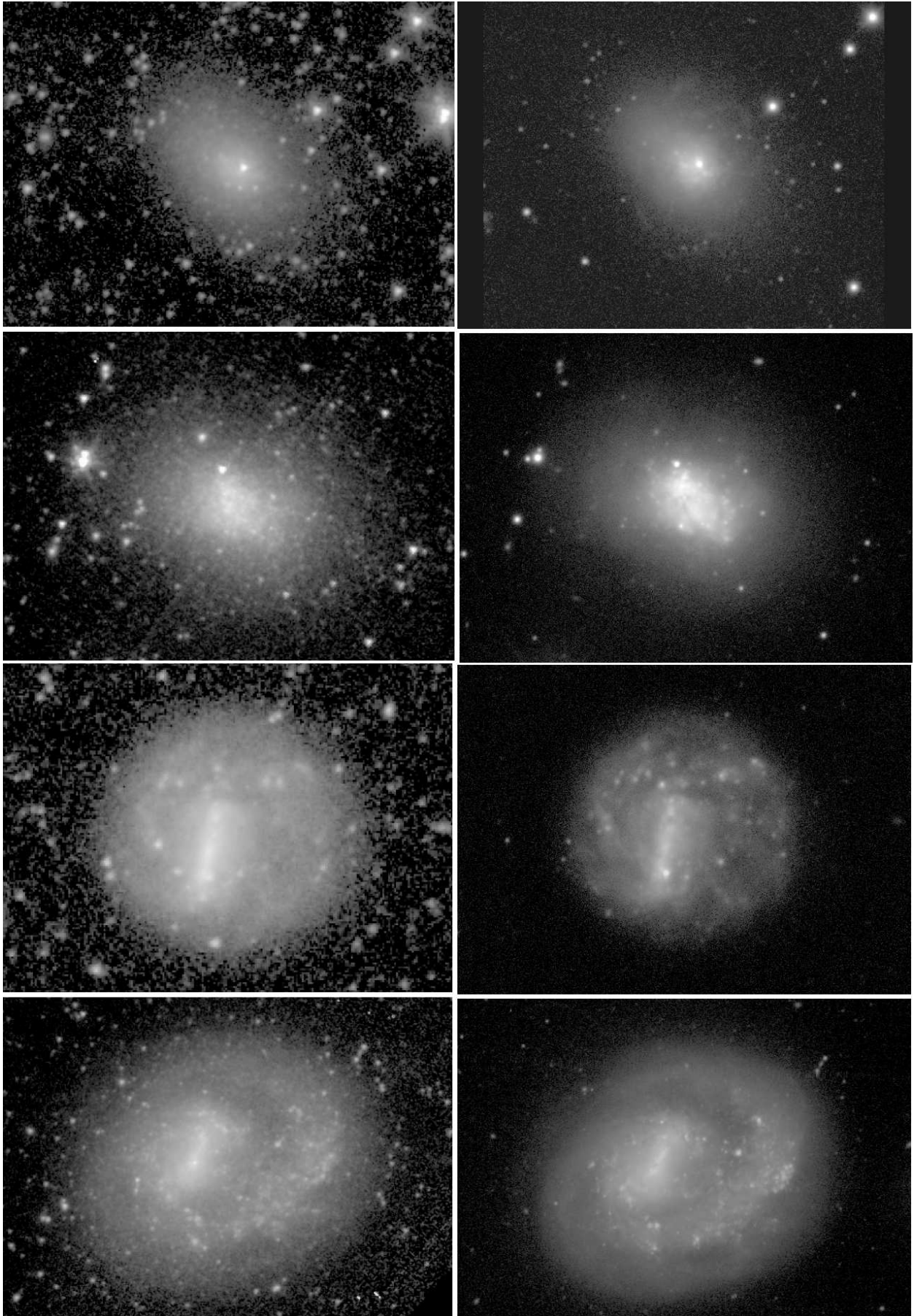


Fig. 10 (cont.).— Comparison between $3.6\mu\text{m}$ images (left) and B -band images (right) for four late-type galaxies (top-to-bottom): NGC 1705, NGC 3738, NGC 3906, and NGC 4618. All of the images are in units of mag arcsec^{-2} . The B -band images of NGC 1705, 3906, and 4618 are from the dVA. The B -band image of NGC 3738 is from Taylor et al. (2005).

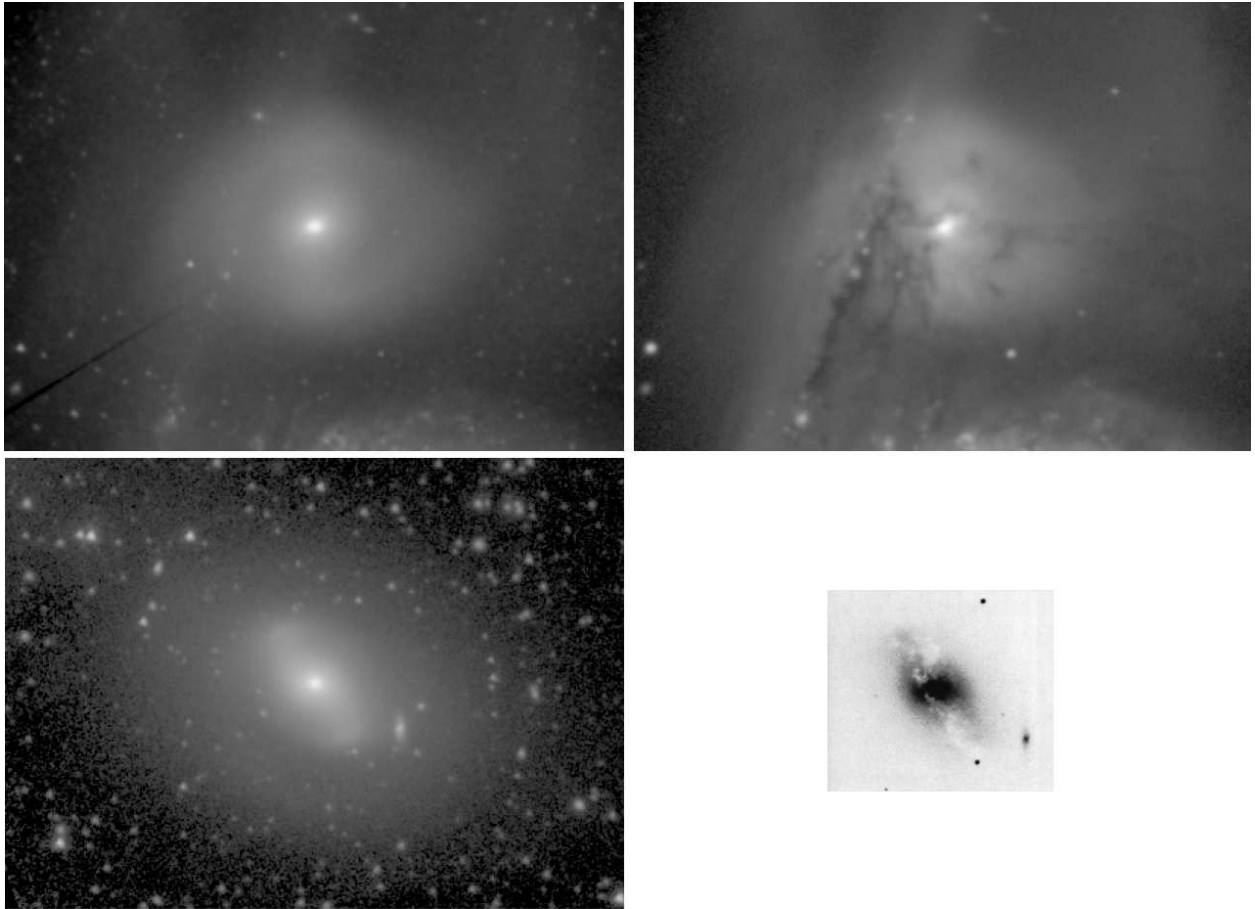


Fig. 11.—

Fig. 11 (cont.).— Comparison between $3.6\mu\text{m}$ images (left) and B -band images (right) of two I0 galaxies: top panels: NGC 5195; bottom panels: NGC 2968. The B -band image of NGC 2968 is from the Carnegie Atlas of Galaxies (Sandage & Bedke 1994).

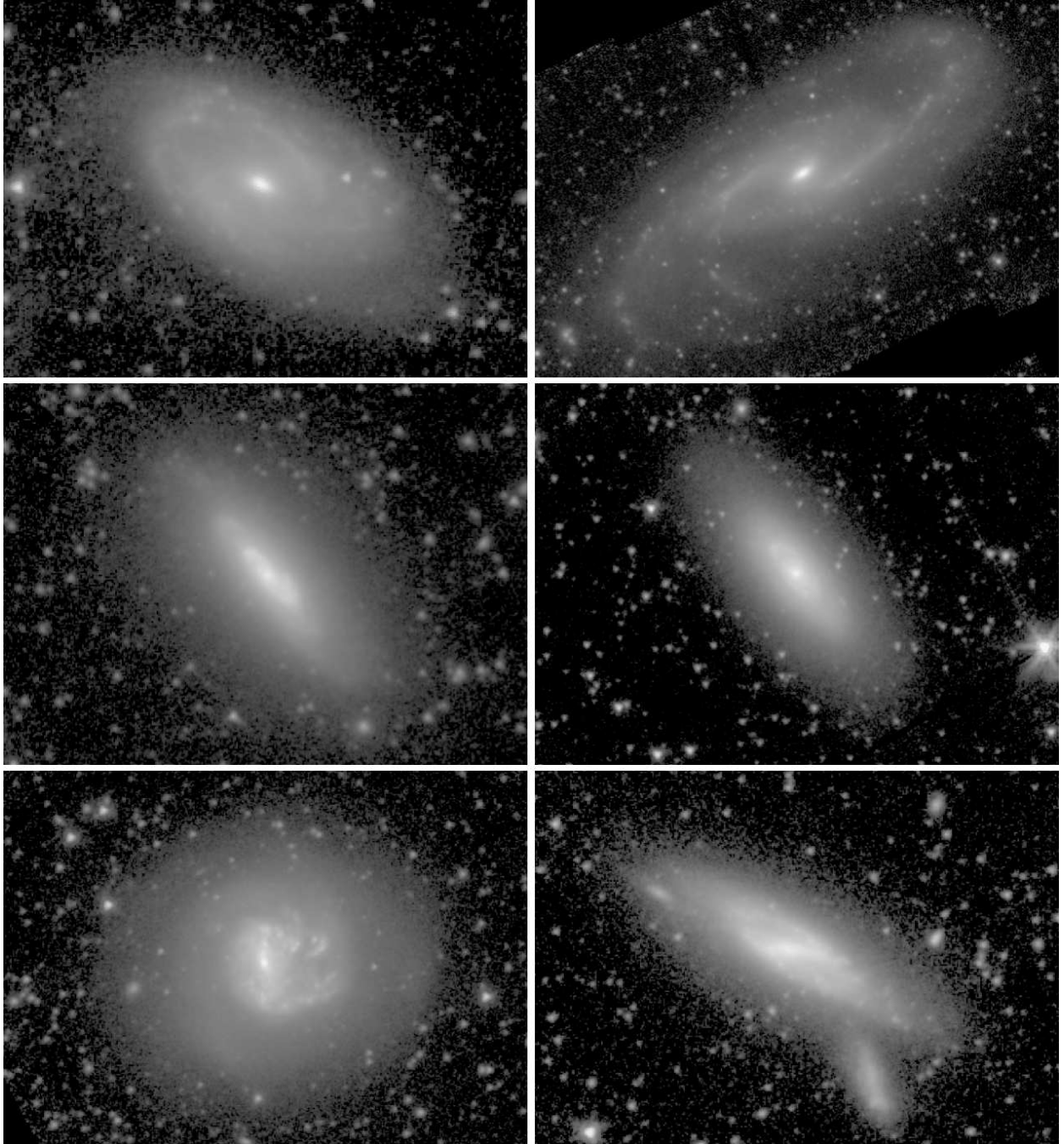


Fig. 12.—

Fig. 12 (cont.).— $3.6\mu\text{m}$ images of six special cases: top panels: NGC 470 (left) and 4536 (right), showing prominent, highly-flattened pseudobulges. Middle panels: IC 750 (left) and IC 3392 (right), two “double-stage” galaxies having bright inner spirals imbedded in an S0 or S0/a-like background disk. Bottom panels: NGC 5713 (left) and NGC 3769 (right), two more double-stage galaxies.

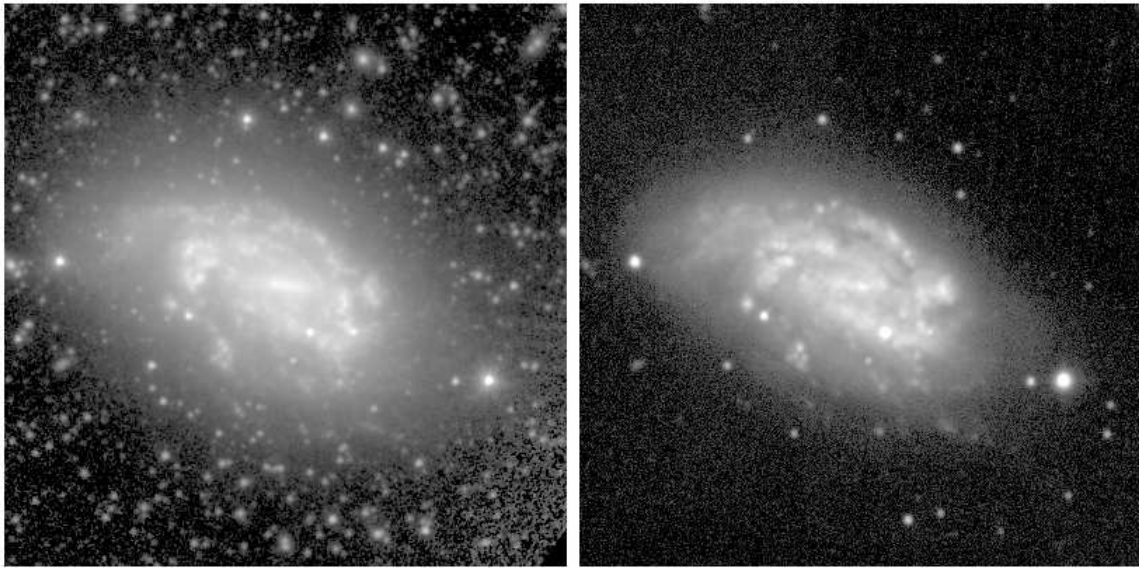


Fig. 13.— Comparison between $3.6\mu\text{m}$ (left) and B -band images of the late-type spiral galaxy NGC 1559, showing the strong correspondence between $3.6\mu\text{m}$ resolved sources and B -band star-forming regions. The B -band image is from the OSUBSGS (Eskridge et al. 2002).

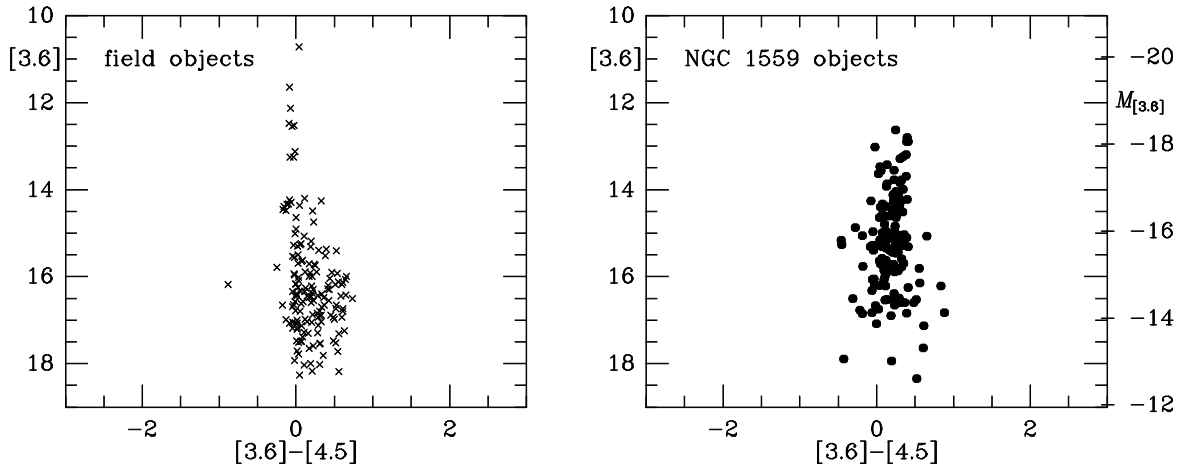


Fig. 14.— Color-magnitude diagrams for foreground stars and background galaxies (left panel) and resolved objects in the spiral arms of NGC 1559 (right panel).

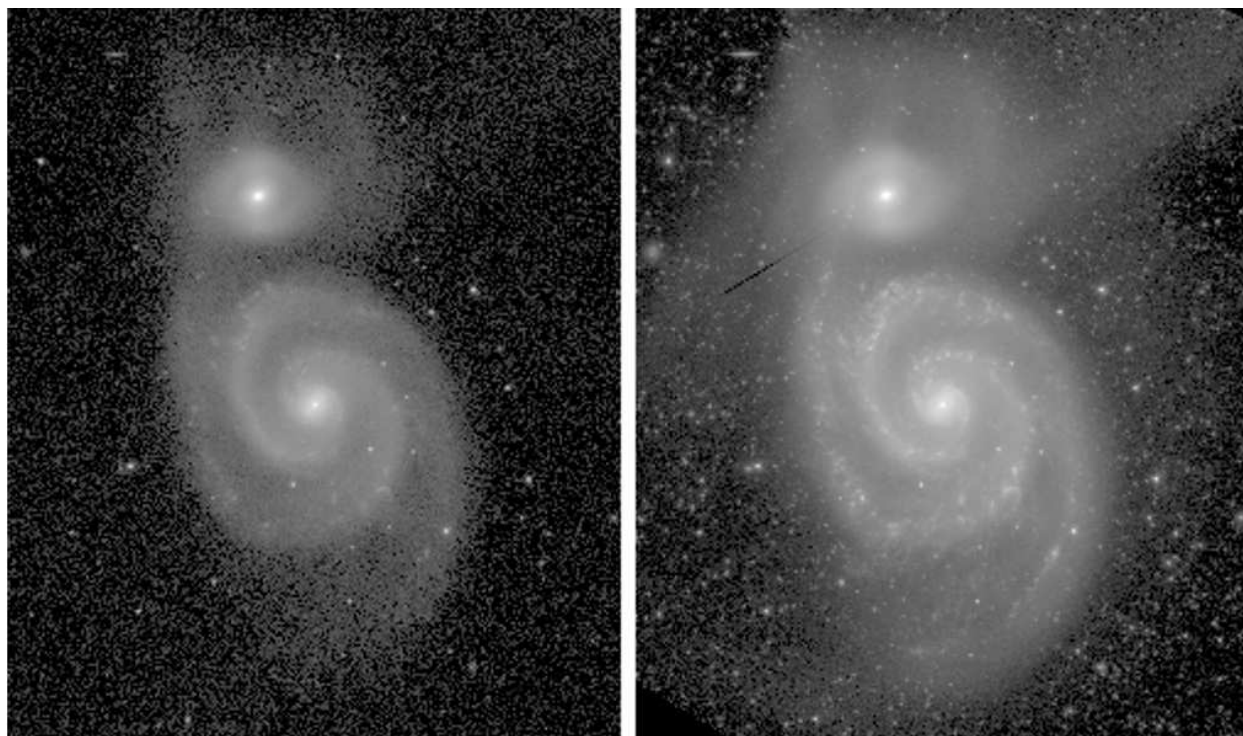


Fig. 15.— A comparison of the morphology of the M51 system in the $2.2\mu\text{m}$ K_s band (left frame) and the IRAC $3.6\mu\text{m}$ band.